

ATLAS-BASED SEGMENTATION AND CLASSIFICATION OF MAGNETIC RESONANCE BRAIN IMAGES

THÈSE N^o 2875 (2003)

PRÉSENTÉE À LA FACULTÉ SCIENCES ET TECHNIQUES DE L'INGÉNIEUR

Institut de traitement des signaux

SECTION D'ÉLECTRICITÉ

ÉCOLE POLYTECHNIQUE FÉDÉRALE DE LAUSANNE

POUR L'OBTENTION DU GRADE DE DOCTEUR ÈS SCIENCES

PAR

Meritxell BACH CUADRA

enginyeria de telecomunicacions, ETSETB - UPC, Barcelona, Espagne
et de nationalité espagnole

acceptée sur proposition du jury:

Prof. J.-P. Thiran, directeur de thèse
Dr O. Cuisenaire, rapporteur
Prof. B. Dawant, rapporteur
Prof. M. Kunt, rapporteur
Prof. G. Szekely, rapporteur
Prof. J.-G. Villemure

Lausanne, EPFL
2003

A les meves arrels: els meus
estimats avia, mare i germans.

*When you set out on the voyage to Ithaca,
pray that your journey may be long, full of
adventures, full of knowledge...*

Kostas Kavafis

I al Dani, el meu estimat company de viatge.

Contents

Contents	vii
Acknowledgments	xiii
Abstract	xv
Version abrégée	xvii
Resumen	xix
Resum	xxi
List of Figures	xxiii
List of Tables	xxvii
1 Introduction	1
1.1 Motivation	1
1.2 Aims of this thesis	2
1.3 Main contributions	2
1.4 Organization of the text	3
I Background	5
2 Brain imaging	7
2.1 Introduction	7
2.2 Brain image modalities: an overview	7
2.3 Magnetic Resonance (MR) Imaging	10
2.3.1 Physical principles of MR imaging	10
2.3.2 MR image formation	11
2.3.3 Components of a MR imaging system	11
2.3.4 Clinical applications of MRI	11
2.4 Reference imaging	12
2.4.1 History of the brain atlases	12

2.4.2	Digitized brain templates	13
2.4.3	Digitized brain atlas applications	14
2.5	Summary	15
3	Image Registration	17
3.1	Introduction	17
3.2	Medical image registration	17
3.2.1	Features and cost function	18
3.2.2	Domain of transformation	19
3.2.3	Registration problem formulation	19
3.3	Non-rigid Registration	20
3.3.1	Parametric transformations	21
3.3.2	Non-parametric transformations	21
3.4	Demons algorithm	22
3.4.1	Optical Flow Concept	22
3.4.2	Demon points	23
3.4.3	Demon forces	24
3.4.4	Iterative process	25
3.4.5	Regularization	25
3.4.6	Multiscale implementation	26
3.4.7	Bijectivity	28
3.4.8	Variations of the demons algorithm	31
3.4.9	Limitations	31
3.5	The problem of medical image registration assessment	31
3.6	Summary	32
II	Atlas-based segmentation	33
4	Atlas-based segmentation of normal anatomy	35
4.1	Introduction	35
4.2	Atlas-based segmentation	35
4.3	Analysis of demons algorithm	36
4.3.1	Global correspondence	36
4.3.2	Intensity correspondence	37
4.3.3	Demon points selection	37
4.3.4	Elasticity study	45
4.3.5	Algorithm convergence	47
4.4	Application to the segmentation of normal anatomy	53
4.4.1	Problem definition	53
4.4.2	Proposed method	53
4.4.3	Data sets and results	54
4.4.4	Discussion	56
4.5	Conclusions	56

5	Atlas-based segmentation of pathological brains	57
5.1	Introduction	57
5.2	Problem definition	57
5.3	Existing methods	58
5.3.1	Nonlinear elastic registration	58
5.3.2	Seeded atlas deformation method (SAD)	59
5.4	Proposed solution: using a model of lesion growth (MLG)	59
5.4.1	Lesion segmentation	60
5.4.2	Atlas seeding	61
5.4.3	Non-rigid deformation using a model of tumor growth	61
5.5	Data sets and Results	63
5.5.1	Deformed atlas images and deformation field	63
5.5.2	Segmentation results study	65
5.5.3	Variation of the MLG method	69
5.6	Validation	69
5.6.1	Validation of the lesion growth	72
5.6.2	Validation of the seed position	75
5.7	Discussion	78
5.8	Conclusions	79
III	Classification	81
6	Segmentation of brain tissues	83
6.1	Introduction	83
6.2	Problem definition	83
6.3	Image model	84
6.3.1	Intensity distribution model	84
6.3.2	Spatial distribution model	86
6.3.3	Anatomical prior model	89
6.4	Classification criteria	90
6.4.1	Cost function	90
6.4.2	Bayesian criterion	90
6.4.3	Maximum <i>a posteriori</i> (MAP)	90
6.5	Parameter estimation of a stochastic process	91
6.5.1	Maximum Likelihood (ML)	91
6.5.2	Expectation Maximization (EM)	91
6.6	Parametric methods	92
6.6.1	Finite Gaussian Mixture Model: FGMM (A)	92
6.6.2	Gaussian Hidden Markov Random Field model: GHMRF (B)	93
6.6.3	Gaussian and Partial Volume model: GPV (C)	94
6.6.4	GPV and HMRF model: GPV-HMRF (D)	94
6.6.5	GPV-HMRF model and Anatomical prior: GPV-HMRF-AP	95
6.7	Non parametric methods	96
6.7.1	Error probability minimization: EP (E)	96
6.7.2	Non-parametric HMRF: NP-HMRF (F)	96
6.8	Results and Validation	96
6.8.1	Data set	96

6.8.2	Results	97
6.9	Discussion	98
6.9.1	General performance	98
6.9.2	Real MRI conditions	98
6.9.3	Pure tissues and partial volume	98
6.9.4	Robustness in front of noise and inhomogeneities	99
6.9.5	Intensity versus spatial prior	101
6.9.6	Parametric vs Non-parametric	101
6.9.7	Using prior class atlases	101
6.10	Summary	102
6.11	Figures	103
IV	Applications	129
7	Potential applications	131
7.1	Introduction	131
7.2	In continuous evolution	131
7.2.1	Static analysis: image segmentation	132
7.2.2	Dynamic analysis: deformation field study	132
7.3	Gray Matter Degeneration	133
7.3.1	Data set	133
7.3.2	Proposed method	134
7.3.3	Results	136
7.3.4	Discussion	140
7.4	Multiple Sclerosis	140
7.4.1	Data set	140
7.4.2	Method and results	141
7.4.3	Discussion	144
7.5	Summary	145
V	Conclusions	147
8	General conclusions	149
8.1	Introduction	149
8.2	Review of the discussed topics	149
8.3	Achievements	150
8.4	Future directions	150
8.4.1	Prior knowledge to guide the registration	150
8.4.2	Atlas-based segmentation of pathological brains	151
8.4.3	Prior knowledge to guide the brain tissue segmentation	151
VI	Annex	153
A	Notation	155
A.1	Registration	155
A.2	Classification	156

B MAP for GHMRF	157
Bibliography	159
Curriculum Vitæ	167

Acknowledgments

I present in this thesis the research work carried out during the last 4 years at the Signal Processing Institute (ITS). Of course, this would not have been possible without the help of many people. I would like to thank them all.

Particularly, I would like to thank Prof. Murat Kunt who gave me the opportunity to join the ITS and who has always followed my work with a lot of interest. My greatest thanks to my thesis advisor Prof. Jean-Philippe Thiran who received me so kindly and gave me the opportunity to join the Computer Vision group. His enthusiasm has always been one of my greatest encouragements. I am also grateful to all the members of my jury for their interest in reading and discussing my work. Special thanks to Prof. Benoit M. Dawant, for his precious comments that have always improved my work. Also, I would like to gratefully acknowledge the enormous scientific support and friendship of Dr. Olivier Cuisenaire, who has co-directed my thesis. Merci Oli !

During these years I have strongly collaborated with many people. Particularly, it has been a great pleasure to work with neurosurgeon Dr. Claudio Pollo. I have really appreciated his availability and medical knowledge. Many thanks to Torsten Butz, Eduardo Solanas, Mathieu De Craene, Leila Cammoun, Patric Haggmann, Valerie Duay and Olivier Ecabert for their valuable help. Special thanks to the people at CHUV, Eleonora Fornari and Roberto Martuzzi, who have provided the images. Also, many thanks to all my students, Anton, Martin, Julien, Val, Bram, Jesus, Olivier, Georg, for their motivating questions and precious work.

It has been a great satisfaction to work in the nice and familiar atmosphere that ITS people produce: thanks to all the members! Special thanks to the members of the Computer Vision Group, for their support and complicity. I am also grateful to the secretaries of the laboratory, Marianne Marion, Fabienne Vionnet, Isabelle Bezzi and Corinne Degott, for their efficient work and patience and also to Gilles Auric for his logistic support. Also, thanks to Nicolas Aspert and Diego Santa Cruz for always helping me with Linux and L^AT_EX. My gratitude goes also to all my *estupendos* office mates Andrea Cavallaro, Raphael Grosbois and Adel Rahmoune for their patience and kindness.

I would like to thank also all the people in Lausanne that made my life so enjoyable during all these years. Particularly, to Maria Eugenia and Ruth for all the great moments we spent together and the hours of discussions. My acknowledgment goes also to my old friends in Barcelona who have always encouraged me. My greatest acknowledgement to the members of the Rodellar Gomez family for the support they have given me, specially to Bea and Neil for the professional correction of my English mistakes of this manuscript.

Last, but not least, I would like to thank all the members of my family for their support and love. Special thanks to my sister Anna who has come here many times to take care of me.

Finally, I would like to thank my love Dani for having always the strongest confidence in me. Thanks Dani for your unconditional love and friendship.

Abstract

A wide range of different image modalities can be found today in medical imaging. These modalities allow the physician to obtain a non-invasive view of the internal organs of the human body, such as the brain. All these three dimensional images are of extreme importance in several domains of medicine, for example, to detect pathologies, follow the evolution of these pathologies, prepare and realize surgical planning with, or without, the help of robot systems or for statistical studies. Among all the medical image modalities, Magnetic Resonance (MR) imaging has become of great interest in many research areas due to its great spatial and contrast image resolution. It is therefore perfectly suited for anatomic visualization of the human body such as deep structures and tissues of the brain.

Medical image analysis is a complex task because medical images usually involve a large amount of data and they sometimes present some undesirable *artifacts*, as for instance the noise. However, the use of *a priori* knowledge in the analysis of these images can greatly simplify this task. This prior information is usually represented by the *reference* images or *atlases*. Modern brain atlases are derived from high resolution cryosections or *in vivo* images, single subject-based or population-based, and they provide detailed images that may be interactively and *easily* examined in their digital format in computer assisted diagnosis or intervention. Then, in order to efficiently combine all this information, a battery of *registration* techniques is emerging based on transformations that bring two medical images into voxel-to-voxel correspondence.

One of the main aims of this thesis is to outline the importance of including prior knowledge in the medical image analysis framework and the indispensable role of registration techniques in this task. In order to do that, several applications using atlas information are presented. First, the atlas-based segmentation in normal anatomy is shown as it is a key application of medical image analysis using prior knowledge. It consists of registering the brain images derived from different subjects and modalities within the atlas coordinate system to improve the localization and delineation of the structures of interest. However, the use of an atlas can be problematic in some particular cases where some structures, for instance a tumor or a sulcus, exists in the subject and not in the atlas. In order to solve this limitation of the atlases, a new atlas-based segmentation method for pathological brains is proposed in this thesis as well as a validation method to assess this new approach. Results show that deep structures of the brain can still be efficiently segmented using an anatomic atlas even if they are largely deformed because of a lesion.

The importance of including a priori knowledge is also presented in the application of brain tissue classification. The prior information represented by the tissue templates can be included in a brain tissue segmentation approach thanks to the registration techniques. This is another important issue presented in this thesis and it is analyzed through a comparative study of several non-supervised classification techniques. These methods are selected to represent the whole range of prior information that can be used in the classification process: the image intensity, the local spatial

model, and the anatomical priors. Results show that the registration between the subject and the tissue templates allows the use of prior information but the accuracy of both the prior information and the registration highly influence the performance of the classification techniques.

Another aim of this thesis is to present the concept of *dynamic* medical image analysis, in which the prior knowledge and the registration techniques are also of main importance. Actually, many medical image applications have the objective of *statically* analyzing one single image, as for instance in the case of atlas-based segmentation or brain tissue classification. But in other cases the implicit idea of *changes detection* is present. Intuitively, since the human body is changing continuously, we would like to do the image analysis from a *dynamic* point of view by detecting these changes, and by comparing them afterwards with templates to know if they are *normal*. The need of such approaches is even more evident in the case of many brain pathologies such as tumors, multiple sclerosis or degenerative diseases. In these cases, the key point is not only to detect but also to quantify and even characterize the evolving pathology. The evaluation of lesion variations over time can be very useful, for instance in the pharmaceutical research and clinical follow up. Of course, a sequence of images is needed in order to do such an analysis.

Two approaches dealing with the idea of *change detection* are proposed as the last (but not least) issue presented in this work. The first one consists of performing a *static* analysis of each image forming the data set and, then, of comparing them. The second one consists of analyzing the non-rigid transformation between the sequence images instead of the images itself. Finally, both static and dynamic approaches are illustrated with a potential application: the cortical degeneration study is done using brain tissue segmentation, and the study of multiple sclerosis lesion evolution is performed by non-rigid deformation analysis.

In conclusion, the importance of including *a priori* information encoded in the brain atlases in medical image analysis has been put in evidence with a wide range of possible applications. In the same way, the key role of registration techniques is shown not only as an efficient way to combine all the medical image modalities but also as a main element in the *dynamic* medical image analysis.

Version abrégée

Dans le domaine de l'imagerie médicale il existe une grande variété de modalités d'images 3D qui permettent aux médecins d'obtenir une visualisation non invasive des organes du corps humain, comme par exemple du cerveau. Toutes ces modalités d'images sont très importantes dans divers domaines de la médecine comme par exemple pour détecter certaines pathologies, pour suivre l'évolution des ces pathologies, pour préparer et pour réaliser des opérations chirurgicales avec ou sans l'aide de systèmes robotiques ou même pour des études statistiques. Parmi toutes les modalités d'images médicales, l'Imagerie par Résonance Magnétique (IRM) est devenue très importante grâce à sa grande résolution spatiale et son fort contraste pour les tissus mous. L'IRM est donc très bien adaptée pour la visualisation anatomique du corps humain, par exemple des structures profondes ou des tissus du cerveau.

L'analyse des images médicales est très complexe car ces images sont représentées par de grandes quantités de données et elles présentent parfois des effets non désirables comme le bruit. Cependant l'utilisation d'information a priori pendant le traitement d'images peut faciliter beaucoup leur analyse. Normalement, cette information a priori est représentée par les images dites de *référence* ou *atlas*, qui déterminent un espace commun où l'anatomie humaine peut être précisément représentée comme c'est le cas du cerveau. Aujourd'hui les atlas sont dérivés des images cryosectionnées de grande résolution ou des images *in vivo* et ils sont basés sur un seul individu ou sur une population d'individus. Dans tous les cas, elles fournissent des images très détaillées qui peuvent être facilement analysées dans leur format digital pour des applications comme la vision et l'aide au diagnostic par ordinateur. Finalement, il existe une grande variété des techniques de recalage basées sur des transformations qui donnent une correspondance voxel-a-voxel des images et qui permettent de combiner très efficacement toutes les informations contenues dans les images médicales.

Un des principaux objectifs de cette thèse c'est de souligner l'importance d'inclure dans l'analyse des images médicales l'information connue a priori et le rôle indispensable des techniques de recalage. Différentes applications qui utilisent l'information contenue dans des atlas sont présentées. Tout d'abord, la segmentation basée sur un atlas est présentée car c'est une application de pointe dans l'utilisation d'information a priori. Il s'agit de recaler des images du cerveau dérivées des différents individus ou modalités d'image avec un atlas qui permettra d'améliorer la localisation et segmentation des structures d'intérêt. Cependant, l'utilisation d'atlas est parfois limitée dans certains cas ou quelques structures, par exemple un sulcus ou une tumeur, sont présents dans le patient mais ne sont pas présents dans l'atlas. On propose dans ce travail une nouvelle méthode de segmentation basée sur un atlas dans les cas de cerveaux pathologiques ainsi qu'une méthode pour sa validation. Les résultats montrent que les structures profondes du cerveau peuvent encore être segmentées efficacement à l'aide d'un atlas même si elles ont été largement déformées par une lésion.

La pertinence d'inclure l'information a priori est aussi présentée dans le cadre de la segmentation des tissus principaux du cerveau. L'information contenue dans les atlas des tissus peut être incluse

dans la méthode de classification du cerveau grâce au recalage des images. Celle-ci est analysée grâce à une étude comparative des diverses techniques de classification non supervisées. Les méthodes étudiées ont été sélectionnées de façon à bien représenter toutes les informations a priori qui peuvent être incluses: l'intensité de l'image, le modèle spatial local, et les informations a priori anatomiques. Les résultats montrent que le recalage entre le sujet et les atlas des tissus permet l'utilisation des informations a priori mais que la précision des deux, recalage et information a priori, influence fortement la qualité finale de la classification.

Un autre objectif de ce travail est de présenter le concept d'analyse *dynamique* des images médicales, où l'information a priori et les techniques de recalage jouent aussi un rôle important. En fait, diverses applications de l'analyse d'image ont pour but d'étudier de façon *statique* une image. C'est le cas par exemple de la segmentation des images basée sur un atlas ou de la classification des tissus du cerveau. Mais dans d'autres cas, l'idée implicite de détection des changements est présente. Intuitivement, comme le corps humain change continuellement, on voudrait faire une analyse de façon dynamique, c'est à dire, détecter quels sont les changements qui se sont produit et, en les comparant avec des informations a priori sur les changements, pouvoir détecter s'il s'agit de changements normaux ou pathologiques. Le besoin de cette approche est encore plus évident dans les cas de certaines pathologies comme une tumeur, la sclérose en plaque ou les maladies dégénératives du cerveau. Dans ces cas, l'objectif ce n'est pas seulement de détecter la pathologie mais aussi de la quantifier et même de la caractériser. L'évaluation des variations de certaines lésions tout au long du temps permet d'avancer les recherches pharmaceutiques et un meilleur suivi clinique. Bien évidemment, de telles études ont besoin d'une séquence temporelle d'images du patient à traiter.

Deux approches différentes sont présentées afin d'illustrer cette idée de détection des changements. La première consiste à faire une analyse statique de chaque image de la séquence et de comparer après les résultats. La deuxième est basée sur l'analyse de la transformation non rigide utilisée pour déformer une image de la séquence vers une autre. Les deux approches sont présentées à l'aide d'un exemple: l'étude de la dégénération du cortex du cerveau est fait grâce à la segmentation des tissus et l'étude de la sclérose en plaques est faite grâce à l'analyse de la déformation non rigide.

En conclusion, l'importance d'utiliser l'information a priori contenue dans des atlas dans le domaine de l'analyse d'images médicales est présentée ainsi que ses applications. De même, le rôle décisif des techniques de recalage n'est pas seulement présenté comme une façon efficace de combiner les différents types d'images mais aussi comme un élément principal dans les approches d'analyse dynamiques des images médicales.

Resumen

Hoy en día existen muchas modalidades de imágenes médicas digitales que permiten a los médicos el estudio *in vivo* de los órganos del cuerpo humano, como por ejemplo del cerebro. Estas imágenes son muy útiles en muchos campos de la medicina como por ejemplo en la detección, seguimiento y estudio de patologías, en la preparación y realización de operaciones quirúrgicas asistidas por ordenador o en estudios estadísticos. De entre todos los tipos de imágenes medicas, destaca la imagen de Resonancia Magnética (RM) por su alta resolución espacial, su gran variedad de posibles contrastes y su inocuidad al no utilizar radiación ionizante. Estas características hacen que la imagen por RM sea muy adecuada para la visualización anatómica del cuerpo humano, por ejemplo para visualizar las estructuras y los tejidos del cerebro.

El análisis de imágenes médicas es una tarea compleja ya que normalmente estas imágenes consisten en grandes volúmenes de datos y, además, presentan ruido y otros *artefactos* de la imagen como los cambios de iluminación. Sin embargo, la inclusión de información a priori en el análisis de estas imágenes puede facilitar mucho su estudio. La información a priori está normalmente representada por las *imágenes de referencia* o *atlas* que determinan un espacio concreto en el cual se describe la anatomía, por ejemplo, del cerebro humano. Actualmente los atlas del cerebro (creados a partir de secciones criogénicas o de imágenes *in vivo*, basados en un solo sujeto o en toda una población) proporcionan imágenes digitales muy detalladas que pueden ser examinadas interactiva y fácilmente en el diagnóstico de tratamientos y planificación de los mismos por ordenador. En consecuencia, para poder combinar de manera eficiente toda la información contenida en los distintos tipos de imágenes médicas surgen las técnicas de registro* que proporcionan las transformaciones geométricas que sitúan dos imágenes en correspondencia anatómica voxel a voxel.

Uno de los objetivos principales de esta tesis es remarcar la importancia de incluir información a priori en el proceso de análisis de imágenes médicas así como resaltar el papel indispensable de los métodos de registro en este proceso. Para demostrarlo, presentamos distintas aplicaciones que utilizan atlas. Primero, presentamos la aplicación de *segmentación basada en atlas* en sujetos con anatomía normal ya que es una de las aplicaciones principales que incluyen información a priori. La segmentación basada en atlas consiste en registrar una o varias imágenes del cerebro en el sistema de referencia del atlas para facilitar la localización y segmentación de las estructuras de interés. Sin embargo, el uso del atlas está limitado en algunos casos donde puede haber estructuras, como un tumor o un sulcus, que estén presentes en el paciente pero no en el atlas. Para solventar este problema, se propone un nuevo método de segmentación basado en atlas para cerebros patológicos así como un método para su validación. Los resultados obtenidos demuestran que las estructuras de interés del cerebro se pueden segmentar utilizando la información contenida en un atlas aunque estén muy deformadas debido a una lesión.

*Anglicismo de *registration*.

La importancia de la utilización de la información a priori se demuestra también en la clasificación de los distintos tejidos del cerebro. La información a priori contenida en los atlas de tejidos del cerebro puede ser utilizada por los métodos de clasificación gracias al registro de imágenes. Ésta es también una aplicación importante y se presenta a través del estudio comparativo de varias técnicas de clasificación no supervisadas. Los métodos de clasificación analizados han sido elegidos de manera que representen la diversidad de información a priori que se puede utilizar, es decir, la intensidad de la imagen, la información local espacial y la información global contenida en los atlas. Los resultados obtenidos demuestran que el uso de atlas es posible gracias a las técnicas de registro pero que la calidad de la clasificación depende mucho de la precisión del método de registro y de la calidad de la información a priori utilizados.

El tercer objetivo de esta tesis es presentar el concepto de análisis *dinámico* de las imágenes médicas, en el cual, la información a priori y los métodos de registro siguen siendo de mucha importancia. En realidad, muchas aplicaciones de las imágenes medicas tienen como objetivo el análisis *estático* de una imagen como, por ejemplo, en el caso de la segmentación basada en atlas o en la clasificación de tejidos del cerebro. Pero en otros casos la idea de *detección de cambios* es implícita. Intuitivamente, ya que en el cuerpo se producen cambios continuamente, podríamos analizar las imágenes medicas desde un punto de vista dinámico, es decir, detectando los cambios que se producen y comparándolos con modelos de cambios para determinar si son normales. La necesidad de detección de cambios es aún más evidente en el estudio de ciertas patologías del cerebro como por ejemplo tumores, esclerosis múltiple o enfermedades degenerativas. En estos casos, la clave está no sólo en detectar sino también en cuantificar e incluso caracterizar la evolución de la lesión. Este tipo de estudios pueden ser muy útiles por ejemplo en la investigación farmacéutica o en el seguimiento clínico. Evidentemente, para realizar este tipo de estudios evolutivos se considera que se dispone de una secuencia de imágenes a distintos intervalos de tiempo.

Dos métodos distintos que lidian con la idea de detección de cambios son presentados en esta tesis. El primero consiste en realizar el análisis estático de cada una de las imágenes que forman la secuencia y luego comparar los resultados. El segundo método consiste en realizar el análisis de la transformación obtenida entre las imágenes de la secuencia, en vez de realizar el análisis de cada imagen. Finalmente, presentamos una aplicación potencial de cada uno de los métodos como ejemplo: el estudio de la degeneración cortical del cerebro que esta hecho a partir de la clasificación de tejidos y el estudio de la evolución de esclerosis múltiple que esta hecha a partir del análisis de la transformación obtenida por registro.

En conclusión, se ha puesto en evidencia la importancia de considerar la información a priori de los atlas anatómicos del cerebro en el análisis de imágenes médicas en una gran variedad de aplicaciones. De la misma manera, el papel decisivo de los métodos de registro ha sido presentado no sólo como una manera eficiente de combinar las distintas modalidades de imágenes médicas sino también como un elemento importante en el análisis dinámico de las mismas.

Resum

Avui en dia podem trobar una gran varietat de modalitats d'imatges mèdiques que permeten l'estudi *in vivo* dels òrgans del cos humà. Aquestes modalitats d'imatge són de gran utilitat en diversos camps de la medicina com per exemple en la detecció, seguiment i estudi de patologies, en la preparació i realització d'operacions quirúrgiques assistides, o no, per ordinador o en estudis estadístics. D'entre totes les modalitats d'imatge destaca la Resonància Magnètica (RM) per la seva alta resolució espacial, contrast d'intensitat i la seva innocuïtat, ja que no utilitza radiació ionitzant. Totes aquestes característiques fan que la RM sigui molt adequada per a la visualització del cos humà, per exemple per a visualitzar les estructures i els teixits del cervell.

L'anàlisi d'imatges mèdiques és, però, complexa ja que normalment les imatges estan formades per grans volums de dades i presenten soroll i d'altres *artefactes* com els canvis d'il·luminació. Amb tot, la introducció d'informació *a priori* en l'anàlisi d'imatges mèdiques pot facilitar enormement aquesta tasca. En molts casos aquesta informació *a priori* està continguda en les anomenades imatges de *referència*, o *atles*, les quals determinen un espai concret on es pot representar l'anatomia humana, com per exemple, l'anatomia del cervell. Actualment els atles del cervell (creats a partir d'imatges criogèniques o *in vivo*, basats en un sol individu o en tota una població) proporcionen imatges digitals molt detallades que poden ser examinades interactivament i fàcilment en el procés de diagnosi i planificació de tractaments per ordinador. Conseqüentment, per poder combinar eficientment totes aquestes informacions contingudes en les diferents modalitats d'imatge, emergeixen les tècniques de registre* que tenen com a objectiu trobar la transformació geomètrica que situa dues imatges en correspondència anatòmica voxel a voxel.

Un dels principals objectius d'aquesta tesi és demostrar la importància de considerar la informació *a priori* en l'anàlisi d'imatges mèdiques així com ressaltar el paper indispensable de les tècniques de registre en aquesta anàlisi. Per demostrar-ho, diferents aplicacions mèdiques on s'utilitzen els atles són estudiades en el marc de l'anàlisi d'imatges. En primer lloc presentem la *segmentació basada en atles* ja que és una de les aplicacions destacades de la utilització de la informació *a priori*. La segmentació basada en atles consisteix en alinear el sistema de referència de l'atles amb el d'una o varies imatges del cervell per facilitar-ne la localització i delineació de les estructures d'interès. L'ús de l'atles queda, però, limitat en els casos on algunes estructures, com per exemple un tumor o un solc, poden existir en l'individu i no en l'atles. Per resoldre aquest problema, proposem un nou mètode de segmentació basada en atles en el cas de cervells patològics així com un mètode de validació. Els resultats obtinguts demostren que les estructures d'interès es poden segmentar utilitzant un atles encara que estiguin molt deformades per culpa d'una lesió.

La importància de la utilització de la informació *a priori* es demostra també en la classificació dels diferents teixits del cervell. La informació *a priori* continguda en els atles de teixits cerebrals

*Anglicisme de *registration*

pot ser introduïda en els mètodes de classificació gràcies al registre d'imatges. Aquesta és una altra aplicació important de l'ús d'informació *a priori* i la presentem a través d'un estudi comparatiu de diversos mètodes de classificació *no supervisats*. Els mètodes analitzats han estat escollits de manera que representen el ventall d'informació *a priori* disponible, és a dir, la intensitat de la imatge, la informació espacial local i la informació espacial global continguda en els atlas. Els resultats obtinguts demostren que la qualitat final de la classificació depèn molt de la precisió del mètode de registre i de la qualitat de la informació utilitzats *a priori*.

El tercer objectiu principal d'aquesta tesi és presentar el concepte d'anàlisi *dinàmica* de les imatges mèdiques, en el qual la informació *a priori* i els mètodes de registre segueixen sent de molta importància. Hem vist que algunes aplicacions de l'anàlisi d'imatges mèdiques tenen com a objectiu l'estudi estàtic d'una imatge, com és el cas de la segmentació basada en atlas o de la classificació dels teixits del cervell. Però en d'altres casos, la idea de detecció de canvis és implícita. Intuïtivament, ja que el cos humà canvia contínuament, les imatges mèdiques es podrien analitzar també des d'un punt de vista dinàmic, és a dir, detectant els canvis que es produeixen en una seqüència d'imatges i comparant-los amb un patró de canvis per saber si són normals o patològics. La necessitat de la detecció de canvis és encara més evident en el cas de certes patologies del cervell com per exemple un tumor, l'esclerosi múltiple o d'altres patologies degeneratives. En aquests casos, la clau no és només detectar sinó també quantificar i fins i tot caracteritzar l'evolució de la lesió. L'estudi evolutiu pot ser de molta utilitat per exemple en la recerca farmacèutica o en el seguiment clínic. Evidentment, per a realitzar aquest tipus d'estudi es considera que una seqüència d'imatges a diferents intervals de temps és disponible.

En aquesta tesi són presentats dos mètodes diferents que tracten la idea de detecció de canvis. El primer consisteix a realitzar l'anàlisi estàtica de cada una de les imatges de la seqüència i, després, a comparar-ne els resultats. El segon mètode consisteix a realitzar l'anàlisi de la transformació obtinguda gràcies al registre de les imatges de la seqüència, en comptes de realitzar l'anàlisi estàtica de cada imatge. Finalment, presentem una aplicació potencial de cada un dels mètodes com a exemple il·lustratiu: l'estudi de la degeneració del còrtex cerebral es fa a partir de la classificació dels teixits del cervell i l'estudi de l'evolució de l'esclerosi múltiple es fa a partir de l'anàlisi de la transformació obtinguda en el registre d'imatges.

En conclusió, s'ha demostrat la importància d'incloure la informació *a priori* continguda en els atlas del cervell en diverses aplicacions de l'anàlisi d'imatges mèdiques. Així mateix, hem presentat el paper clau dels mètodes de registre, no només com una manera eficaç de combinar les diferents modalitats d'imatge, sinó també com un element important de l'anàlisi dinàmica d'aquestes.

List of Figures

2.1	Anatomical brain images	8
2.2	Functional brain images	9
2.3	Magnetic Resonance Imaging	12
2.4	Reference imaging	13
2.5	Digital brain atlas of the Surgical Planning Laboratory of Harvard Medical School	16
2.6	Digital brain phantom from McConnell Brain Imaging Center	16
2.7	SPM probability maps of brain tissue.	16
3.1	Domain and nature of a transformation. Figure extracted from [17].	19
3.2	Polarity in demon points.	24
3.3	Iteration i of demons algorithm.	26
3.4	Multiscale.	27
3.5	Asymmetry of demons algorithm transformation.	28
3.6	Definition of the residual vector field.	29
3.7	Improvements of the bijective demons algorithm.	30
3.8	Residual vector field study.	30
4.1	Scheme of the atlas-based segmentation process.	36
4.2	Demon points selection: synthetic images.	38
4.3	Analysis of the demon points selection.	39
4.4	Demon points selection: Histogram of the intensity gradient.	40
4.5	Optimization functions for demon points selection.	41
4.6	Analysis of demon points selection in MR-T1 brain images.	43
4.7	Comparison with B-splines: input data set	45
4.8	Comparison with B-splines: deformation analysis	46
4.9	Deformation in function of the elasticity parameter.	48
4.10	Elasticity study	49
4.11	Convergence analysis in function of the elasticity.	50
4.12	Demons algorithm convergence study: MR-T2 weighted brain images.	51
4.13	Demons algorithm convergence for different stopping criteria.	52
4.14	Region of interest: trunk and cerebellum of the SPL atlas.	54
4.15	Contour of the trunk and cerebellum after the affine and non-rigid registrations.	54
4.16	Qualitatively analysis of automatic trunk an cerebellum segmentation.	55
5.1	Segmentation of different types of tumors using ATM SVC.	61
5.2	Transformation inside the tumor.	62

5.3	MLG block diagram.	62
5.4	Data set of 4 meningiomas.	64
5.5	Comparison between seeded atlas deformation (SAD) and a model of lesion growth (MLG) methods.	66
5.6	Comparison between SAD and MLG segmentations.	67
5.7	Atlas-based segmentation using a model of lesion growth.	68
5.8	Initialization errors.	69
5.9	Block diagram: modification of the atlas-based segmentation method using a model of lesion growth.	70
5.10	Atlas-based segmentation using a model of lesion growth <i>modified</i>	71
5.11	Results of the proposed validation.	73
5.12	Atlas-based segmentation of the <i>synthetic atlas-patient</i>	74
5.13	Different locations of the initial seed.	76
5.14	Tumor growth for different seed positions.	76
5.15	Segmentation results for each seed position.	77
5.16	Zoom of segmented ventricles and thalamus.	77
5.17	Discussion of deformation errors	79
6.1	Partial volume density	86
6.2	Probability maps for the 5 brain tissues constructed from the ground truth.	95
6.3	Probability maps for the 5 brain tissues constructed from SPM	95
6.4	Analysis of CSF and WM mixture tissue distribution.	99
6.5	Robustness of the classification methods.	100
6.6	Digital brain phantom T1-MRI with 5% noise and 0% RF	103
6.7	Classification image results of 5N0RF	104
6.8	Histogram fitting for 5N0RF	105
6.9	Digital brain phantom T1-MRI with 7% noise and 20% RF	107
6.10	Classification image results of phantom 7N20RF	108
6.11	Histogram fitting for phantom 7N20RF	109
6.12	Digital brain phantom T1-MRI with 9% noise and 40% RF	111
6.13	Classification image results of phantom 9N40RF	112
6.14	Histogram fitting for phantom 9N40RF	113
6.15	Percentage of correct classification for all phantoms.	115
6.16	Percentage of false classification for all phantoms.	116
6.17	Correct classification: intensity vs spatial priors.	117
6.18	False classification: intensity vs spatial priors.	118
6.19	Classification image results of 5N0RF using atlas prior	119
6.20	Histogram fitting for 5N0RF	120
6.21	Classification image results of 7N20RF using atlas prior	122
6.22	Histogram fitting for 7N20RF	123
6.23	Classification image results of 9N40 using atlas prior	125
6.24	Histogram fitting for 9N40RF using atlas prior	126
6.25	Correct and false classification of methods using atlas	128
7.1	Cortical degeneration: sequence of T1-MR brain images after affine registration.	133
7.2	Block diagram of the proposed method.	134
7.3	Inhomogeneity correction of the image 1	134
7.4	Brain tissue segmentation of image 1.	135

7.5	Smoothing of CSF, CG and GM posterior probability maps	136
7.6	GM degeneration maps.	137
7.7	Region of degeneration	138
7.8	Candidate to degeneration region 1	138
7.9	Candidate to degeneration region 2	139
7.10	Candidate to degeneration region 3	139
7.11	Mathematical operators	142
7.12	Selection of the regions of interest	142
7.13	Multiple Sclerosis manual segmentation	143
7.14	Evolving lesions: automatically detected	143
7.15	Evolving lesions: not detected	143
7.16	Candidates to a lesion or false alarms	143
7.17	Lesion increment volume profile	144

List of Tables

2.1	Anatomical brain image modalities	8
2.2	Functional brain image modalities	10
2.3	Reference brain imaging	15
3.1	Different registration techniques classification.	20
3.2	Classification of the warping techniques.	22
3.3	Statistics on the residual error fields.	30
4.1	Analysis of demon points selection: synthetic images.	40
4.2	Analysis of demon points selection in MR-T1 brain image.	44
4.3	Comparison between B-splines and demons deformation	44
4.4	Elasticity study.	47
4.5	Study of the demons algorithm convergence in synthetic images.	51
4.6	Study of the demons algorithm convergence in MR-T2 brain images.	52
4.7	Estimated gray and white matter volumes of the brain.	56
5.1	Variability of the segmentation in function of the initial seed position.	78
6.1	Confusion Table of 5N0RF	106
6.2	Percentage of correct classification for 5N0RF	106
6.3	Confusion Table of 7N20RF	110
6.4	Percentage of correct classification for 7N20RF	110
6.5	Confusion Table of 9N40RF	114
6.6	Percentage of correct classification for 9N40RF	114
6.7	Confusion Table of 5N0RF using atlas prior	121
6.8	Percentage of correct classification for 5N0RF with atlas prior	121
6.9	Confusion Table of 7N20RF using atlas prior	124
6.10	Percentage of correct classification for 7N20RF with atlas prior	124
6.11	Confusion Table of 9N40RF using atlas prior	127
6.12	Percentage of correct classification for 9N20RF with atlas prior	127
7.1	Increment of the active detected lesions.	144

Introduction

1

*Questa è una storia semplice,
ma non è facile da raccontare.*
Giosué Orefice, "La Vita è bella"(1997).

1.1 Motivation

Nowadays, different modalities of images can be found in medical imaging that allow us to obtain a non-invasive view of the internal organs of the human body, such as the brain. All these three dimensional image modalities are of extreme importance in several domains of medicine, for example, to detect pathologies, follow the evolution of these pathologies, prepare and realize surgical planning with, or without, the help of robot systems or for statistical studies. The different types of medical images do not exclude each other, on the contrary, they usually contain complementary information even within the same modality.

Among all the medical image modalities, Magnetic Resonance Imaging (MRI) has recently become of great interest in many research areas. MRI creates a 3D image of the object under study, exploiting the magnetic properties of the water (hydrogen) contained in the human body. Thanks to its great spatial and contrast image resolution, MR images are perfectly suited for anatomic visualization of the human body such as deep structures and tissues of the brain, the neck, the heart, the breast, etc. Also, MRI has the advantage over other medical image modalities that it does not use ionizing radiation. However, it also presents some limitations. For instance, a MR exam cannot be performed on patients with metallic devices such as pacemakers or with patients who are claustrophobic (although new MRI systems are more open).

The analysis of medical images is a complex task because they usually involve a large amount of data and they present sometimes some undesirable *artifacts*, as for instance the noise. However, the use of *prior* knowledge on the medical image analysis can greatly simplify this task. This prior information is usually represented by the *reference* or *atlases*. Modern brain atlases derived from high resolution cryosections or *in vivo* images, single subject-based or population-based, provide detailed images and may be interactively examined in their digital format. These new digitized

brain atlases try to overcome the earlier textbook limitations and their main advantages are that they provide a lot of detail and may *easily* be used in computer assisted diagnosis or intervention.

The *brain warping or registration* techniques are a battery of methods and algorithms that emerges in order to efficiently combine all these different sources of information. They consist of finding the transformation that brings two medical images into voxel-to-voxel correspondence. Many variables participate in the registration paradigm and they allow many ways of classifying the registration techniques. For instance, the warping methods can be divided into global or local transformations. Global transformations are typically applied to compensate for the different position between two acquisitions (rotation, translation, scaling and shearing). Local registration is usually applied to capture or compensate for the morphological variability in brain anatomy by performing a real *deformation*. However, many local registration methods require a global transformation as initialization steps that makes the registration process a tandem of both types of transformations.

Thanks to the registration algorithms, the brain images derived from different subject and modalities can be for instance placed within the atlas coordinate system to improve localization and delineation of structures, enabling correlations between individuals and modalities. Thus, digital atlases may be used to calculate and provide morphometry and morphological measurements within a precise anatomical framework by mapping the template onto the target image. In the same way, population-based templates provide a representation of the human diversity neuroanatomy. Then, these templates can be used to detect and measure possible *abnormal* neuroanatomies.

1.2 Aims of this thesis

The first aim of this thesis is to outline the importance of including reference imaging in the medical image analysis framework. The application of atlas-based segmentation in the case of normal anatomy is presented as it is one important application of medical image analysis using prior knowledge. Then, the problem of using the anatomical atlas in the case of pathological anatomy arises. Thus, the second aim of this thesis is to efficiently segment deep structures of the brain using an anatomical atlas even if they are largely deformed because of a lesion. In order to do that a new atlas-segmentation method for pathological brains is proposed as well as a validation method to assess this new approach.

The effect of including a priori knowledge is also shown in the case of brain tissue segmentation through a comparative study of several classification techniques. The third goal of this work is to quantify the influence of prior information on the performance of several classification techniques. The methods presented in this validation are selected to represent the whole range of prior information that can be used in the classification: the voxel intensity, the local spatial model, and the prior templates.

Finally, the fourth aim of this work is to present the concept of *dynamic* medical image analysis, in which prior knowledge and registration techniques are also of major importance. The idea is to analyze and quantify the anatomy *changes* since the human body is in continuous motion. Two different approaches dealing with the idea of *changes detection* are proposed and they are illustrated by two potential applications: the cortical degeneration study is done using the brain tissue segmentation, and the study of multiple sclerosis evolution is performed by non-rigid deformation analysis.

1.3 Main contributions

The main contributions of this thesis can be summarized as follows:

- A complete analysis of the demons algorithm input parameters.
- A new atlas-based segmentation approach of deep structures in pathological brains using a model of tumor growth.
- A new validation method of the proposed model of lesion growth.
- Validation of brain tissue classification techniques using a whole range of prior information, i.e. intensity, spatial and anatomical priors.
- A new approach for localizing and quantifying gray mater degeneration using a 5 tissue classification technique.

1.4 Organization of the text

This dissertation is organized as follows. First, Chapter 2 and Chapter 3 present the background of this thesis. An overview of the existing medical image modalities is introduced in Chapter 2. Among these modalities, special attention is paid to MR imaging and to the digitized brain atlas since these two types of images are the object of the research presented here. Then, in Chapter 3, the registration problem and its basic theoretical concepts are presented. Focus on the non-rigid registration techniques is done and special attention is paid also to the *demons* algorithm that is described in detail because it is the warping technique used in this work. Second, Chapter 4 and Chapter 5 presents the atlas-based segmentation of deep brain structures. In Chapter 4, the solutions overcoming the main limitations of the *demons* algorithm are presented and the choice of its input parameters is discussed. Then, an example of atlas-based segmentation of normal anatomy is shown. The problem of using a priori information to register pathological brains is presented in Chapter 5. A new atlas-based segmentation method is proposed that tries to overcome the limitations of the existing solutions. Also, a new validation method to assess the final segmentation is proposed. Third, the brain tissue segmentation process is presented in Chapter 6 through comparative study of some of the most commonly used approaches. These methods were selected to represent the whole range of prior information that can be used in the tissue classification, i.e. intensity, spatial and prior templates. Fourth, the concept of *evolution study* in medical image analysis is presented in Chapter 7. Two different approaches leading with the *study of changes* are presented and they are illustrated with two different applications: the gray mater degeneration study is done using the brain tissue segmentation, and the study of multiple sclerosis evolution is performed by non-rigid deformation analysis. Fifth, general conclusions and an outline of some future directions are presented in Chapter 8. Finally, complementary information is given in the annex of this dissertation. Appendix A presents the general notation and Appendix B shows how the Maximum a Posteriori (MAP) classification is done when using a Markov Random Field.

Part I

Background

Brain imaging

2

- *I haven't got a brain... only straw.*
- *How can you talk if you haven't got a brain?*
- *I don't know... But some people without brains do an awful lot of talking... don't they?*
Scarecrow and Dorothy, "Wizard of Oz "(1939).

2.1 Introduction

Many image modalities can be used in medical image analysis. This chapter presents a brief overview of these images focusing on brain imaging. Then, the basic principles of magnetic resonance imaging and state of the art of the reference imaging are explained in more detail within this framework since these are the image modalities used in this thesis.

2.2 Brain image modalities: an overview

There exists a wide range of 3D medical image modalities that allow neuroscientists to *see* inside a living human brain. This 3D brain imaging allows, for instance, to better localize specific areas inside the brain and to understand the relationships between them. Brain imaging can be divided into three main groups: *anatomical*, *functional* and *reference* imaging.

Anatomical imaging allows the study of the anatomical structures of the head such as the bones or the different brain tissues. For instance, the *Computed Tomography (CT) scan* uses a series of X-ray beams passing through the head, followed by a tomographic reconstruction, to build a 3D image of the head where bones and soft tissues are clearly identified. *Magnetic Resonance (MR) imaging* provides also an anatomical view of the tissue and deep structures of the brain thanks to the magnetic properties of the water contained in the human body (a detailed description of MR imaging is presented in section 2.3). Diffusion tensor MR brain imaging is a relatively new image modality that permits in vivo measures of the self-diffusion properties of water in living tissues [8]. This measure becomes highly anisotropic and oriented in areas of compact nerve fiber organization

ANATOMICAL IMAGING			
Organ	<i>X-ray</i>	<i>MRI</i>	<i>Ultrasounds</i>
Soft tissue	CT	T1,T2,PD	B-Mode
Water diffusion		DT-MRI	
Bone	CT		
Blood vessels	CTA	MRA	Doppler
Blood flow, volume	Perfusion CT	Perfusion MR	

Table 2.1: Classification of anatomical image modalities in function of the visualized structures.

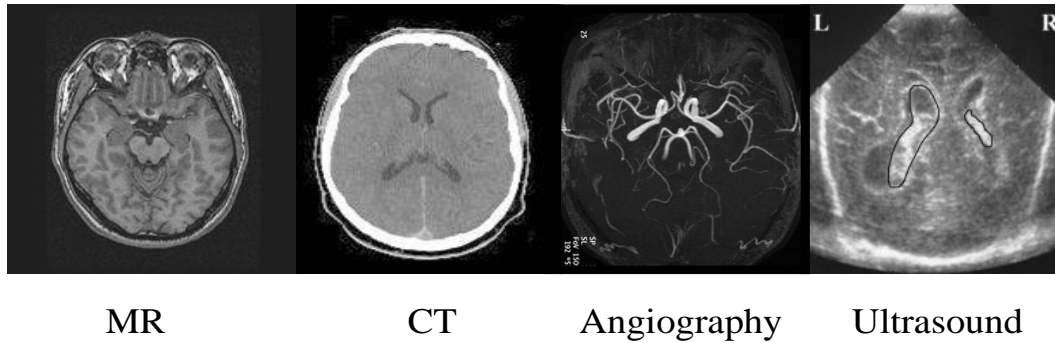


Figure 2.1: Anatomical Brain Images. MRA is from <http://radi.med.hokudai.ac.jp>. Ultrasound is from <http://www.medphys.ucl.ac.uk>.

of the brain providing an indirect way of white matter mapping and fiber tract identification [52, 64]. Other anatomical images can be obtained, for instance, using MR or CT principles for *Angiography* (MRA or CTA respectively), that provide a 3D image of blood vessels. In between anatomical and functional imaging, there are CT and MR *perfusion* that are used to assess cerebral blood flow and blood volume in various brain regions. A contrast agent is injected and the volume of interest is then scanned over time. Then, the resulting time series are processed to extent perfusion parameters. Finally, the *echography* generates an image by measuring the reflected sound waves of high frequency (hence, it is also called *ultrasound* imaging). Because high-frequency sound waves cannot penetrate bone or air, this modality is specially useful in imaging soft tissues and fluid filled spaces. Echography is thus quite often used in brain imaging, mainly in pediatrics and in blood vessels analysis. As seen, there is a large diversity of anatomical imaging and they are usually complementary to each other. For instance, in the case of radiotherapy, MR and CT are both necessary: the areas to treat are firstly localized in the MR and the doses to use are then determined using the CT. However, MRI usually presents the best spatial and contrast image resolution and is perfectly suited for anatomic visualization of deep structures of the brain.

Table 2.1 summarizes the above classification of anatomical imaging in function of the physical support used in the acquisition process and in function of the structures that are better visualized. Figure 2.1 shows some examples of anatomical brain imaging.

Functional imaging allows the study of the brain activity by picturing the motor, sensor or cognitive tasks of the brain. Most of the functional imaging techniques can be classified into two major types of images: *hemodynamic-metabolic* and *electric-magnetic* [62]. *Positron Emission Tomography (PET)*, *Single Photon Emission Computed Tomography (SPECT)* and *Functional Magnetic Resonance Imaging (fMRI)* are included in the first group while *Electroencephalography (EEG)* and *magnetoencephalography (MEG)* belong to the second.

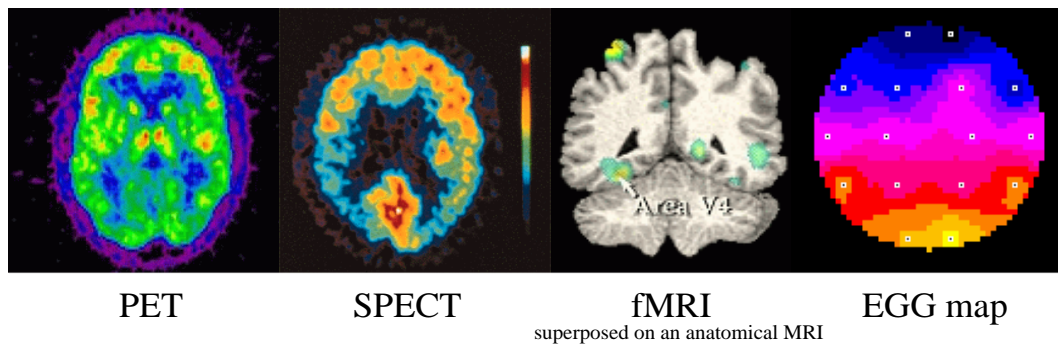


Figure 2.2: Functional Brain Images. SPECT is from <http://webnt.physics.ox.ac.uk>. EEG is from www.chasque.net.

PET and SPECT measure emissions from radioactively labelled chemicals, also known as *tracers* (e.g., fluoro-desoxy glucose FDG in PET), that have been injected into the bloodstreams. These tracers distribute over the body in a way that depends on its own properties and on the state of the brain. Then, the 2D or 3D-image reconstruction of the distribution of these chemicals throughout the brain is done. A particular tracer is used for each of the brain system or process to be studied. For instance blood flow, oxygen and glucose metabolism, protein synthesis, or drug concentrations can be measured. Both PET and SPECT have the disadvantage of having low temporal resolution. PET have more spatial resolution that SPECT though, particularly of deeper brain structures. SPECT studies are longer since its tracers deteriorate more slowly than PET.

fMRI relies on the so-called *Blood Oxygenation Level Dependent (BOLD)* effect. Brain activation leads to changes in the concentration and ratio of deoxyhemoglobin within the activated region which acts as an endogenous paramagnetic contrast agent. Indeed, increased blood flow reduces the local concentration of deoxyhemoglobin causing an increase in the MR signal in a PD-weighted MRI (see Section 2.3). The fMRI acquisition is faster than PET or SPECT and that allows greater precision in determining active areas and how long the areas remain active: one image of brain activity per second can be acquired with fMR imaging while PET studies take about 40 seconds or longer to acquire image brain activity. However, in some cases, the use of PET has some advantages over fMRI. For instance, in the case of auditive or language studies fMRI scans can be badly suited because the gradient coils used in MR imaging are quite noisy. Also, since fMRI scans are more sensitive to the subject movement than PET, for some particular patient groups PET studies could be preferable than fMRI.

EEG and MEG use electrodes and sensors placed on the scalp to detect and measure patterns of electrical and magnetic activity emanating from the brain. Thus, they directly measure the neuronal activity while PET, SPECT and fMRI rely on the induced physiology of the neurons activity. They have greater temporal resolution than fMRI, PET or SPECT (they can record patterns of neural activity occurring within fractions of a second). However, its spatial localization is less precise than fMRI and PET. Figure 2.2 shows some examples of functional brain imaging.

Reference imaging refers to all the *a priori* brain imaging information available. First, the *textbook brain atlas* and, then, the *digitized brain atlas* compose the reference imaging. This image modality is extensively presented in section 2.4.

FUNCTIONAL IMAGING		
Measure	<i>Hemodynamic-metabolic</i>	<i>Electric-Magnetic</i>
Electric field		EEG
Magnetic field		MEG
rCBF	PET, SPECT	
rCMRglc	PET, SPECT	
BOLD	fMRI	

Table 2.2: Classification of functional brain image modalities. Either electric and magnetic field refer to the ones generated by neural activity. rCBF denotes the regional cerebral blood flow. rCMRglc refers to the regional cerebral glucose metabolism. BOLD denotes the blood oxygenation level dependent effect.

2.3 Magnetic Resonance (MR) Imaging

Magnetic resonance imaging (MRI) creates a 3D image of the object under study exploiting *Nuclear Magnetic Resonance (NMR)* phenomena and the magnetic properties of water (hydrogen) contained in the human body. In 1946, the NMR phenomenon was first observed independently by Bloch [12] and Purcell [91]. Then, in 1973, Lauterbur [68] generates the first MR images.

A brief introduction to the NMR phenomenon and the basic principles of the MRI formation are presented. This overview is based on several documents as well as online sources [44, 56, 59, 78] to which the interested reader can refer for more details.

2.3.1 Physical principles of MR imaging

Atomic nuclei with an odd number of protons (for instance, hydrogen nuclei) possess an intrinsic characteristic known as *spin-angular momentum* derived from the motion, or *precession* of the charged particles. When a human body is placed in a large magnetic field (B_0), many of the free hydrogen nuclei align themselves along or opposite to the magnetic field direction. The excess of spins create a net magnetic moment, M , parallel to B_0 . That is called *polarization* and the direction along the polarization field B_0 is known as *longitudinal*, z-axis, and the *transverse plane* is the plane perpendicular to B_0 , xy plane. The hydrogen nuclei actually precess about the magnetic field direction like gyroscopes at a rate

$$\omega_0 = \gamma B_0, \quad (2.1)$$

where the angular frequency ω_0 is called Larmor frequency and it is proportional to the applied magnetic field strength by a *gyromagnetic* ratio, γ , characteristic of the atom being imaged ($\gamma \simeq 42.6\text{MHz/Tesla}$ for hydrogen).

Then, a radio-frequency (RF) pulse, B_{rf} , with a frequency ω_0 is applied perpendicular to B_0 and it causes M to tilt away from the polarization magnetic field. This effect is called *resonance*. When the RF pulse stops, the nuclei return to the equilibrium such that M is again parallel to B_0 . This behavior is known as *relaxation*. During this relaxation process, the nuclei lose energy and produces a RF signal, the *free-induction decay (FID)*, that can be measured by an antenna or receiver coil. There are two interactions that describe this relaxation. One is the longitudinal relaxation that results from “spin-lattice” interactions (T_1) and the other is the transverse relaxation that results from “spin-spin” interactions (T_2), and results in an exponential decay of the transverse magnetization towards zero. Longitudinal and transverse relaxation are much slower effects than precession. For biological tissue the relaxation times vary from hundreds of microseconds to several

seconds. The differences in relaxation times (T_1 and T_2) and proton densities (PD) of different tissue types are exploited as a mechanism of generating contrast between different tissues in imaging, i.e. the voxel intensity that is visualized (see Fig. 2.3).

2.3.2 MR image formation

To produce a 3D image, the FID resonance signal must be encoded in each dimension. That is done by applying a spatially linearly variable (stationary in time) magnetic field, B'_0 that induces spatial distribution of the Larmor frequencies over the volume. Spatially constant derivatives of B'_0 , (G_x, G_y, G_z) , determine the local resolution of the image. The image reconstruction process can be summarized by three steps: selective excitation, phase encoding and frequency encoding. Selective excitation applies a linear magnetic field that causes the Larmor frequencies to linearly change in the longitudinal. Thus, a transversal plane can be selected by choosing the B_{rf} frequency to correspond to the Larmor frequency of that plane or *slice*. Then, the 2D spatial reconstruction in each slice is done by phase and frequency encoding. A linear field of gradient G_y is first applied causing the Larmor frequencies distribution to linearly vary according the y-direction. This causes a variation to the phase magnetization. When G_y is switched off, frequency returns to a constant value over the slice while phase remains proportional to y. Finally, a constant gradient G_x is applied perpendicular to G_y . Then, Larmor frequencies distribution linearly changes, this time according to the x-direction, while they still have a phase variation in y-direction. The resulting signal after successively applying G_z, G_y , and G_x corresponds to the Fourier transform of the transversal magnetization M_{xy} and produces a single row in the spatial frequency space also known as *k-space*. After repeating this process for different values of G_y a spatial matrix in the k-space is recovered and applying the inverse Fourier transform one slice of the MR image is obtained. The image volume is completed by repeating this process for different values of the selective excitation frequency.

A *typical* 3D MRI data set is formed by $256 \times 256 \times 124$ voxels with $0.9375 \times 0.9375 \times 1.5\text{mm}^3$ voxel resolution. Its acquisition in a 1.5 Tesla magnetic field can takes from 30 to 60 min.

2.3.3 Components of a MR imaging system

In summary, the MR system is composed by the following elements:

- a large magnet to create the magnetic field,
- shim coils to make the magnetic field as homogeneous as possible,
- a RF coil to transmit a radio signal into the body being imaged,
- a receiver coil to detect the returning radio signal,
- gradient coils to provide spatial localization of the signal,
- and a computer to reconstruct the radio signal into the final 3D image.

Figure 2.3 shows how an MRI scanner device looks like and the different MR modalities that can be obtained: T_1 , T_2 and PD weighted.

2.3.4 Clinical applications of MRI

MRI has the advantage over other medical image modalities that it does not use ionizing radiation. This modality is extensively used for medical visualization of most parts of the human body due to its high sensitivity for water. A few examples are enumerated in what follows.

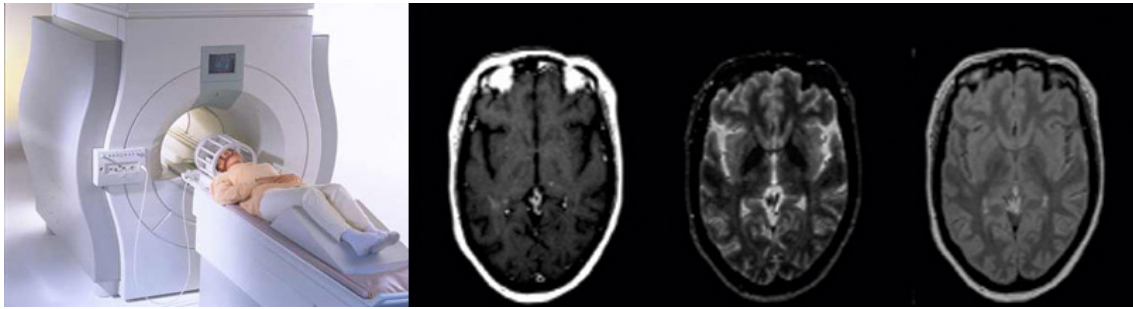


Figure 2.3: Magnetic Resonance Imaging: MRI Scanner, MR-T1, MR-T2, and MR Proton Density.

- Brain MR is generally more precise for detecting brain abnormalities during the early stages of a disease due to its high contrast between brain tissues. For instance, in the case of brain tumors, the MRI will be positive before the CT does. Also, MR scans are very sensitive to white matter diseases such as *multiple sclerosis (MS)*. Other medical applications where MRI is preferred are temporal lobe epilepsy, traumatic shear contusions, and gray matter degenerative disease.
- MRI of the neck helps distinguish differences between lymph nodes and blood vessels. It can help detect tumors and other lesions, as well as vascular abnormalities, and structural abnormalities.
- MRI is now able to utilize the blood as its own contrast agent to evaluate the blood vessels of the head and neck. This technique is known as *MR angiography (MRA)*. It can evaluate blood vessels of the head and neck without injecting the patient with a contrast agent. This non-invasive technique requires only one additional set of pictures taken in addition with a standard MRI exam. MRA of the head and neck can help detect vessel narrowing (stenosis), blood vessel blockage, cerebral aneurysm, arteriovenous malformation (AVM), and blood vessel dissection.

However, MRI also presents some limitations. MR examinations cannot be used in patients with metallic devices such as pacemakers or with patients who are claustrophobic (although new MRI systems are more open). It is absolutely necessary that the patient not move during the acquisition time, thus, the patient must be able to be quiet during the exam period (from 20 to 60 min).

2.4 Reference imaging

As already presented in the introduction of this chapter, reference imaging involves the *a priori* information available usually called *atlas*. The terms atlas and template represents the same reality: something that establishes a reference. Thus, a *brain atlas* is the abstract representation that serves as a pattern for comparing brains [55].

2.4.1 History of the brain atlases

The interest in brain anatomy and functionality started almost five millennia ago when an Egyptian surgeon called Imothep described localization of brain function. After that, some philosophers and physicians progressively discovered the motor, mental and sensory functions of the brain. In 1508 A.D., first neuroatomical drawings were done by Leonardo da Vinci and few years later Vesalius

presented the first complete study of human anatomy. Many other brain studies were carried out but it is not until *modern times* that the first textbooks of brain function and anatomy were proposed by Brodmann in 1909 [16], Talairach and Tournoux [106, 107] in 1957, and Schaltenbrand and Wahren [98] in 1977. A slice of Talairach and Tournoux textbook atlas is shown in Figure 2.4(a). These standardized atlases provide a precise common space in which to describe the anatomy of the

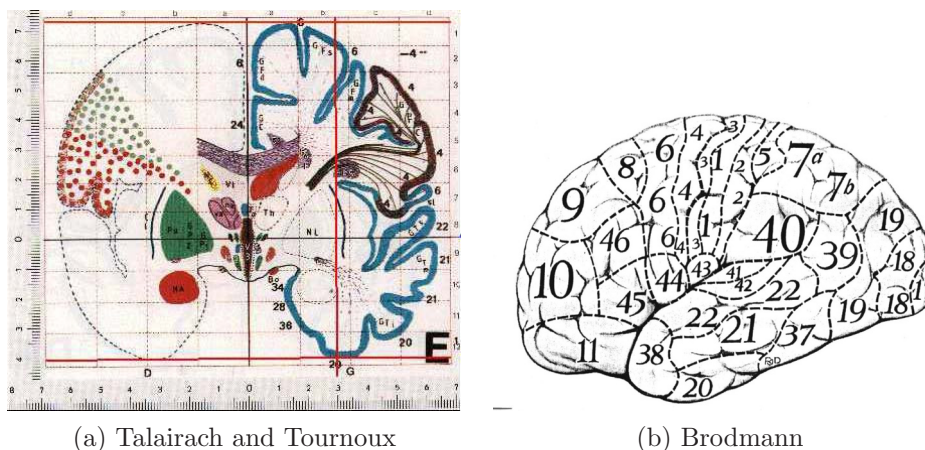


Figure 2.4: Reference imaging. (a) Talairach slice (from www.mrc-cbu.cam.ac.uk). (b) Brodmann lateral areas (from www.public.iastate.edu).

human brain. However, textbook atlases also present some limitations. For instance, they usually cannot easily evolve and they are not usually compatible with each other. Digitized brain atlas try to overcome these limitations and their advantage is that they provided a lot of detail and may be *easily* used in computer assisted diagnosis or intervention.

2.4.2 Digitized brain templates

Many efforts have been recently made in order to digitize and compare some of the existing textbook atlas [86] as well as in the creation of digitized brain templates from high resolution cryosections [47] or *in vivo* medical images [37, 92]. Some of the existing computerized brain atlas are enumerated in what follows. They are classified in two main groups: single subject and population-based atlas. A more detailed description is given for the atlases used in this work.

Single subject-based atlas

Cryosection-based atlas. One of the first digitized atlases was proposed by the *Visible Human Project* [1] of the National Library of Medicine. Their goal is the creation of complete, anatomically and detailed, three-dimensional representations of the normal male and female human bodies by the acquisition of transverse CT, MR and cryosection high resolution images of representative male and female cadavers. However, the frozen brain sections appear compressed and there is not much intensity contrast in the MR images since they scanned the brains after death. Also derived from a digitized cryosectioned human brain, Greitz, Seitz, Thurfjell et al. [47, 102, 113] created a *Computerized Brain Atlas (CBA)* project that was designed for display and analysis of tomographic brain images. The atlas includes the brain surface, the ventricular system and about 400 structures and all Brodmann areas, that are outlined (see Figure 2.4(b)).

MRI-based atlas. Another type of atlas are those that are created from a MR image. For instance, the *digital brain atlas* developed by the Surgical Planning Laboratory (SPL) of Harvard

Medical School [92]. The template they proposed is a 3D MR digitized atlas of the human brain to visualize spatially complex structures. The MRI acquisition they used is from a single normal subject and it has $256 \times 256 \times 160$ voxels with $0.92 \times 0.92 \times 1.5\text{mm}^3$ per voxel. The manually generation of anatomical labels finalized in 150 differentiated structures. Their work also includes 3D display tools. Figure 2.5 shows an axial view of the MRI, the corresponding labelled slice, and a 3D view of deep brain structures (ventricles, thalamus and central nuclei). In what follows, this atlas is called *SPL* atlas.

Also, the *digital brain phantom* from McConnell Brain Imaging Center [27] is based on 27 high-resolution scans of the same individual (1mm isotropic voxels low-noise). Then, a preprocessing with non-uniformity reduction, an automatic segmentation (by minimum distance classifier), and, finally a manual correction of these scans was done. That resulted in a known classification: 10 3-dimensional ‘fuzzy’ tissue membership volumes where voxel values reflect the proportion of tissue present within the voxel. The Brainweb web-site also provides several simulated MRI acquisitions of this phantom including RF non-uniformities (bias of 0%, 20%, and 40%) and noise levels (0%, 1%, 3%, 5%, 7%, and 9%). This makes them suitable for segmentation algorithm assessment. Figure 6.6 shows an image with 5% of noise and 0% of inhomogeneities next to a 5-class ground truth classified image created from the tissue membership volumes.

CT-based atlas. Bajcsy et al. [7] created an artificial CT anatomical volume based on the brain sections taken from the Yakovlev Collection.

Population-based atlas

In principle, a single brain is not representative of a population. That is why population-based atlases exploit the human brain variability in order to create a *probabilistic* brain atlas where the cross-subject anatomical and functional variations of a representative population are encoded. A first attempt of population-based model was presented by Hohne et al. in [60], where a framework for generating an atlas from a collection of real volumes (MRI and a CT) was introduced. Woods et al. [121] created two average brain atlas in T1 and T2 from ten normal subjects registered into a Talairach space. A composite MRI data set was constructed by Evans et al. [37] from several hundreds of normal subjects (239 males and 66 females of 23.4 ± 4.1 years old). All the scans were first individually registered into the Talairach coordinate system. Then, they were intensity normalized and, finally, all the scans were averaged voxel-by-voxel. This *average* template is part of the widely used *Statistical Parametric Mapping (SPM)* package [39].

The population-based atlas are in continuous evolution since a new-subject can be easily incorporated. Also, the population that a probabilistic atlas represents can be easily subdivided into groups according to specific criteria (age, sex, handedness, etc). Recently, population-based atlases are also based in representative subgroups of some disease, instead of using a *healthy* representative group of subjects, that is, *disease-based atlas*. For instance, functional and morphological atlases for Alzheimer, Parkinson or Schizophrenic diseases are being of increasingly research interest [36, 81, 111, 116]. Such atlases would provide the way to examine the history and evolution (due to *natural* disease evolution or reaction in front of a clinical treatment) of a specific disease.

2.4.3 Digitized brain atlas applications

Modern brain atlases derived from high resolution cryosections or in *vivo images*, single subject-based or population-based, provide detailed images and may be interactively examined in their digital format. Then, brain images derived from different subject and modalities can be placed within the atlas coordinate system to improve localization and delineation of structures, enabling

REFERENCE IMAGING				
Textbooks	Digitized atlas			
	Single-subject based			Population based
Brodmann [16]	Cryosection	MRI	CT	Hohne [60]
Talairach Tournoux [106]	Visible Human [1]	Kikinis [92]	Bacsy [7]	Woods [121]
Schalterbrand Wahren [98]	CBA [47]	Collins [27]		Evans [37]

Table 2.3: Classification of reference brain imaging.

correlations between individuals and modalities. Thus, digital atlases may be used to calculate and provide morphometry and morphological measurements within a precise anatomical framework by mapping the template onto the target image. Then, the resulting 3D transformation can be used to define and quantify the brain morphology. In the same way, population-based templates provide a representation of the human diversity neuroanatomy. Then, these templates can be used to detect and measure possible *abnormal* neuroanatomies or, on the contrary, to keep new transformations inside their space of *normal* anatomy.

2.5 Summary

In the last century, a rapid advance in neuroimaging produced important changes in clinical neuroscience. There exist a large variety of image modalities that usually address a particular aspect of the underlying physiology. However, among all the different brain images, complementary information is usually provided even within the same image modality. In this chapter, basic concepts on anatomical, functional and reference brain imaging have been introduced. Focus on magnetic resonance imaging and digitized brain atlases has been done since they form the data sets used in this thesis.

The MRI principles have been first presented as well as the advantages of MRI versus other image modalities. For instance, MRI usually presents the best spatial and contrast image resolution and is perfectly suited for anatomic visualization of deep structures of the brain. There are however some exceptions where a MR exam cannot be considered. For instance, for patients having implanted a metallic device or claustrophobia a MR exam cannot be executed.

A wide discussion on the existing brain atlases presented two main group of digitized templates: single-based and population based. The importance of brain atlases has been put in evidence with their wide range of possible applications. All digitized templates have the same major advantage: anatomical and/or functional structures and large number of subjects can be automatically compared to a brain atlas. However, their principle itself is its main limitation since templates are defined to represent the anatomy of the majority of the individuals. Thus, they are used to compare similar topologies. But there are some cases where some structures, such as a tumor or minor sulci, are present in the subject but not in the template.

Now, an important question arises within all the brain image modalities: how to efficiently combine all these different sources of information? A battery of methods and algorithms emerges in order to answer this question: the *brain mapping or registration* techniques and they will be treated in the next chapters.

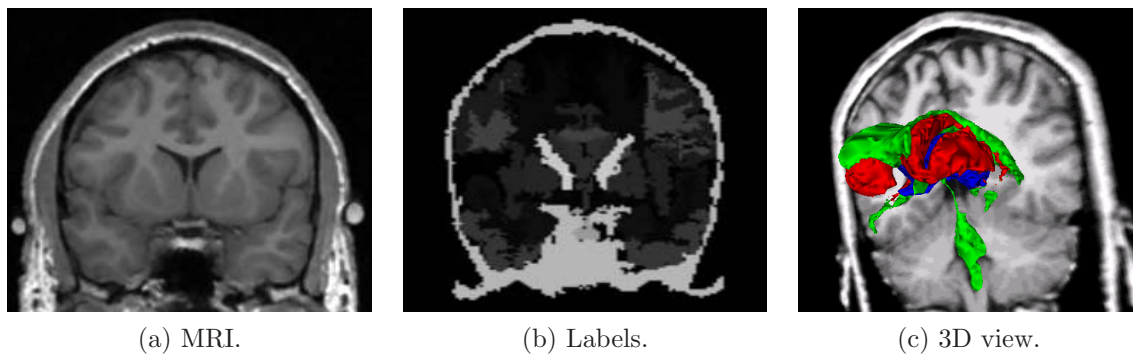


Figure 2.5: Digital brain atlas of the Surgical Planning Laboratory of Harvard Medical School: (a) Magnetic resonance of the atlas. (b) Atlas with all labelled brain structures. (c) 3D view of deep structures of the brain: ventricles (green), central nuclei (red) and thalamus (blue).

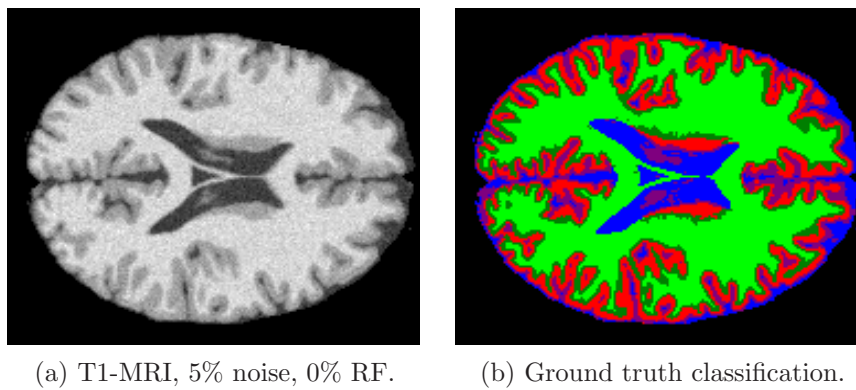


Figure 2.6: Digital brain phantom from McConell Brain Imaging Center. (a) Brainweb phantom simulated T1-MRI with 5% noise and 0% RF. (b) 5-class ground truth classification.

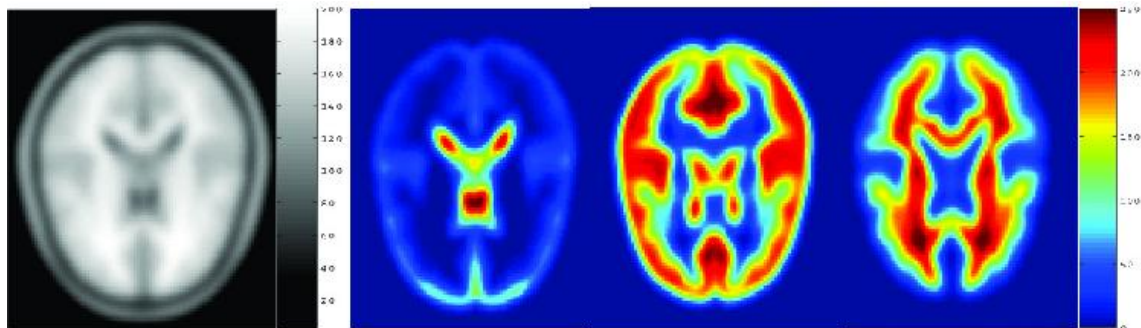


Figure 2.7: SPM probability maps of brain tissue.

3

Image Registration

*At night my mind would come alive with voices and stories.
I gave myself up to it, longing for transformation.*
Jo, "Little women"(1994).

3.1 Introduction

In this chapter the basic theoretical concepts of image registration are exposed focusing on non-rigid registration techniques. First, a theoretical formulation and a general classification of registration techniques are presented. After that, a brief state of the art of non-rigid registration is done in order to introduce the warping method used in this work that is described and analyzed in detail at the end of the chapter.

3.2 Medical image registration

There is a lot of information available in medical imaging. All this information can be efficiently combined by medical image registration: it consists of finding the transformation that brings two medical images into a voxel-to-voxel correspondence. Generally, the terms **registration** and **matching** are both used to refer to any process that determines correspondence between data sets.

Many variables participate in the registration paradigm and they make the classification of registration techniques a difficult task. A wide overview of medical image registration is done in [53, 79, 118]. Maintz et al. present in [79] a survey of medical image registration techniques under nine different criteria. The more relevant criteria are also used here.

The main actors in the registration process are the brain images. Two images are matched one to the other: the target image, also called *reference image* or *scene* (f), and the image that will be transformed, also called *floating image* or *deformable model* (g). If the images to register belong to the same modality it is said to be *monomodal* registration and if they belong to different modalities it is said to be *multimodal* registration.

We can also distinguish between *intra-subject* and *inter-subject* registration. In the first case, both reference and floating images belong to the same patient. The goal of intra-subject registration is usually to compensate the different positioning of the patient in the acquisition process as well as other possible geometrical artifacts of the images. This kind of registration is usually needed in surgical planning, lesion localization or pathology evolution. Some examples are the registration of a CT and a MR image for radiotherapy or the registration of an anatomical MRI with a fMRI for lesion localization. In the second case, images are acquired from different patients or from a patient and a template image. The goal of this kind of registration is to compensate the inter-subject anatomical variability in order to perform statistical studies or to profit from reference data, for instance for surgical planning.

The image modalities to register and the application will determine the rest of the variables that belong to the registration process:

- the **features** to be matched,
- a **cost function** to minimize,
- the **domain of possible transformations** \mathcal{T} ,
- and the evaluation of the results.

A more detailed classification of the registration techniques under the first three criteria follows. Validation is discussed at the end as conclusion of the chapter.

3.2.1 Features and cost function

Registration techniques can also be divided into *voxel-based* and into *model-based* techniques. On one hand, voxel-based approaches directly use voxel intensity. Some of them encode the image intensity into a set of scalars and orientation (principal axes and moments-based registration). But most of the voxel-based registration approaches uses the whole image intensity (*intensity-based* registration) and, once a cost function is defined between the reference and the floating images, the transformation is successively adjusted until the cost is minimized.

On the other hand, model-based approaches are *landmark-based* or *segmentation-based*: identifiable anatomical elements (point landmarks, lines or surfaces) are extracted in both reference and floating image and their correspondence determine the volumetric transformation. They use high-level anatomical information (sulcal lines, functional surfaces, important point landmarks) and that explicitly guarantees the physical validity required in the brain registration process. But they present also the disadvantage of having a previous feature extraction step (not always an automatic method can be used) and consequently the registration validity depends on the feature extraction accuracy.

Of course, feature selection depends on the image modality and the definition of the cost function depends on the selected features. Usually,

$$\text{Cost function} = -\text{Similarity measure},$$

and this similarity measure can be intensity-based (voxel-based registration) or distance-based (model-based registration). Some *similarity intensity* measures are: normalized cross-correlation [6], absolute or squared intensity difference [24], measures based on optical flow concept [33], mutual information [19], etc. And some *distance* measures are: Procrustean metric [45], Euclidean distance [29], curvature [30], etc.

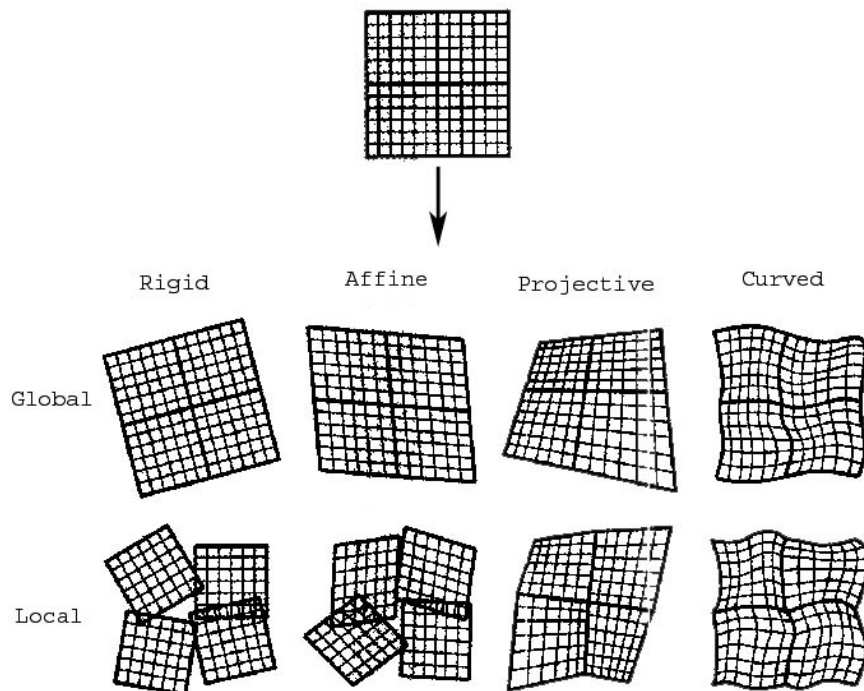


Figure 3.1: Domain and nature of a transformation. Figure extracted from [17].

3.2.2 Domain of transformation

Another possible classification criteria used in [79] is the nature and domain of the transformation. The nature of transformation is *rigid* (only translations and rotations are allowed), *affine* (parallel lines are mapped onto parallel lines), *projective* (lines are mapped onto lines) or *curved* (lines are mapped onto curves). Then, the transformation domain can either be *local* or *global*. A transformation is called global when a change in any one of the transformation parameters influences the transformation of the image as a whole. In a local transformation a change in any transformation parameter only affects a part of the image.

According to Brown [17], the domain of the transformation is the main characteristic of any registration technique. But the *local-global* paradigm can be attributed not only to the transformation itself but also to the computation domain. That is, the information on which the registration is based and the similarity function domain can span from very local to very global. However, *global* usually refers to rigid (6 parameters in 3D) and affine (12 parameters in 3D) registrations and we consider curved registration as a *local* transformation. Curved registration is also called *non-rigid* registration or *warping* (see section 3.3).

3.2.3 Registration problem formulation

The image registration problem can be formulated by the following minimization equation:

$$T^* = \underset{T \in \mathcal{T}}{\operatorname{argmin}} \operatorname{cost}(f, T \circ g) \quad (3.1)$$

Note that all transformations in \mathcal{T} have to follow some physical constraints in order to model *realistic* deformation between two brains (we can deform a brain into an apple but it is not very likely

CRITERIA	CLASSIFICATION			
Image modality	Monomodal		Multimodal	
Subject	Inter-subject		Intra-subject	
Features	Voxel-based		Model-based	
	Set-based	Intensity-based	Landmark-based	Segmentation-based
Cost	Similarity	Distance	Deformability-Similarity	
Nature	Rigid	Affine	Projective	Curved
Domain	Global		Local	

Table 3.1: Different registration techniques classification.

to happen). Global transformations defined by an analytical expression (rigid, affine or splines) use few parameters and explicitly fulfill these physical constraints. The cost function in these cases is just defined by a similarity criteria (either intensity or distance-based). But in more local transformations the complexity of the transformation might increase until a large number of parameters and they usually assure a physically valid transformation by adding to the similarity criteria a term representing the allowed deformability (fluid models, elastic models or diffusion models):

$$Cost = Deformability - Similarity. \quad (3.2)$$

To conclude the state of the art of registration techniques, Table 3.1 summarizes the possible classification under the selected criteria.

3.3 Non-rigid Registration

As seen before, the available image data and the final application of the registration process determine the nature and domain of the transformation. Some possible needs of registration in medical imaging could be:

- the analysis of functional imaging to locate functionally homologous brain regions,
- to remove position, inter-subject size and shape difference between the brain images for statistical studies or a reference atlas construction,
- the *atlas-based segmentation*, that is, the registration between an atlas and a patient to automatically identify template structures into the subject brain,
- to localize, model and quantify the brain's anatomical variability, in the healthy-to-healthy or the healthy-to-pathological case.

All these applications have a common denominator: the need to capture the morphological variability in brain anatomy. That is why a global registration is not enough to finally obtain the desired correspondence and a more local deformation is needed. However, many local registration methods require a global transformation as initialization step that makes the registration process a tandem of both types of transformations. The registration methods that are neither rigid nor affine are named here *non-rigid* registration or *warping*.

There are among all the warping techniques several matching criteria and several types of transformation, thus there is not one hierarchy which is better than another. As for registration only a few surveys exist in brain warping [73, 115]. The state-of-the-art presented here is limited to

intensity-based non-rigid registration techniques. All the existing techniques are summarized in two main groups, *parametric* and *non-parametric*, in order to better identify the matching method used in this work.

3.3.1 Parametric transformations

We have seen that global transformations (rigid or affine) are represented by few parameters. The complexity increases up to hundreds of parameters for the local transformations: instead of using a matrix or polynomial representation of the transformation, a linear combination of basis functions can be used. These methods are called here *parametric* warping techniques. For instance, trigonometric [4], wavelets [2] or splines could be used as basis functions. These methods are *control point*-based, that is, the transformation is calculated at some points and the continuity of the transformation at the rest of the image is ensured by an interpolation function*. The number of parameters is strictly dependent on the number of control points. The grid must be a regular one for some basis functions such as B-splines [117] but may be non-uniform grid for *radial* basis functions (thin-plate splines [13], Gaussian, etc). However, the use of a non-regular distribution of control points makes their choice a critical aspect of the registration process. These approaches have the advantage of having a free choice of the cost function and many times the mutual information measure is used so multimodal data can be matched [66, 96].

3.3.2 Non-parametric transformations

In the extreme case one or more parameters per voxel can be used. This kind of registration is called here *non-parametric* transformations. Non-parametric transformations are usually defined by their associated displacement field \vec{D} (three coordinates per voxel in 3D) at each voxel position \vec{P} . The transformation of one image by this vector field can be formulated as follows:

$$T \circ g(\vec{P}) = g(T(\vec{P})) = g(\vec{P} + \vec{D}(\vec{P})). \quad (3.3)$$

This is known as *Lagrangian* reference frame, i.e. deformations are defined with respect to the initial position.

Elastic registration techniques have been introduced earlier by Bajcsy et al. [6] where image registration is treated as the physical deformation described by the stretching of an elastic material. Two forces drive this deformation: the *internal* and *external* forces. Internal forces are defined by the elastic properties of the deforming media (Lame's elasticity constants) and they represent the deformability term of the cost function. External forces are the cost function similarity term and they actually drive the registration process. Usually, these forces are gradients of the chosen similarity measure: cross-correlation [6], squared differences in pixel intensities[82] and a mix of intensity and curvature and edge features[42]. The elastic registration problem is formulated by the Navier linear elastic partial differential equation (PDE). It can be solved numerically by finite differences [30] or finite elements [38]. In these cases the regularity of the transformation is driven by the laws of the continuum mechanics.

In order to allow more deformability than the elastic methods, Christensen et al. [24] propose a transformation driven by a viscous-fluid model which allows non-linear topological behavior while satisfying the laws of the continuum mechanics. In contrast to elastic registration techniques, viscous-fluid deformation is formulated in terms of the instantaneous field instead of the displacement field (in fact, deformation is here defined with respect to the final position, that is, the *Eulerian*

*In a non-control point the transformation is defined by an analytical expression of the transformation computed at the control points within the region of influence of the considered non-control point.

WARPING TECHNIQUES								
PARAMETRIC: Basis functions					NON-PARAMETRIC			
Non-radial			Radial		PDE		Diffusion	
Trigonometric	Wavelets	Splines			Gaussian	Elastic	Fluid	Demons
		B-Splines	Thin-plate Splines					

Table 3.2: Classification of the warping techniques.

reference frame). Two methods are proposed to solve the fluid PDE: using successive over relaxation [24] or using spectral methods [15].

All the approaches presented can be seen as *attractor* techniques: where deformation forces are usually defined from the deformation model and directed towards the target image. In opposition to these methods, Thirion [109] presents a different approach inspired by thermodynamics: the *demons-based* algorithm. In this approach, the forces are originated from the scene and they are directed inward or outward of the scene objects. The regularity of the transformation is ensured by a simple linear convolution of the deformation field with a separable filter. That makes the demons algorithm a *fast* warping algorithm. This is one of the reasons why this method has been chosen in this work. A detailed description of this technique will follow in the next section.

3.4 Demons algorithm

J.Ph. Thirion introduces the image registration problem as a *diffusion* process [109, 110] based on an analogy with a thermodynamic concept (Maxwell's demons) and on the optical flow estimation. A detailed analysis of this method is presented in the following sections since this is the non-rigid registration method used in this thesis.

3.4.1 Optical Flow Concept

The optical flow is an *estimation of motion* [9] and it can be used in a wide range of applications such as 3D scene analysis in robotics or virtual reality, motion image compensation in remote sensing or image compression. The estimation problem can usually be seen as an object to track in a sequence of images. The optical flow estimation is based on the following assumption: *in an image sequence, the intensity of a real point does not change in time*. The formulation of this assumption in the 2-D case is as follows:

$$I(x(t), y(t), t) = I(x(t_0), y(t_0), t_0) = C, \quad (3.4)$$

where (x, y) represents the spatial coordinates, I is the intensity, t is the index time, and C is a constant. Taking the derivative with respect to the time, the above assumption can be rewritten as

$$\frac{\partial I(x(t), y(t), t)}{\partial t} = \frac{\partial I}{\partial x} \frac{dx}{dt} + \frac{\partial I}{\partial y} \frac{dy}{dt} + \frac{\partial I}{\partial t} = 0. \quad (3.5)$$

Remark that the instantaneous speed of a point can be defined as:

$$\vec{v} = \left(\frac{dx}{dt}, \frac{dy}{dt} \right). \quad (3.6)$$

Then, equation 3.5 becomes

$$\vec{\nabla} I \cdot \vec{v} = -\frac{\partial I}{\partial t}, \quad (3.7)$$

that is known as the optical flow equation and estimates the motion using both the spatial gradient and the temporal derivative of the image intensity. However, this equation formulates an *ill-posed* problem since a scalar equation has to determine two unknowns, the two components of the speed $\vec{v} = (v_x, v_y)$. Actually, only the motion along the intensity gradient (object contours) can be determined while no access to the component along the object contours is available. This is called the *aperture problem*. An additional assumption is needed to solve this problem. The smoothest solution is the *regularization* that supposes the component of the speed orthogonal to the gradient is zero and a regular optical flow in the whole image [61] and this is the one used here (see Section 3.4.5). Other possible solutions are the *block matching* which assumes the optical to be constant on small windows in the image [3] or the spatiotemporal filtering methods which rely on the assumption that the optical flow is constant over the support of their filters [26].

3.4.2 Demon points

Demon points are the features matched in the demon algorithm. Opposite to the attractor-based methods, in this approach the feature set is extracted from the scene image and not from the deformable image. Several kind of demons can be defined. A grid of demons is considered here. All voxels where $\vec{\nabla} I \neq 0$ are selected to be demons. In this case, the interface at each point is an iso-surface. Notice that in the case of medical imaging, and particularly MR images, the iso-surfaces represent the shapes of object, because the intensity in a MRI represents the different biological tissues. It is assumed that demon polarity can be determined. This assumption is easily fulfilled since MR intensity gradient determines the normal to object contour, that is, the inside-outside orientation. So, a demon should be understood as an *intelligent* agent that, being placed at a point of the scene, pushes the deformable model in the normal direction of the scene contour*. The formal expression of this idea is:

Definition 1 (Regular grid of demons) *Let f be the 3D image intensity function of the scene, and g be the 3D image intensity function of the deformable model. A demon is associated to each voxel P of the scene image where $|\vec{\nabla} f(P)| > \varepsilon$, meaning that an iso-surface comes through voxel P , whose implicit equation is $f = f(P)$, and whose oriented normal is $\vec{\nabla} f(P)$.*

The threshold ε defines the type of demons and in this work is defined by the quantification step ($\varepsilon = 0$). A more detailed discussion about the choice of this threshold is presented in section 4.3.3. In summary, note that the information contained at each demon is:

1. the spatial position (\vec{P}),
2. the inside-outside polarity($\vec{\nabla} f(\vec{P})$),
3. the current displacement ($\vec{D}(\vec{P})$),
4. and the intensity ($f(\vec{P})$).

*Maxwell's demons were introduced in physics to model the paradoxical idea that a semi-permeable membrane could violate the second law of thermodynamics (about entropy). Situated in the membrane, those demons are supposed to sort locally two different types of molecules of a mixed gas, to put one type on one side and the other type on the other side of the membrane, hence giving a decrease in entropy. As each demon needs to consume some energy to sort, the global entropy of the system is still increased, which suppresses the paradox.

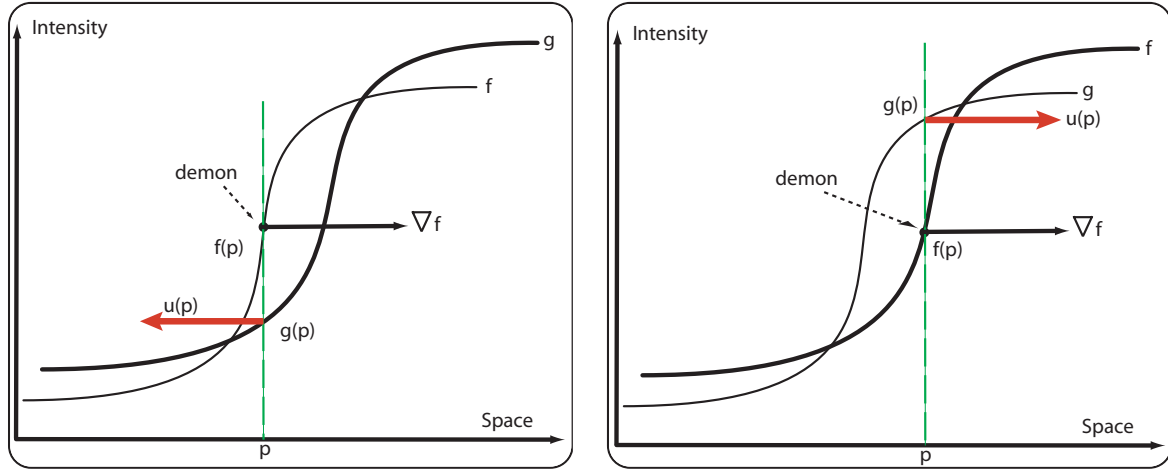


Figure 3.2: Demon polarity. Figure extracted from [109]. $\vec{u}(p)$ corresponds to $\vec{d}(P)$.

3.4.3 Demon forces

Object boundaries in the scene image f are viewed as semi-permeable membranes. The floating image g is considered as a deformable grid, and diffuses through these interfaces driven by the action of demons situated within the membranes. In the particular case of voxel-by-voxel intensity similarity, the *demons* paradigm is similar to optical flow methods: f and g are seen as two frames of a motion sequence, and the target is to find the motion vector \vec{v} that brings g closer to f . The assumption that there is a conservation of the intensity of points under motion is applied, which can be expressed as:

$$\frac{\partial I}{\partial x} \frac{\partial x}{\partial t} + \frac{\partial I}{\partial y} \frac{\partial y}{\partial t} + \frac{\partial I}{\partial z} \frac{\partial z}{\partial t} = -\frac{\partial I}{\partial t} \quad (3.8)$$

It can be considered that f and g are separated by only one unit of time: $\partial I / \partial t = f - g$. The motion vector is defined as $\vec{v} = (\partial x / \partial t, \partial y / \partial t, \partial z / \partial t)$, and corresponds to the instantaneous velocity from g to f . Therefore, the expression of the motion from g to f is:

$$\vec{v} \cdot \vec{\nabla} f = g - f \quad (3.9)$$

And, therefore the instantaneous velocity can be computed from the intensities of the *scene* and *model* images with the following expression:

$$\left. \begin{aligned} \frac{\partial I}{\partial t} &= f - g \\ \vec{v} &= \left(\frac{\partial x}{\partial t}, \frac{\partial y}{\partial t}, \frac{\partial z}{\partial t} \right) \\ \vec{\nabla} f &= \left(\frac{\partial f}{\partial x}, \frac{\partial f}{\partial y}, \frac{\partial f}{\partial z} \right) \end{aligned} \right\} \Rightarrow \vec{v} = \frac{(g - f) \vec{\nabla} f}{|\vec{\nabla} f|^2} \quad (3.10)$$

The expression above of the motion vector \vec{v} could be used as demon's pushing force, as this force would push inward (in the direction of $\vec{\nabla} f$) when $f < g$, and outward (toward $-\vec{\nabla} f$) when $f > g$, which is the desired behavior of a demon (see Figure 3.2). However, the expression in Equation (3.10) is unstable when the gradient norm is small, which would lead to infinite values of the pushing force for the regions having small variations of intensity. The desired behavior of the pushing force equation would be that the force should be given by Eq. (3.10) when the gradient is high, and close to zero when the gradient is low. J.-P. Thirion proposes multiplying the expression in Eq. (3.10) by $\{\vec{\nabla} f^2 / [\vec{\nabla} f^2 + (g - f)^2]\}$, which provides the desired effect of limiting the force to

finite values. Finally, the expression of the demons pushing force is:

$$\vec{v}_p = \frac{(g - f)\vec{\nabla}f}{|\vec{\nabla}f|^2 + (g - f)^2}. \quad (3.11)$$

Definition 2 (Demon forces) *The demon in P pushes the deformable model image according to $\vec{\nabla}f(P)$ if $f(P) < g(P)$ and according to $-\vec{\nabla}f(P)$ if $f(P) > g(P)$. Hence, a whole 3D grid of demons acts to deform the deformable model using the intensity gradient as direction of the deformation, and using the difference in intensity as orientation of the direction and magnitude.*

In the particular case where $f(P)$ is equal to $g(P)$, the demon force in equation 3.11 is zero, i.e. there is no displacement necessary since intensities are already matched. The instantaneous displacement of the *non-demon* points is also zero. Finally, note that relationship between demon force \vec{v}_p and the instantaneous displacement \vec{d} is defined as $\vec{d} = -\vec{v}_p$.

3.4.4 Iterative process

As for *attraction-based* approaches, demons algorithm performs better in an iterative scheme. First, a computation of the demon points P_{demon} in the scene f is done and, then, the iterative estimation of the total deformation field \vec{D} is done. At each iteration i , we have the current estimated deformed field \vec{D}_i , and 2 steps are performed:

1. For each demon $P \in P_{demon}$, the instantaneous deformation field is computed, $\vec{d}(P)$, which depends on the demon direction, $\vec{\nabla}f(P)$, and on the polarity of $g(P + \vec{D}_i(P))$ with respect to $f(P)$.
2. Update $\vec{D}_{i+1} = \vec{D}_i + \vec{d}(P)$ and constrain it using the relations between the image model voxels (see section 3.4.5).

Using this iterative approach the spatial influence of the demon points becomes less local but the assumption of small displacements is still considered. Now, the number of iterations should be determined and it is usually done empirically. An algorithm convergence study is done in section 4.3.5.

3.4.5 Regularization

Eq. (3.11) estimates demon displacements when considered separately. Thus, there is no constraints on the displacement field \vec{D} that ensures global smoothness of the transformation. The problem is solved thanks to Tikhonov regularization theory [114] which looks for a differentiable function (deformation), which is, in some sense, closest to our signal (\vec{D}). There exist a wide range of possible solutions, from simple linear regularization to complex non-linear physical models. For simplicity, Thirion proposes to deal with a linear regularization. Let us write it formally [83],

Definition 3 (Linear regularization) *The Tikhonov regularized solution \hat{D} of the signal $D \in \mathcal{L}^\infty(\mathbb{R})$ is the one that minimizes the energy (E) functional*

$$E[\hat{D}] \equiv \frac{1}{2} \int dx ((\hat{D} - D)^2 + \sum_{i=1}^{\infty} \frac{\sigma^i}{i!} (\frac{\partial^i \hat{D}}{\partial x^i})^2). \quad (3.12)$$

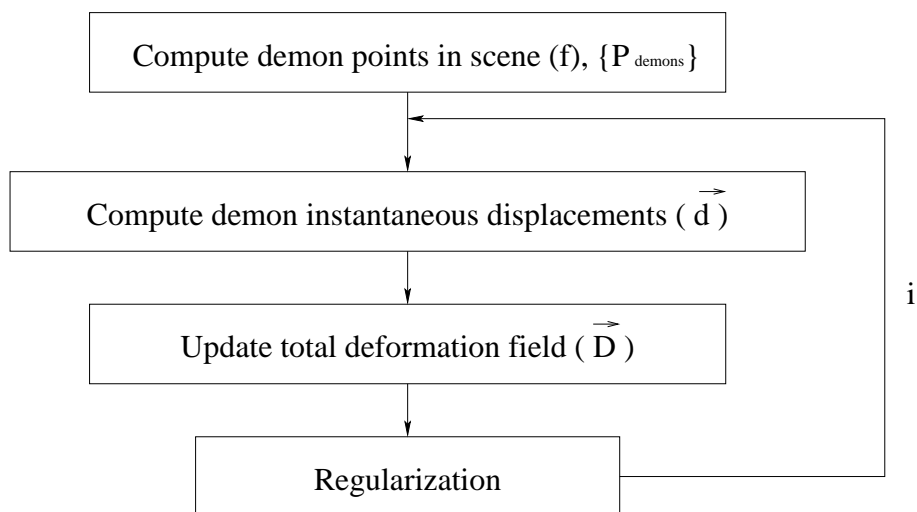


Figure 3.3: Iteration i of demons algorithm.

The solution of the regularization problem is the linear convolution of the signal D by the filter h , having the Fourier transform

$$G(w, \sigma) = \frac{1}{\sum_{i=0}^{\infty} \frac{\sigma^i}{i!} \omega^{2i}} = e^{-\omega^2 \sigma}, \quad (3.13)$$

which is the well known Gaussian filter defined by its standard deviation σ (expressed in mm). Practically, the deformation field regularization becomes a discrete convolution. A fast separable implementation is done by filtering consecutively each spatial direction by a vector of Gaussian distributed weights*.

Intuitively, demon algorithm can be seen as an elastic-like algorithm if the total displacement field \vec{D} is filtered since elastic models smooth the elastic body displacements [21]. Inversely, if the instantaneous vector field \vec{d} is filtered, demon algorithm can be seen as viscous fluid-like since viscous fluid models smooth the velocities of the fluid body.

Then, the deformability of the algorithm is only modelled by the σ parameter of the Gaussian filter (we also call it *elasticity parameter*). But this simplicity is both the strong and weak point of the algorithm since the choice of this parameter is a key aspect of the non-rigid registration process and it is however done empirically (see section 4.3.4).

3.4.6 Multiscale implementation

In order to make the algorithm more robust to large differences (these differences could render optical flow methods completely ineffective because the assumption of small displacement is violated), the deformation algorithm is applied in a hierarchical way. By hierarchical way we understand a multiscale implementation: a first match is made with downsampled images (coarsest scale) and the resulting transformation is upsampled to initialize the next match with finer image resolution. Thus, the solution is refined from coarse-to-fine scales as represented in Fig. 3.4.

There are several advantages in using a hierarchical implementation. First notice that the same number of Gaussian filter coefficients are used at each scale. Then, the filter coefficients represent

*Note that the weights of the discrete Gaussian filter are computed from σ in a way that the same number of filter coefficients are used at each scale (see Section 3.4.6).

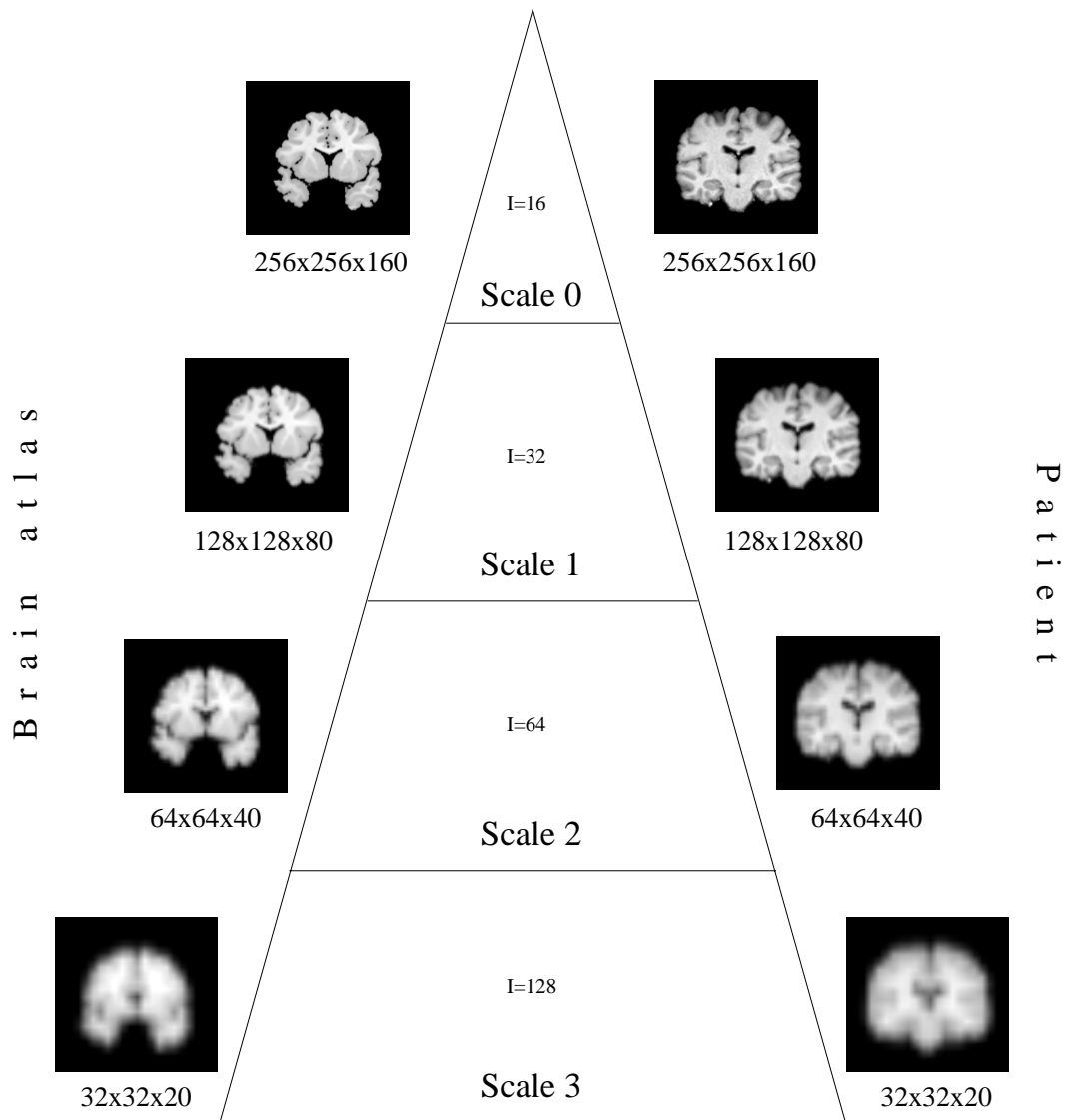


Figure 3.4: Multiscale.

different voxel sizes for each scale, i.e. in the first scales we have a less elastic filtering (biggest morphological differences are compensated) and in latest scales much more elasticity is allowed. Thus, human anatomy is better modelled since macroscopic features (coarse scales) are generally more *rigid* than microscopic features (finer scales). Then, it speeds up the convergence since the action of the demon points becomes less local for coarse scales. Another advantage of the multiscale implementation is that it speeds up the computation since many iterations are usually done in coarse scales while fewer iterations are done in finer scales.

Finally, the number of scales is defined as follows. The images are downsampled by a factor of 2 while an anatomical significance is contained in them. Depending on the image size, 3 or 4 scales are used.

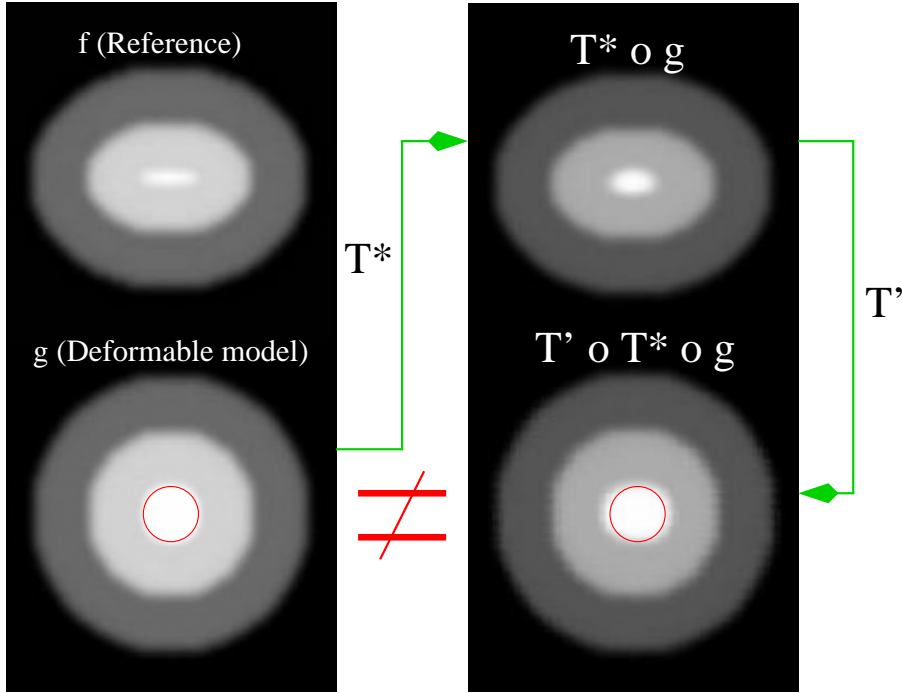


Figure 3.5: Asymmetry of demons algorithm transformation. The direct, T^* , and the inverse T' transformations are successively applied to the deformable model g . The red contour represents the original sphere that should be recovered if $T' \circ T^* = \text{Identity}$. Unfortunately, $(T' \circ T^* \circ g) \neq g$.

3.4.7 Bijectivity

Medical image registration is *a priori* a symmetrical problem because measures based on results coming from non-rigid matching should not depend on the choice of model or reference image. So, if f and g images are interchanged in equation 3.1 the resulting transformation (T') should be the inverse transformation of T^* . Mathematically, if

$$T' = \underset{T \in \mathcal{T}}{\operatorname{argmin}} \operatorname{cost}(g, T \circ f), \quad (3.1')$$

then,

$$(T')^{-1} = T^*. \quad (3.14)$$

Unfortunately, the demon algorithm does not verify equation 3.14 because of demon points are differently placed depending on which image is considered as the reference. Figure 3.5 illustrates this lack of symmetry. The demon algorithm is applied between an ellipse (f) and a sphere (g), both with 3 concentric regions equally labelled (the effect of the noise is thus not considered). The *direct* T^* (the deformation field warping g onto image f , see Eq. (3.1)) and the *inverse* T' transformation (the deformation field warping f onto g , see Eq. (3.1)') are computed. Then, T^* is applied to the sphere in order to deform it as the reference (see top right image of Figure 3.5). Note that a perfect deformation is not obtained mainly for the whitest central region. The combination of $T' \circ T^*$ must be equal to the *identity* transformation, thus T' applied to $T^* \circ g$ must be equal g . However, note that $T' \circ T^* \circ g$ does not bring back to the original sphere g . Notice for instance the remaining ellipsoidal form of the whitest region in the bottom right of Figure 3.5 that outcomes the *ideal* black circle.

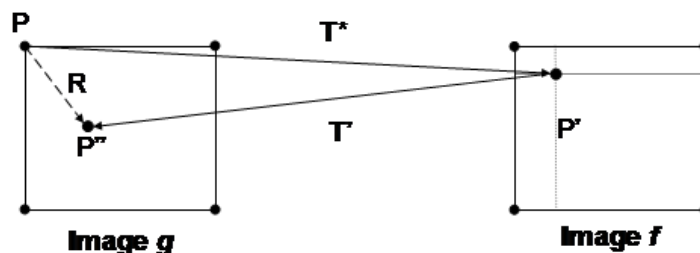


Figure 3.6: The bijectivity is imposed by the computation of the residual deformation $R = T^* \circ T'$ and the redistribution of a half of the residual to both transformations, at each iteration of the algorithm. Figure inspired from [110].

In [110], J.-P. Thirion presented a solution to provide bijectivity to the *demons* algorithm, and therefore, to provide a way of finding the inverse transformation. Although various solutions exist for ensuring bijectivity in deformation fields (some of them by using a model such a viscous fluids, some others by locally controlling the Jacobian of the transform and forcing it to be positive), a simpler method is chosen in order not to drastically increase the computation time of the algorithm. This is done by computing at each iteration both the direct deformation field T^* and the inverse deformation field T' and, then, a residual $R = T^* \circ T'$ is equally distributed onto the two deformation fields. This bijective implementation, coupled with the smoothing of the field, helps in the image anatomy preservation.

Improvement of the demons algorithm: bijective implementation

The bijective version of the demon algorithm is applied also to deform the sphere (g) onto the ellipse (f) and viceversa. This leads respectively to the *direct* Tb^* and *inverse* Tb' bijective deformation fields. The comparison between both, initial version and bijective implementation, demon algorithms is made in Figure 3.7.

First, the direct transformation is applied to g . Both versions lead to similar results (see central images in Figure 3.7). Note that there is almost no difference between both *direct* deformed images, $T^* \circ g$ and $Tb^* \circ g$. Then, *inverse* transformation has been applied in order to recover the sphere. Now the resulting contours are displayed on the original sphere g . The red one corresponds to $T' \circ T^* \circ g$ and the blue is extracted from $Tb' \circ Tb^* \circ g$. The bijective implementation (blue contour) recovers better the original central circle than demons algorithm (red contour) that has retained a more ellipsoidal shape.

The improvement performed by the bijective implementation can be also observed in the residual vector field norms (see Figure 3.8). In both cases, largest errors (whitest values) are placed at demon positions. However, notice that the norm of Rb is much less diffused. These results are quantified by the statistics on R and Rb shown in Table 3.3. The mean and the variance of the residual field norm decreases by around a factor of 10 when using the bijective version of the *demons* algorithm. The maximum error is reduced by 2 and becomes in mean lower than the 1 mm (the voxel size). The bijective implementation requires though twice the computation time of the original *demons* as well as more memory.

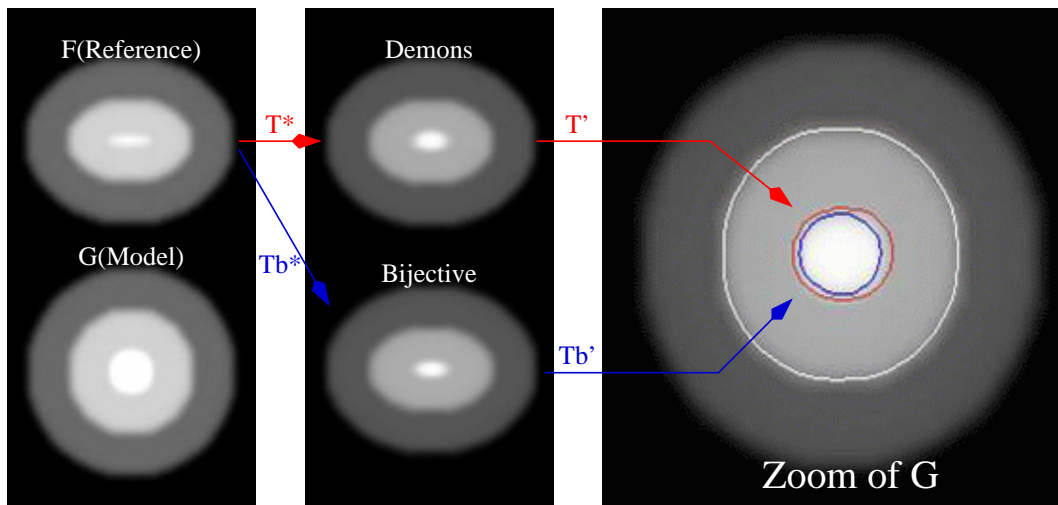


Figure 3.7: Comparison between demons and demons bijective implementation. Input data is shown in the first column. Results after applying both direct transformations T^* and Tb^* are in the middle column. Results after $T' \circ T^* \circ g$ and $Tb' \circ Tb^* \circ g$ are represented by red (gray) and blue (black) contours respectively in the center of the zoom. Blue contour shows that the original form of g (G in the figure) can be recovered by using the bijective implementation.

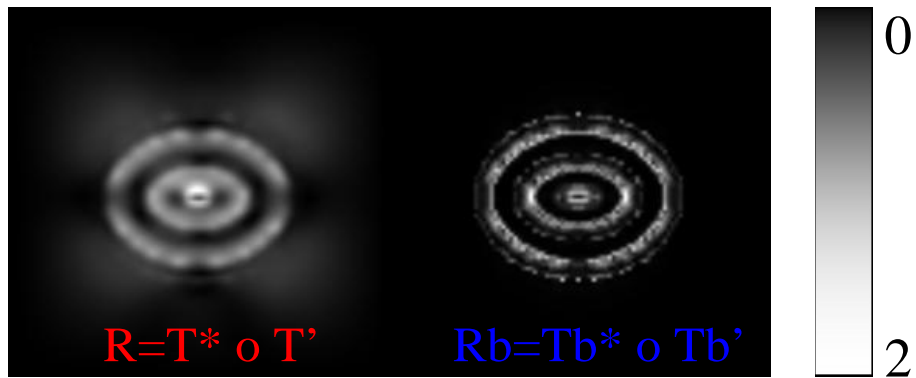


Figure 3.8: Norm of both residual error vector fields of Figure 3.7. Left: demons algorithm. Right: bijective version of demons algorithm. The error varies from 0 to 2 mm.

R	Statistics	Rb
0.0379	Mean	0.0049
0.0320	Variance	0.0048
1.8	Maximum Error	0.9

Table 3.3: Statistics on the residual deformation fields of Figure 3.7. Values are expressed in mm.

3.4.8 Variations of the demons algorithm

We previously defined the demons algorithm as we implemented it in this thesis. But there are some possible variants to consider [110]:

- the demon points selection,
- the demon force,
- the nature of the transformation,
- and the interpolation function.

The threshold ε of the image gradient can make demons correspond one demon per voxel (almost the whole image grid if $\varepsilon = 0$), demons almost in contour objects only or demons between already segmented images where each object has a label value (see Section 4.3.3 for more details). Thirion also proposes several demon forces, different from equation 3.11, where the deformable model intensity gradient is also used. This makes the instantaneous field more robust since not only the scene information but also the floating image information are used. However, it also requires much more computation since the floating image intensity gradient must be recomputed at each iteration. Here, a 3D vector per voxel defines the deformation field but the deformation space could also be rigid, affine, spline, etc., as seen in Section 3.3. The interpolation refers to the fact that when applying the transformation we usually obtain a floating position in the image, somewhere between voxel locations. Then, the interpolation give an estimation of the value at the non-voxel position. We can use any kind of interpolation as for instance linear, spline, sinc, etc. but the selected interpolation should be adapted to the image type. In this work, nearest neighborhood interpolation is used when considering labelled images and a tri-linear interpolation is used for gray level images.

3.4.9 Limitations

There are two main restrictions in the demons algorithm that are nevertheless shared by most non-rigid registration techniques. First, the original positioning: indeed, the demons algorithm requires at least a partial overlap of the corresponding deformable model and reference structures in order to match them. Second, image intensities must be the same for the same anatomical structures since the instantaneous vector field is driven by a factor $(f - g)$ which must be zero in the perfect matching case. Solutions to overcome these limitations are presented in Chapter 4.

3.5 The problem of medical image registration assessment

There is an important element left in all this chapter: the evaluation of the registration. It is very difficult to say if a transformation is *good* in the sense of *biological validity*. Many approaches ensure the smoothness of the transformation by modelling the registration as an elastic process. Probably, the elastic deformation is *realistic* for a brain shift compensation or a tumor growth model but surely not to compensate the inter-subject variability.

Unfortunately, the lack of a gold standard makes validation a difficult task. Recently, many publications discuss this problem and identify the principal requirements of a validation system [14, 72, 122]. The evaluation process is defined mainly in terms of *accuracy* and *precision* [79] but other validation criteria are also usually considered: robustness, reliability, consistency, functional complexity, computation time or clinical use. There exist in the literature many instances of validation:

- reference to external markers,

- comparison with manually identified anatomical landmarks,
- cross-method validation,
- use of a physical phantom,
- or expert criteria.

It is not evident to define a quantitative *accuracy* measure in the particular case of inter-subject non-rigid registration. But, recently, Warfield et al. [104] proposed a binary minimum entropy criterion that allows the identification of an intrinsic coordinate system of the subjects under study. Schnabel et al. [99] propose a biomechanical *gold standard* of non-rigid registration based on finite element methods.

Validation is often *application-based* and, usually, the evaluation process is presented as a section of a paper. However, few comparative studies are published concerning the evaluation of different non-rigid registration techniques. For instance, West et al. [63] present a survey and comparison of multimodal registration techniques. The same is done by Hellier et al. [58, 87, 88] for inter-subject image registration and their study is particularly relevant since the *demons* algorithm is included among four other registration methods. Their validation is done using both local and global quality measures. Their results show that *demons* algorithm performs almost better for global measurements while all methods under study perform almost equally under local measures.

3.6 Summary

In this chapter a general formulation of the medical image registration problem is presented. The main characteristics of the registration process are used to drive a possible classification of the warping methods. After that, special attention is paid to the non-rigid registration techniques and particularly to the *demons* algorithm since this is the method used in this thesis. The theoretical concepts have been presented in detail while its main limitations and the input parameter selection will be discussed in the next chapter. The problems of validation in medical image warping are presented as the conclusion of the chapter.

Part II

Atlas-based segmentation

Atlas-based segmentation of normal anatomy

4

*Would you tell me, please, which way I ought to go from here?
That depends a good deal on where you want to get to.
Alice and the Cat, "Alice in Wonderland"(1951).*

4.1 Introduction

In this chapter, the atlas-based segmentation process is presented as a monomodal registration problem. Then, since the demons algorithm is chosen for registration, the solutions used to overcome its main limitations are presented. After that, the selection of the input parameters of the algorithm is discussed. Finally, an example of atlas-based segmentation of several patients is shown.

4.2 Atlas-based segmentation

The importance in brain image analysis of both a priori information and registration techniques has been shown in the previous chapters. Here, the particular case of deforming a brain atlas into a subject's brain in order to create a new individualized brain atlas is presented. That is known as *atlas-based segmentation* and it relies on the existence of a reference MRI within which structures of interest have been previously segmented (*labelled* image). Then, a non-rigid registration between the reference and MRI of a subject is done. The resulting transformation encodes a voxel-by-voxel correspondence between the two MR images that can be applied to the reference *labelled* image in order to find out the structures of interest of the subject. This process is represented in Figure 4.1.

In summary, once the non rigid registration can be efficiently applied between an atlas and a patient, segmentation becomes an easy task. Some possible applications of atlas-based segmentation include surgical planning [119], radiation therapy planning [34, 51], automatic labelling [31, 74] or morphological and morphometrical studies of brain anatomy [54].

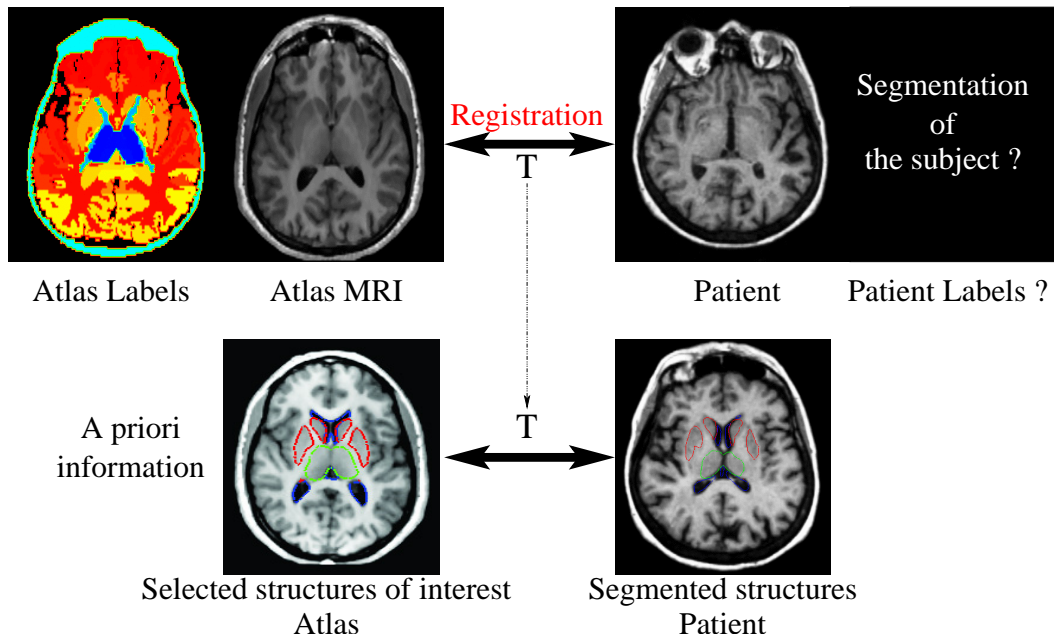


Figure 4.1: Atlas-based segmentation process.

4.3 Analysis of demons algorithm

Since the segmentation problem can be reduced to a non-rigid registration process between two MR images, let us see first how to perform this registration. The demons algorithm is used in this thesis because of its simplicity and low computation time and because it has been validated successfully as a mono-modal non-rigid registration technique [58, 87]. Its theoretical principles have been presented in Section 3.4. However, there are some practical and important aspects of the algorithm that have not been discussed yet. In what follows a practical implementation of the demons algorithm is described by addressing its limitations and discussing the choice of the input parameters:

1. How do we bring both images in global correspondence before applying the demons algorithm?
2. How do we compensate for variations of intensity profiles between both images?
3. How do we select the demon points?
4. How do we choose the elasticity parameter σ ?
5. How do we stop the algorithm?

4.3.1 Global correspondence

The first limitation refers to the initial positioning since demons algorithm requires having at least a partial overlap between the structures to be matched. So, it is necessary to bring the scene and floating volumes into global correspondence before performing the non-rigid deformation in order not to violate the small displacement assumption. Two different approaches have been used in this work.

Cuisenaire et al proposed in [29] a parametric registration where a global transformation $\mathbf{y} = T(\mathbf{x})$ between the brain cortical surfaces is modelled by a linear combination of N elementary scalar

functions $f_j(\mathbf{x})$ for each coordinate $y_i (i = 0, 1, 2)$ of \mathbf{y} . These functions are decorrelated and, then, the coefficients of the linear combination are optimized in order to minimize the Euclidian distance between the atlas cortical surface and the correspondent cortical surface in the target image. These surfaces are previously segmented using simple morphological operations [100]. Here, an affine transform is used, i.e. to $N = 4$ and $f_j(\mathbf{x}) = 1, x_0, x_1, x_2$.

Also, Butz presented in [18, 19] a general framework of feature-space mutual information for multi-modal signal processing and a particular application to the medical image registration problem. The global registration is formulated in terms of maximization of the efficiency coefficient. They proposed a global matching that not only finds the 12 geometrical parameters of the affine transformation but also the optimal number of quantification bins in order to minimize the influence of noise in the registration process.

The first approach has been mostly used in this work as preliminary step of the non-rigid registration. However, the second approach has been particularly used in Section 4.3.3 where the main interest is on the optimal feature selection (demon points) for registration and also in the cases where the brain surface cannot be extracted precisely because of the image artifacts.

4.3.2 Intensity correspondence

The second main limitation of the demons algorithm is the intensity correspondence. The objects to register must be represented by the same intensity in both images since the matching criterion is guided by the intensity difference. In general, the intensity distribution of the volumes to match is not the same since it depends on the MRI acquisition process and therefore one structure does not necessarily have the same intensity values in both images. Since the monomodal (MR-MR) registration case is considered here, a simple polynomial conversion is done to match the intensity distributions of the *deformable model* and *scene* images. Actually, Guimond et al. [49] show that demons algorithm is very well-suited for either monomodal and multimodal image registration. However, in the case of multimodal registration a monofunctional dependence is usually not enough to match image intensity distributions and he suggests to use *bifunctional* function instead to estimate the image intensities correspondence.

Then, the intensity transformation can be expressed by the following polynomial of degree $M - 1$:

$$y(x) = a_1 + a_2x + a_3x^2 + \dots + a_Mx^{M-1}, \quad (4.1)$$

where x is the original intensity, $y(x)$ is the new intensity value, and all the coefficients are denoted by a_k . They are computed by solving the following estimation problem. The representative values of the background, cerebrospinal fluid, gray matter and white matter are automatically extracted from both image histograms by modelling each image histogram using a Gaussian mixture (refer to Section 6.6.1 for more details). Then, the linear* *least squares* on these values determines the a_k coefficients (M is set to 2).

4.3.3 Demon points selection

The Demons algorithm presents 4 main variations: the choice of the demon points, the demons force equation, the nature of the transformation and interpolation function (Section 3.4.8). In this thesis, three of these variants are fixed as follows: Eq. (3.11) guides the instantaneous displacement, a 3D vector field defines the free-form transformation, and tri-linear and nearest neighborhood interpolation are respectively used for gray-level and *labelled* images. The goal of this section is to

*Note that 'linear' refers here to the model dependence on the parameters a_k and not to the basis functions $\{1, x, x^2, x^3, \dots\}$.

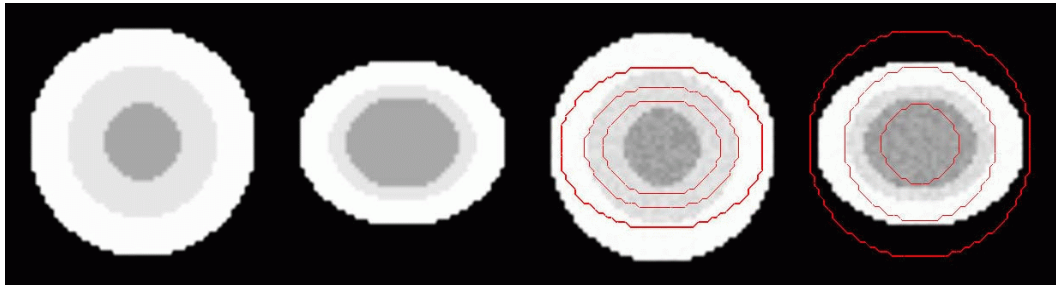


Figure 4.2: Synthetic data: original images and noisy images with target contours.

study using synthetic images how the demon points selection influences the *quality* of the registration, the smoothness and bijectivity of the transformation.

Let us first remind the concept of *demons*. It was introduced by Thirion with a parallel with Maxwell’s demons: intelligent agents placed in a semi-permeable membrane that separates two different particles of a gas [110]. Thus, demon points are in principle located on the object contours. The intensity gradient should extract automatically the demon points since, in a MRI, anatomical structures are represented by the iso-intensity contours. But this contour extraction is usually corrupted by the presence of noise and other inhomogeneities. A simple solution in order to avoid noise is for instance to select only the image voxels that have a norm of the intensity gradient above a certain threshold, i.e. a demon is associated to each voxel P of the *scene* image where $|\vec{\nabla}f(P)| > \varepsilon$.

Data sets and results

The registration is done between concentric spheres (floating image) and concentric ellipses (reference image). Volumes have dimensions of $100 \times 100 \times 100$ voxels and $1mm^3$ voxel size. Similar conditions to a MR brain image have been simulated as follows: the background is set to zero and the objects have gray levels similar to brain tissue intensities. Also, white Gaussian noise has been added to the images resulting in a signal to noise ratio (SNR) approximatively equal to the SNR calculated in a *typical* MRI. The original synthetic images without noise and the noisy images where the target contours have been superimposed are shown in Figure 4.2 and the histogram of the intensity gradient of the spheres with noise is shown in Figure 4.4.

The Demons algorithm has been run with the following input parameters: 3 scales, $256+128+64$ iterations (from low to high resolution scales), and the elasticity parameter σ is equal to 0.8 mm. Demon point selection is done by changing the value of the threshold ε : a complete grid of demons ($\varepsilon = 0$), demons inside the object ($\varepsilon = 5$), and demons located only at object contours ($\varepsilon = 20$ and in the case of images without noise with $\varepsilon = 0$). Each row of Figure 4.3 shows the results for these ε values. The binary images that represent the selected demon points are shown in the first column of Figure 4.3. The second column represents the absolute intensity difference between the deformed spheres and the target ellipses. The third column corresponds to the norm of the transformation field. Finally, the fourth column is the norm of the residual vector field.

Table 4.1 summarizes the effect of the most significant ε in terms of the percentage of voxels selected as demon points with respect to the total number of voxels (Demons(%)), the mean absolute intensity difference per voxel (Error), the computation time (Time), and the statistics on the norm of the deformation field (T) and on the norm of the residual vector field (R). Finally, the ε optimization functions are shown in Figure 4.5. The mean absolute intensity difference is plotted (*Error vs ε*) in Figure 4.5(a). The mean absolute error between the norm of the transformation and the norm of an *ideal* transformation is shown Figure 4.5(b).

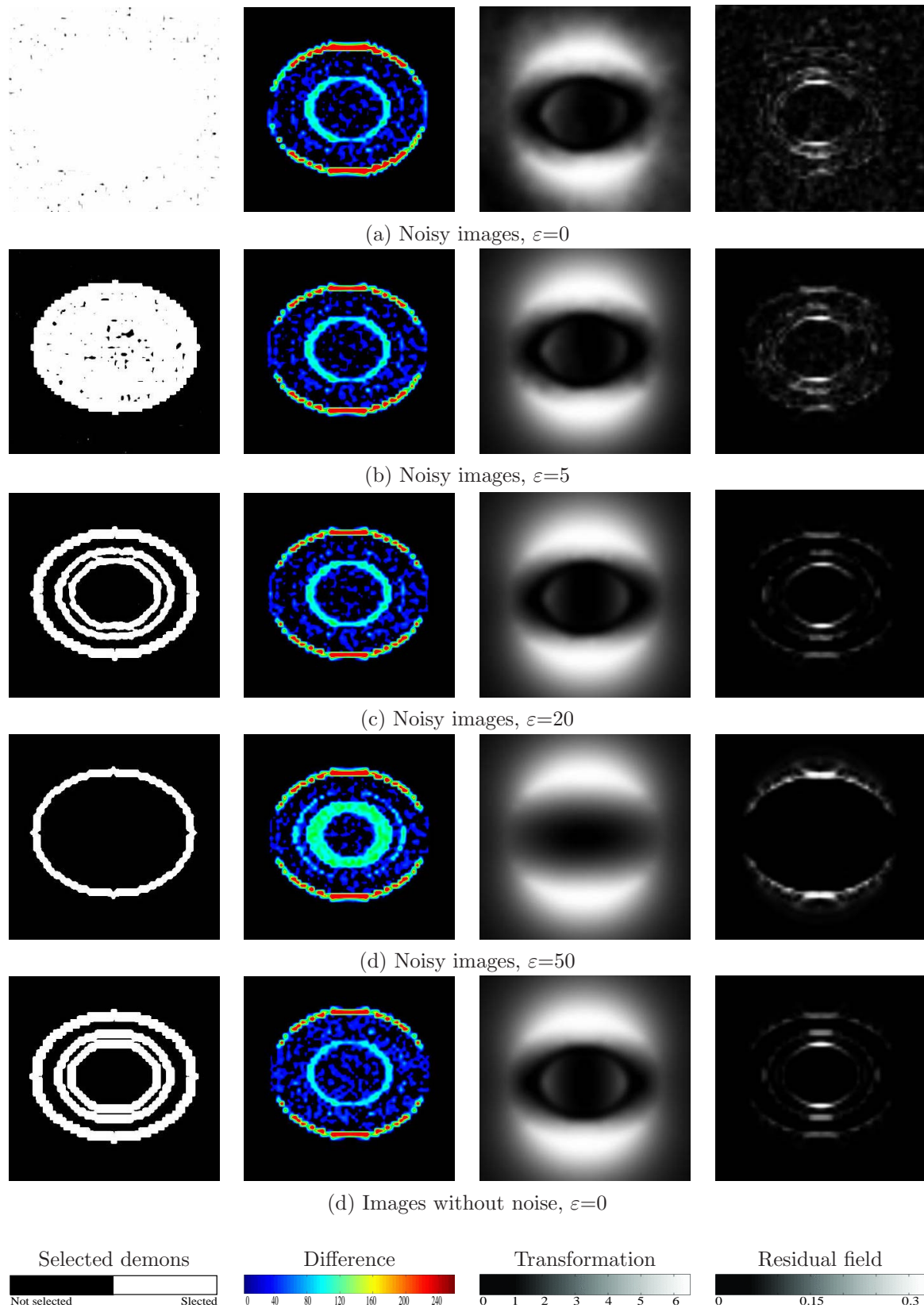


Figure 4.3: Analysis of the demon points selection as function of the threshold ε . Each column represents (from left to right): selected demon points, absolute intensity difference between reference image and deformed image, norm of the direct transformation field and norm of the error field between the direct and inverse transformations. These two last are expressed in mm.

ε	Demons(%)	Error	Time	T			R		
				Max	Mean	Var	Max	Mean	Var
No noise	1.71	0.83	28m21s	6.20	0.91	0.58	0.314	0.0015	4.8×10^{-5}
0	93.40	3.29	28m54s	6.13	1.41	0.46	0.350	0.0341	3.3×10^{-4}
5	4.47	3.21	28m53s	6.27	0.96	0.56	0.295	0.0029	9.9×10^{-5}
10	2.55	3.19	28m18s	6.24	0.97	0.57	0.369	0.0019	6.3×10^{-5}
15	1.74	3.20	28m52s	6.23	0.97	0.57	0.302	0.0015	4.5×10^{-5}
20	1.67	3.21	28m46s	6.22	0.97	0.57	0.280	0.0015	4.1×10^{-5}
25	1.56	3.22	28m23s	6.18	0.95	0.56	0.122	0.0014	3.4×10^{-5}
50	0.97	3.35	28m24s	6.10	0.94	0.55	0.125	0.0011	2.1×10^{-5}
150	0.95	4.52	28m27s	6.12	0.95	0.58	0.128	0.0011	2.0×10^{-5}

Table 4.1: Analysis of demon points selection: measures and statistics are made on the deformed image and on the transformation vector field. *Demons(%)* is the percentage of selected points respect to the total number of voxels. *Error* is the mean absolute intensity difference per voxel. *Time* is the computation time. *Max*, *Mean* and *Var* are the maximum displacement, the mean value and the variance of the deformation field (T) norm and of the residual vector field norm (R), respectively, all expressed in mm.

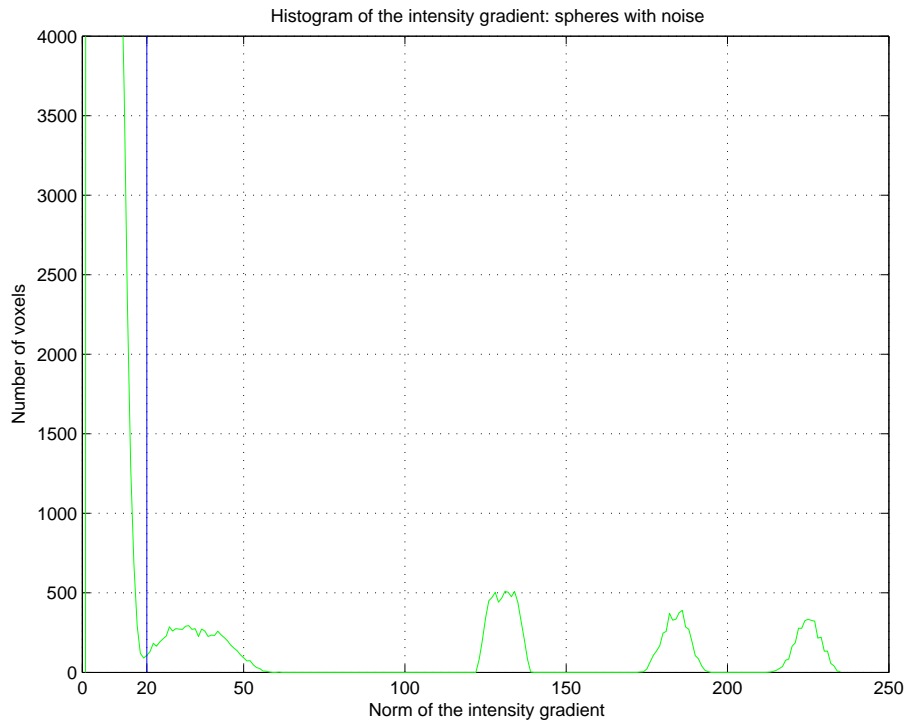


Figure 4.4: Histogram of the intensity gradient.

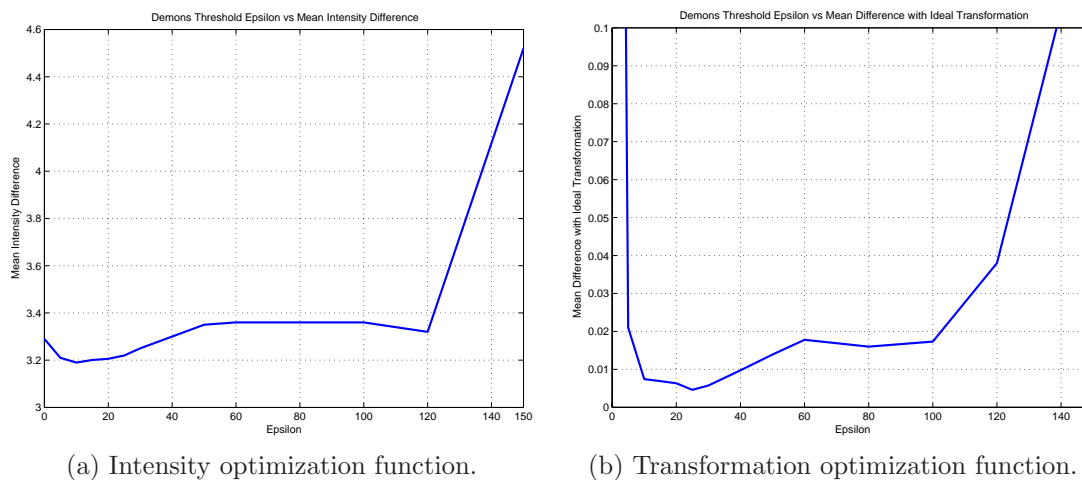


Figure 4.5: Optimization functions for demon points selection: (a) ϵ vs the mean absolute intensity error. (b) ϵ vs the mean absolute difference between the norm of the deformation field and the norm of the *ideal* deformation field.

Discussion

In the ideal case where no noise is present, a threshold of $\epsilon = 0$ extracts the object contours precisely and only 1.71% of the image voxels are considered demons (see first column of Figure 4.3). However, the same ϵ for the noisy images results into almost a complete grid of demons with a 93.4% of voxels as demon points. This percentage is quickly reduced to 4.47% when $\epsilon = 5$. The same percentage as in the noiseless case is almost obtained by ϵ equals 15 or 20. Finally, values of ϵ above 30 do not correctly represent the object topology. This is clearly shown in Figure 4.4 where the values of the norm of the intensity gradient lower than 20 are due to the background noise and the values upper 20 represent the image contours we are interested in. Also, note that the number of demons does not influence the computation time (around 28 min in a Pentium 4 and 1.8 GHz). Actually, demon force is computationally simple and fast (it costs less than the 3% of the total computation time).

One criteria used for the deformation assessment is the mean absolute intensity difference between the resulting image (the sphere has deformed into a ellipse) and the target. Originally, the mean absolute difference between the sphere and the ellipse is 6.94 in the case without noise and 9.74 for the noisy images. The lowest error is obtained in the noiseless case where the initial error is reduced to 0.83. For values of ϵ between 0 and 50, differences in the deformed spheres or in the mean absolute intensity difference images are hardly noticeable visually. Only when the selected demons are not representative of the image topology (ϵ above 50) the error starts increasing (see first and second column of Figure 4.3). Figure 4.5 summarizes the evolution of the mean absolute intensity difference error respect to ϵ : after a minima, the error increases first slowly (from $\epsilon = 30$ to $\epsilon = 120$) and, then, more quickly (from $\epsilon = 130$ to $\epsilon = 150$).

The smoothness of the transformation is as important as the quality of the deformation. Unfortunately, a *ground truth* transformation is not available to compare with. Instead, the transformation obtained when registering the images without noise is considered here as the *ideal* transformation. The statistics on the transformation field norm show that measures are similar to the ideal transformation (see Table 4.1) for almost all thresholds. However, visually, $\epsilon = 0$ leads to a very noisy transformation, $\epsilon = 5$ and $\epsilon = 15$ are the most similar to the ideal case, and with $\epsilon = 50$ the smoothest but wrong transformation is obtained (see third column of Figure 4.5). The MSE with respect to the ideal transformation quantifies these differences. The resulting objective function is

shown in Figure 4.5(b) and the threshold that minimizes it is placed around $\varepsilon = 25$.

The bijectivity is also considered in this validation. It is represented by the norm of the residual vector field between the direct and inverse transformation. Visually, as for the smoothness, $\varepsilon = 0$ and $\varepsilon = 5$ result in the most noisy residual fields. Contrary, $\varepsilon = 15$ performs similarly as the ideal transformation. Notice that the residual field is however directly related to the number of demon points: the fewer demon points, the less residual vector field (see in Table 4.1 that mean and variance directly decrease with respect to Demons(%)). Consequently, bijectivity is a necessary, but not sufficient, quality to assess the non-rigid transformation.

As a conclusion, ε should be optimally chosen in order to avoid the noise while preserving anatomical information. However, a threshold on the intensity gradient norm could hardly be used to feature extraction when a high level of noise or other artifacts such as inhomogeneities are present. Pre-processing the image by an anisotropic filter or a bias corrector can improve the demon points selection. Also, other methods such an image quantization could be used to better extract the anatomical information.

Demon points selection in MR brain images

In this section, feature selection is analyzed in the case of MR-T1 weighted brain images. Both the floating and the reference images are volumes of $256 \times 256 \times 150$ voxels with $0.9735 \times 0.9735 \times 1.5 \text{mm}^3$ voxel size. They have been globally matched and optimally quantified using the method proposed by Butz in [18, 19]. Figure 4.6(a) and (b) show the floating and reference images after affine registration and Figure 4.6(c) and (d) show the images after the quantization step.

Then, the demons algorithm is run with the following parameters: 4 scales, $256 + 128 + 64 + 16$ iterations from coarse to finer scales, and elasticity $\sigma = 0.8 \text{mm}$. Three cases are studied. First, registration is done between original gray-level images with a threshold $\varepsilon = 0$ and $\varepsilon = 20$ (Figure 4.6(e) and (f) respectively). Then, quantified images using $\varepsilon = 0$ have been matched. This last case is denoted by ε_Q and the resulting image, Figure 4.6(g), is obtained by applying the resulting transformation between quantified images to (b). Finally, the demon points are respectively shown in last row of Figure 4.6.

The same measures as in the synthetic images analysis are used for the assessment and they are presented in Table 4.2. In this case, the feature selection reduces the percentage of demons from 88% ($\varepsilon = 0$) to around 32.5% ($\varepsilon = 20$ and ε_Q). The MSE, that is 5402 initially, is reduced to around 1330 when using gray-level images and to 1570 in the case of quantified images. However, these differences are hardly visible when comparing the resulting deformed images to the target (see Figure 4.6(e), (f), (g) and (a) respectively). Central nuclei and ventricles are deformed almost equally for all the cases. Actually, the main differences are placed at the gyrus and sulci where, in fact, for some applications*, it is preferable to keep the topology of the floating subject than to deform it to perfectly match the target.

Statistics on the transformation vector field greatly differ depending on the threshold (see Table 4.2). The smoothest transformation (smallest variance) is obtained for $\varepsilon = \varepsilon_Q$, next by $\varepsilon = 20$ and, finally, $\varepsilon = 0$. That is not surprising since the transformation is less influenced by noise when using demons only at object contours than when using a complete grid of demons. Exactly the same conclusions are obtained from the statistics on the norm of the residual vector field between the direct and inverse transformations. The classification from more to less *bijective* transformation is ε_Q , $\varepsilon = 20$ and, finally, $\varepsilon = 0$.

*For instance consider the case where atlas-based registration is applied in order to create an statistical model of sulci and gyri anatomy.

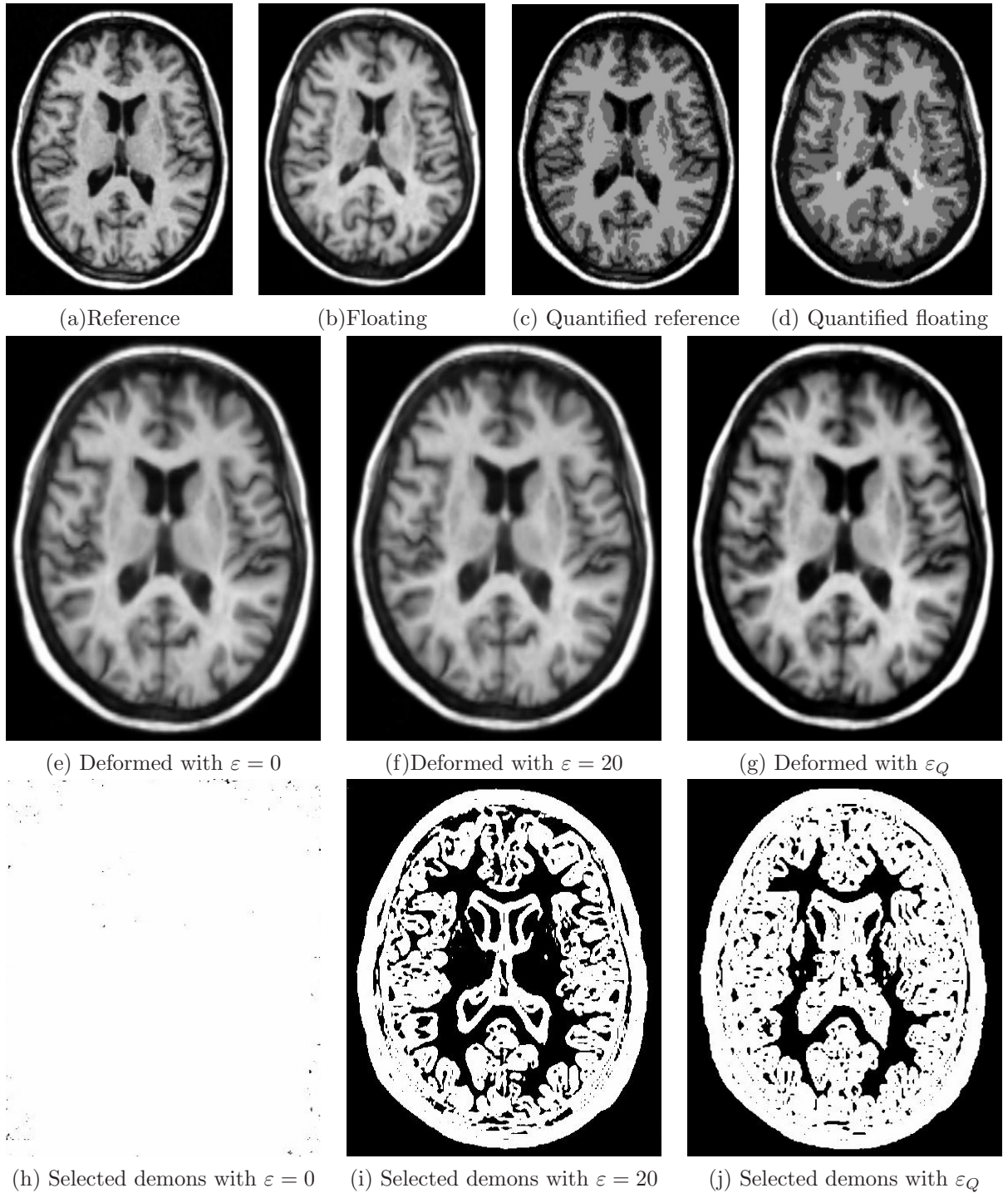


Figure 4.6: Qualitative analysis of the demon points selection in T1-MR brain images.

ε	Demons(%)	Error	T			R		
			Max	Mean	Var	Max	Mean	Var
Quantified	32.20	1567.8	15.75	3.2	7.3	1.8	0.0264	0.00166
0	88.61	1317.7	28.49	6.1	21.0	3.8	0.0773	0.00469
20	32.69	1335.3	25.48	4.8	17.7	2.5	0.0373	0.00382

Table 4.2: Analysis of demon points selection. MSE between the target and floating images is 5403.

ε	Error	ErrorT	T			R		
			Max	Mean	Var	Max	Mean	Var
No noise	85	0.26	8.31	1.85	1.48	3.3	1.1	0.17
0	279	1.03	7.57	2.19	1.16	5.7	1.5	0.42
10	262	0.86	7.65	2.50	0.96	4.8	1.8	0.27
20	220	0.77	7.63	2.17	1.08	4.6	1.3	0.16

Table 4.3: Comparison between B-splines and demons deformation. Initial MSE between is 19644 and 21079 between the target and the floating images without noise and with noise respectively. Maximum, mean and variance of the B-splines deformation field are 8.59, 0.83 and 0.92 respectively.

The same conclusions have been obtained in both synthetic and medical images. The non-rigid registration between quantified images has demonstrated that a compromise between the quality of the deformation and the smoothness and bijectivity of the transformation is obtained. However, the quantization step presents an important disadvantage since its accuracy to extract anatomical structures directly influences the quality of the registration. A pre-processing of the input images to avoid noise is of course desirable but also a more robust classification method could be used instead of the quantization (see Chapter 6).

Demon points selection: comparison with B-splines transformation

In this section, feature selection is analyzed by using a *ground truth* B-splines transformation. The synthetic data set has been created as follows. An arbitrarily B-splines deformation is applied to the floating image, concentric spheres without noise ($100 \times 100 \times 100$ voxels and $1mm^3$ voxel size) using a regular grid of 15625 control points. The deformed image is the target image. Then, some noise is added to both target and floating images. The resulting data set is shown in Figure 4.7. Demons algorithm is run to recover the B-splines transformation in two different cases (before and after adding noise), with the following parameters: 3 scales, 256+128+64 iterations (from low to high resolution scales), and $\sigma = 0.5$ mm.

Figure 4.8 shows the resulting deformed images and the norm of the deformation field. Table 4.3 summarizes the effect of most significant ε in terms of the mean squared intensity difference per voxel (Error), the mean squared error per voxel between B-splines and demons transformation fields (ErrorT), the statistics on the norm of the deformation field (T) and on the norm of the residual vector field (R). Here, the residual vector field is computed by combining B-splines ground truth transformation with the inverse transformation obtained with demons algorithm.

The obtained results show that in all cases demons algorithm recovers almost perfectly the target image (notice left column of Figure 4.8). However, that is not the case when looking at the transformation field. Of course, the best results have been obtained for the images without noise

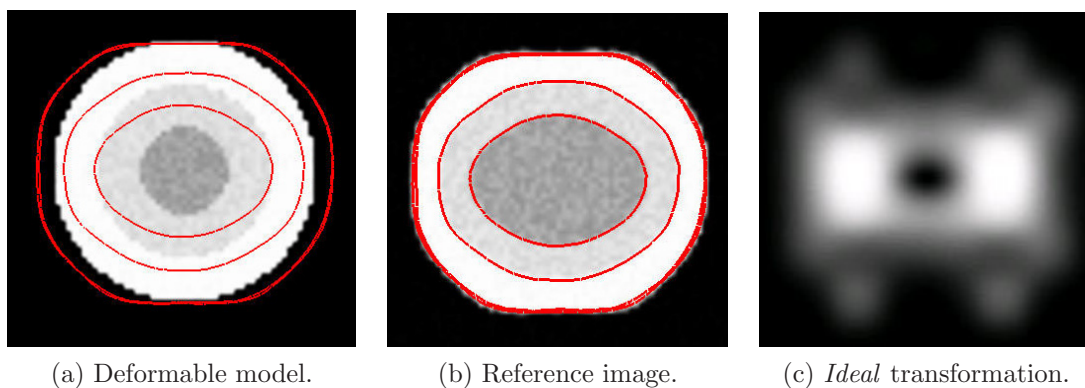


Figure 4.7: Comparison of demons algorithm with B-splines: input data set. (a) Deformable model. (b) Target image. (c) Ground truth B-splines deformation: norm of the transformation.

(ErrorT=0.26). In the presence of noise, the more robust transformation is obtained if demon points are correctly placed at the object contours ($\varepsilon = 20$), as it has been seen in Section 4.3.3. Here, the *best* transformation, i.e. the most similar to the B-splines ground truth, is obtained for the same value. Notice that the statistics on the residual vector field (see Table 4.3) would be similar to the ones previously shown in Table 4.1 if demons deformation would have recovered perfectly the B-splines transformation.

As a conclusion, the goal of this section has been to compare the deformation field of the demons algorithm with a parametric non-rigid transformation. A B-splines transformation has been selected as reference for comparison since it is widely used [96, 117]. However, this choice is arbitrary and we do not assume this kind of transformation as the ground truth deformation for brain image registration.

4.3.4 Elasticity study

In Section 3.4.5 the problem of the deformation field regularization has been explained. The solution that is used in this work is a discrete convolution of the transformation field by a Gaussian kernel. Then, the concept of *elasticity* has been defined as the standard deviation σ of the Gaussian filter. In what follows, the influence of the elasticity parameter is analyzed on both the quality of the deformed images and the roughness of the deformation vector field.

Data sets and results

This study is completed with the SPL atlas (see Section 2.4.2) as deformable model and a patient as reference image. Both images have $256 \times 256 \times 124$ voxels and $0.92 \times 0.92 \times 1.5mm^3$ of voxel size. After the global registration [29], the demons algorithm is run using the following parameters: 4 scales, and $256 + 128 + 32 + 16$ iterations from coarsest to finest scale. The elasticity varies in the range of 0.5, 1, 1.5, 2 and 2.5 mm. The input and the resulting deformed atlas images are shown in Figure 4.10.

As in the previous section, this study is done in terms of both a distance metric between the images (MSE) and the smoothness of the transformation field (the maximum and mean displacement and the variance of the deformation). All these measures are collected in Table 4.4. They are computed both in the whole brain volume (the background is not considered) and in a small volume

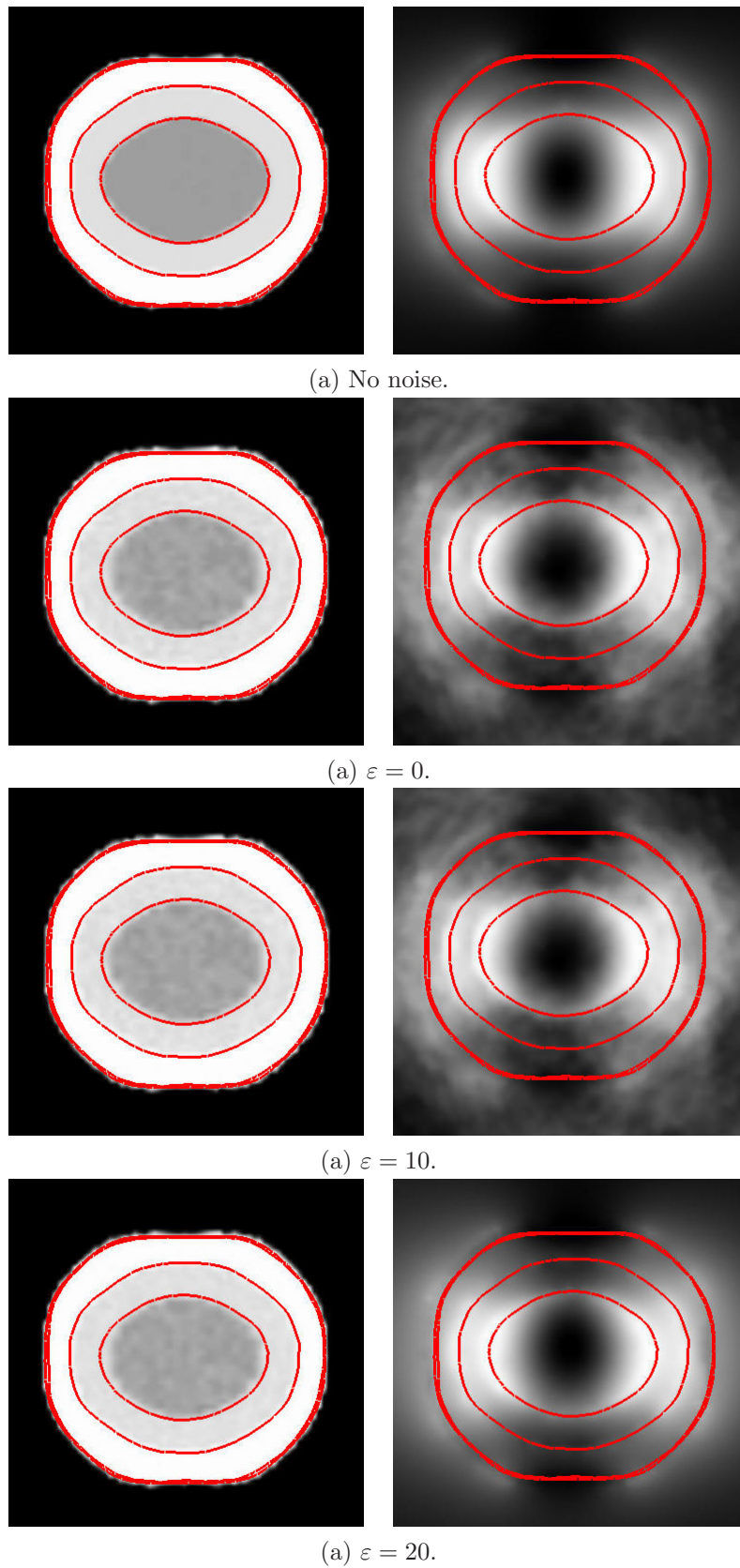


Figure 4.8: Comparison of demons algorithm with B-splines: deformation analysis. Left column: deformed image. Right column: norm of the deformation field.

		Whole Brain				VOI			
Sigma	Coefficients	MSE	Max	Mean	Variance	MSE	Max	Mean	Variance
0.5	3	22.1	11.7	0.80	1.6	0.37	9.41	3.46	2.20
1.0	5	37.0	7.3	0.70	0.7	0.76	6.95	2.70	1.03
1.5	7	47.7	5.5	0.67	0.4	1.38	4.99	2.27	0.56
2.0	9	52.6	4.1	0.61	0.2	1.90	3.67	1.89	0.32
2.5	11	56.5	3.0	0.56	0.1	2.37	2.85	1.60	0.20

Table 4.4: Computations are done in function of σ and in both the whole image and a VOI that contains deep brain structures. MSE, maximum displacement (Max), Mean and Variance of the transformation field norm are displayed.

of interest (VOI) containing the central nuclei, the ventricles and the thalamus (red, blue, and green structures respectively in Figure 4.10).

Discussion

The larger the standard deviation of the filter is, the less elastic the transformation is, since a large σ represents a large neighborhood influence. Qualitatively, this assumption is clearly verified by the ventricles deformation (see deformed atlas in Figure 4.10). Only σ between 0.5 mm and 1 mm seems to reach the same ventricles morphology and morphometry as in the reference ventricles. Less deformation is allowed for σ values above 1 mm where deformed atlas ventricles have not matched the reference ones. Thus, the results demonstrate that anatomical variability can be difficult to capture by σ larger than 1.0 mm. The allowed elasticity is less evident, but still visible, in the brain sulci and gyrus.

MSE increases as σ increases. That is, less anatomical variability can be compensated by less elastic registration. The MSE increment is almost constant (around 0.5) in a VOI while it changes (from 15 to 4) when computations are done in the whole image.

Statistics on the deformation field clearly show the influence of σ on the registration elasticity. The variance of the deformation field continuously decreases as σ increases (see Figure 4.9(a)), where σ is within the range of 0.4 and 1.2 mm. The maximum displacement and the variance of the deformation field are almost equal in both the VOI and whole brain (see Figure 4.9(b)). Thus, the VOI could be representative of the statistics in whole image. That is probably because the selected VOI contains the ventricles and they usually are the structure of the brain that presents largest morphological and morphometrical differences between subjects.

As a conclusion, in the case of *normal* anatomy non-rigid registration, the elasticity parameter is set to a value between 0.5 and 1 mm depending on the desired deformability.

4.3.5 Algorithm convergence

The number of scales and the number of iterations at each scale are the other inputs of the demons algorithm. The number of scales is fixed in a way that the global morphology of the object has still to be identifiable at the lowest resolution scale. Also, the *optimal* number of iterations at each scale to obtain a *good* matching in the minimum computation time should be determined. However, the algorithm behavior is complex and, therefore, the number of iterations is not easy to predict. The convergence study that is proposed in this thesis starts by analyzing the instantaneous demons displacement Eq. (3.11). That brings to the following conclusions:

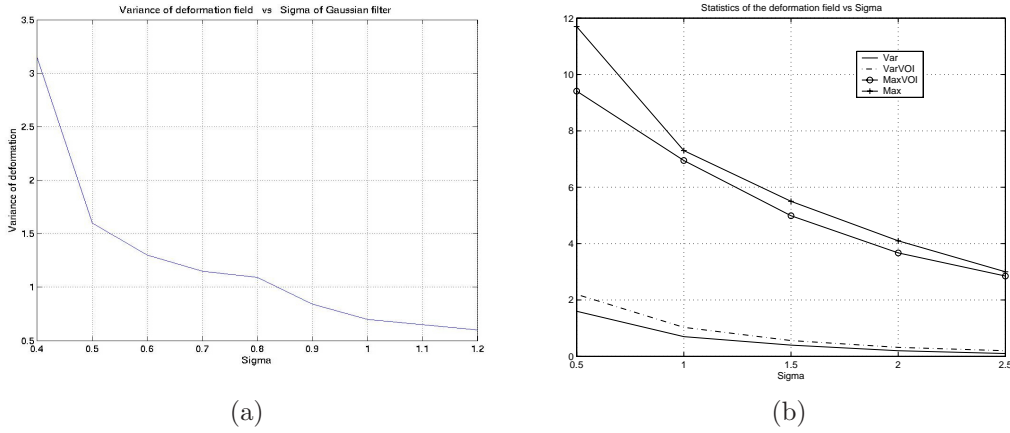


Figure 4.9: Statistics on the non-rigid transformation in function of the elasticity parameter: (a) Variance of deformation field computed in the whole brain for σ between 0.4 and 1.2 mm. (b) Comparison between computations on the brain and in a VOI of the maximum displacement and the variance of the deformation field norm as a function of the elasticity.

1. the intensity difference, $T_i \circ g(P) - f(P)$, should decrease until all the demon points, $\forall P \in P_{demon}$, match the intensity of the corresponding points of the deformable model. That is,

$$\lim_{i \rightarrow \infty} \sum_P (T_i \circ g(P) - f(P))^2 = C, \forall P \in P_{demon} \quad (4.2)$$

where i denotes the current iteration and C is a convergence threshold that represents the equilibrium between the demon forces and the elasticity.

2. The instantaneous displacement $\vec{d}(P)$ should decrease, in the same way as the intensity difference, to zero when the intensities match perfectly.

Analysis of the demons algorithm convergence

An example of algorithm convergence is presented here in order to empirically illustrate the above conclusions. The demons algorithm is run to register two synthetic images (a sphere and an ellipse) with $\sigma = 0.5$ mm and 0.8 mm (300 iterations per scale). The resulting MSE evolution for all the image voxels as a function of the current scale is plotted in Figure 4.11.

First, notice the different convergence evolution obtained at each scale. The convergence is less variable in finer than in coarser scales (Figure 4.11(a) and (b)), so the stopping criterion should be more restrictive in the finer scales.

Second, note that the convergence variability is in fact proportional to σ : for large values of σ the instantaneous displacement of a single voxel affects significantly its neighbors' movement and, consequently, the mean intensity difference has a larger variability. This effect is shown in Figure 4.11 where the MSE at the coarsest scale results more variable in the less elastic deformation ($\sigma = 0.8$ mm).

Third, note that the MSE sometimes presents a discontinuity when switching of scale. Actually, MSE increases with respect to the last error obtained at the previous scale. This effect is due to the fact that the transformation is upsampled and new errors appear at the new voxel locations. However, the MSE increment between scales 1 and 2 is largest than the other increments. That is because the downsampled sphere at the coarsest scale becomes really similar to the ellipse.

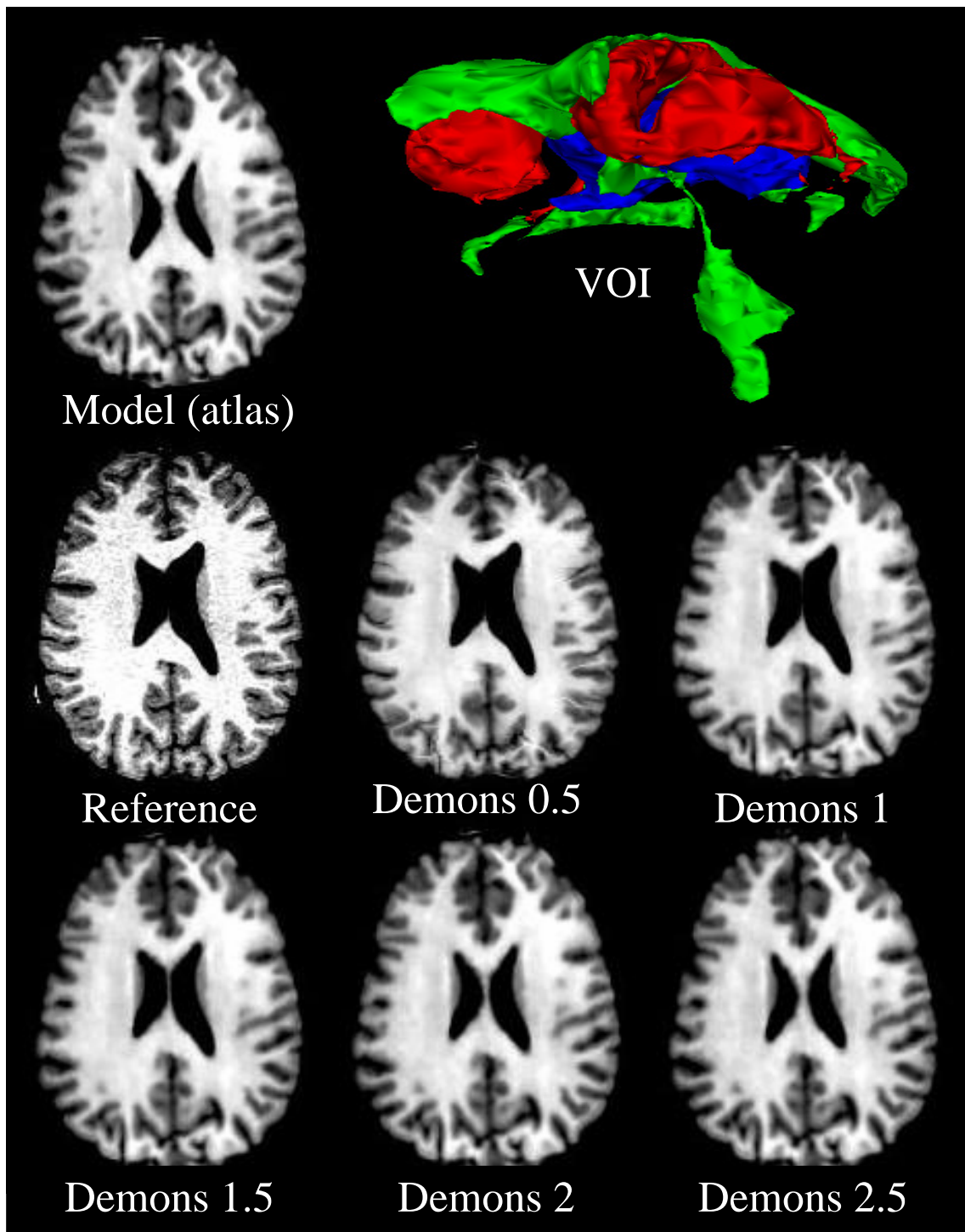


Figure 4.10: Input data for the elasticity study are the SPL atlas (deformable model) and a subject with normal anatomy (reference image). The volume of interest is formed by the caudate nuclei (red), the thalamus (blue), and the ventricles (red). Finally, deformed brain atlas for different values of the elasticity parameter.

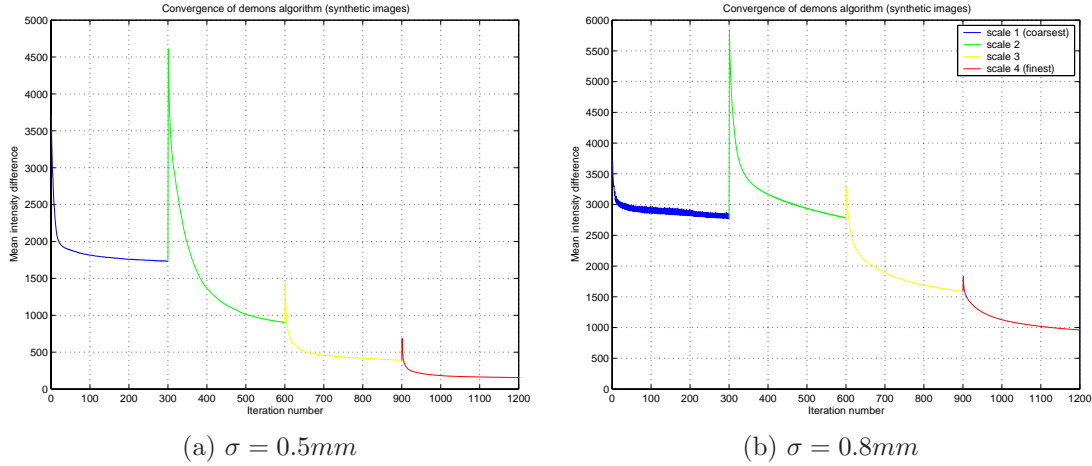


Figure 4.11: Convergence of the demons algorithm applied to deform a binary sphere into a binary cube.

Proposed stopping criterion

Then, a convergence criterion is proposed in what follows. Let us first define

$$\alpha_i = \frac{1}{N} \sum_P (T_i \circ g(P) - f(P))^2, \quad (4.3)$$

where α_i is the MSE between the scene, f , and the current estimation, $T_i \circ g$, at iteration i , and N is the number of image voxels. The idea is to stop the iteration process, and switch to the next scale, when α_i is close enough to the past values of α to conclude that the algorithm has converged. Mathematically,

$$m_i = \alpha_i - \frac{1}{M} \sum_{k=i-M}^{i-1} \alpha_k, \quad (4.4)$$

where m_i is the difference between the current MSE, α_i , and the past intensity differences averaged over M iterations. Then, the following expression is checked at each iteration:

$$0 \leq |m_i| \leq q \cdot \alpha_i \cdot \sigma \cdot \text{scale}, \quad (4.5)$$

where $\text{scale} \in \{1, 2, 3, 4\}$ denotes respectively coarse to fine scales, σ is the elasticity parameter, and q , is an arbitrary *quality factor*, defines the fraction of m_i that is considered irrelevant for a given set of images. Note that the influence of both σ and scale on the stopping criteria is defined according to the conclusions obtained in the above section. Also, M is arbitrarily set as function of the scale, that is, more iterations are averaged in coarse than in finer scales to be more robust in front of the MSE convergence variability.

In summary, the algorithm is assumed to have converged when the intensity difference does not change significantly during several consecutive iterations.

Demons algorithm using a stopping criterion

The convergence criterion proposed here is tested in both synthetic and medical images registration. Synthetic images are a sphere (deformable model) and an ellipse (target image) of $100 \times 100 \times 100$ voxels and a voxel size of $1m^3$ (see Figure 4.2 in Section 4.3.3). Medical images are two T2-weighted MR brain images of $256 \times 256 \times 64$ voxels with $0.92 \times 0.92 \times 3mm^3$ voxel size (see Figure 4.12(a)

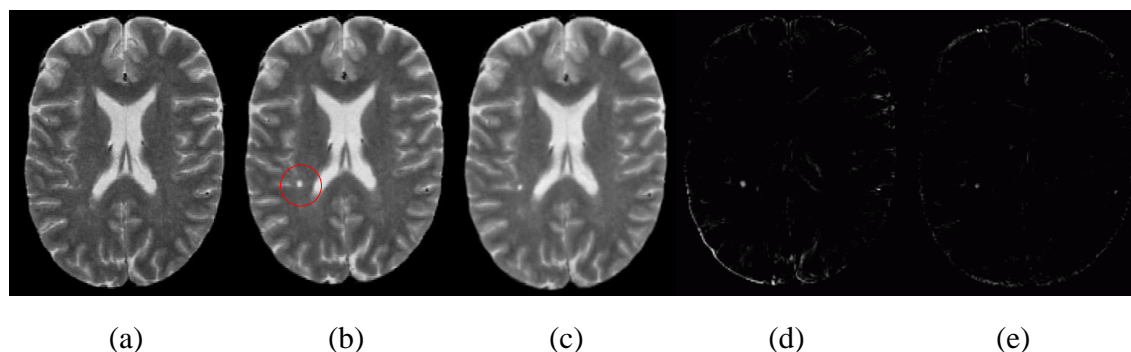


Figure 4.12: Study of demons algorithm convergence in MR-T2 brain images. (a) Image at time 1. (b) Image at time 2. (c) Deformed image 2 to image1. (d) Difference between (a) and (b). (e) Difference between (a) and (c).

Sphere to Ellipse	Number of iterations	MSE	Processing Time [min]
Arbitrary stopping	512/256/64/32	169	10
Arbitrary stopping	30/30/30/30	315	7.8
Arbitrary stopping	64/32	265	9
Arbitrary stopping	32	912	7.6
Stopping Criterion	21/42/134/19	157	8

Table 4.5: Comparison between an arbitrary stopping and the proposed stopping criterion applied to synthetic images. $\sigma = 0.8mm$, $M=\{16/9/4/2\}$, and $q=0.2\%$.

and (b)). Medical images are denoted by the indexes 1 (reference image) and 2 (floating image). They are both of the same patient and they show evolving multiple sclerosis* where image 2 was acquired around one year after image 1. Note that image 2 contains a little white nodule (circled by a red contour) that did not exist at image 1 (Figure 4.12(b)).

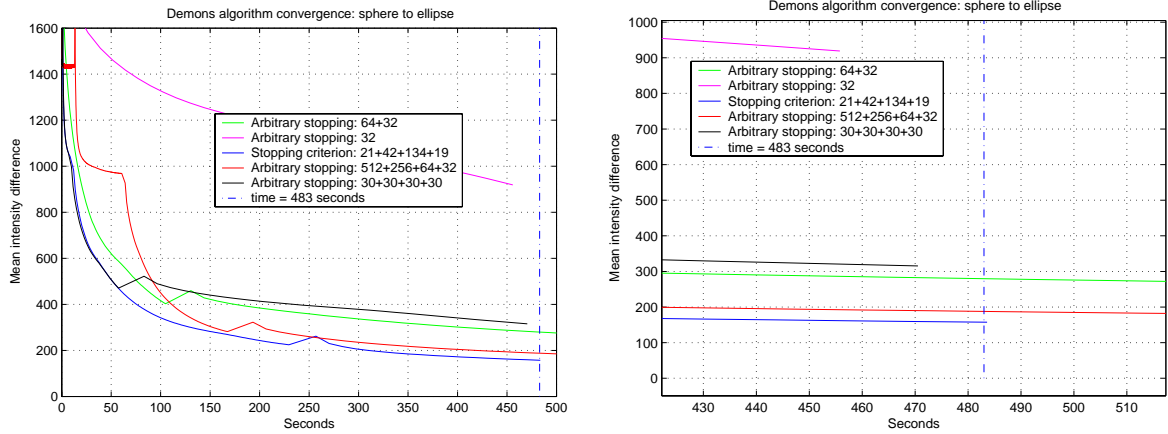
First, the stopping criterion (SC) is applied with the following parameters to the synthetic images: $\sigma = 0.8mm$, 4 scales $M = \{16, 9, 4, 2\}$ from coarse to finest scale, and, $q = 0.2\%$. Then, the performance of the demons algorithm using the SC is compared with respect to stopping arbitrarily using different number of scales and iterations. Results are shown in Table 4.5 and the MSE convergence is shown in Figure 4.13(a).

The SC is also applied to T2-MR images using 4 scales, $\sigma = 0.7 mm$, $M = \{16, 9, 4, 2\}$ from coarse to finest scale, and $q = 0.1\%$ as smaller displacements (only changes in some little nodules) than in the synthetic case are expected. The deformed image, the initial intensity difference and the intensity difference after deformation are respectively shown Figure 4.12(c), (d) and (e). The final MSE and the computation time are compared with the algorithm performance using an arbitrary number of iterations and scales in table Table 4.6 and the MSE convergence behavior at each scale is presented in Figure 4.13(b).

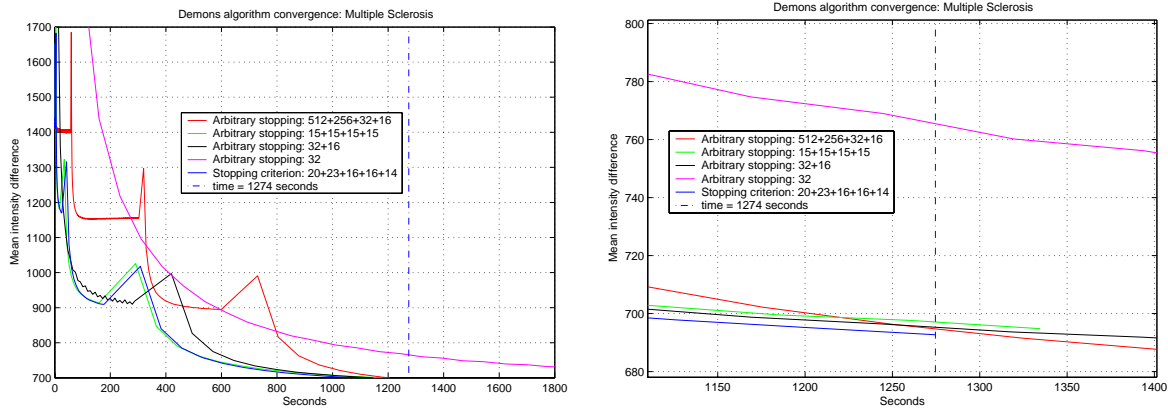
Discussion

The analysis of the results is presented in this section. In the case of synthetic images, results show that the difference of using an arbitrary number of iterations or the proposed stopping criterion is

*The multiple sclerosis is degenerative pathology that affects white matter of the brain.



(a) Synthetic images



(b) T2-MR brain images

Figure 4.13: Demons algorithm convergence for different stopping criteria.

T2-MR images	Number of iterations	MSE	Processing Time [min]
Arbitrary stopping	512/256/32/16	673	31
Arbitrary stopping	15/15/15/15	695	22
Arbitrary stopping	32/16	689	26
Arbitrary stopping	32	711	40
Stopping Criterion	20/23/16/14	692	22

Table 4.6: Comparison between an arbitrary stopping and the proposed stopping criterion applied to synthetic images. $\sigma = 0.7mm$, $M=\{16/9/4/2\}$, and $q=0.1\%$.

not significant in some cases. The error quantification is presented in Table 4.5 where it is shown that the lowest MSE is achieved by the SC but similar results have been obtained with arbitrary stopping criteria in almost the same computation time (see zoom in Figure 4.13). The worst result has been obtained with 1 scale since the MSE convergence is always very slow at high resolution scales.

In Figure 4.12(d) and (e) the reduction of the initial differences between T2-MR images is shown. The final MSE is almost equal in all cases (see Table 4.6) but the computation time is significantly different. The best compromise between both, MSE and time, is obtained when using the convergence criterion. That is because in this application few iterations are necessary until convergence since small displacements are expected. Finally, Figure 4.13(b) shows the continuous decreasing of the MSE over the scales where it can be seen that the slowest MSE convergence is also obtained for 1 scale.

It is logical to apply more iterations at coarser scales, as suggested in [109], in order to speed up the algorithm computation. However, in this section, it has been demonstrated that in some cases fewer iterations are actually needed until convergence in coarse than in finer scales. Thus, a compromise exists between both computation time and convergence when determining the number of iterations. It has been also seen how the multiscale implementation of demons algorithm speeds up the convergence.

4.4 Application to the segmentation of normal anatomy

An example of application of the atlas-based segmentation is presented in this section. This work was previously presented at [74].

4.4.1 Problem definition

The accurate analysis of internal structures of the brain is undoubtedly of great interest for the study and the treatment of various pathologies. Among them, the quantization of gray and white matter volumes may be of major interest in neurodegenerative disorders such as Alzheimer's disease, in movement disorders such as Parkinson's or Parkinson's related syndrome, in white matter metabolic or inflammatory disease, in congenital brain malformations or perinatal brain damage, or in post-traumatic syndrome. In such cases, it is necessary to consider only the volume of white and gray matter in specific regions of the brain such as hemispheric lobes or individual deep gray matter nucleus, excluding other regions like the cerebral trunk and the cerebellum.

It is therefore essential to accurately segment the brain structures in order to detect the regions of interest for the volumetric quantization. As it is important for this process to be robust, inclusion of *a priori* information about the task to be carried out is necessary.

4.4.2 Proposed method

The atlas-based segmentation process is the same as presented at the introduction of the chapter (Figure 4.1). The demons algorithm is chosen to compensate the morphological and morphometrical differences between internal structures of the brain. After the affine registration [29], the non-rigid registration of the atlas and the patient image is completed. Then, the trunk and cerebellum are removed simply by not considering the regions of the patient brain included in the trunk and cerebellum of the deformed atlas. Finally, thanks to previous works of our group [100, 101], an algorithm based on the parametric estimation of mixtures using genetic algorithm optimization is used to calculate the WM and GM volumes in the regions of interest.

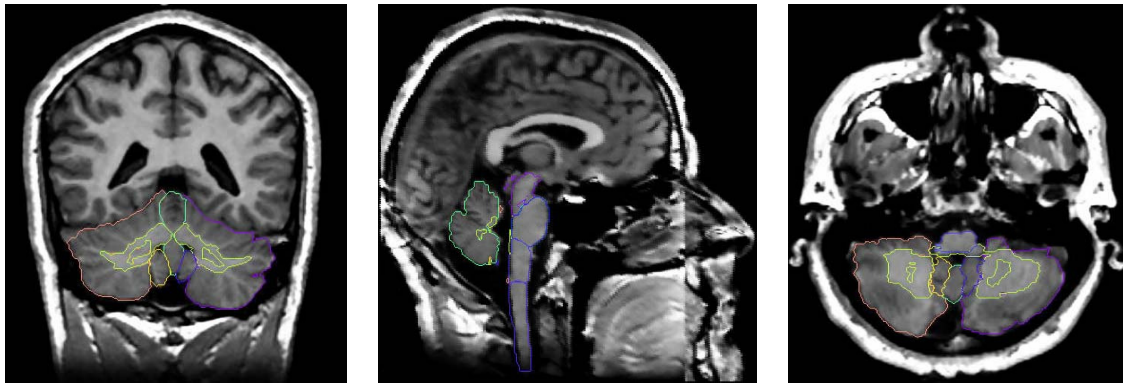


Figure 4.14: Region of interest: trunk and cerebellum of the SPL atlas.

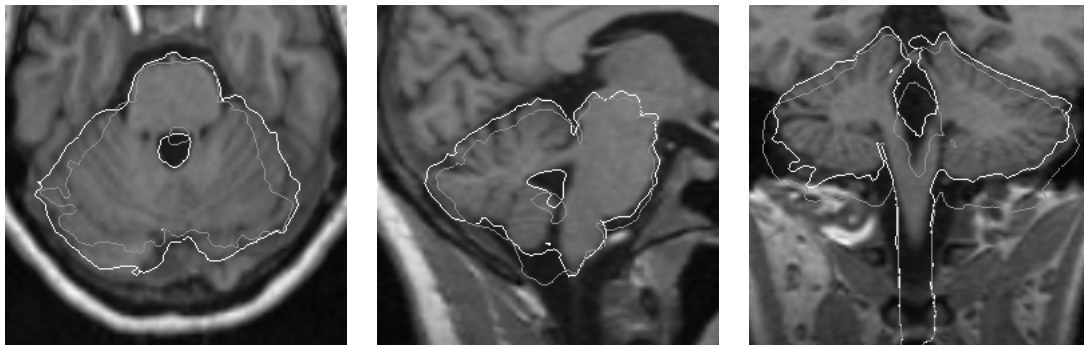


Figure 4.15: Deformed trunk and cerebellum of the SPL atlas. Contours after affine registration are in gray and after non-rigid registration are in white. It can be seen as white contour matches much better the structures than the gray one even if when large differences exist.

4.4.3 Data sets and results

The a priori information used in this application is the SPL digital anatomic atlas. The patient data set to segment is composed by 5 females and 3 males aged from 29 to 66-years. The 8 volumes are T1w-MR images of $256 \times 256 \times 124$ voxels with $1 \times 1 \times 1.25mm^3$ of voxel size.

The following parameters of the demons algorithm were found to lead to appropriate results: $\sigma = 1mm$, 4 scales and $256 \times 128 \times 32 \times 16$ iterations from coarse to finest scale. The non-rigid registration was executed on a PC-Linux, Pentium III at 700 MHz and computation time is about 30 minutes. Once the non-rigid transformation is found, it is applied on the atlas label map and a mask of the objects of interest (the cerebral trunk and the cerebellum) is extracted. Figure 4.15 compares the object contour before and after the non-rigid registration and Figure 4.16 shows the obtained deformed contours superimposed on some of the patient images. Finally, the calculation of the WM and GM volumes is done by a Bayesian classification. The volume computation is done before and after cerebral trunk and cerebellum extraction in Table 4.7.

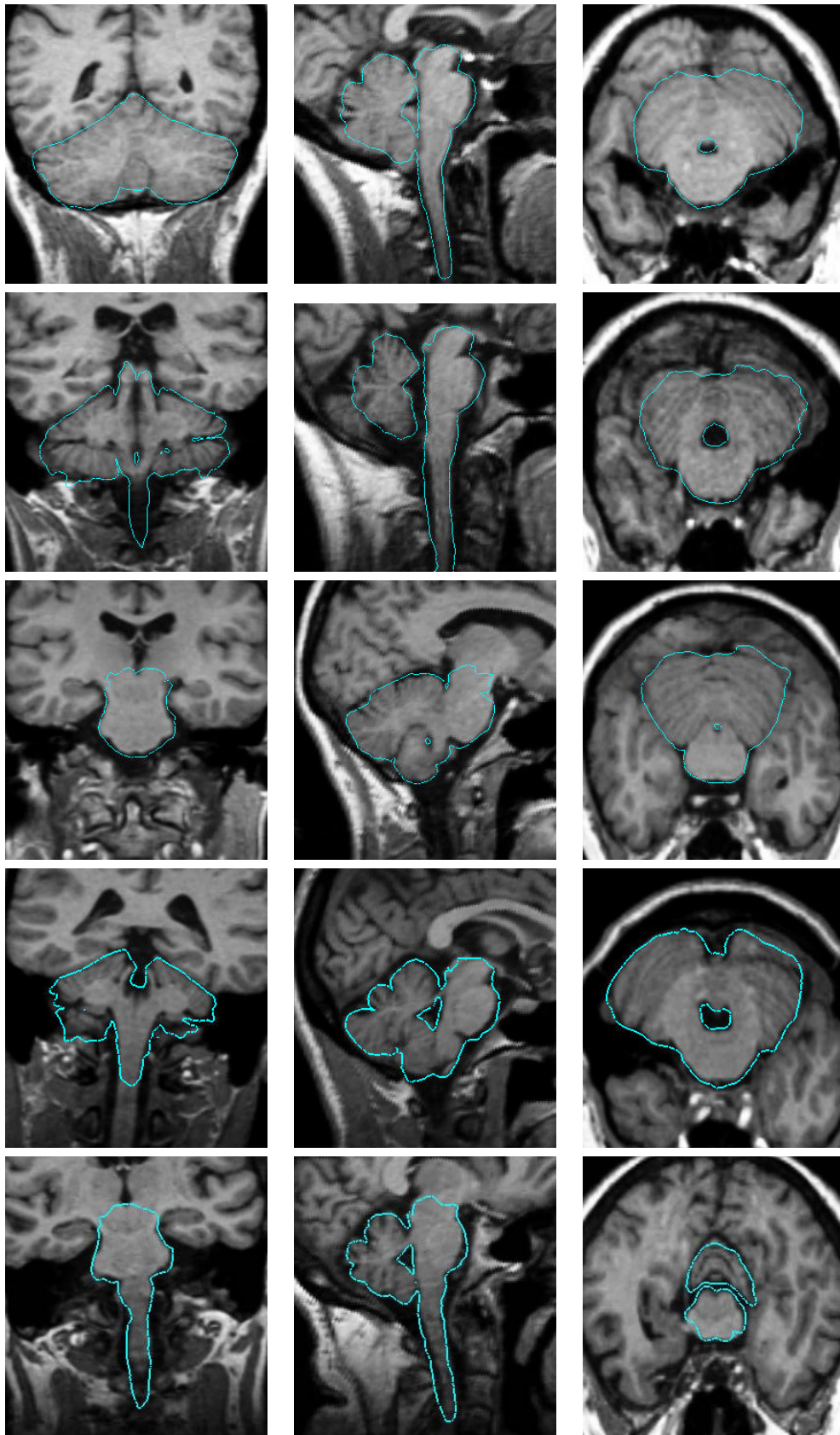


Figure 4.16: Trunk and cerebellum segmentation obtained by registering a digitized anatomical atlas to the patients.

	Before extraction		After extraction	
Patient	G.M.	W.M.	G.M.	W.M.
1	544	580	458	532
2	549	511	471	454
3	653	595	551	544
4	642	534	543	486
5	522	517	451	443
6	603	480	520	414
7	560	506	488	461
8	584	487	493	439

Table 4.7: Gray and white matter volumes in mm^3 .

4.4.4 Discussion

Non-rigid registration has been visually validated by an expert. Axial, sagittal and coronal views of both affine (gray) and non-rigid (white) deformed contours are displayed in Figure 4.15 for one patient. These images show that a good segmentation is obtained even in the areas where large displacements are needed. Also, in Figure 4.16, different slices of several patients have been shown to qualitatively assess the non-rigid matching. The final results of gray and white matter quantization are shown in Table 4.7. No more emphasis is made here in the gray and white matter quantization method since a detailed analysis and validation of [100, 101] and other classification techniques are made in Chapter 6.

This is a preliminary work done in atlas-based segmentation of normal anatomy. Unfortunately, no expert segmentation was available for quantitative validation. Thus, only qualitative assessment by an expert was possible. However, the atlas-based segmentation process should be validated with many more subjects and with some clinical data of reference.

4.5 Conclusions

It has been seen in this chapter how the complex task of segmentation is finally reduced to a non-rigid registration problem between a subject and an atlas. The demons algorithm has been proposed for the non-rigid registration. Then, the solutions used in this work to overcome its limitations have been briefly presented.

The input parameters for the registration have been analyzed in detail. Different criteria for demon points selection have been presented in order to minimize the effects of the noise to the final transformation. Also, a simply study of the algorithm elasticity has shown values of σ are able to compensate the anatomical variability. Finally, a stopping criterion that performs a good trade-off between the MSE minimization and the computation time has been proposed. It is a very general criterion and it can be applied to any kind of images, as it is based on the definition of the demon force. However, in medical imaging, minimizing the MSE does not necessarily mean performing the *best* possible registration.

As a conclusion of the chapter, an application of atlas-based segmentation is presented to demonstrate the importance of including a priori information to be robust in the segmentation task.

Atlas-based segmentation of pathological brains

5

*The most important words are not "I love you"
but "It's benign."*
Harry Block, "Deconstructing Harry"(1997).

5.1 Introduction

This chapter introduces the problem of using a priori information to register pathological brains. A new atlas-based segmentation method is proposed that tries to overcome the limitations of the existing solutions. Also, a new validation method to assess the final segmentation is introduced.

5.2 Problem definition

Precise segmentation of functionally important brain anatomical structures is of major interest in the minimally invasive approaches to brain space-occupying lesions treatment, including tumors and vascular malformations. It aims to reduce morbidity or mortality and to improve the outcome of surgical, radiosurgical, or radiotherapeutic management of such lesions. Despite the spatial information and higher anatomical resolution provided by MR imaging, precise visual segmentation may be a difficult task when anatomic structures are shifted and deformed. As has been seen in the previous chapters, the use of deformable models to segment and project structures from a brain atlas onto a patient's MR image is a widely used technique. But, when large space-occupying tumors or lesions drastically alter shape and position of brain structures and substructures, these methods have been of limited use. Potential applications for the methods using deformable models include segmentation of structures and substructures of the patient's brain for quantitative anatomical studies, radiation therapy planning, radiosurgical planning, and neurosurgery.

The purpose of this work is to deform a brain atlas onto a patient's MR image in the presence of large space-occupying tumors or lesions. In this approach, only pushing lesions such as meningioma are considered. Hence, this method does not yet apply to infiltrating tumors or take into account the presence of the edema.

To the best of our knowledge, only two approaches related to atlas-based segmentation on pathological brains have been published. Kyriacou and Davatzikos [67] propose to use a biomechanical model of brain using finite-element method. The soft tissue deformations induced by tumor growth are modelled first. Then, non-rigid registration matches the anatomical atlas with a transformed patient image from which the tumor was removed. On the other hand, Dawant et al. [32] rely on a simpler approach based on optical-flows - Thirion's demons algorithm [110] - for both tumor growth modelling and atlas matching deformations. Their solution is called *seeded atlas deformation (SAD)*, as they put a *seed* with the same intensity properties as the lesion in the atlas image and, then, they compute the non-rigid registration. Unfortunately, this requires the use of a large seed that masks atlas structures, potentially leading to erroneous results. In [77] preliminary results were presented with an improved seeding procedure, i.e. using a smaller seed, but it still masked some atlas structures.

The approach presented in this thesis is also inspired by the work of Dawant et al. [32], but introduces a number of important changes. Instead of applying the non-linear registration algorithm to the whole image, a specific *a priori* model of tumor growth is used inside the tumor area, which assumes that the tumor has grown radially from a single voxel seed [76]. Compared to previous approaches, this minimizes the amount of atlas information that is masked by the tumor seed. It also allows use of a single non-linear registration step with an adaptive regularization instead of the two step approach advocated by Dawant. A further improvement comes from the automation of the segmentation of the patient's lesion. Finally, a new validation method using a synthetic patient-specific atlas is proposed. This distinguishes between deformations due to interpatient anatomical variability and those induced by tumor growth. Results obtained on real patient images and the assessment of these results by an expert show that atlas registration onto the MR image of a patient with large space-occupying lesions can be correctly performed.

This chapter is organized as follows. Section 5.3 details the relevant state of the art, i.e. Kyriacou's biomedical deformation model and Dawant's seeded atlas deformation. Section 5.4 describes the proposed method in details. In Section 5.5 it is applied to patient data and results are discussed qualitatively. They are further validated in Section 5.6. Finally, those results are extensively discussed in Section 5.7.

5.3 Existing methods

Atlas-based medical image segmentation techniques have been widely studied in the bibliography. These techniques convert the segmentation of a MR image into a non-rigid registration problem between the MR image of the patient and the MR image used to create the brain atlas. An exhaustive review of these techniques is done in Chapter 3 and Chapter 4. Here, the approaches of Kyriacou [67] and Dawant [32], both dealing with the problem of atlas-based segmentation for pathological brains are presented.

5.3.1 Nonlinear elastic registration

A first approach for registration with anatomical atlas for pathological brains was presented by Kyriacou and Davatzikos [67] in 1999. The method they proposed is based on a biomechanical model of the brain using finite-elements. The idea is to model first the soft tissue deformations induced by the growth of a tumor and then proceed to the registration with an anatomical atlas. The method can be summarized as follows:

1. First, an estimate of the anatomy prior to the tumor growth is obtained through a simulated

contraction of the tumor region, using finite-elements and knowing the position of the skull, the ventricles, and the falx and tentorium, resulting in an estimation of the patient anatomy before the lesion growth.

2. Then, the treatment of the brain is like a healthy brain, so a *normal* to *normal* atlas registration is applied between an atlas and the estimation of the *healthy* patient using an elastic deformable model.
3. Finally, the estimation of the tumor growth process is applied to the registered atlas. However, the inverse transformation found in the first step is not used for this purpose. Instead, a nonlinear regression method that is driven by distinct anatomical features used to estimate the origin of the tumor and the level of strain is applied.

This method presents good results, but has some important drawbacks. The model for tumor growth has a tendency to uniform growth and does not take into account infiltration models. Also, it requires the previous accurate segmentation of many structures in order to perform the linear regression estimation. Finally, due to some implementation difficulties such as computational requirements, mesh generation and visualization, the method is currently implemented in 2D while the problem is by nature 3D.

5.3.2 Seeded atlas deformation method (SAD)

The other attempt of atlas-based registration of pathological brains that can be found in the bibliography was introduced by Dawant et al. [32]. Their method consists of a simple approach relying on an optical-flow based technique instead of a complex model of biomechanics. This registration technique is a modification of the demons algorithm [110], but introducing a lesion template. This introduction of the new template is completely necessary because the demons algorithm is really useful to warp healthy brains, with the atlas structures overlapped with the same structures in the patient, but not so effective when large anatomical differences exist between the images to match. Demons algorithm works poorly in this case because the assumption of small displacement is violated. Moreover, if a lesion template is not applied into the model, some healthy parts from the brain could warp to the lesion and produce wrong results. The solution that they introduced is *seeding a brain atlas*, that is to say, placing a small *seed* with the same intensity properties as the lesion and then apply the demons algorithm. A basic explanation of the algorithm follows:

1. Apply bijective demons algorithm in a very rigid way ($\sigma = 2.0$ mm), to warp the brain atlas onto the patient's image.
2. Insert lesion template into the warped brain atlas (the *seeded* atlas is obtained).
3. Apply bijective demons algorithm in a very elastic way ($\sigma = 0.5$ mm), to warp the *seeded* atlas onto the patient's image.

This method succeeds in lesion growth, but presents an important drawback because seed has to be a considerable size to obtain good growth in the tumor. Then, the anatomical information masked by the seed cannot be recovered and produces errors in the segmentation. Also, the seed deformation is strongly dependent on both the number of iterations and the elasticity parameter.

5.4 Proposed solution: using a model of lesion growth (MLG)

A new method for brain atlas deformation in the presence of large space-occupying tumors based on a simple *a priori* model of lesion growth is proposed in this section. Only pushing lesions such

as meningioma are considered. Hence, this method does not apply to infiltrating tumors or take into account the presence of the edema. This new approach is based on Dawant’s SAD algorithm but differs from it on three major points. Firstly, automated segmentation of the patient’s lesion is performed instead of manually drawing the tumor contour. Secondly, an *a priori* model of tumor growth is applied inside the lesion area, which assumes that the tumor has grown in a radial way. There is no more dependency to the seed size, either to the elasticity parameter of regularization, or the number of iterations. Thirdly, the algorithm is implemented in a single step thanks to the introduction of an adaptive Gaussian filter. The proposed method, that is called *model of lesion growth (MLG)*, works in 4 steps:

- An affine transformation is applied to the brain atlas in order to globally match the patient’s volume.
- Also, the lesion is automatically segmented.
- After that, the atlas is manually seeded with a voxel synthetic lesion placed on the estimated origin of the patient’s lesion.
- Finally, the non-linear registration algorithm is performed in order to deform the seeded atlas to match the patient. The non-linear registration algorithm is not applied to the whole volume, but only to the area outside the tumor location. Within the tumor, an *a priori* model of tumor growth is used which assumes that the seed grows radially until it reaches the tumor contour.

The result after applying these steps is a deformed brain atlas in which a tumor has grown from an initial seed, causing displacement and deformation to the surrounding tissues. After this, structures and substructures from the brain atlas may be projected to the patient’s image.

5.4.1 Lesion segmentation

The patient’s lesion needs to be segmented in order to specify the volume in which the model of tumor growth will be applied. To this purpose, we use a variant of the *Adaptive Template Moderated Spatially Varying Statistical Classification (ATM SVC)* algorithm proposed by Warfield et al. [65, 119]. The *ATM SVC* algorithm overcomes the limitations of spectral segmentation techniques and deformable model segmentation techniques by embedding both image and model information into a higher dimensionality space in which a k-Nearest Neighbors (k-NN) classification is performed. Voxels within the segmented brain mask [100] are classified into three classes: tumor, brain tissue (both grey and white matter) and ventricles. This is done in several steps, alternating k-NN classification and non-rigid registration using demons algorithm between the segmented image and the same classes from the brain atlas. At first, the only feature used for classification is the image intensity. Gradually, spatial localization features are extracted from the warped brain atlas. A bi-dimensional feature space is obtained by taking into account the distance to the brain atlas surface. In later steps, additional features such as the distance to the atlas ventricles and distance to the tumor bring a better accuracy and coherence to the classification.

Sample results for various lesion types are displayed in Figure 5.1. These results were obtained with $k = 7$ for the k-NN classification, and using 100 prototypes for each one of the classes. In Figure 5.1, the results of the *ATM SVC* segmentation with those of a manual segmentation performed by experts are compared (green and red contour respectively).

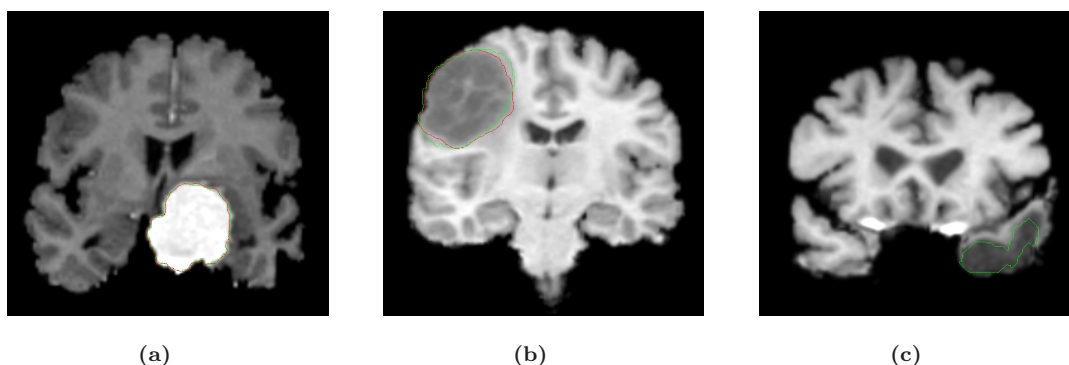


Figure 5.1: Segmentation results obtained with the *ATM SVC* algorithm on various lesion and tumor types. Red: manual segmentation. Green: *ATM SVC* segmentation. (a) Meningioma with left parasellar location. (b) Low grade glioma with right frontal location. (c) Cardiovascular accident (CVA) also called stroke.

5.4.2 Atlas seeding

After the affine transformation, the atlas and patient volumes are globally in correspondence except in regions that have been drastically deformed by the tumor. The atlas is seeded by manually selecting the point of origin of the tumor growth in the affine-registered brain atlas.

Both the previous work [77] and Dawant's [32] use an extended seed in order to drive the tumor deformation. It makes the positioning of the seed a relatively easy task but unfortunately masks atlas structures under the seed. In this thesis, the single-voxel seed induces no masking but - as will be discussed in section Section 5.6 - the selection of the correct seed location requires anatomical and biological knowledge of tumor growth.

5.4.3 Non-rigid deformation using a model of tumor growth

At this point, the affine registration ensures that the small displacement assumption is respected in the region of the brain that is far from the tumor. Meanwhile, the segmentation of the tumor volume and the manual selection of the tumor seed provides an adequate model for the tumor and its influence on immediately surrounding tissues.

The proposed non-rigid deformation method distinguishes between those two areas. Outside the lesion, the demons force as defined in Eq. (3.11) is applied. Inside the tumor, the tumor growth model assumes a *radial* growth of the tumor from the tumor seed, i.e.

$$\vec{d}_{lesion} = \frac{\overrightarrow{DM}_{seed}}{N_{it}}, \quad (5.1)$$

where \vec{d}_{lesion} is the instantaneous displacement field inside the lesion area, $\overrightarrow{DM}_{seed}$ is a vector that comes from the transformed point ($\vec{T}_i(\vec{P}) = \vec{P} + \vec{D}_i(\vec{P})$) to the seed (see Figure 5.2), N_{it} is the number of iterations of the deformation algorithm that have to be performed*. Without outside interference, vectors \vec{d}_{lesion} , $\overrightarrow{DM}_{seed}$ and $\vec{T}_i(P)$ would of course be aligned. Practically, it is not so both because of the regularization step occurring between each iteration, and because of interpolation and rounding. This model allows the points inside the lesion area to converge towards

*Remind that it is an iterative process: the total deformation is updated at each iteration i by the instantaneous deformation field, i.e., $\vec{D}_{i+1}(\vec{P}) = \vec{D}_i(\vec{P}) + \vec{d}(\vec{P})$. \vec{D} is regularized at each iteration by a Gaussian filter $G(\sigma)$.

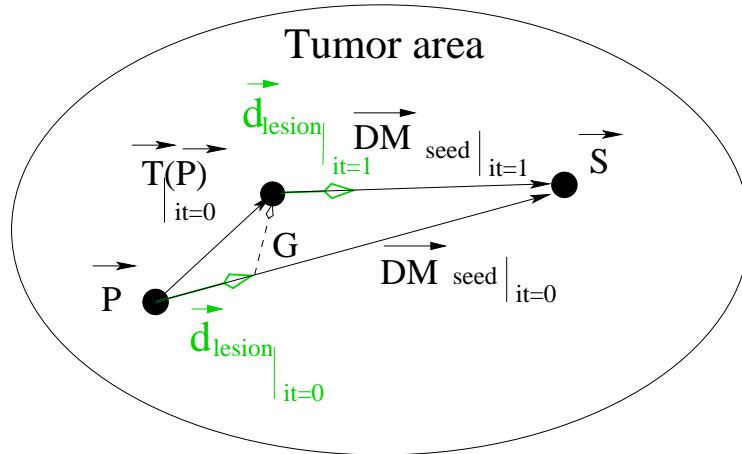


Figure 5.2: Transformation field inside the tumor at first iteration. \vec{d}_{lesion} is the instantaneous displacement. $\vec{T}_i(P)$ is the total transformation after regularization (G). Actually, there is no filtering inside the tumor (only in the tumor contour). However, the vector field could be misguided because of interpolation and rounding. \overline{DM}_{seed} is the distance between the current point $\vec{T}_i(P)$ and the seed voxel \vec{S} .

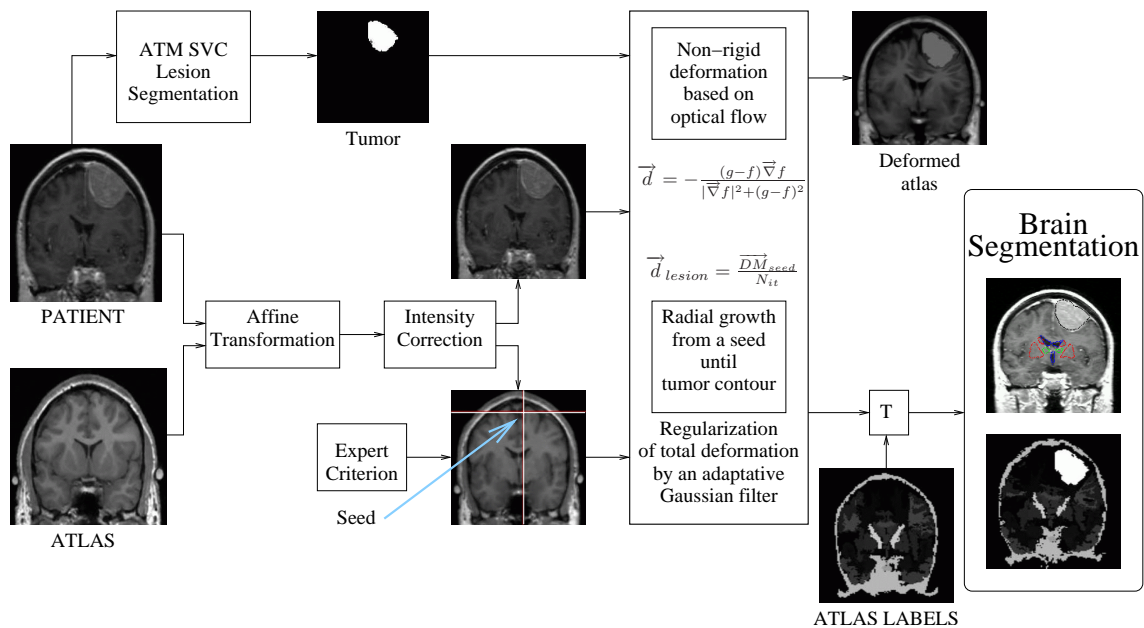


Figure 5.3: Block diagram of the atlas-based segmentation method using a Model of Lesion Growth (MLG algorithm).

the seed voxel*, while remaining simple and allowing any number of iterations to take place outside the tumor volume. The displacement vector computed at every voxel using either the demons force Eq. (3.11) or the tumor growth model Eq. (5.1) is regularized by an adaptive Gaussian filter to avoid possible discontinuities. Three areas are considered: inside the lesion area, close to the lesion

*Remind that the vector field points the origin, and not the destiny, of a voxel.

(tumor border and voxels within a distance to the tumor contour smaller than 10 mm) where large deformations occur and the rest of the brain. Smoothing is not necessary inside the lesion because the vector field induced by Eq. (5.1) is highly regular and the continuity is ensured. Actually, some smoothing could modify the transformation field and prevent some distant voxel to converge to the seed. Moreover, the elasticity does not have to be ensured to be a radial growing and not an optical-flow based algorithm. So, $\sigma = 0$ inside the lesion area. In the region close to the tumor there are large deformations due to the tumor growth. Then, it is necessary to allow large elasticity, i.e. σ should have a small value, typically 0.5 mm. In the rest of the brain, deformations are smaller, due primarily to inter-patient anatomical variability. So, a larger σ proves to be better, as it simulates a more rigid transformation. Previous studies (Section 4.3.4) suggest that a typical σ to match two healthy brains is about 0.5 mm and 1 mm. In what follows, $\sigma = 0.8$ mm is used.

5.5 Data sets and Results

Data sets

The patient images used in this study have been retrieved either from the Surgical Planning Laboratory (SPL) of the Harvard Medical School & NSG Brain Tumor Database [65] and from the Department of Radiology in Lausanne University Hospital. They consist of 4 volumes of 128 coronal slices of 256 x 256 pixels and 0.9375 x 0.9375 x 1.5 mm^3 of voxel size. All of them present a meningioma. This kind of tumor is usually benign and its extracerebral growth usually induces a pure shift and deformation of the underlying brain structures (see MR patient images on Figure 5.4). Meningiomas are lesions of interest because they are typically suitable for radiosurgery or stereotactic radiotherapy. No brain edema was observed on the data set. Notice that most of the patient image have been acquired using a contrast agent. The digital anatomic brain atlas used in this section is the SPL atlas.

5.5.1 Deformed atlas images and deformation field

The results obtained by the *MLG* method are presented in this section from the point of view of the deformation field. The deformation field analysis is done by comparing *MLG* to the *SAD* method. Here only the study for one patient (Patient 2, Fig. 5.4(b)) is presented and similar results have been obtained for the other patients of the data set. Patient 2 has a left parasellar meningioma of approximately dimensions 41x42x52 mm^3 . *SAD* method has been applied for two different seed sizes (resulting from the tumor mask erosion of 8 mm and 12 mm respectively, see Figure 5.5(a) and (b)). The *MLG* has been run as presented in Figure 5.3 and using the parameters defined in Section 5.4. In Figure 5.5(c) the one-voxel seeded atlas is shown.

Figure 5.5(g) and Figure 5.5(i) represent the vector field of the *SAD* and the *MLG* respectively, and Figure 5.5(j) and Figure 5.5(l) represent the norm of the deformation of the *SAD* and the *MLG* respectively. It can be seen that the performance of *SAD* when using the largest seed is, in terms of deformed atlas and deformation field, comparable to the performance of the *MLG*. Note that the deformation field is almost the same for both methods (compare Figure 5.5(d) and Figure 5.5(f)).

However, when using the small seed, the deformation obtained by the *SAD* method inside the tumor area does not reach the tumor border (Figure 5.5(e)). The force inside the lesion area is actually misguided as it can be seen in Figure 5.5(h) and (k).

The different behavior between the two approaches can be explained as follows. The *SAD* highlights the tumor and seed masks to obtain a strong gradient on the tumor and seed contours. But between them, only the intensity gradient of the atlas MRI is used since the intensity gradient

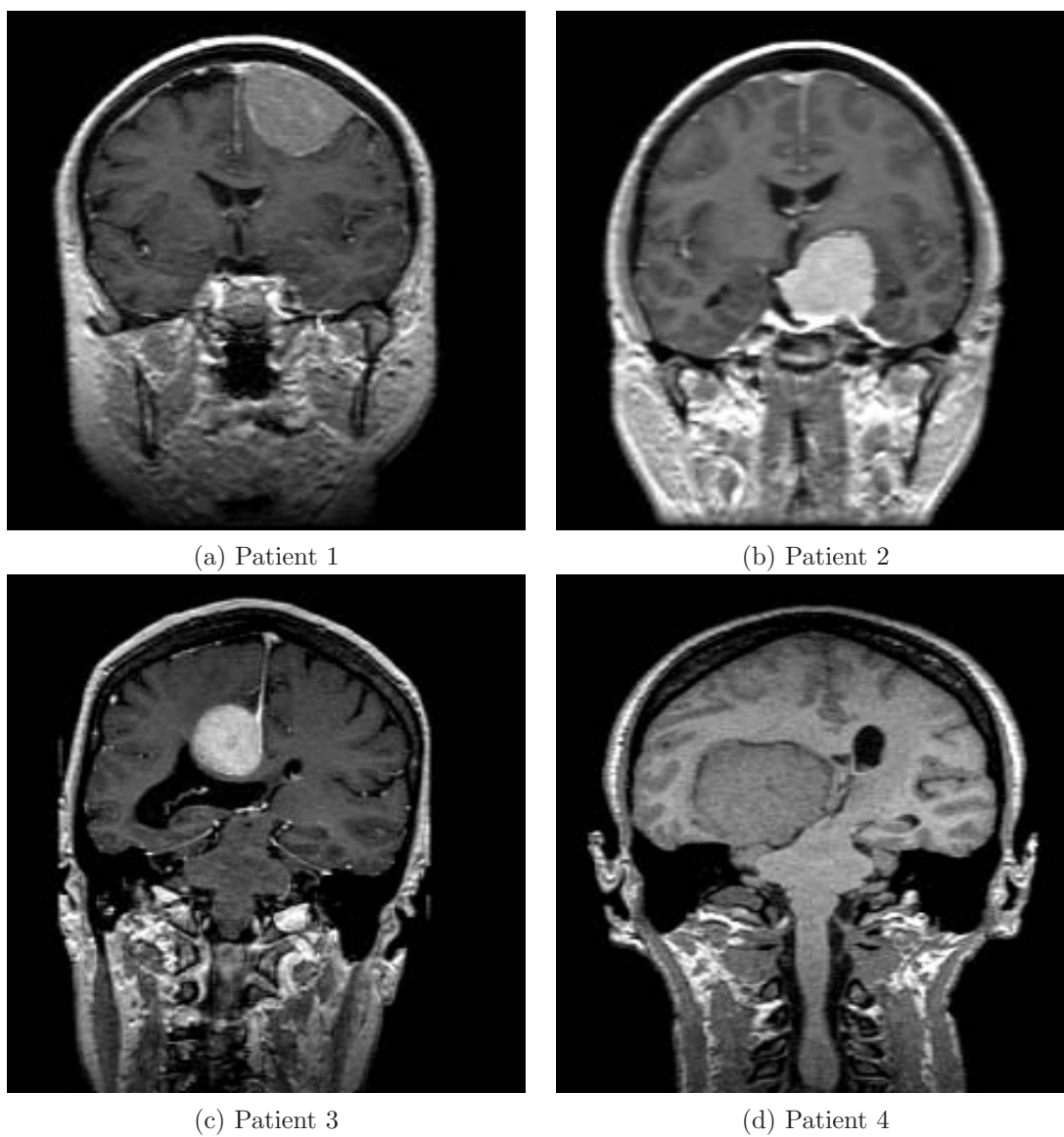


Figure 5.4: Sagittal slices of data set with tumors.

within the highlighted tumor area is zero. Having only gradient information on the contours is not strong enough when using a small seed since a large deformation is needed to make the seed grow towards the tumor. Furthermore, that explains the dependency of the SAD method on the seed size and iteration number. On the contrary, the MLG can compensate the large anatomical differences between the one-voxel seed and the tumor thanks to *a priori* information from the growth model.

5.5.2 Segmentation results study

Importance of the tumor growth model

It has been seen in the section above that SAD cannot grow the small seed until the final tumor size. However, it seems that a good deformation has been obtained in the rest of the brain. Thus, since we are interested in the deep brain structures and not in the tumor itself, the need of simulating the lesion growth could be questionable. In this section, the segmentation of the ventricles, the thalamus and the central nuclei is analyzed by comparing MLG and SAD using the smaller seed. The obtained results show that the MLG performs clearly better in the case of the structures near the tumor (thalamus and central nuclei).

The axial, sagittal and coronal view of final segmentations are shown in Figure 5.6. The ventricles are almost exactly segmented by both approaches (MLG in blue and SAD in magenta). The thalamus segmentation is performed slightly better by MLG (in cyan) than by SAD (in yellow). Their differences can be appreciated in Figure 5.6(c) and (d). The most critical structure is the central nuclei (MLG in green and SAD in red) since it is initially placed inside the tumor area. In this case, SAD method fails because the central nuclei segmentation is placed inside the tumor area. On the contrary, MLG pushes the central nuclei out of the tumor region and it obtains a better segmentation.

As a conclusion, the need of a correct estimation of the tumor growth in order to obtain a good final segmentation of the structures directly displaced and deformed by the lesion has been shown.

MLG segmentation results

Here, the segmentation results for all the patients of the data set are analyzed. Some structures and substructures of interest from the deformed brain atlas have been projected to the patient's image: the tumor (in red), the ventricles (in green), the thalamus (in yellow), and the central nuclei (in dark blue) (see Figure 5.7). To initiate the algorithm, the expert has been asked to indicate the most probable position of the tumor seed and that is what we call the most *logical* seed position.

Segmentations of both patient 1 and patient 2 are really satisfactory (see fig5.7(a) and (b)). The structures have been correctly pushed outside the tumor area and the final deformation converges accurately to the target image. Actually, these two patients do not present large anatomical differences with respect to the atlas (see Figure 5.4(a) and (b)), except of course the lesion itself.

The segmentation results for both patient 3 and 4 are less satisfactory (errors are denoted by red arrows in Figure 5.7(c) and (d)). These two cases are much more complex since large morphological differences exist between the atlas and the patients' brains in addition to the lesion (see the ventricle inflammation in Figure 5.4(c) and (d)). In patient 3, the structures of interest have been correctly pushed outside the lesion area, but some important structures, for example the ventricles, have not been correctly deformed. In patient 4, the assumption of overlapping between same anatomical structures required by the demons algorithm has been largely violated. For example, left ventricle of the atlas is actually placed over the right ventricle of the patient (see Figure 5.8). This makes the non-rigid registration fail outside the lesion area even if the seed has correctly grown until the tumor edges.

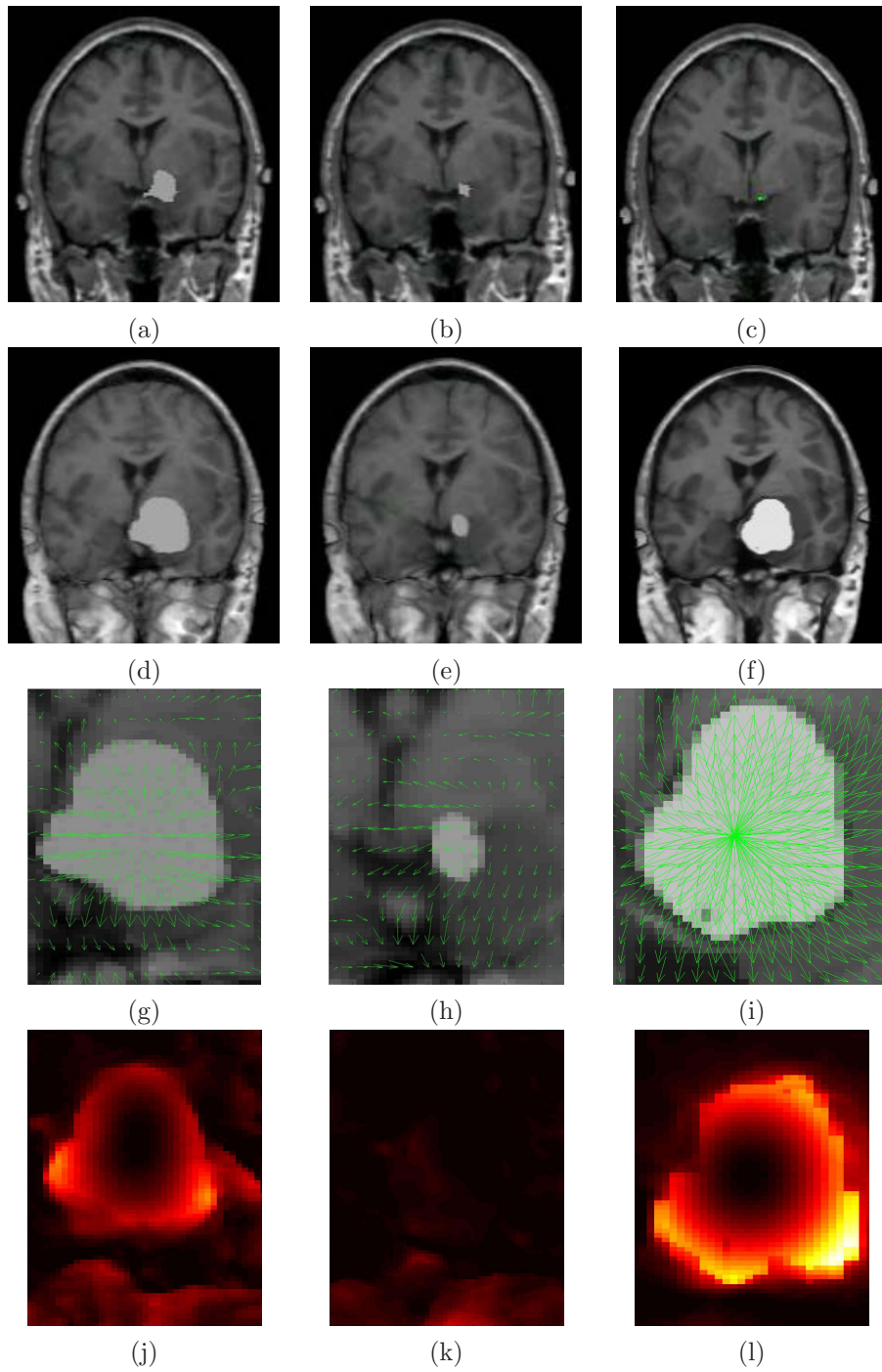


Figure 5.5: Atlas seeding, lesion growth and deformation field analysis. (a) Seeded atlas, big seed. (b) Seeded atlas, small seed. (c) Seeded atlas, one voxel seed (in green). (d) Deformation of seeded atlas with the big seed using SAD. (e) Deformation of seeded atlas with the small seed using SAD. (f) Deformation of seeded atlas with one voxel seed using MLG. (g) SAD: deformation field using a big seed. (h) SAD: deformation field using a small seed. (i) MLG: deformation field. (j) SAD: norm of deformation field using a big seed. (k) SAD: norm of deformation field using a small seed. (l) MLG: norm of deformation field. NOTE: Deformation field corresponds to a zoom of the lesion. Brightest area correspond to large deformation.

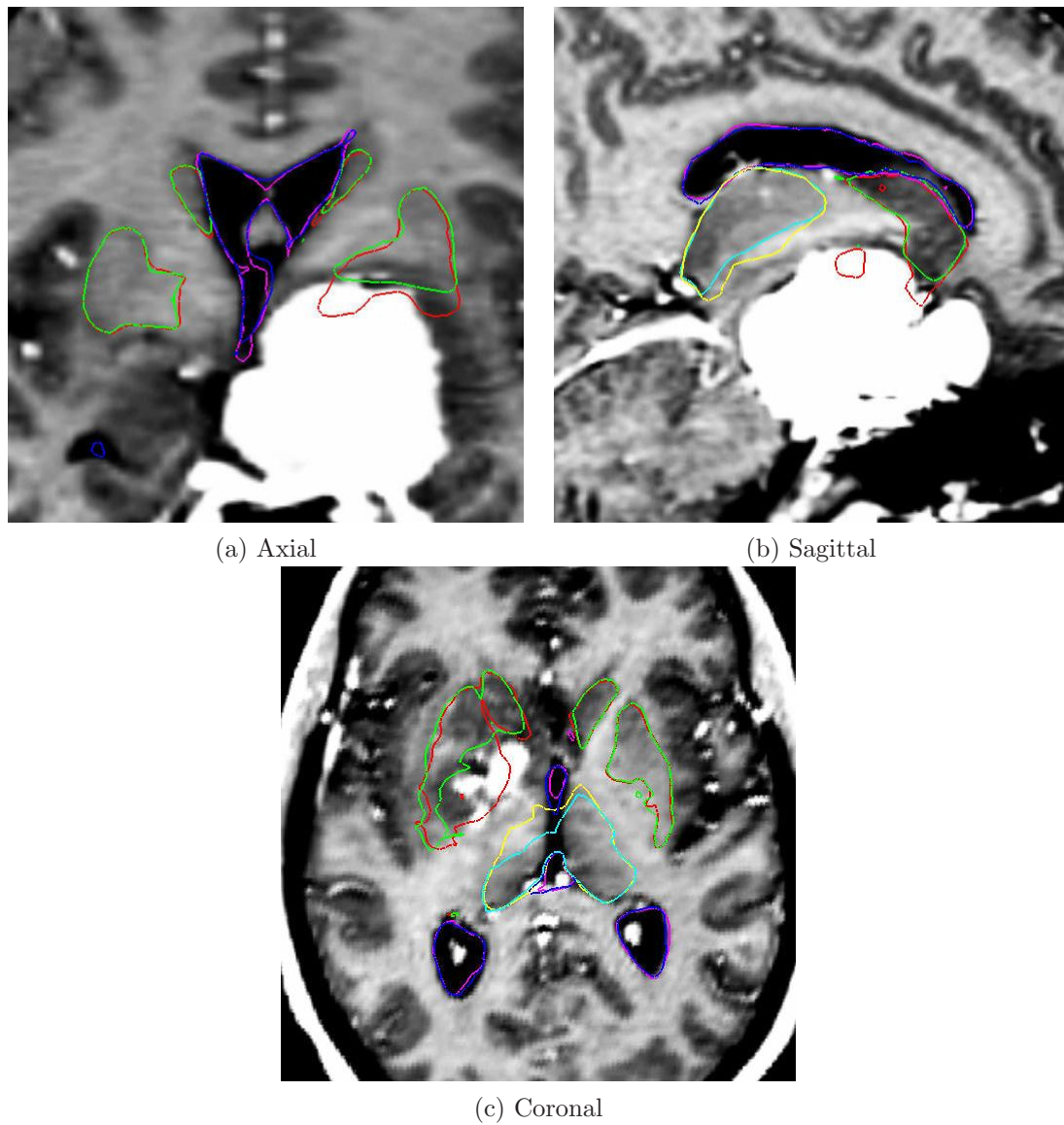
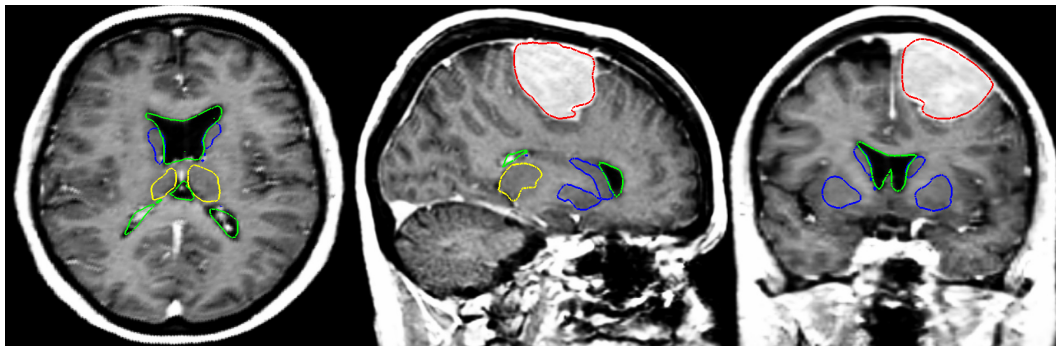
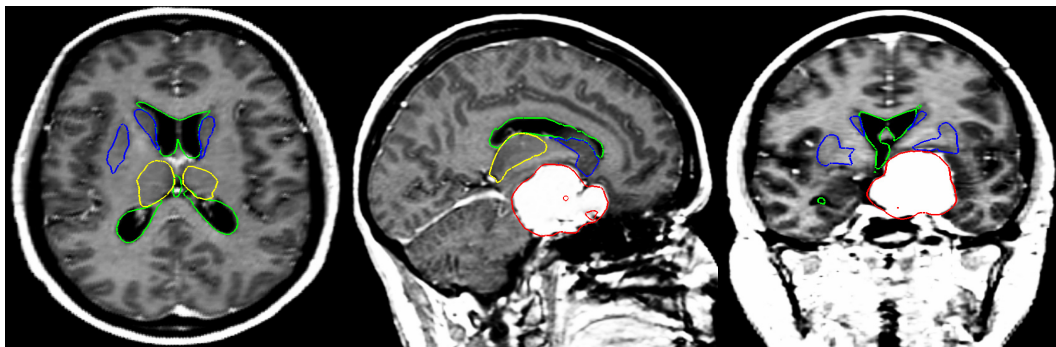


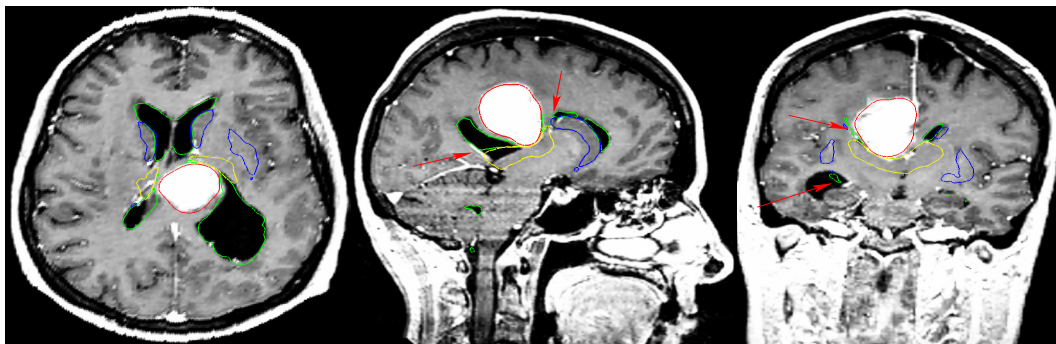
Figure 5.6: Segmented structures: the ventricles (MLG in blue and SAD in magenta), the thalamus (MLG in cyan and SAD in yellow), and the central nuclei (MLG in green and SAD in red).



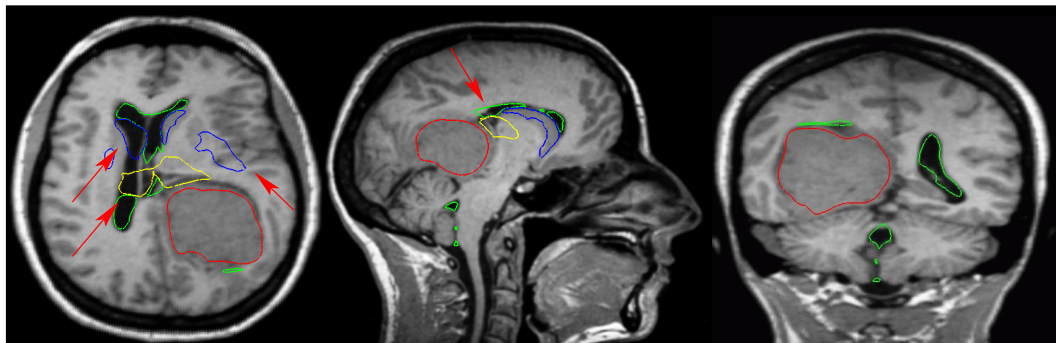
(a) Patient 1



(b) Patient 2



(c) Patient 3



(d) Patient 4

Figure 5.7: Segmentation results after applying the *MLG* algorithm. Displayed structures are: tumor (red), ventricles (green), thalamus (yellow), and central nuclei (blue).

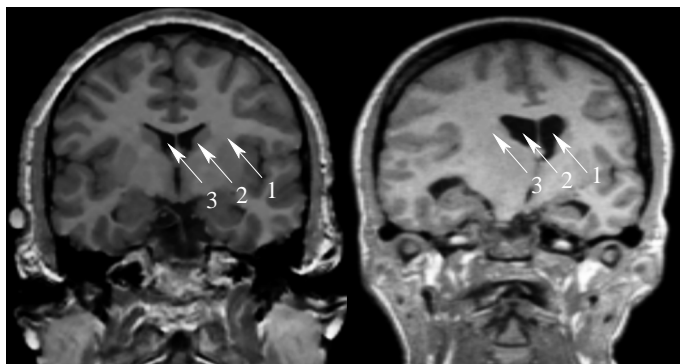


Figure 5.8: Wrong initialization of MLG method for patient 4: the enumerated arrows represent the same spatial position. Note that anatomical structures do not correctly overlap.

5.5.3 Variation of the MLG method

As it has been seen in the previous section, in some cases, MLG fails when there are large morphological difference between the patient and the atlas in addition to the lesion itself. A modification of the MLG method is proposed in this section in order to obtain a seeded atlas as similar as possible to the patient.

First, the MLG algorithm is applied as explained in Section 5.4 but in a very rigid way: $\sigma = 2mm$ far away from the lesion, $\sigma = 0.5mm$ near the lesion, and no filtering is applied inside. Moreover, the MLG uses a tumor mask that has been eroded (typically 3 mm) in order not to impose so much deformation next to the lesion area at a first time. So, a *rigid* match between the main structures is made and a new *atlas* with a lesion template is obtained. Now, a non-rigid registration between two brains with an overlap between the corresponding structures (including the tumor) can be applied. Therefore the demons algorithm is valid for this objective. The algorithm is used in an elastic way ($\sigma = 0.7$) because these brains have larger deformability than in the case of normal anatomy. Figure 5.9 summarizes the performance of the new proposed algorithm. This *variation* of the MLG algorithm has been applied for patient 3 and patient 4. Segmentation results are shown in Figure 5.10. Much better results are obtained for patient 3 (compare the arrows in Figure 5.7(c) and Figure 5.10(a)) where the ventricles inflammation have been correctly match. However, no improvement has been obtained for patient 4. Neither the ventricles nor the central nuclei of the atlas have overlapped with the patient structures. Notice that patient 4 is a very complex case since even the mid sagittal plane, that is usually much more rigid than the brain tissues, has been largely deformed.

In summary, we propose to apply the MLG *one-step* when the lesion is the main anatomical difference between the patient and the atlas, and, the MLG *two-steps* when large deformations exist in the patient brain moreover the lesion.

5.6 Validation

One of the most important questions to solve when a new algorithm is proposed is how to validate it. Actually, this is one of the key problems of the non-rigid registration techniques in medical images: a gold standard for validation. This problem is even more difficult in this case since two different deformations have to be validated: inter-patient (or atlas-patient) registration and healthy

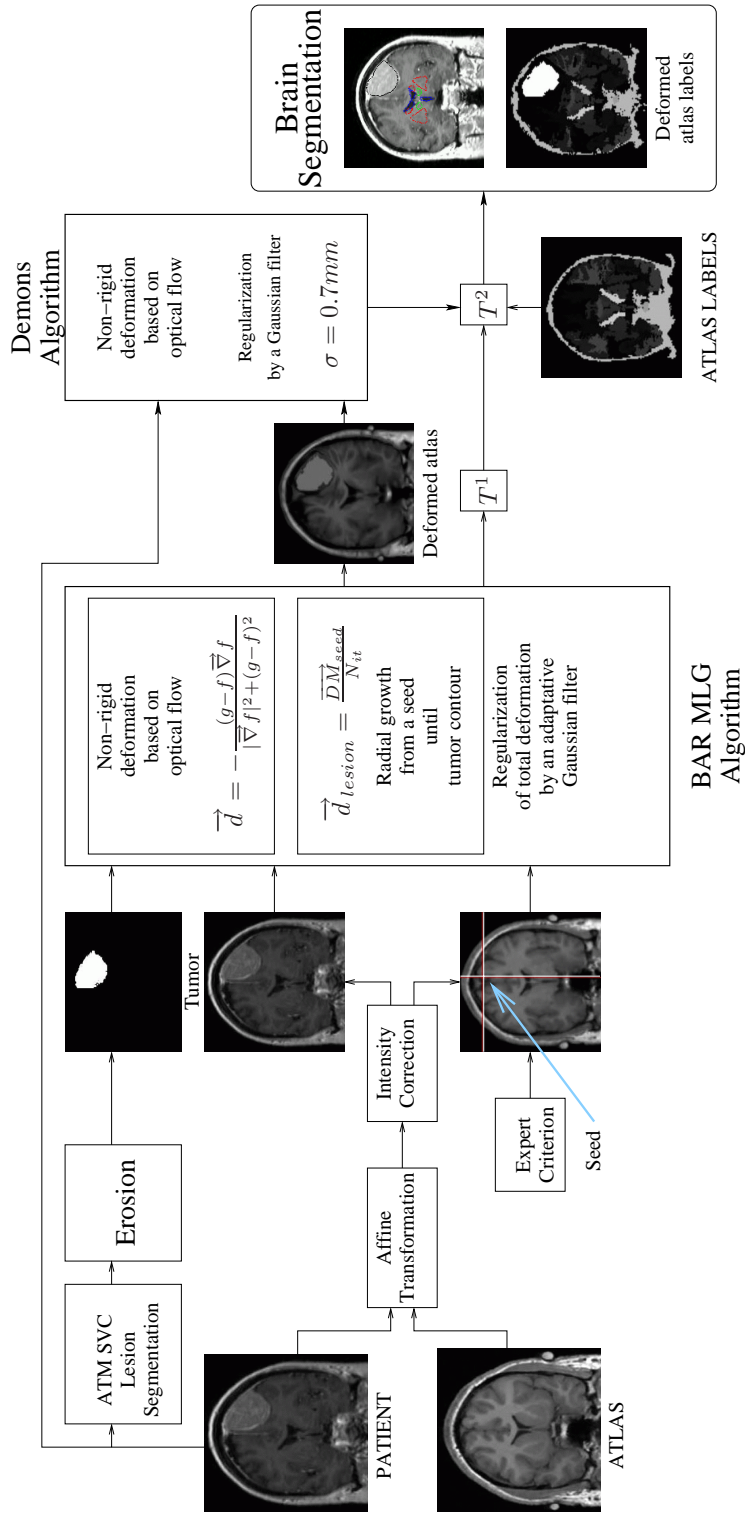
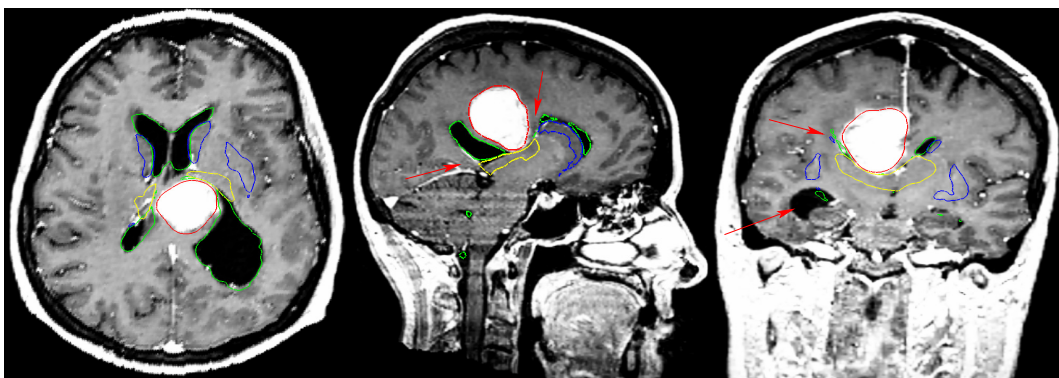
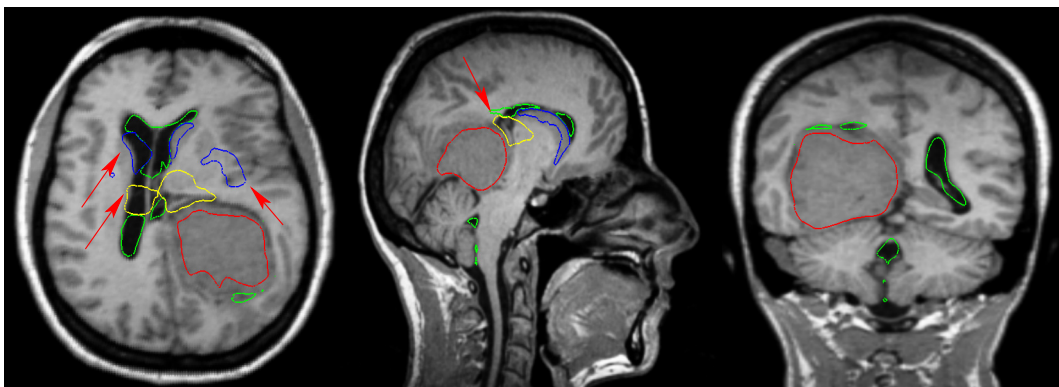


Figure 5.9: Block diagram of the variation of the MLG algorithm.



(a) Patient 3



(b) Patient 4

Figure 5.10: Segmentation results after applying the *variation of the MLG* algorithm. Displayed structures are: tumor (red), ventricles (green), thalamus (yellow), and central nuclei (blue).

to pathological registration. The first case of validation has been studied extensively [63, 87, 104], and it is still a very active area of research. However, the demons algorithm validation will not be treated here [58, 87].

The goal of this section is twofold: validate not only the lesion growth but also the seed position. We first propose a validation method that will then be used to assess the MLG variability depending on the seed position.

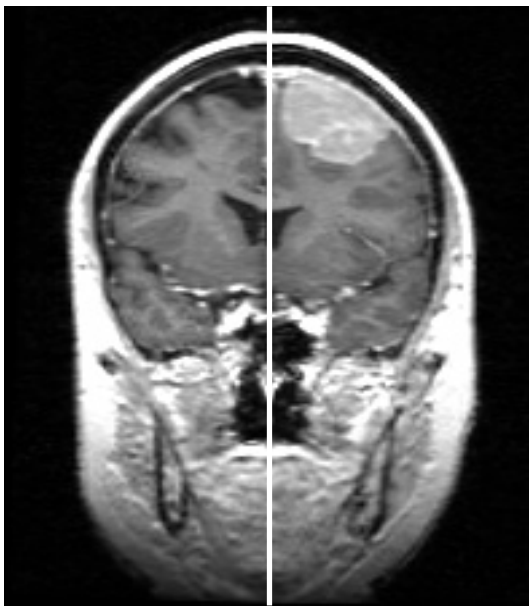
5.6.1 Validation of the lesion growth

The validation method should demonstrate that the one-step MLG algorithm warps the brain in the same way as the growth of the lesion. To show it, the MLG algorithm should be applied to the patient before the lesion growth but this information is usually not available. Thus, another question arises: how to have a good estimation of how the patient brain was before the appearance of the tumor. We know that the brain has, more or less, symmetrical structures. Therefore, the *damaged* hemisphere was almost like the *healthy* one before the tumor grew. This idea is the basis of the validation. The proposed method is summarized as follows:

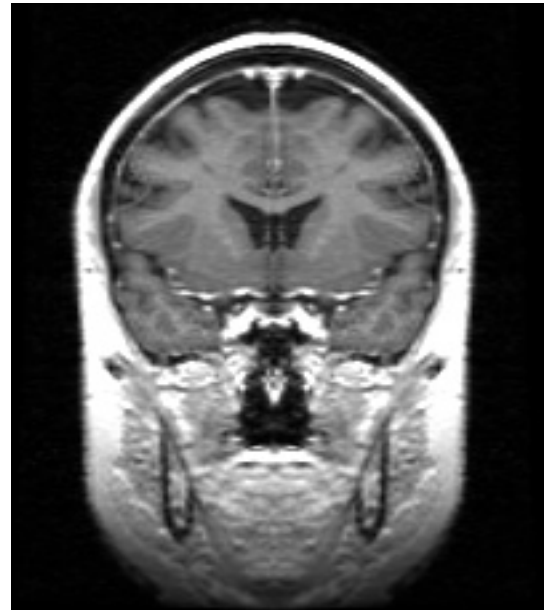
1. The brain *symmetry plane* that separates the right and the left hemispheres, called *Mid Sagittal Plane (MSP)*, is found.
2. A *synthetic healthy* patient is created by mirroring the *healthy* hemisphere of the brain.
3. The MLG algorithm is applied between the patient and the synthetic healthy patient as explained in Section 5.4.3.
4. The differences between the deformed synthetic healthy patient and the patient are evaluated.

To find the MSP, the MSE between both sides of the axial plane is minimized. The tumor and its mirror are not taken into account because they do not have a symmetrical structure. The minimization algorithm used is the *Powell* algorithm as described in [90]. In Figure 5.11(a), the MSP found for the Patient 2 is shown.

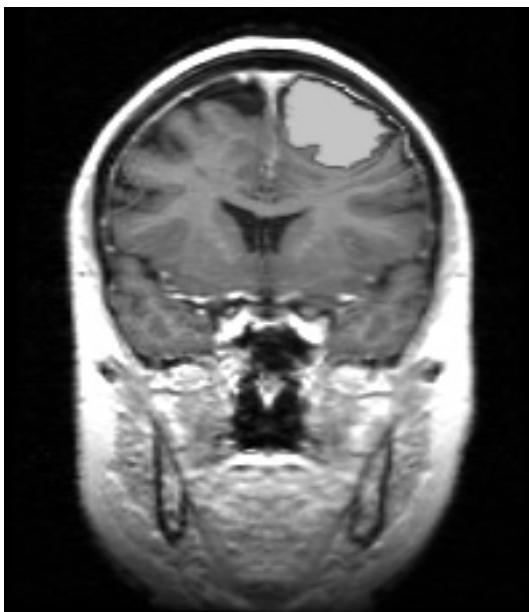
Once the symmetry plane is found, the *healthy* and the *damaged* hemispheres have been determined. To generate a new synthetic patient-atlas, a simple mirroring of the *healthy* side is done. Note that, with this new atlas (see Figure 5.11(b)), the most similar brain *a posteriori* to the *healthy* brain of the patient is obtained. Only patients who do not present large deformations on the MSP and those who have a tumor only in one hemisphere of the brain can be used in this validation approach because of the mirroring step. Unfortunately, there is only one patient in our data-base fulfilling these conditions (see patient 2 on Figure 5.4(b)). The result of the validation for this patient is presented in Figure 5.11(c) and (d). It shows the warped synthetic atlas and the resulting segmentation of patient respectively. To obtain the final segmentation, a non-rigid match between the digitized atlas and the *synthetic atlas* has been previously done in order to obtain a previous segmentation of the *synthetic atlas* (see Figure 5.12). Then, the transformation found by the MLG algorithm can be applied to the *synthetic atlas* image and a final segmentation of the patient is obtained. So, two transformations have been applied to the original atlas image. That means that, if there was some imprecision on the first non-rigid registration algorithm, the MLG method will propagate a wrong initial segmentation. But, according to the expert criteria, the final segmentation obtained for this case is correct. Of course, to obtain a more accurate assessment, the proposed validation method should be applied to many more cases.



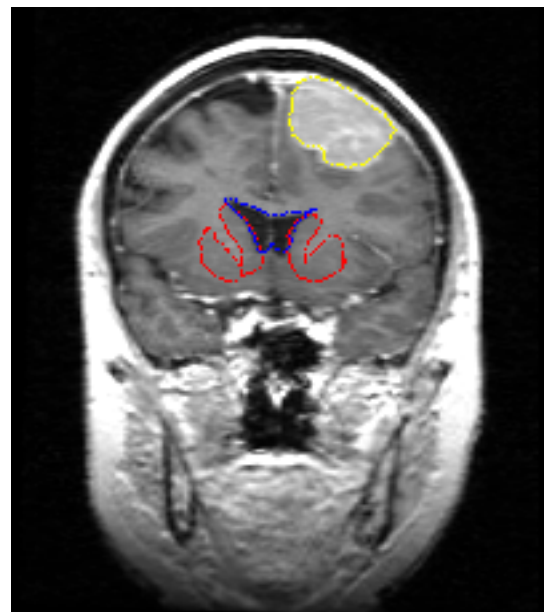
(a) Patient



(b) Synthetic atlas-patient



(c) Deformed atlas-patient



(d) Segmented patient

Figure 5.11: Validation method results. Displayed structures are the central nuclei (red), thalamus (green), ventricles (blue) and tumor (yellow).

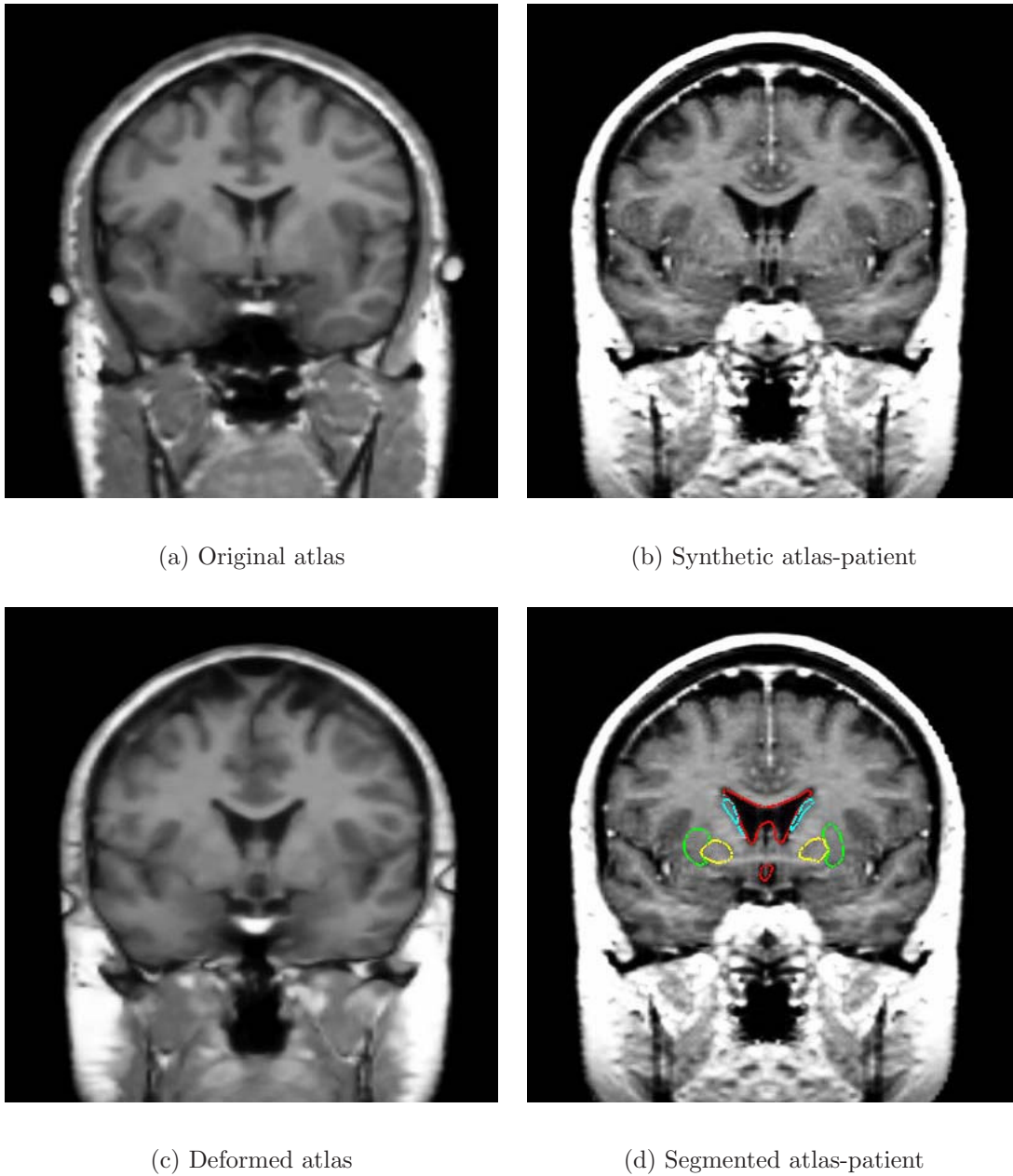


Figure 5.12: First non-rigid registration to obtain a preliminary segmentation of the *atlas-patient*.

5.6.2 Validation of the seed position

Seed position is a critical point of the MLG since it simulates where the tumor has begun to grow. A variability study of the MLG depending on seed position using the validation method proposed in the previous section is presented in what follows.

The *synthetic atlas-patient* and the original patient are considered as the deformable model and the target image respectively. Then, the MLG method is applied as described in section 5.4.3. This has been done for six different initial positions of the seed voxel that an expert has chosen as possible origins of the tumor (see Figure 5.13). The resulting deformation after applying the MLG algorithm for each seed is shown in Figure 5.14. The original patient and the resulting deformed *synthetic atlas-patient* are displayed. The seed position is represented by a little sphere. For this patient, the most *logical* position, under expert criteria, is the one placed at coordinates (205, 136, 47) (colored in magenta in Figure 5.13 and Figure 5.14(a)). It is actually placed in the *middle* of the cerebral convexity since, in principle, there is no more probable growing direction than others inside the brain.

First, the deformation has been visually validated by the assessment of an expert. The areas where the MLG method has performed correctly are marked using green arrows and the areas where MLG has not performed correctly using red arrows. The most *logical* seed position has correctly displaced gyrus but it has also performed too much deformation at the mid sagittal plane. That is because large elasticity near the lesion has been supposed while, in fact, in this case, the MSP is near the lesion and it is a largely rigid structure. The rest of the seed positions, as desired, have not deformed too much the MSP (Figure 5.14(d) and (e)) but they have not correctly displaced the gyrus.

Second, the deformation error has been quantified calculating the MSE per voxel between the original patient and the deformed *synthetic atlas-patient* (Figure 5.14). A small MSE represents, for this particular case, a good deformation since the two images are supposed to be the same patient before and after the lesion growth and both images have the same intensity distribution. The lowest error is 34.08 for (205, 136, 47), the most *logical* initial seed position, and the largest error corresponds to (206, 139, 53). However, these values are not significantly different to conclude if one position performs much better deformation than another. In our opinion, MSE measure could hardly be used to validate the deformation in the case of inter-patient matching because the images do not have a perfect intensity correspondence. Furthermore, even if we know the most probable initial position of the tumor in the *synthetic atlas-patient*, it is not sure that it will be exactly the same position in the SPL atlas since both, *synthetic atlas-patient* and SPL atlas, are morphological and morphometrically different.

Third, validation of the segmentation for some deep structures of the brain such as the ventricles, the thalamus, the central nuclei and the tumor is performed. In Figure 5.15 a global view of all the segmented structures superimposed can be seen. Each color corresponds to the result of each seed position. Actually, not too much variability has been detected either in the position or in the morphology of the studied structures as expected (see Figure 5.16(b)). However, there are some morphological differences when looking at the ventricles region (Figure 5.16(a)). This could be explained as follows. For this patient, almost all structures under study are quite far from the tumor, so they are not really influenced by the initial seed position. Only the ventricles seem to be more influenced by the seed since they are the most deformed structure due to the lesion growth.

Finally, volume statistics of the segmented structures have been calculated (see Table 5.1). The ventricles is the brain structure having largest volume variability, 0.35%, due to the different seed positions and, the tumor follows it with 0.18%. These measures quantify the qualitative segmentation results presented above (see Figure 5.16(a)).

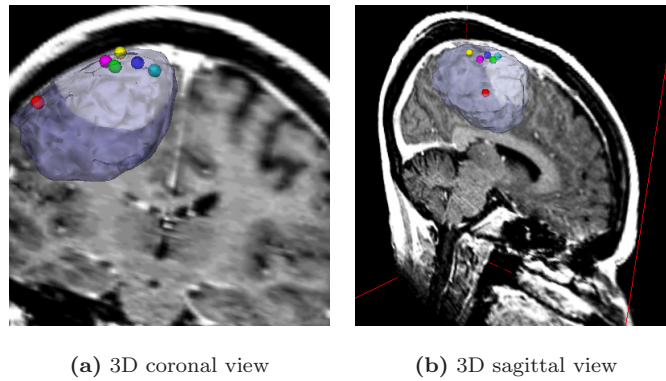


Figure 5.13: Different locations of the initial seed. Magenta (205,136,47), red (192,119,38), green (205,131,50), cyan (205,137,57), yellow (207,145,48) and blue (206,139,53).

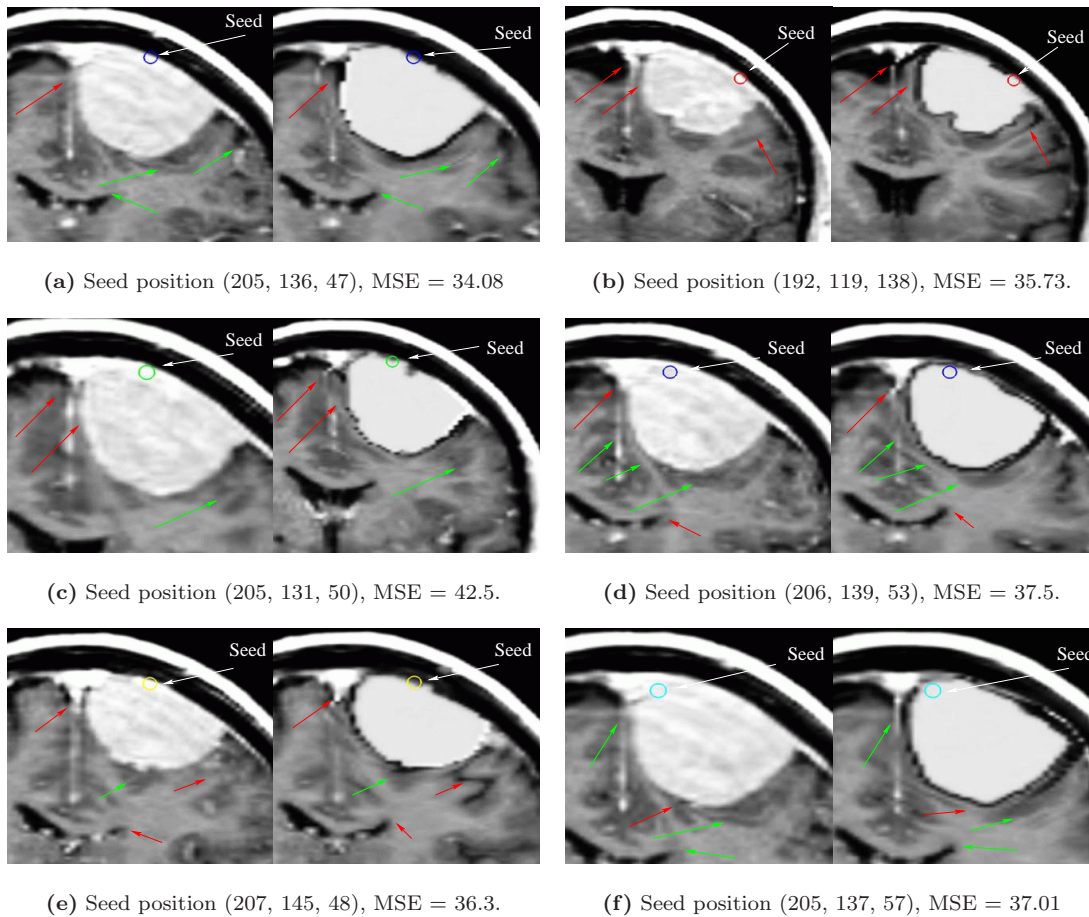


Figure 5.14: Preliminary study of the deformation variability depending on the seed position. MSE is the mean squared error per voxel between the original patient and the deformed synthetic patient-atlas. Green arrows denote the regions where MLG has deformed correctly. Red arrows denote the errors.

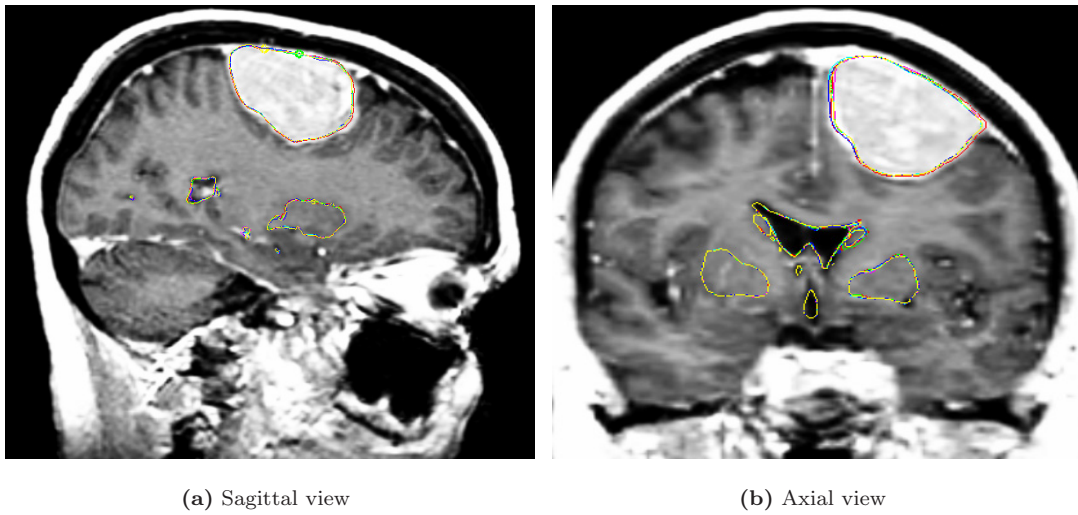


Figure 5.15: Segmentation results for each seed position. Visualized structures are: central nuclei, ventricles, thalamus and tumor.

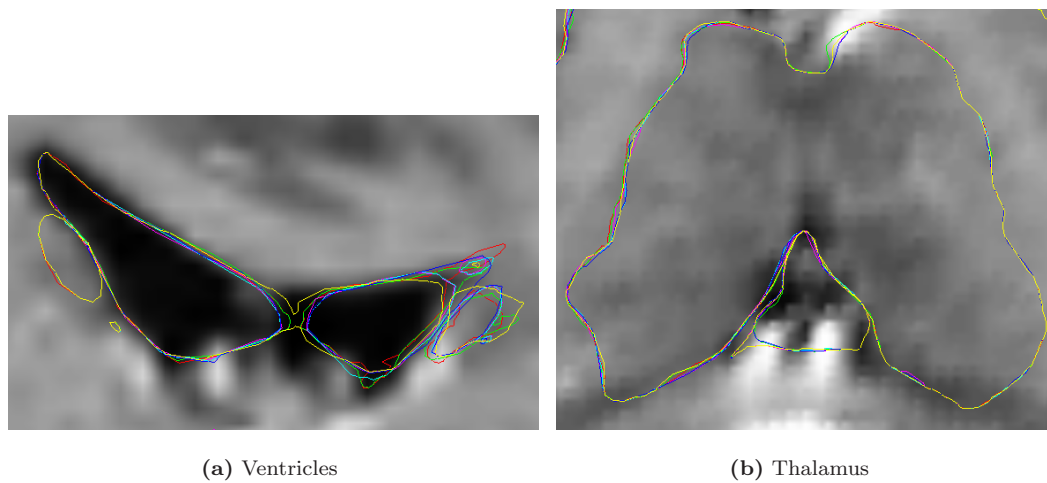


Figure 5.16: Segmentation results for each seed position: zoom at ventricles and thalamus.

Seed position	Tumor	Ventricles	Central Nuclei	Thalamus	MSE
(192,119,38)	33168.60	19133.40	12851.52	10115.16	35.73
(205,131,50)	33302.28	19054.20	12801.36	10091.40	42.50
(205,136,47)	33040.92	19256.16	12726.12	10072.92	34.08
(205,137,57)	33365.64	19171.68	12728.76	10087.44	37.01
(206,139,53)	33249.48	19170.36	12732.72	10080.84	37.50
(207,145,48)	33333.96	19110.96	12773.64	10071.60	36.30
Mean	33291.72	19149.24	12769.20	10086.12	37.19
Std. Dev.	62.92 (0.18%)	68.01 (0.35%)	50.30 (0.03%)	16.02 (0.15%)	2.86 (7.69%)

Table 5.1: Volume measure of segmented structures for each seed position. Volume and statistics are in mm^3 . Percentage values are calculated respect to the mean value. MSE between the original patient and the deformed synthetic atlas-patient intensities.

5.7 Discussion

The *a priori* model of tumor growth tries to increase the robustness of the SAD algorithm rendering their method independent to the seed size, independent of the number of iterations inside the tumor area. Moreover, the use of an adaptative filter has done the non-rigid registration much less sensitive to the regularization parameter. Actually, in MLG, deformation is applied only once while the demons algorithm is applied twice in SAD and in the two steps MLG: first, a low elastic deformation is applied to match the structures that are not largely deformed, and then, a more elastic deformation is allowed to match the structures close to the lesion, that are, in principle, highly deformed. In fact, that could be a questionable point since it is not exactly the same to perform twice a non-rigid registration technique (first, rigidly and, then, more elastically) than to perform it only once. It has been proven that successive applications of a non-rigid registration algorithm as the optical flow can result more in a fluid than an elastic registration (see Section 3.4.5).

Of course, the use of such a simple model of tumor growth can be questionable. The exact biological mechanisms and vectors of growth of meningiomas are not known. However, radiological follow-up performed in patients provides information confirming that growth may be considered spatially homogeneous at least into directions where it is not restrained by anatomical structures like bone, cerebral falx or tentorium. Actually a large majority of meningioma have a dural attachment and dura, except the falx and tentorium, is adherent to bone. As bone is rigid, it is reasonable to consider that there is no growth into the bone direction, even if bone may be invaded in rare cases. In conclusion, it is realistic to assume from a biological point of view that growth of meningiomas is radial and starts from the center of their dural attachment surface, defined as the seeding point.

The seed position has to be manually chosen by an expert. That represents a drawback because the presented results clearly show that the brain deformation induced by the lesion growth is correlated with the position of the seeding point (see Section 5.6.2). Actually, this observation is not surprising considering that radial growth is assumed. Furthermore, the best deformation accuracy is not necessarily obtained when seeding point is *logically* placed in the center of the surface of dural attachment (Figure 5.14). As proof, the two first cases, patient 1 and patient 2, show no shift of neither the falx nor the *sella turcica* (bone) despite the presence of the meningioma while the corresponding deformed images by the MLG method have deformed these structures (Figure 5.17). Actually, falx and tentorium, although less rigid than bone, have significantly higher resistances against tumor growth than brain. So, they should be considered almost non-deformable structures



Figure 5.17: Deformation errors for patient 1 and 2. Falx and bone have been too much deformed since there is no special constraints of deformation for such structures while they have in fact much less elasticity than the rest of the brain.

until the tumor reaches a significant size. Consequently, in a future work, the algorithm will be modified in order to prevent too much deformability of these structures.

In the near future, the effect of the contrast product should be also considered. Because of this agent, *meninges* and *sinuses* are represented by different intensities in the patient and atlas images respectively since there is no effect of this product on the atlas. That has caused some problems (for instance, too much deformability of some structures) when applying the non-rigid registration since an optical flow method is used that assumes that the intensity does not change between images. In fact, in the areas where the contrast product is present, the strong gradient intensity in the reference image and also large intensity difference between the reference and the deformable images cause too large deformations. A possible solution would be to create the same contrast effect in the atlas proceeding first by segmenting the *meninges* and *sinuses* and simulating the same intensity as in the patient image. So there would be a perfect intensity correspondence and no misguide in these regions will be performed.

Now, the method should be tested on more data sets containing different kinds and sizes of lesions in order to better validate. Also, it would be important to study a case where the lesion evolution is known to see if the model of lesion growth we have proposed is near or far from the physical reality. Finally, in a more evolved method it would be also very important to consider some anatomical constraints of the structures of interest introducing for example some shape analysis of the most important structures near the lesion as well as to take into account the existence of the edema.

5.8 Conclusions

A new approach for atlas-based segmentation in the presence of large space-occupying tumors which makes use of a simple model of tumor growth has been proposed. This new method is compared to the most similar methods found in the bibliography. Results show that limitations of other methods have been overcome thanks to the use of an *a priori* model, and that a good match is obtained in pathological brains, even when some structures have been drastically altered by the presence of a tumor. Also a new validation method to analyze not only the lesion growth but also the most probable origin of the tumor has been proposed. Finally, the weak points of the proposed method have been deeply analyzed and some solutions to overcome these limitations have been presented.

Part III

Classification

Segmentation of brain tissues

6

*Why is it people who want the truth
never believe it when they hear it?*
Anshel, "Yentl"(1983).

6.1 Introduction

In this chapter the brain tissue segmentation process is presented through comparative study of some of the most commonly used approaches. It is assumed that only T1-weighted MR image modality is available. No enhancement of the image quality is considered either before or during the classification process. This way robustness and accuracy of the methods is tested in front of the image artifacts. The methods presented here were selected to represent the whole range of prior information that can be used in the classification, i.e. intensity, spatial and anatomical priors.

6.2 Problem definition

Accurate and robust brain tissue segmentation from MR images is a key issue in many applications of medical image analysis [25] and, particularly, in the study of many brain disorders [50, 69]. Manual tracing of the three brain tissue types, white matter (WM), gray matter (GM) and cerebrospinal fluid (CSF), in MR images by an expert is far too time consuming as the data involved in most studies is large. On the other hand, automated and reliable tissue classification is a demanding task as the intensity representation of the data normally does not allow a clear delimitation of the different tissue types present in a natural MRI. This is due to the partial volume (PV) effect (presence of more than one brain tissue type in a voxel), image noise and intensity non-uniformities caused by the inhomogeneities in the magnetic field of the MR scanner.

Two main groups can be distinguished in statistical classification: *supervised* and *non-supervised* methods. Supervised classification techniques, also called semi-automatic methods, explicitly need user interaction while non-supervised classification is completely automatic. Actually, a large number of approaches have been proposed to deal with the MR brain image classification problem but a

complete review of all these classification methods is beyond the purpose of this chapter. However, let us briefly present a state of the art of the automatic segmentation methods.

Statistical parametric approaches are widely used for brain MR image segmentation. These approaches usually solve the estimation problem of assigning a class label to a voxel with a suitable assumption about the intensity distribution but the classification can be made also by the estimation of the relative amounts of the various tissue types within a voxel rather than assigning each voxel to one single tissue type [71, 85]. Actually, parametric classification methods try to solve a twofold problem: on one hand, the *classification* which is an easy task if the tissue type model is good while, on the other hand, the *parameter estimation* of the tissue class which is an easy task if all the voxels within this class are known. *Finite Gaussian Mixture (FGM)* models assume a Gaussian distribution for the intensities of the main brain tissues [101]: GM, WM, and CSF. Other algorithms [94] add separate classes to take into account the PV voxels and model them also by independent Gaussian densities. In more elaborate methods [97] mixing proportions are taken into account to build a more realistic model for PV voxels which differs from a Gaussian distribution. However, some of the *finite mixture (FM)* models have the limitation of not considering the spatial information. That is the reason why increasing attention has been paid recently to methods that model the mixing proportions of the PV voxels by a Markov Random Field (MRF) [123]. Finally, non-parametric classification techniques can be considered when no well justified parametric model is known [18], as for instance the intra-class statistics.

As in the case of registration and atlas-based segmentation, validation of brain tissue classification is a complex issue in medical image processing. Visual inspection and comparison with manual segmentation are labor intensive and almost not reliable since the amount of data to deal with is usually large. Tissue classification methods can also be assessed by using synthetic data even if these kind of images can hardly capture the complexity and the artifacts present in a MRI. There is however the possibility to validate brain tissue segmentation methods on a brain *phantom* [27]. This phantom is very well-suited for this purpose since a ground-truth classification is known while different types of T1w MR modalities and image artifacts can be reproduced.

The goal of this chapter is to assess the robustness and accuracy of some of the most used unsupervised classification methods. In this comparative analysis and validation only T1w MR brain image are considered. The goal is to be able to specify the most suitable tissue classification technique depending on the different conditions that could be encountered in T1w MR brain image. The work presented here is the continuation of [75].

The chapter is organized as follows. First, in Section 6.3, the general theory used in this work for both intensity and spatial prior models is presented. Section 6.4 and Section 6.5 briefly introduce the basic theoretical concepts of the classification criteria and parameter estimation. Then, in Section 6.6 and Section 6.7, the methods analyzed in this comparative study are summarized. Next, Section 6.8 and Section 6.9, the classification results and their validation are discussed. Finally, important conclusions resulting from the presented work are given.

6.3 Image model

6.3.1 Intensity distribution model

In this thesis, the theory behind the intensities in T1w MR brain images is similar to the one introduced by Noe et al. [85]. Its main concepts are recalled in what follows.

Let us index N data points to be classified with $i \in \mathcal{S} = \{1, 2, \dots, N\}$. In the case of 3D images, such as MR images, they index the image's voxels. Let us furthermore denote the data

feature vectors by $y_i \in \mathbb{R}$. In the case of classification of single MR images, y_i represent the i th-voxel intensity. Y is the random variable associated to the data features y_i , with the set of possible outcomes, \mathcal{D} . Any simultaneous configuration of the random variables, Y_i , is denoted by $\mathbf{y} = \{y_1, y_2, \dots, y_N\} \in \mathcal{D}^N \subset \mathbb{R}^N$.

The classification process aims to classify the data \mathcal{S} into one of (hidden) underlying classes present in the image labelled by one of the symbols $\mathcal{L} = \{CSF, GM, WM, CG, CW, GW, CGW\}^*$. The family of random variables X represents these classes, $\mathbf{x} = \{x_1, x_2, \dots, x_N\} \in \mathcal{L}^N$ denotes a possible configuration of X , and \mathcal{X} is the space of all possible configurations.

Now, let us suppose that all the random variables, Y_i , are identically and independently distributed. Then, the probability density function of the intensity voxel can be defined by:

$$P(y_i) = \sum_{\forall x_i \in \mathcal{L}} P(x_i)P(y_i|x_i), \quad (6.1)$$

where $i \in \mathcal{S}$, $P(x_i)$ is the probability of the tissue class x_i and $P(y_i|x_i)$ is the probability density function of y_i given the tissue class x_i .

The simplest intensity model that could be used considers only the three pure tissues of the brain, that is, $\mathcal{L}_p = \{CSF, GM, WM\}$ and the probability density function for the observing intensity y_i given the pure tissue class x_i is given by the Gaussian function:

$$P(y_i|x_i) = \frac{1}{\sigma_{x_i}\sqrt{2\pi}} \text{Exp} \left[\frac{-(y_i - \mu_{x_i})^2}{2\sigma_{x_i}^2} \right], x_i \in \mathcal{L}_p, \quad (6.2)$$

where the model parameters $\theta_{x_i} = \{\mu_{x_i}, \sigma_{x_i}\}$ are respectively the mean and variance of the Gaussian function. This is a good approximation since the noise present in a MRI follows a Rician distribution that, at high signal-to-noise ratio (SNR), can be modelled by a Gaussian distribution[†].

In this thesis, a more evolved intensity model that adds to the main brain tissues their most important mixtures is used, i.e., $\mathcal{L}_{pm} = \{CSF, GM, WM, CG, GM\}^\ddagger$. A voxel containing only a pure tissue is still modelled by a Gaussian distribution while a mixture voxel is modelled as suggested in [97] by

$$P(y_i|x_i, \alpha) = \frac{1}{\sigma_{x_i}(\alpha)\sqrt{2\pi}} \text{Exp} \left[\frac{-(y_i - \mu_{x_i}(\alpha))^2}{2\sigma_{x_i}^2(\alpha)} \right], x_i \in \mathcal{L}_{pm} \setminus \mathcal{L}_p, \quad (6.3)$$

where the two pure tissues composing the mixture voxel are denoted by $l_1, l_2 \in \mathcal{L}_p$, and α is a uniformly distributed random variable that represents the fraction of l_1 present in the mixture voxel (then, tissue l_2 is present in a fraction of $1 - \alpha$). The mean and variance of the mixture are determined by the model parameters of the pure tissues:

$$\mu_{x_i}(\alpha) = \alpha\mu_{l_1} + (1 - \alpha)\mu_{l_2} \quad (6.4)$$

$$\sigma_{x_i}^2(\alpha) = \alpha^2\sigma_{l_1}^2 + (1 - \alpha)^2\sigma_{l_2}^2. \quad (6.5)$$

Finally, the probability density function of a partial volume tissue is computed by

$$P(y_i|x_i) = \int_0^1 P(y_i|x_i, \alpha)d\alpha. \quad (6.6)$$

The integral in Eq. (6.6) is numerically computed and its form can largely vary depending on the parameters $\theta_l = \{\mu_l, \sigma_l\}$. Some particular cases of Eq. 6.6 are plotted in Fig. 6.1. It can be

*CG, CW, GW and CGW are the mixtures of CSF+GM, CSF+WM, GM+WM, and CSF+GM+WM, respectively.

[†]Note that for low SNR, i.e. the background image, the Rician noise can be modelled by a Rayleigh distribution.

[‡]CW and CGW are not considered because these mixtures are uncommon, and thus $P(CW)$ and $P(CGW)$ are not relevant in explaining $P(\mathbf{y})$.

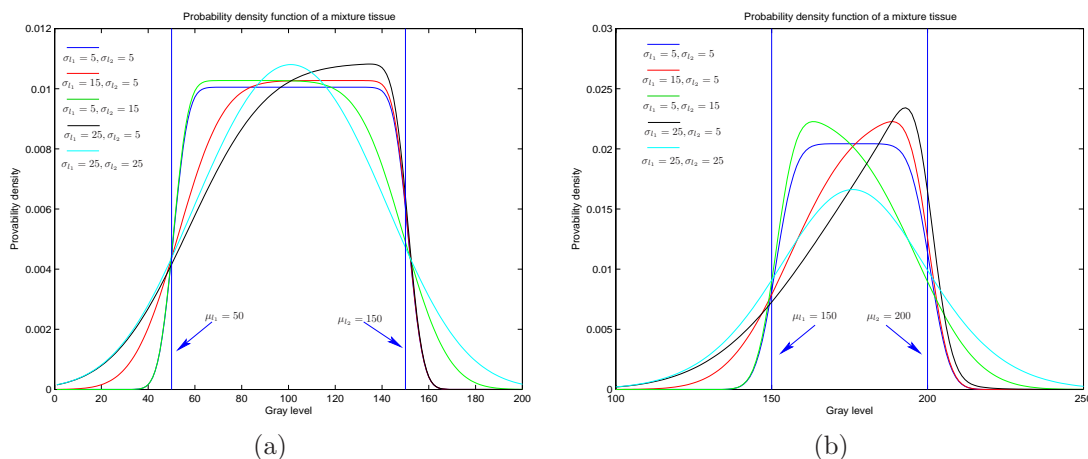


Figure 6.1: Plot of Equation 6.6 varying σ_{l_1} and σ_{l_2} with (a) $\mu_{l_1} = 50$ and $\mu_{l_2} = 150$ and (b) $\mu_{l_1} = 150$ and $\mu_{l_2} = 200$.

observed that the probability density function of the mixture between two pure tissues, l_1 and l_2 , varies depending on how much different σ_{l_1} and σ_{l_2} are and also depending on the difference between μ_{l_1} and μ_{l_2} .

Note that this more evolved intensity model that includes some mixture tissues does not actually add any additional parameter to the 3-class model. Only the *weight* of each new tissue type ($P(CG)$ and $P(GW)$) should be also considered.

6.3.2 Spatial distribution model

Markov Random Fields

The spatial information can be encoded in terms of correlated pixels using the theory of Markov Random Fields (MRF) to characterize relationships between spatial features [123]. The MRF theory, as in the case of Markov chains, considers that the dependence of one voxel state on the whole image information can be reduced to the information contained in a local neighborhood.

Then, all the sites in the image S are related with a *neighborhood system* $N = \{\mathcal{N}_i, i \in S\}$, where \mathcal{N}_i is the set of sites neighboring i , with $i \notin \mathcal{N}_i$, and $i \in \mathcal{N}_j \Leftrightarrow j \in \mathcal{N}_i$. A random field \mathbf{x} is said to be a MRF on S with respect to a neighborhood system N if and only if

$$P(\mathbf{x}) > 0, \mathbf{x} \in \mathcal{X}, \text{ and}, \quad (6.7)$$

$$P(x_i | x_{S-\{i\}}) = P(x_i | x_{\mathcal{N}_i}), \quad (6.8)$$

where x_i denotes the current estimate at location i , and $x_{S-\{i\}}$ denotes all the locations at S except i . According to the Hammersley-Clifford theorem, an MRF can be equivalently characterized by a Gibbs distribution,

$$P(\mathbf{x}) = Z^{-1} e^{-U(\mathbf{x}, \beta)}, \quad (6.9)$$

that has several *free* parameters to be determined: the *normalization factor* Z , the *spatial* parameter β , and the *energy function* $U(\mathbf{x})$. Let us briefly discuss in what follows how these parameters can be determined in the particular framework of image segmentation.

The energy function $U(\mathbf{x})$

First, the choice of the energy function is arbitrary and there are several definitions of $U(\mathbf{x})$ in the framework of image segmentation. A complete summary of them is done in [89] where a general expression for the energy function is denoted by

$$U(\mathbf{x}|\beta) = \sum_{\forall i \in \mathcal{S}} \left(V_i(x_i) + \frac{\beta}{2} \sum_{j \in \mathcal{N}_i} V_{ij}(x_i, x_j) \right). \quad (6.10)$$

This is known as Potts model with an *external field*, $V_i(x_i)$, that weighs the relative importance of the different classes present in the image. Eq. (6.10) can be for instance modelled by an Ising model at 2 states [71]. However, the use of an external field includes additional parameter estimation, thus this model is less used in image segmentation [22]. Instead, a simplified Potts model with no external energy, $V_i(x_i) = 0$, is used. Then, only the local spatial transitions are taken into account and all the classes in the label image are considered equally probable. The key point is how to model $V_{ij}(x_i, x_j)$ to guide the final segmentation, $\hat{\mathbf{x}}$, as near as possible to the real image \mathbf{x}^* . They can be defined for instance as in [123]:

$$V_{ij}(x_i, x_j) = \delta(x_i, x_j) = \begin{cases} -1 & \text{if } x_i = x_j \\ 0 & \text{otherwise.} \end{cases} \quad (6.11)$$

Intuitively, the equation above encourages one voxel to be classified as the tissue that the most of its neighbors belongs to. However, this model does not take into account the distance between neighbors but the class they belong to. It is not moreover well suited to model partial volume since it tends to eliminate it. A more evolved function is used in this work as proposed in [84, 103]:

$$V_{ij}(x_i, x_j) = \frac{\delta(x_i, x_j)}{d(i, j)}, \quad (6.12)$$

where,

$$\delta(x_i, x_j) = \begin{cases} -2 & \text{if } x_i = x_j \\ -1 & \text{if they share a tissue type} \\ +1 & \text{otherwise,} \end{cases} \quad (6.13)$$

and $d(i, j)$ represents the distance between voxels i and j . With this energy function configurations that are not likely to occur (e.g. CSF inside WM) are penalized while smooth transitions, more likely to occur in a brain (e.g. WM next to the partial volume GW), are encouraged.

The spatial parameter β

The *spatial* value of β controls the influence of the spatial prior over the intensity. Note that its influence on the final segmentation* is important. $\beta = 0$ corresponds to a uniform distribution over the \mathcal{L} possible states, that is, the maximization is done only on the conditional distribution of the observed data $P(y|x)$ (Eq. (B.1)). On the contrary, if the spatial information is dominant over the intensity information, that is $\beta \rightarrow \infty$, MAP tends to classify all voxels to a single class [89].

The value of β can be estimated by ML estimation. However, many problems arise due to the complexity of MRF models and alternative approximations have to be done (for instance, Monte-Carlo Simulations or by maximum pseudo-likelihood [10]). The β parameter can be also determined *arbitrarily* as proposed in [11] by gradually increasing its value over the algorithm iterations. Here,

*Note that classification is done here by MAP estimation and this requires the application of the ICM algorithm. We refer to Appendix B for more details.

the value of β has been fixed empirically by choosing the one that results in a better classification on a training set. In this work, β is fixed to 1.2.

The normalization factor Z

Fianlly, the normalization factor of Gibbs distribution is theoretically well-defined as

$$Z(U) = \sum_{\mathbf{x}} e^{-U(\mathbf{x},\beta)}, \quad (6.14)$$

but it requires a high computational cost or it is even intractable since the sum among all the possible configurations of \mathbf{x} is usually not known [43]. Note also its dependence on the definition of the energy function U . Instead, the conditional probabilities $P(x|x_{\mathcal{N}_i})$ can be easily normalized by forcing:

$$\sum_{\forall x_i \in \mathcal{L}_{pm}} P(x_i|x_{\mathcal{N}_i}) = 1. \quad (6.15)$$

Hidden Markov Random Fields

The theory of a *Hidden Markov Random Field (HMRF)* model is derived from *Hidden Markov Models (HMM)*, which are defined as stochastic processes generated by a Markov chain whose state sequence cannot be observed directly (X), only through a sequence of observations (Y). Here we consider the special case since, instead of a Markov chain, a MRF will be used as the underlying stochastic process. The concept of a *hidden* MRF is different from that of an MRF, in the sense that HMRF is defined with respect to a pair of random variable families (X, Y) while MRF is only defined with respect to X .

In summary, a HMRF model is characterized by the following:

1. **Hidden Random Field (MRF):** $X = \{X_i, i \in S\}$ is an underlying MRF assuming values in a finite state space \mathcal{L} with probability distribution as defined in Eq. 6.9. The state of X is unobservable.
2. **Observable Random Field:** $Y = \{Y_i, i \in S\}$ is a random field with a finite state space \mathcal{D} . Given any particular configuration $\mathbf{x} \in \mathcal{L}^N$, every Y_i follows a known conditional probability distribution $P(y_i|x_i)$ of the same functional form $f(y_i; \theta_{x_i})$, where θ_{x_i} are the involved parameters. This distribution is called the *emission probability function* and Y is also referred to as the *emitted random field*.
3. **Conditional Independence.** For any $\mathbf{x} \in \mathcal{L}^N$, the random variables Y_i are supposed to be independent, which means that

$$P(\mathbf{y}|\mathbf{x}) = \prod_{i \in S} P(y_i|x_i). \quad (6.16)$$

Based on this, the joint probability of (X, Y) can be written as

$$P(\mathbf{y}, \mathbf{x}) = P(\mathbf{y}|\mathbf{x})P(\mathbf{x}) = P(\mathbf{x}) \prod_{i \in S} P(y_i|x_i). \quad (6.17)$$

According to the local characteristics of MRF's, the joint probability of any pair of (X_i, Y_i), given X_i 's neighborhood configuration $X_{\mathcal{N}_i}$, is

$$P(y_i, x_i|x_{\mathcal{N}_i}) = P(y_i|x_i)P(x_i|x_{\mathcal{N}_i}). \quad (6.18)$$

So now it is possible to compute the marginal probability distribution of Y_i dependent on the parameter set θ (in this case θ is treated as a random variable) and $X_{\mathcal{N}_i}$,

$$\begin{aligned} P(y_i|x_{\mathcal{N}_i}, \theta) &= \sum_{\forall x_i \in \mathcal{L}} P(y_i, x_i|x_{\mathcal{N}_i}, \theta) \\ &= \sum_{\forall x_i \in \mathcal{L}} P(x_i|x_{\mathcal{N}_i})P(y_i|\theta_x), \end{aligned} \quad (6.19)$$

where $\theta = \{\theta_{x_i}, x_i \in \mathcal{L}\}$. A density function of this form is called *finite mixture (FM) density*. The conditional densities $P(y_i|\theta_{x_i})$ are called *component densities* and, in this case, they encode the intensity information. The *a priori* probabilities $P(x_i|x_{\mathcal{N}_i})$ are the *mixing parameters* and they encode the spatial information.

6.3.3 Anatomical prior model

In the previous section, the mixing parameters of the FM model encode the local spatial information. Other additional information could be used to define the energy function (Eq. (6.10)). For instance, for each tissue class, the probability of a voxel belonging to the class can be obtained after the registration with a probabilistic atlas. Intuitively, in this case, the accuracy of including the prior probability information depends on the errors of the registration process. It is not obvious where the anatomical prior probability should be introduced. It could be for instance included in the classification process as:

$$\hat{\mathbf{x}} = \arg \max_{\mathbf{x} \in \mathcal{X}} \{P(\mathbf{y}|\mathbf{x})P(\mathbf{x})P_A(\mathbf{x})\}, \quad (6.20)$$

where $P_A(x)$ is the anatomical prior probability, according the chosen template. However, as proposed in [85], the anatomical probability influence can be better controlled if it is included in the energy function $U(\mathbf{x})$ by

$$V_{ij}(x_i, x_j) = \frac{\delta(x_i, x_j) - \gamma P_A(x_i)}{d(i, j)}, \quad (6.21)$$

where γ is a constant defined to control the influence of the probability maps over the local spatial information. Note that no external energy is considered.

No prior anatomical information of mixture tissues is usually considered in a class template. Then, anatomical prior of partial volume voxels can be computed from the pure tissue probability composing the mixture as proposed in [85]:

$$P_A(x) = 2\sqrt{P_A(l_1)P_A(l_2)}, \quad x \in \mathcal{L}_{pm}, \text{ and } l_1, l_2 \in \mathcal{L}_p \quad (6.22)$$

That is, PV voxels are assumed to be most likely at locations where the anatomical prior probability of both pure tissues within the voxels are high. Of course, Eq. (6.22) is arbitrary and its validity depends, in this case, on how the reference image used to assess the results is constructed. For instance, the reference image used here considers a most relaxed assumption of having a mixture tissue voxel when both pure tissues probabilities are different from zero. So, pure tissue and new mixture anatomical priors are arbitrarily raised to the power of ε_p and ε_m respectively in order to widen ($\varepsilon < 1$) or shrink ($\varepsilon > 1$) the tissue borders:

$$P'_A(x_i) = P_A^{\varepsilon_p}(x_i), \quad x_i \in \mathcal{L}_p, \quad (6.23)$$

and,

$$P'_A(x_i) = P_A^{\varepsilon_m}(x_i), \quad x_i \in \mathcal{L}_{pm} \setminus \mathcal{L}_p, \quad (6.24)$$

where $P'_A(\mathbf{x})$ denotes the new anatomical probability maps. Finally, all the probability maps are normalized so that they sum up to unity over all tissue classes.

6.4 Classification criteria

6.4.1 Cost function

The notion of *cost function* should be recalled before introducing the Bayesian criterion. The classification process can be seen as an estimation problem: using the available data, the real value of the unknown labelling configuration, denoted by x^* , is estimated by \tilde{x} , where both are a particular realization of random field X . The elementary cost function is defined as [23]:

$$L : \mathcal{L} \times \mathcal{L} \rightarrow \mathcal{R}^+ \quad (6.25)$$

$$L(\tilde{x}, x^*) \begin{cases} = 0 & \Leftrightarrow x^* = \tilde{x} \\ > 0 & \text{otherwise} \end{cases} \quad (6.26)$$

6.4.2 Bayesian criterion

The Bayesian estimation assumes that a cost function L is defined and that *a posteriori* distribution $p(x|y)$ and an observation y of Y are known. Then, the objective is to find an estimator \tilde{x} that minimizes the *Bayes risk*, that is, the expected cost. Mathematically,

$$\bar{L}(\tilde{x}) = E[L(\tilde{x}, X)|Y = y], \quad (6.27)$$

is the expected cost and,

$$\hat{\mathbf{x}} = \arg \min_{x \in \mathcal{L}} \bar{L}(x) \quad (6.28)$$

is the Bayesian estimation of x^* .

The Bayesian strategy is optimal in the sense of the minimization of error probability. In fact, among all the other strategies it is the one for which the average cost is minimal.

Different cost functions can be defined. For instance, if a quadratic cost function is defined as

$$L(\tilde{x}, x^*) = (x^* - \tilde{x})^2, \quad (6.29)$$

the Bayes estimator is called Minimum Mean Squared Error (MMSE) estimator and it corresponds to the conditional mean of the posterior probability density function $p(x|y)$. If the cost function is defined by the absolute error

$$L(\tilde{x}, x^*) = |x^* - \tilde{x}|, \quad (6.30)$$

the Bayesian estimate is called Minimum Mean Absolute Error (MMAE) estimator and it corresponds to the median of $p(x|y)$.

6.4.3 Maximum *a posteriori* (MAP)

If the cost function is uniform,

$$L(\tilde{x}, x^*) = \begin{cases} 0, & \Leftrightarrow x^* = \tilde{x}, \\ 1, & \text{otherwise,} \end{cases} \quad (6.31)$$

the Bayes estimator is reduced to a Maximum *a posteriori* estimator (MAP). That is,

$$\bar{L}(x) = 1 - P(x|y), \quad (6.32)$$

and,

$$\hat{\mathbf{x}} = \arg \min \bar{L}(x) = \arg \max_{\mathbf{x} \in \mathcal{X}} \{P(\mathbf{x}|\mathbf{y})\}. \quad (6.33)$$

Note that MMSE, MMAE and MAP are the same if the posterior probability density function is a Gaussian.

6.5 Parameter estimation of a stochastic process

It has been seen in the previous section that an optimal Bayesian classifier can be applied if the a posteriori probability density function is known. However, a complete knowledge of the probabilistic structure of the problem is rarely available [35] but it can be simplified if some assumptions on the available data can be made:

- The conditional density function, $P(y|x, \theta_x)$, has a known parametric form and it is uniquely defined by the value of the parameter vector θ_x .
- The set of unlabelled samples $\mathcal{Y} = \{y_1, y_2, \dots, y_N\}$ are independent.

In what follows, the concept of Maximum Likelihood estimate and the Expectation Maximization algorithm used to find this estimate are briefly presented.

6.5.1 Maximum Likelihood (ML)

Let $\mathcal{Y} = \{y_1, y_2, \dots, y_N\}$ be a set of unlabelled data with a marginal probability function (Eq. (6.19)) that can be written as

$$P(y, \theta) = \sum_{\forall x \in \mathcal{L}_{pm}} P(y, x, \theta_x) = \sum_{\forall x \in \mathcal{L}_{pm}} P(x)P(y|x, \theta_x), \quad (6.34)$$

The likelihood of the observed sample is by definition the joint conditional probability :

$$L(\theta) = P(\mathcal{Y}|\theta) \quad (6.35)$$

The maximum likelihood estimate $\hat{\theta}$ is that value of θ that maximizes $L(\theta)$:

$$\hat{\theta} = \arg \max_{\theta} L(\theta) \quad (6.36)$$

Maximizing the likelihood is equivalent to making the derivative of the log-likelihood zero. The derivative of the log-likelihood can be expressed in terms of the expectation of the gradient with respect to the probability $P_{\theta}(x|\mathcal{Y}, \theta)$,

$$\frac{d}{d\theta} \log(L(\theta)) = E\left[\frac{d}{d\theta} \log P(\mathcal{Y}, x, \theta)\right] = 0. \quad (6.37)$$

6.5.2 Expectation Maximization (EM)

Expectation Maximization (EM) is an iterative algorithm that estimates the maximum of the log-likelihood by solving:

$$\frac{d}{d\theta} \log(L(\theta)) = 0. \quad (6.38)$$

Another way to solve the above equation is to determine θ that verifies:

$$E_{\theta}\left[\frac{d}{d\theta} \log P(\mathcal{Y}, x, \theta)\right] = 0; \quad (6.39)$$

We can note that the unknown parameter θ appears in the expectation and in the derivative. The basic idea of the EM algorithm is to give a current $\theta(k)$ related to the expectation to make the solution easier (Expectation step). The algorithm is then reduced to give an initial solution $\theta(0)$ and to calculate at the $(k+1)^{th}$ step the current estimation $\theta(k+1)$ solution of :

$$E_{\theta(k)}\left[\frac{d}{d\theta} \log P(\mathcal{Y}, x, \theta)\right] = 0; \quad (6.40)$$

For any k step, this Expectation can be written as:

$$\frac{d}{d\theta} E_{\theta^{(k)}}[\log P(\mathcal{Y}, x, \theta)] = 0; \quad (6.41)$$

So, the ML can be estimated by the maximization of $E_{\theta^{(k)}}[\log P(\mathcal{Y}, x, \theta)]$ instead of solving the annulling of the derivative equation (Maximisation Step). Then, the steps of the algorithm are:

Step 0: Choose the best initialization for $\theta(0)$.

Step ($k+1$): Calculate $\theta(k+1)$ solution of $\max_{\theta} E_{\theta^{(k)}}[\log P(\mathcal{Y}, x, \theta)]$.

6.6 Parametric methods

Here the different parametric classification methods that participate in the comparative study are defined in detail. The methods that model all the brain tissues having a Gaussian distribution are described first. Then, the methods that consider a different intensity distribution for the partial volume voxels are presented. Finally, the method that consider *prior* tissue templates is presented.

6.6.1 Finite Gaussian Mixture Model: FGMM (A)

The finite Gaussian mixture model (FGMM) is one of the most commonly used approaches to solve the classification problem for MR images of the brain in its main tissues [101]. This model considers only the intensity information: each of the brain tissues is modelled by a Gaussian distribution. No spatial information is taken into account. Moreover the random variables X_i are assumed to be independent of each other, which means that,

$$P(x|x_{\mathcal{N}_i}) = P(x) = w_x, \forall x \in \mathcal{L}_{pm}, \text{ and } \forall i \in \mathcal{S}. \quad (6.42)$$

Then, Eq. 6.19 is reduced to

$$P(y|\theta) = \sum_{\forall x \in \mathcal{L}_{pm}} w_x \cdot P(y|x) = \sum_{\forall x \in \mathcal{L}_{pm}} w_x \cdot f_x(y|\theta_x), \quad (6.43)$$

where the component densities $f_x(y|\theta_x)$ are a Gaussian distribution defined by the parameters $\theta_x = (\mu_x, \sigma_x)$. The mixing parameters ω_x can also be included among the unknown parameters. Thus, the mixture density parameter estimation tries to estimate the parameters $\theta = (\omega_x, \theta_x)$ such that,

$$\sum_{x \in \mathcal{L}_{pm}} \omega_x = 1. \quad (6.44)$$

As presented in Section 6.5, a possible approach to solve the parameter estimation problem is to find the maximum of the log-likelihood function. One of the most used methods to solve the maximization problem is the EM algorithm (Section 6.5.2). For the particular case of Gaussian distributions, the resulting equations of the EM algorithm that numerically approximate the parameters of the mixture are:

Initialization Step. Choose the best initialization for $\theta(0)$.

Expectation Step. Calculate the *a posteriori* probabilities $\forall x \in \mathcal{L}_{pm}$:

$$\hat{P}^{(k)}(x|y_i, \hat{\theta}) = \frac{P(y_i|\hat{\theta}_x^{(k-1)})\hat{P}^{(k-1)}(x)}{\sum_{l, \forall l \in \mathcal{L}_{pm}} P(y_i|l, \hat{\theta}_l^{(k-1)})\hat{P}^{(k-1)}(l)} \quad (6.45)$$

Maximization Step:

$$\widehat{\omega}_x^{(k)} = \widehat{P}^{(k)}(x) = \frac{1}{N} \sum_{i \in S} \widehat{P}^{(k)}(x|y_i, \widehat{\theta}) \quad (6.46)$$

$$\widehat{\mu}_x^{(k)} = \frac{\sum_{i \in S} \widehat{P}^{(k)}(x|y_i, \widehat{\theta}) y_i}{\sum_{i \in S} \widehat{P}^{(k)}(x|y_i, \widehat{\theta})} \quad (6.47)$$

$$(\widehat{\sigma}_x^{(k)})^2 = \frac{\sum_{i \in S} \widehat{P}^{(k)}(x|y_i, \widehat{\theta}) (y_i - \widehat{\mu}_i^{(k)})^2}{\sum_{i \in S} \widehat{P}^{(k)}(x|y_i, \widehat{\theta})} \quad (6.48)$$

Note that, in this case, and also for GPV as it will be seen later, the sum among all the image voxels of Eq. (6.45) is equivalent to

$$\sum_{i \in S} \widehat{P}^{(k)}(x|y_i, \widehat{\theta}) \iff \sum_{\forall y_i} h(y_i) \widehat{P}^{(k)}(x|y_i, \widehat{\theta}), \quad (6.49)$$

where h is the image histogram. This decreases significantly the number of computations to be made in Eq. (6.46), Eq. (6.47), and Eq. (6.48). Unfortunately, the methods using the HMRF model cannot use Eq. (6.49). Finally, once the estimation parameter problem is solved, the classification is performed by Bayesian rule (Section 6.4).

6.6.2 Gaussian Hidden Markov Random Field model: GHMRF (B)

The theoretical concepts of this approach are the same as presented in Section 6.3.2. As defined in Eq. 6.19, the intensity image distribution function, dependent on the parameter set θ and on the voxel neighborhood $x_{\mathcal{N}_i}$, is:

$$P(y|\theta) = \sum_{x \in \mathcal{L}_{pm}} P(x|x_{\mathcal{N}_i}) \cdot f_x(y|\theta_x), \quad (6.50)$$

where, $f_x(y|\theta_x)$, is, $\forall x \in \mathcal{L}_{pm}$, a Gaussian distribution (see Eq. (6.2)) defined by $\theta_x = \{\mu_x, \sigma_x\}$, and $P(x|x_{\mathcal{N}_i})$ represents the locally dependent probability of the tissue class x_i . Actually, if this equation is compared with Eq. (6.43), it can be seen that the FGMM model is a special case of an HMRF model.

To solve the parameter estimation problem, an adapted version of the EM algorithm, called the HMRF-EM, is used as suggested in [123]. The update equations for the θ parameters are actually the same update equations as for the FGMM (see Eq. (6.46), Eq. (6.47), and Eq. (6.48)), except that

$$\widehat{P}^{(k)}(x|y_i, \widehat{\theta}) = \frac{P(y_i|\widehat{\theta}_x^{(k-1)}) \cdot \widehat{P}^{(k-1)}(x|x_{\mathcal{N}_i})}{\sum_{l, \forall l \in \mathcal{L}_{pm}} P(y_i|l, \widehat{\theta}_l^{(k-1)}) \widehat{P}^{(k-1)}(l|x_{\mathcal{N}_i})}. \quad (6.51)$$

The calculation of $P^{(k-1)}(x|x_{\mathcal{N}_i})$ involves a previous estimation of the class labels, $\widehat{\mathbf{x}}$, that is, the classification step. In fact, the strategy underlying the EM algorithm consists of applying iteratively the following steps:

1. Estimate the image labelling, $\widehat{\mathbf{x}}$, given the current θ , then use it to form the complete data set $\{\widehat{\mathbf{x}}, \mathbf{y}\}$.
2. Estimate a new θ by maximizing the expectation of the complete-data log likelihood, $\mathcal{E}[\log P(\mathbf{x}, \mathbf{y}|\theta)]$.

The classification step is actually obtained through a MRF-MAP estimation (refer to Appendix B for more details).

6.6.3 Gaussian and Partial Volume model: GPV (C)

The approach described here only uses the intensity information as in the FGMM. It exactly follows the image model defined in Section 6.3.1 that considers a density function for the mixture brain tissues different from a Gaussian distribution. Then, the same probabilistic model as in Eq. (6.43) is used but, in this case, $P(y_i|x, \theta_x)$ is defined either by a Gaussian or by a PV equation Eq. (6.6). Finally, the following minimization problem is defined:

$$\hat{\theta} = \min_{\theta} \sum_{\forall y_i} (h_n(y_i) - p(y_i|\theta))^2, \quad (6.52)$$

where h_n denotes the normalized intensity histogram. The *genetic algorithm* presented in [101] is used to solve the estimation problem. Fewer parameters have to be estimated since the mean and variance of the PV distributions are determined by the mean and variance of the neighborhood pure tissues composing the mixture. As in FGMM, once the distribution parameters are found, the classification is done following the Bayesian rule.

6.6.4 GPV and HMRF model: GPV-HMRF (D)

This method adds to the GPV approach the spatial information that is encoded following the HMRF theory. As usual, the same probabilistic model as in Eq. (6.50) is defined and, as in method GPV, $P(y_i|x, \theta_x)$ is defined either by a Gaussian or by a PV equation Eq. (6.6).

The estimation parameter problem is solved almost identically as for method GHMRF. An adapted version of the EM-algorithm is used as proposed in [85]:

$$\hat{P}^{(k)}(x|y_i, \hat{\theta}) = \frac{\hat{P}(y_i|x, \hat{\theta}_x^{(k-1)}) \cdot \hat{P}^{(k-1)}(x|x_{\mathcal{N}_i})}{\sum_{l, \forall l \in \mathcal{L}_{pm}} \hat{P}(y_i|l, \hat{\theta}_l^{(k-1)}) \hat{P}^{(k-1)}(l|l_{\mathcal{N}_i})}, \quad (6.53)$$

$$\mu_x^{(k)} = \frac{\sum_{i \in S} \hat{P}^{(k)}(x|y_i) y_i}{\sum_{i \in S} \hat{P}^{(k)}(x|y_i)}, \quad (6.54)$$

$$\left(\sigma_x^{(k)}\right)^2 = \frac{\sum_{i \in S} \hat{P}^{(k)}(x|y_i) (y_i - \mu_x^{(k)})^2}{\sum_{i \in S} \hat{P}^{(k)}(x|y_i)}. \quad (6.55)$$

Note that, in this approach, the updating equations Eq. (6.54) and Eq. (6.55) are only computed for pure tissues ($x \in \mathcal{L}_p$), and that $\hat{P}^{(k)}(y_i|x, \hat{\theta}_x)$ is now either a Gaussian or a PV distribution. The strategy underlying the EM algorithm is similar to that of the GHMRF method. However, in this case, the calculation of $P^{(k)}(x|x_{\mathcal{N}_i})$ does not involve a previous estimation of the class labels since $\hat{\mathbf{x}}$ since spatial prior is retrieved from:

$$\hat{\mathbf{x}} = \arg \max_{\mathbf{x} \in \mathcal{X}} \{P(\mathbf{y}|\mathbf{x})\}, \quad (6.56)$$

Finally, the classification is done by the MRF-MAP step:

$$\hat{\mathbf{x}} = \arg \max_{\mathbf{x} \in \mathcal{X}} \{P(\mathbf{y}|\mathbf{x})P(\mathbf{x})\}, \quad (6.57)$$

and no minimization of the energy can be computed instead of Eq. (6.57) (as it is done in Appendix B to solve the MAP estimation in GHMRF) since $P(\mathbf{y}|\mathbf{x})$ does not always follow a Gaussian distribution.

6.6.5 GPV-HMRF model and Anatomical prior: GPV-HMRF-AP

The GPV-HMRF-AP method segments the brain tissues according to the image model presented in the previous section. Moreover, several anatomical prior models (see Eq. (6.21)) are considered:

1. **GT.** The ground truth class priors are considered first. However, it is noticed that adding such *perfect* prior class templates is not realistic since they are not available. In practice, it is used here only as a basis for comparison with other templates. The construction of mixture tissue probability maps is done as presented in Section 6.3.3 using $\gamma = 2$. Then, both PV and pure tissue prior probabilities have been raised to $\epsilon_m = \frac{1}{6}$ and $\epsilon_p = 6$ respectively. The resulting normalized class templates are shown in Figure 6.2.
2. **GTC.** As proposed in [85], the ground truth class templates are slightly corrupted by rotation (1 degree in the axial plane) and translation (2 mm in direction of the axial plane normal vector) in order to simulate registration errors. Here, γ is equal to 1 in order to make the prior class information less important than the local priors since some errors have been introduced.
3. **SPM.** The probability maps of CSF, GM and WM used in SPM [39] are also considered as class priors (see Section 2.4.2). These templates are almost in the same reference as the Brain Web phantom, thus a rigid transformation would be enough to globally register both the phantom and the SPM class templates. However, a non-rigid registration between the phantom image and the T1 average image of SPM is done in order to make the SPM maps less smooth and more similar to the phantom anatomy. Then, mixture maps have been created as done for the ground truth priors. No change on the border tissues is made (ϵ 's are equal to 1) in order not to introduce many errors since the SPM probability maps are very smooth. γ is, as for GTC, arbitrarily fixed to 1. The resulting templates are shown in Figure 6.3.

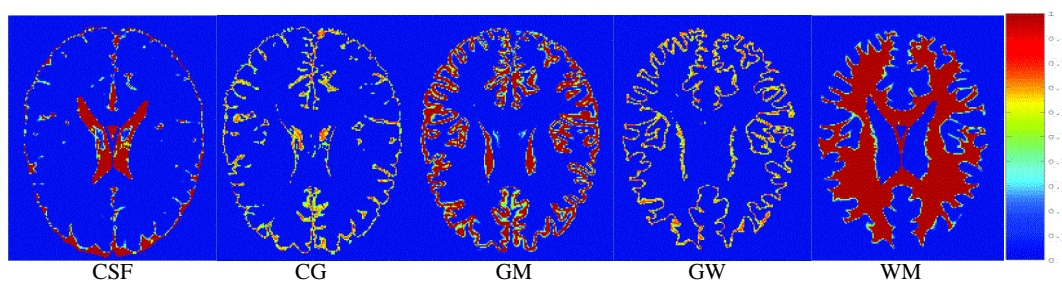


Figure 6.2: Probability maps for the 5 brain tissues constructed from the ground truth.

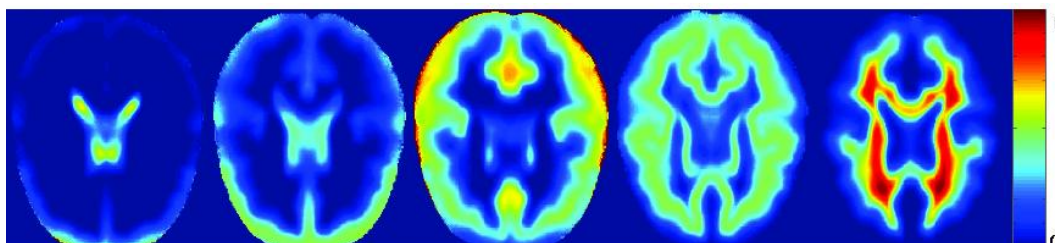


Figure 6.3: From left to right: CSF, CG, GM, GW and WM probability class maps constructed from SPM maps.

6.7 Non parametric methods

In the previous sections, parametric segmentation algorithms were introduced, which means that the intra-class probability densities $P(y|x)$ are modelled by a family of parametric functions $f_x(y|\theta_x)$, such as Gaussian densities. The success of the resulting algorithms is therefore reliant upon the choice of an appropriate family of parametric functions. However, if no well justified parametric model of the data is known, parametric approaches could dramatically fail. Thus, non-parametric, information theoretic alternatives are introduced in what follows. The two non-parametric approaches assessed in this comparative study have been developed and implemented by Butz [18]. It is beyond the scope of this section to present in detail the framework he proposed. Let's however summarize the main concepts of his approach.

6.7.1 Error probability minimization: EP (E)

Let us consider a random variable different from X , called X^{est} , also over \mathcal{L} , which models an estimation of X from the observable data, Y . Naturally, the following stochastic process can be built:

$$X \rightarrow Y \rightarrow X^{est} \rightarrow E, \quad (6.58)$$

where E is an error random variable being 1 whenever the estimated class label, x^{est} , is considered a wrong estimate of the initial class label, x , and 0 otherwise. A key quantity of Eq. (6.58) is the probability of error, $P_{e|x}$, of the transmission from X to X^{est} , for a given class map, \mathbf{x} . This probability also equals the expectation of E .

Considering the introduced formalism (see [18]), the information theoretic classification objective consists of determining the class label map $\hat{\mathbf{x}}$ that minimizes an error probability $P_{e|x}$:

$$\hat{\mathbf{x}} = \arg \min_{\mathbf{x}} P_{e|x}. \quad (6.59)$$

6.7.2 Non-parametric HMRF: NP-HMRF (F)

The approach proposed above does not consider any spatial priors on the class label map. However, the probabilistic nature of the formalism allows the addition of a HMRF, just as for the parametric approaches introduced in the previous sections, resulting in a non-supervised non-parametric hidden markov model (NP-HMRF) segmentation:

$$\hat{\mathbf{x}} = \arg \min_{\mathbf{x} \in \mathcal{L}} P(\mathbf{x}) \cdot P_{e|x}. \quad (6.60)$$

The optimization objective above is called the minimal error probability principle for NP-HMRFs. In complete analogy to parametric HMRFMs, the prior probabilities, $P(\mathbf{x})$, are modeled by a Gibbs distribution (Section 14). The derived non-parametric framework for classification allows the consideration of voxel features for which any particular parametric model is known, as it is the case for e.g. voxel gradients.

6.8 Results and Validation

6.8.1 Data set

All the methods have been validated using the *digital brain phantom* from the McConell Brain Imaging Center [27]. They provide an MRI simulator where different RF non-uniformity (bias of

0%, 20%, and 40%) and noise levels (0%, 1%, 3%, 5%, 7%, and 9%) can be added to the MR brain phantom image.

Then, a 5-class (CSF, CG, GM, GW and WM) ground truth classification image, Figure 6.6(b), has been created from the 3-dimensional ‘fuzzy’ tissue membership volumes provided by [27] where voxel values reflect the proportion of tissue present within the voxel. This makes these images suitable for segmentation assessment. Finally, a ground truth image histogram is created by splitting each image histogram into the specific pure tissue and their mixture histograms (see Figure 6.6(c), Figure 6.9(c), and Figure 6.12(c)).

6.8.2 Results

Validation is made by comparing the results obtained with the classification methods presented in Section 6.6 and Section 6.7 to both the 5-class ground truth classification image and the brain phantom image histograms. Because of limited space, only a complete study of these results for brain phantom images of 5% Noise (N) and 0% of in-homogeneity (RF), 7%N and 20%RF, and 9%N and 40%RF are shown here*. Also, note that the analysis of the methods including anatomical prior is done separately in comparison with GPV-HMRF and that GPV-HMRF-AP are tested in few brain phantom images.

First, each of the resulting volumes classified by each of the algorithms is qualitative validated visually. A comparison of a representative slide of the resulting classified images where all brain tissues are present with the corresponding slide of the ground truth classification volume is presented (see Figure 6.7, Figure 6.10 and Figure 6.13).

Second, the intensity image model is assessed by comparing the histogram fitting to the ground truth brain phantom image histogram (see Figure 6.8, Figure 6.11 and Figure 6.14).

Third, quantitative analysis is performed by computing the *confusion tables* with respect to the 5-class reference classification (Table 6.1, Table 6.3 and Table 6.5). These values assess the quality of the classification for each tissue class.

Fourth, global measures of quality (*Pergood*, *Perhalf* and *Perfault*) are presented in Table 6.2, Table 6.4, and Table 6.6. Percentages are always computed with respect to the 5-class ground truth classification and voxels belonging to the brain phantom background are not considered. *Pergood* is the percentage of voxels correctly classified (confusion table diagonal). *Perghalf+* and *Perghalf-* represent the percentage of voxels that has not been correctly classified but misclassified into a neighbor tissue, e.g. a WM voxel classified as WG, (‘+’ and ‘-’ refer to superior and inferior of the confusion table diagonal, respectively). *Perfalse* is the percentage of voxels that has been completely misclassified.

Fifth, the robustness in front on the noise and in-homogeneities is analyzed separately for each method in Figure 6.5.

Sixth, a global assessment is done for all possible noise and inhomogeneity levels of the digital brain phantom. Both percentage of the correct and false classification are showed in Figure 6.15, Figure 6.16, Figure 6.17 and Figure 6.18 for all methods.

Finally, GPV-HMRF-AP is only applied to the 5N0RF, 7N20RF, and 9N40RF phantoms. All the measures presented before (classified images, histogram fitting and confusion table) are considered here to study the influence of the different class templates on the final classification (see Figure 6.19, Figure 6.21, and Figure 6.23). For each phantom the ground truth class priors (GT), the corrupted ground truth class priors (GTC), and the probabilistic class maps of SPM are compared with respect to GPV-HMRF method.

*In order to simplify the notation, the phantoms will be denoted by 5N0RF, 7N20RF, and 9N40RF.

6.9 Discussion

6.9.1 General performance

One of the goals of this comparative study is to be able to specify the most suitable tissue classification technique for T1-MR brain image. Unfortunately, there is not a single winner. Actually, the answer depends on the noise (N) and the in-homogeneity (RF) level present in the images. It is considered that the best classification corresponds to the highest percentage of correct classified voxels (*pergood*). For low levels of noise ($N = \{0, 1, 3\}\%$), it is not evident to determine a method that better classifies than others (as we can see in In Figure 6.15). However, for higher levels of noise ($N = \{5, 7, 9\}\%$), method GPV-HMRF has almost always performed the best classification closely followed by method GHMRF (their *pergood* differs from less than 2%). Now, we can also determine the methods that perform smaller errors (lowest *perfault*). In this case, method GPV and GPV-HMRF (both using PV equation) always have the lowest *perfault* for low and high noise levels respectively. However, differences between all *perfault* values are not more than 1%.

6.9.2 Real MRI conditions

A wide range of noise level exists in the brain phantom simulator but actually not all of these values are realistic to represent the noise present in a *typical* T1-weighted MR brain image. The signal to noise ratio (SNR) in a *normal* T1-MR image has been computed and, then, it has been compared with the SNR present in the brain phantoms. The conclusion is that a *normal* noisy image corresponds to the mean of the phantom 5N0RF and 7N0RF. Thus, from now on conclusions are based on the classification results of phantoms with $N = \{5, 7, 9\}\%$ and $RF = \{0, 20, 40\}\%$. For these ranges of noise and inhomogeneities, method GPV-HMRF has almost always the highest *pergood* and the lowest *perfault*. It is always closely followed by method GHMRF that usually differs from less than 2% from the *pergood* and less than 0.1% from the *perfault*.

6.9.3 Pure tissues and partial volume

In this work, a T1-MR brain image is modelled by three main tissues (CSF, GM and WM) and two mixtures (CG and GW). As is done by most of the methods described in the literature, the two other possible mixtures, CW and CGW, have been ignored. Actually, the importance of CW and CGW has been measured from the digital brain phantom: 12.8% of the image voxels are CSF, 18% CG, 26% GM, 20% GW and 23% WM while only 0.18% of the images voxels belong to the CW and only 0.02% to the CGW. Visually, the probability density function of the CSF and WM mixture has been drawn in Figure 6.4. Thus, it is justified to affirm that $P(CW)$ and $P(CGW)$ do not significantly contribute in the total probability density function of the MR intensity image.

Thanks to the confusion tables, the study of the classification score for each tissue class becomes an easy task. The best classification for CSF is performed (the 70% of the cases) by method EP, for GM it is method NPHMM (also the 70% of the cases) and method GHMRF performs for more than 50% of the cases the best classification of tissue WM. Method GPV-HMRF almost always achieves the best classification score for both partial volume tissues: 78% of the cases for CG and 100% for GW.

Results show that partial volume distributions are hardly well represented by a Gaussian function. This is obvious when looking at the histogram fitting where CG and GW mixtures are always better fitted by methods C and D using the partial volume equation (Figure 6.8, Figure 6.11, and Figure 6.14). In fact, even if the mixtures may look like a Gaussian for high levels of noise and inhomogeneities, the assumption of using a normal distribution for a PV is false. However, the

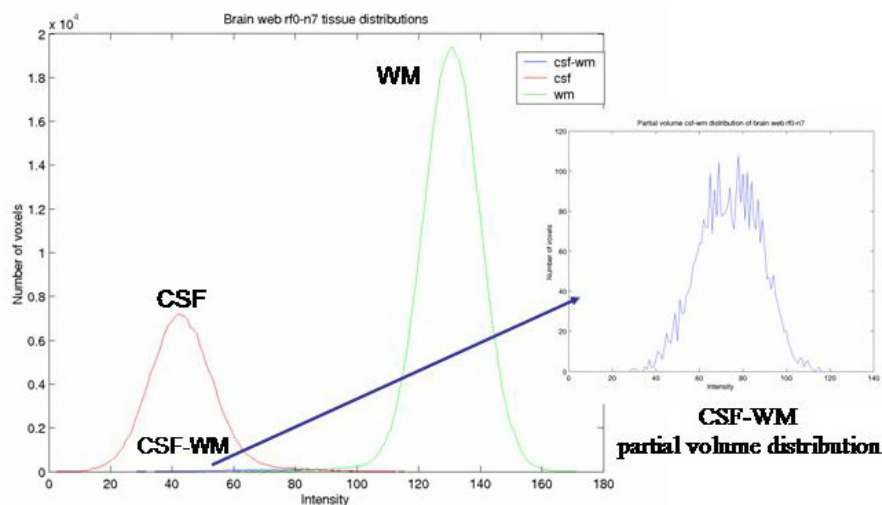


Figure 6.4: Intensity probability distribution of CSF and WM mixture.

percentage of voxels correctly classified for a mixture tissue never reaches more than 73% while the best scores for pure tissues usually reach 90% of voxels correctly classified. This poor result indicates that partial volume distribution does not seem to be completely well modelled yet. Thus, more work has to be done in the study and modelling partial volume intensity distribution. For instance, two different mixtures between GM and WM can be considered as recently suggested in [20]. They propose a pioneer anatomical model that splits the GM and WM mixture into a *geometrical* mixture corresponding to the brain cortico-subcortical interface and a *mosaic* GW mixture corresponding to the deep cerebral nuclei structures such as the thalamus.

6.9.4 Robustness in front of noise and inhomogeneities

None of the classification methods under study tries to compensate for image artifacts such as noise or bias. No pre-processing is applied for image quality enhancement: neither an anisotropic filtering nor a bias correction are considered. This way the robustness of the methods can be analyzed with these artifacts. This is clearly shown in Figure 6.5 where all possible levels of noise and inhomogeneities present in the brainweb simulator are considered again. Methods that consider only intensity information are represented in the left column. In general, the quality of the classification decreases with increasing noise and non-uniformities. Method A is very sensitive to both noise and inhomogeneities. However, for low levels of noise, methods C and E are equally performant in RF=0 than in RF=20. For very high noise levels ($N=\{7,9\}$), all methods perform a classification that converges towards a range of *pergood* equal to [60-65]% for any value of RF. The right-hand column represents all the methods using HMRF. All of these methods present exactly the same behavior with noise and bias. If we consider RF=0, *pergood* decreases proportionally to the increment of noise. For RF=20, there is not a decrease of quality but almost a constant value of *pergood*. And, for RF=40, the *pergood* even increases for high noise levels. That is due to the fact that the phantoms considering low noise levels ($N=\{0,1,3\}$) are actually not realistic to model T1-weighted MR brain images. Then, given a constant level of noise, RF=40 always makes *pergood* decrease about 12% for low and about 7% for high noise levels.

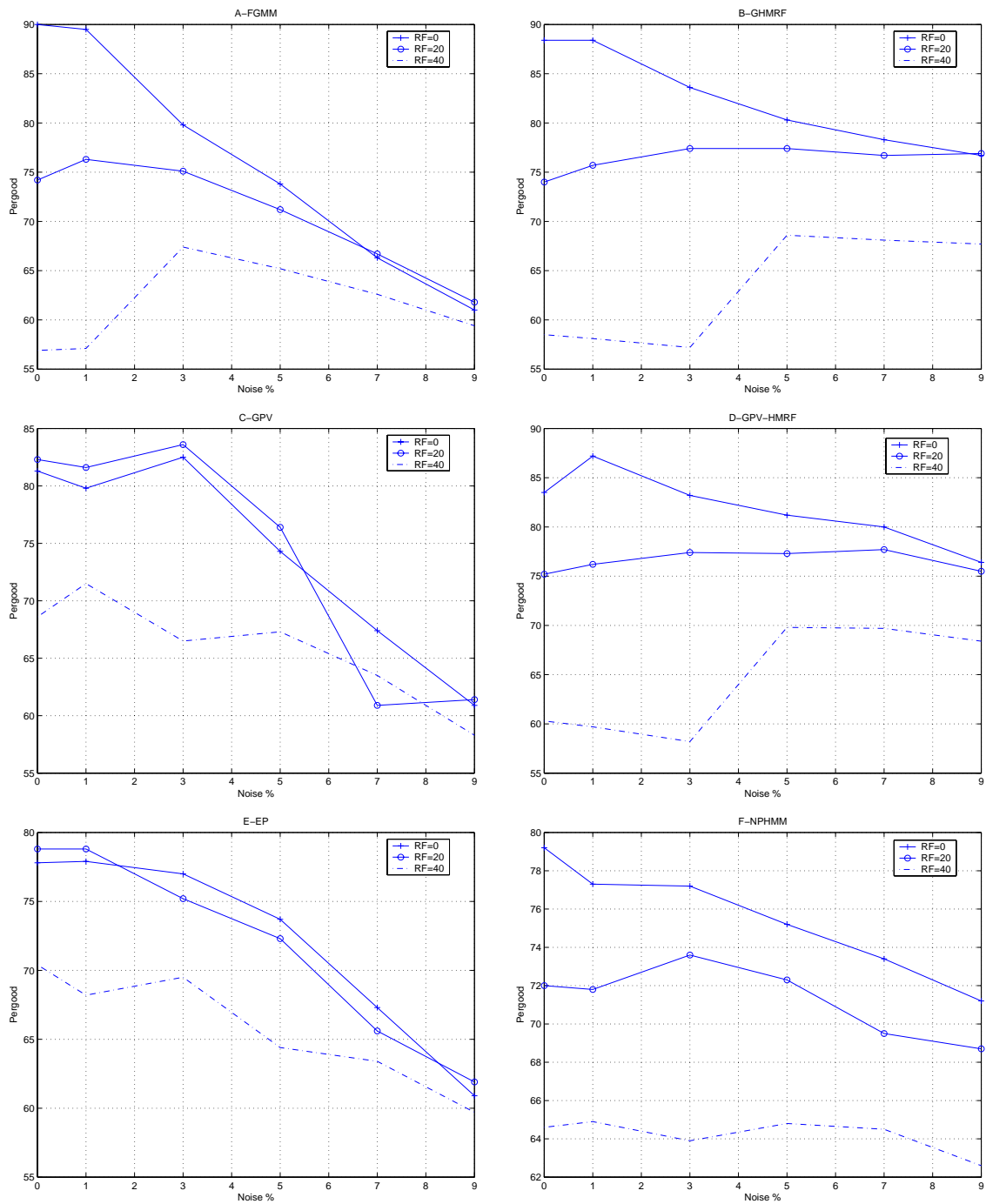


Figure 6.5: Robustness of the classification methods in front of different levels of noise and inhomogeneities.

6.9.5 Intensity versus spatial prior

It can be seen in Figure 6.7, Figure 6.10, and Figure 6.13 that the classification based only on intensity information (methods FGMM, GPV, and EP) is much more noisy than classification that also encodes spatial information. Errors are due to the overlap between tissue distributions and this overlap is larger for higher values of N and RF . On the contrary, when spatial information is also used in the classification process results are much less noisy: methods B, D and F improve the *pergood* percentage, with respect to methods A, C and E, by a 7% on average. However, they still make some errors mostly in the mixtures classification because the partial volume distribution model is probably not well-suited but also because of the MRF. In fact, results show that MRF considerably increases the classification quality and that makes the algorithms more robust when faced with noise than the intensity-based approaches. More evolved MRF are needed though in the particular case of T1W MR image segmentation. Recently, it has been suggested to model either pure or mixture brain tissues with different MRF parameters [71]. Also, the addition of atlas information in the energy function could better guide the MRF model as proposed in Section 6.3.3 and in [85].

6.9.6 Parametric vs Non-parametric

Non-parametric models have performed in many cases equally or even better than parametric approaches. EP has slightly lower *Pergood* than FGMM using a Bayes classification or GPV for low levels of noise and non-uniformities. But almost the same quality of classification or even better than parametric models has been obtained by EP for high levels of noise $N=\{5,7,9\}$.

When spatial information is also included, parametric models (GHMRF and GPV-HMRF) have almost always better *Pergood* than non-parametric approaches (there is usually a difference of 6% between them). Also, parametric methods commit fewer errors, they have a lower *Perfault*, than NP-HMRF. The misclassification made with both non-parametric approaches is mainly due to an overestimation of both mixture classes.

In conclusion, a non-parametric approach is more performant if no well justified assumption about the data model can be made. However, logically, a good data model is better performant than no model.

6.9.7 Using prior class atlases

The results of the methods that include atlas information are discussed here in comparison with the method GPV-HMRF. Three different class priors have been added to the spatial model used in D and they are denoted by GT, GTC, and SPM (see Section 6.6.5). The global performance of these four approaches is presented in Figure 6.25. The GT prior leads logically to the best results: the highest percentage of voxels correctly classified, around 88%, and the lowest percentage of fatal errors, around 0.17%, for any level of noise or inhomogeneity. However, as has been said before, the use of such a *perfect* class prior as GT is not possible in practice. The atlas information introduced by GTC and SPM are more realistic but results show that they do not always improve the results performed by D. Actually, significant changes have only been obtained for the 9N40RF phantom: the *perfault* is reduced from 0.79% to 0.57% for both GTC and SPM and the *pergood* is improved by a 5% with GTC. All resulting classified images look similar (see Figure 6.19, Figure 6.21 and Figure 6.23). Almost no noise is visible either for GT or for GTC methods. Methods D and SPM lead to slightly noisy classifications for 7N20RF and 9N40RF phantoms.

Pure tissues are always better classified by GT and GTC than D while SPM only improves GM (in all three phantoms) and WM (5% and 7% of noise) classification. Significant errors are though

introduced by GTC and SPM in the classification of partial volume voxels (see the histogram fitting in Figures 6.20, 6.24, and 6.23). This effect is quantified in the confusion tables by a percentage of mixture voxels correctly classified much lower in GTC and SPM than in D or GT (from 2 to 12 % of degradation).

Finally, notice that rotation and translation of GT have a significant influence on PV classification while pure tissue classification remain robust with these *simulated* registration errors. Also, SPM probabilistic atlas has not demonstrated important improvements with respect to D. That is probably because SPM maps are too smooth and no anatomical variability is present in the prior class templates, thus, the information added by SPM is not precise.

6.10 Summary

A validation study on MR brain tissue classification techniques has been proposed in this chapter. Both parametric and non-parametric approaches have been assessed in this work. Intensity-based classification methods are compared to the techniques that add spatial prior. The effect of considering prior class templates is also studied.

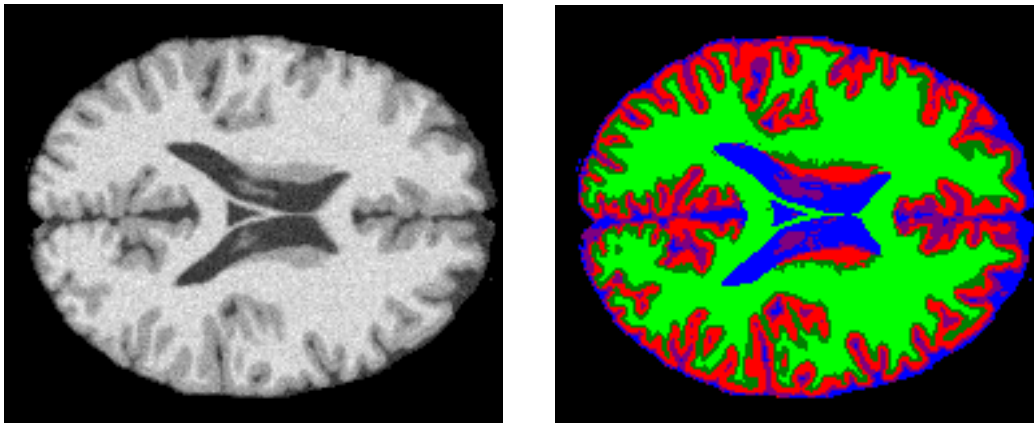
All tests have been done in several phantoms considering different noise and intensity non-uniformity levels. Then, the assessment is done by comparing to a 5 class ground truth image.

Results have shown that the techniques considering spatial information lead in better classification when high noisy images are considered while for low level of noise and in-homogeneities (that is not necessarily near real MR images) histogram-based techniques lead to comparable results. However, it has been demonstrated that percentage of correct classification never reaches the 100% and, even if pure tissues are in general well-classified, partial volumes are still not.

Methods including atlas information have not considerably improved the final classification with respect to the techniques that model local spatial priors. On the contrary, classification has shown to be highly sensitive to the registration errors or to the use of a wrong template. Actually, mixture tissues are particularly affected by prior class template errors while pure tissue classification has been almost always improved by these methods. This is because the initial pure class templates are not precise enough (too smooth or errors because of registration are present) but probably also because PV prior class maps are not optimally defined. In conclusion, no atlas class prior should be included if its quality cannot be assessed before.

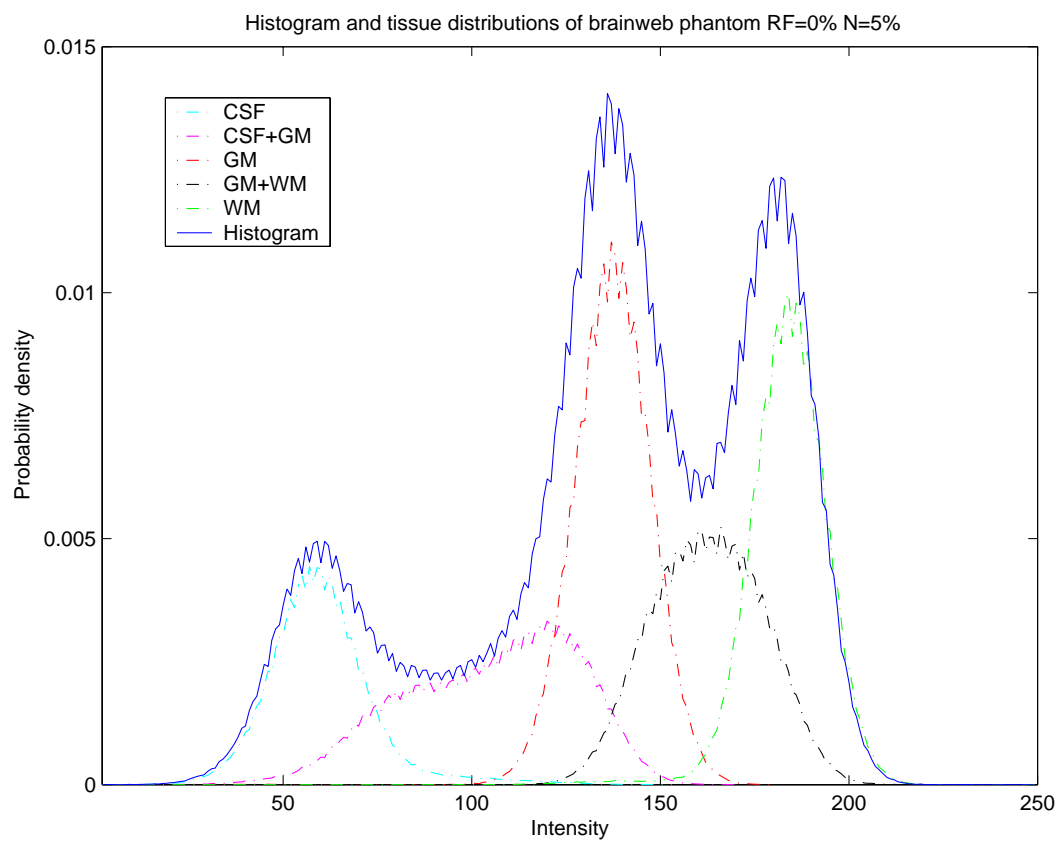
Finally, we plan to measure the effect of pre-processing the images (by an anisotropic filter or a bias corrector) or adding a bias field estimation model (as proposed by [70, 120] for instance). We expect both the pre-processing and bias model to make the classification more robust at high levels of noise and inhomogeneities. However, we suspect the pre-processing to *displace* partial volume voxels, thus some errors would probably be added in mixture tissue classification.

6.11 Figures



(a)

(b)



(c)

Figure 6.6: (a) Brainweb phantom simulated T1-MRI with 5% noise and 0% RF. (b) Ground truth created from Brainweb classification. 5 class (c) Tissue distribution

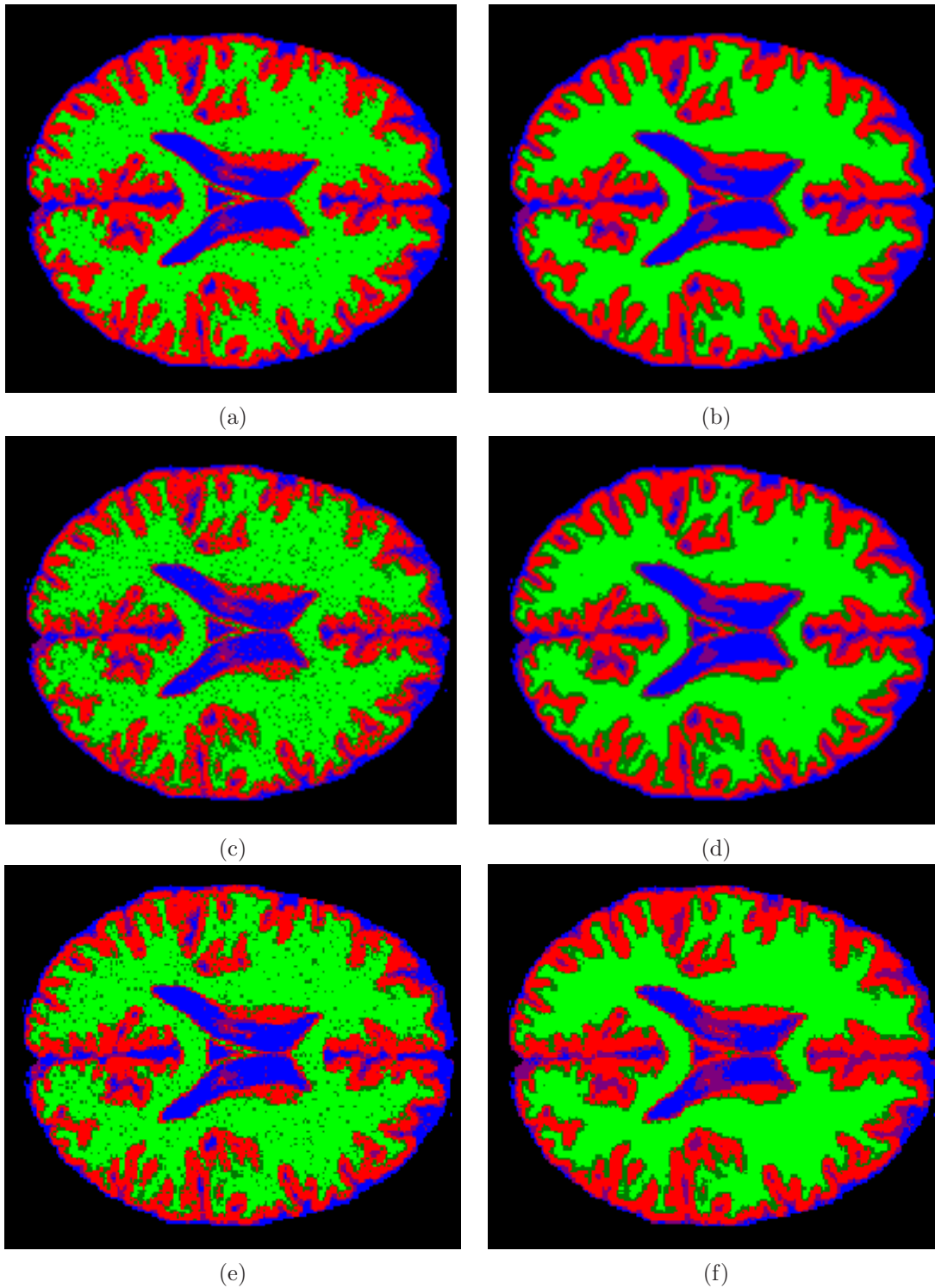


Figure 6.7: Classification of the phantom 5N0RF. (a) Method A: FGMM. (b) Method B: GHMRF. (c) Method C: GPV. (d) Method D: GPV-HMRF. (e) Method E: EP. (f) Method F: NP-HMRF.

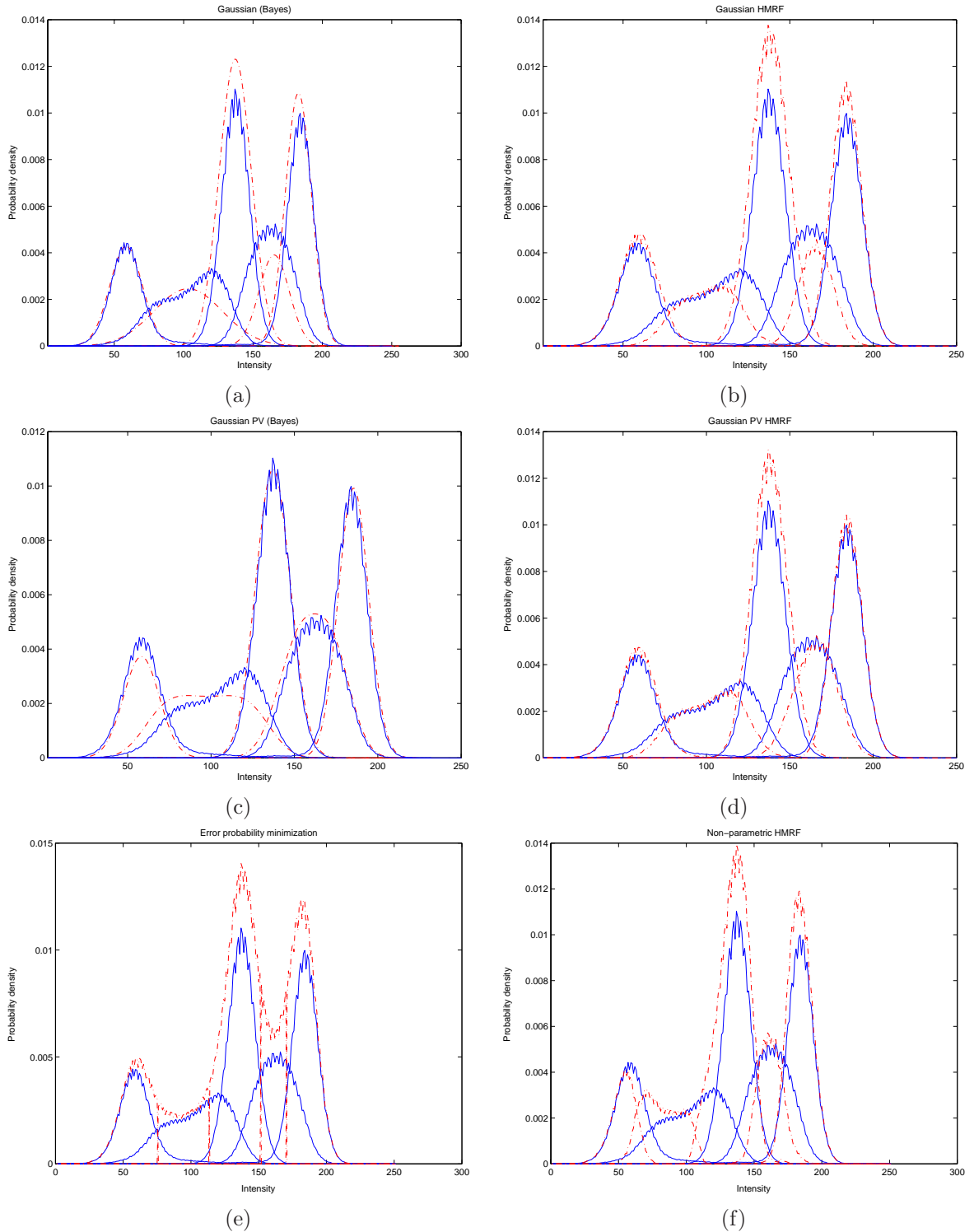


Figure 6.8: Histogram fitting of the phantom 5N0RF. Results are in dotted line. (a) Method A: FGMM. (b) Method B: GHMRF. (c) Method C: GPV. (d) Method D: GPV-HMRF. (e) Method E: EP. (f) Method F: NP-HMRF.

		Reference							Reference				
A		CSF	CG	GM	GW	WM	B		CSF	CG	GM	GW	WM
	CSF	91.4	14.0	0.1	0.0	0.0		CSF	91.5	9.8	0.1	0.0	0.0
	CG	8.0	51.3	2.5	0.0	0.0		CG	8.3	59.1	2.1	0.0	0.0
	GM	0.6	34.6	93.2	30.7	1.0		GM	0.2	31.1	96.7	28.9	0.7
	GW	0.0	0.1	4.2	35.9	5.9		GW	0.0	0.0	1.1	53.6	3.5
	WM	0.0	0.0	0.1	33.3	93.1		WM	0.0	0.0	0.0	17.5	95.7

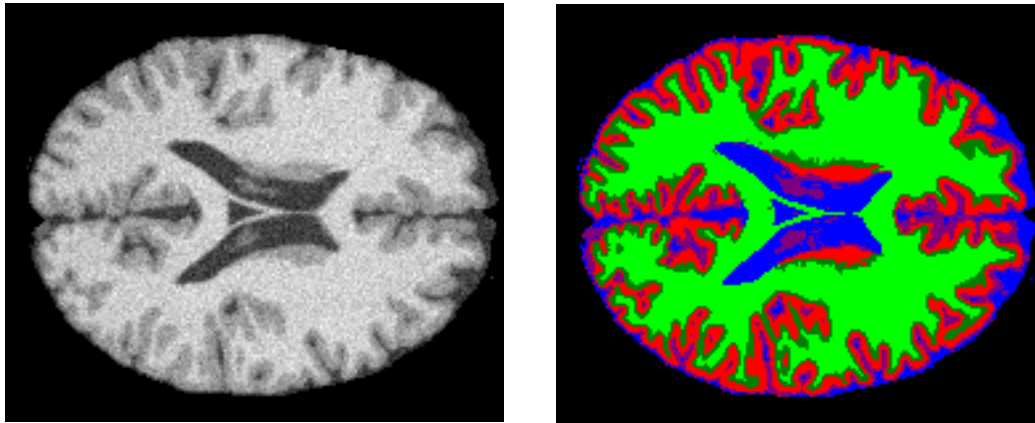
		Reference							Reference				
C		CSF	CG	GM	GW	WM	D		CSF	CG	GM	GW	WM
	CSF	80.3	7.4	0.1	0.0	0.0		CSF	91.2	9.8	0.1	0.0	0.0
	CG	19.1	58.0	2.5	0.0	0.0		CG	8.7	63.9	5.0	0.0	0.2
	GM	0.6	34.3	88.1	22.1	0.8		GM	0.1	26.2	92.0	24.4	0.5
	GW	0.0	0.3	9.4	49.1	8.9		GW	0.0	0.0	2.9	64.8	8.1
	WM	0.0	0.0	0.0	28.8	90.2		WM	0.0	0.0	0.0	10.7	91.2

		Reference							Reference				
E		CSF	CG	GM	GW	WM	F		CSF	CG	GM	GW	WM
	CSF	89.5	12.2	0.1	0.0	0.0		CSF	65.9	2.5	0.1	0.0	0.0
	CG	9.6	46.3	1.0	0.0	0.0		CG	33.1	45.6	0.1	0.0	0.0
	GM	0.8	41.3	91.2	24.2	0.9		GM	1.0	51.9	95.7	21.5	0.9
	GW	0.0	0.3	7.7	44.9	7.4		GW	0.0	0.0	4.1	56.4	2.8
	WM	0.0	0.0	0.0	30.9	91.7		WM	0.0	0.0	0.0	22.1	96.4

Table 6.1: Confusion table of the phantom 5N0RF. Percentages are computed overall voxels for each tissue type.

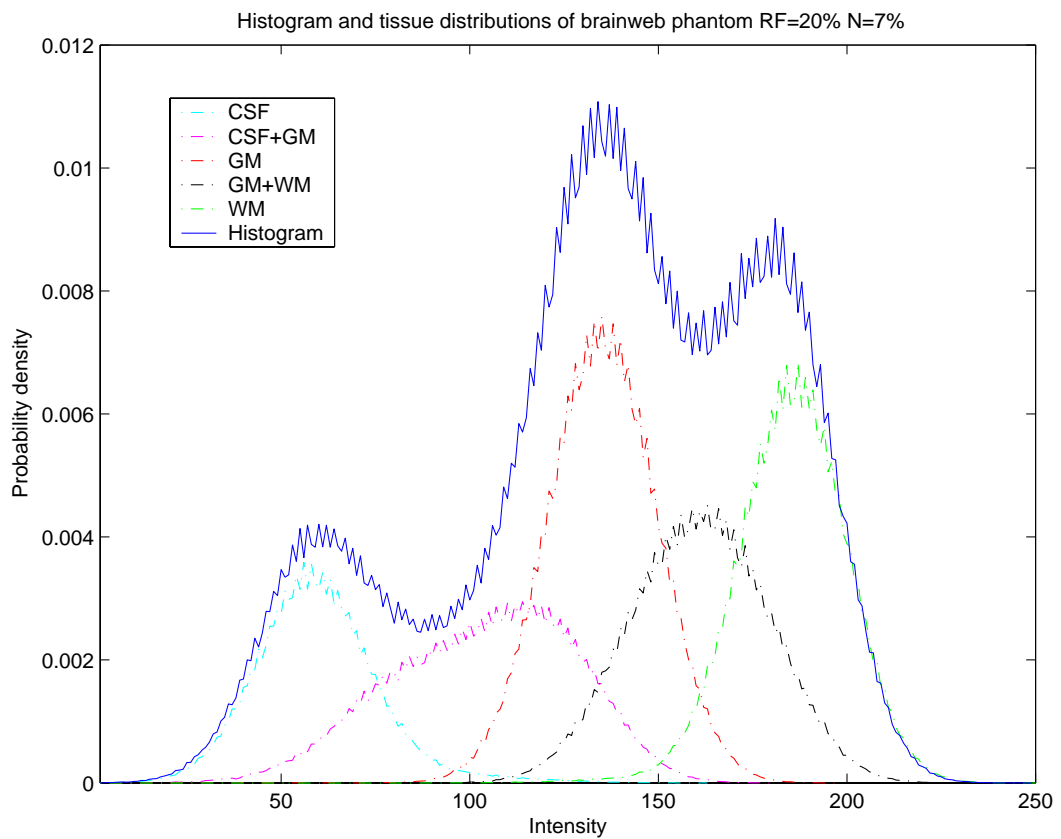
	PerGood	PerFault	PerHalf+	PerHalf-
FGMM	73.83	0.36	10.76	15.05
GHMRF	80.34	0.24	9.00	10.42
GPV	74.30	0.35	8.51	16.84
GPV-HMRF	81.18	0.20	9.91	8.71
EP	73.3	0.38	9.3	17.0
NP-HMRF	75.2	0.34	5.7	19.1

Table 6.2: Percentage of total classification for brain web phantom 5N0RF.



(a)

(b)



(c)

Figure 6.9: (a) Brainweb phantom simulated T1-MRI with 7% noise and 20% RF. (b) Ground truth created from Brainweb classification. 5 class (c) Tissue distribution.

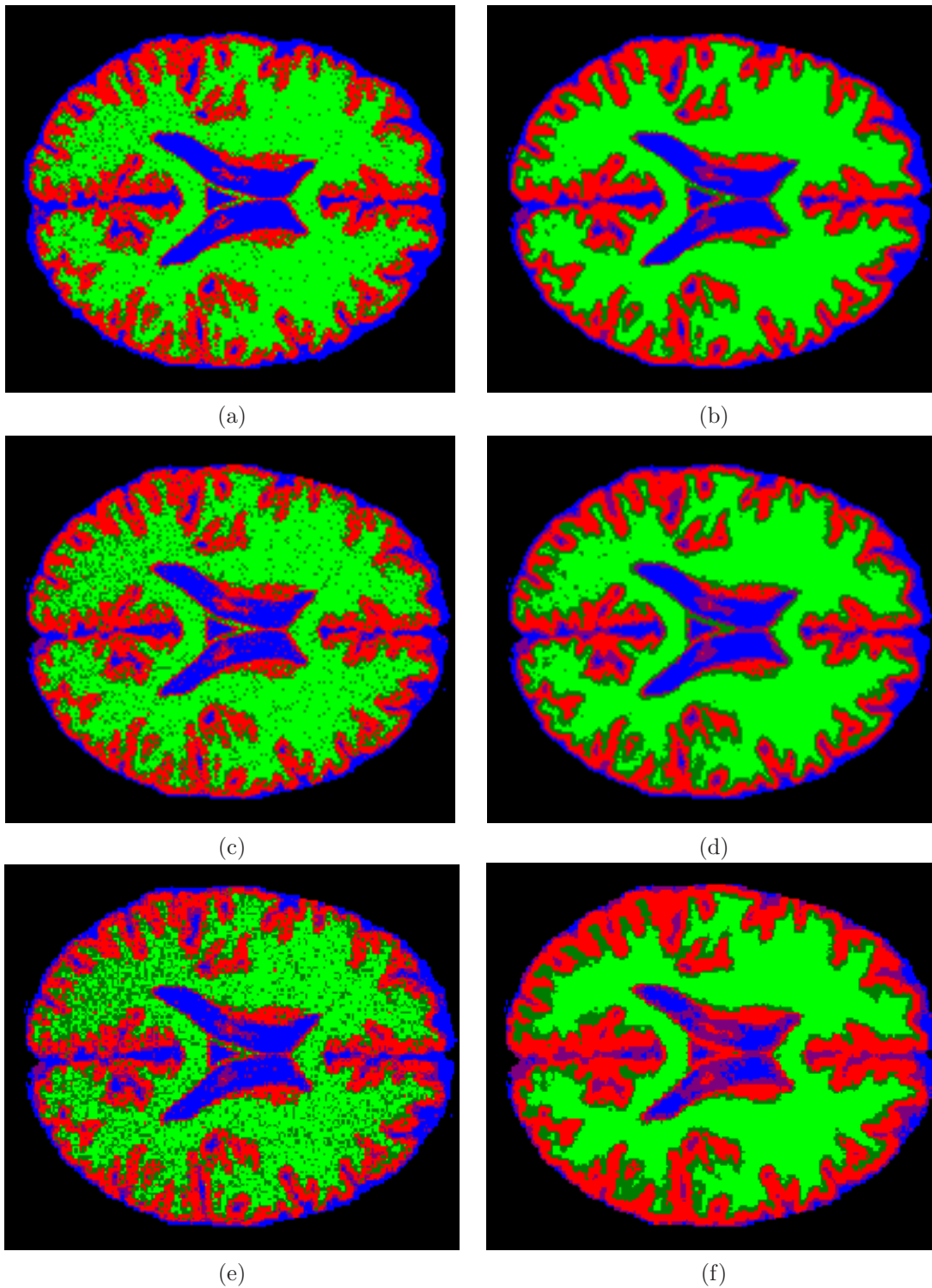


Figure 6.10: Classification of Brainweb phantom 7N20RF. (a) Method A: FGMM. (b) Method B: GHMRF. (c) Method C: GPV. (d) Method D: GPV-HMRF. (e) Method E: EP. (f) Method F: NP-HMRF.

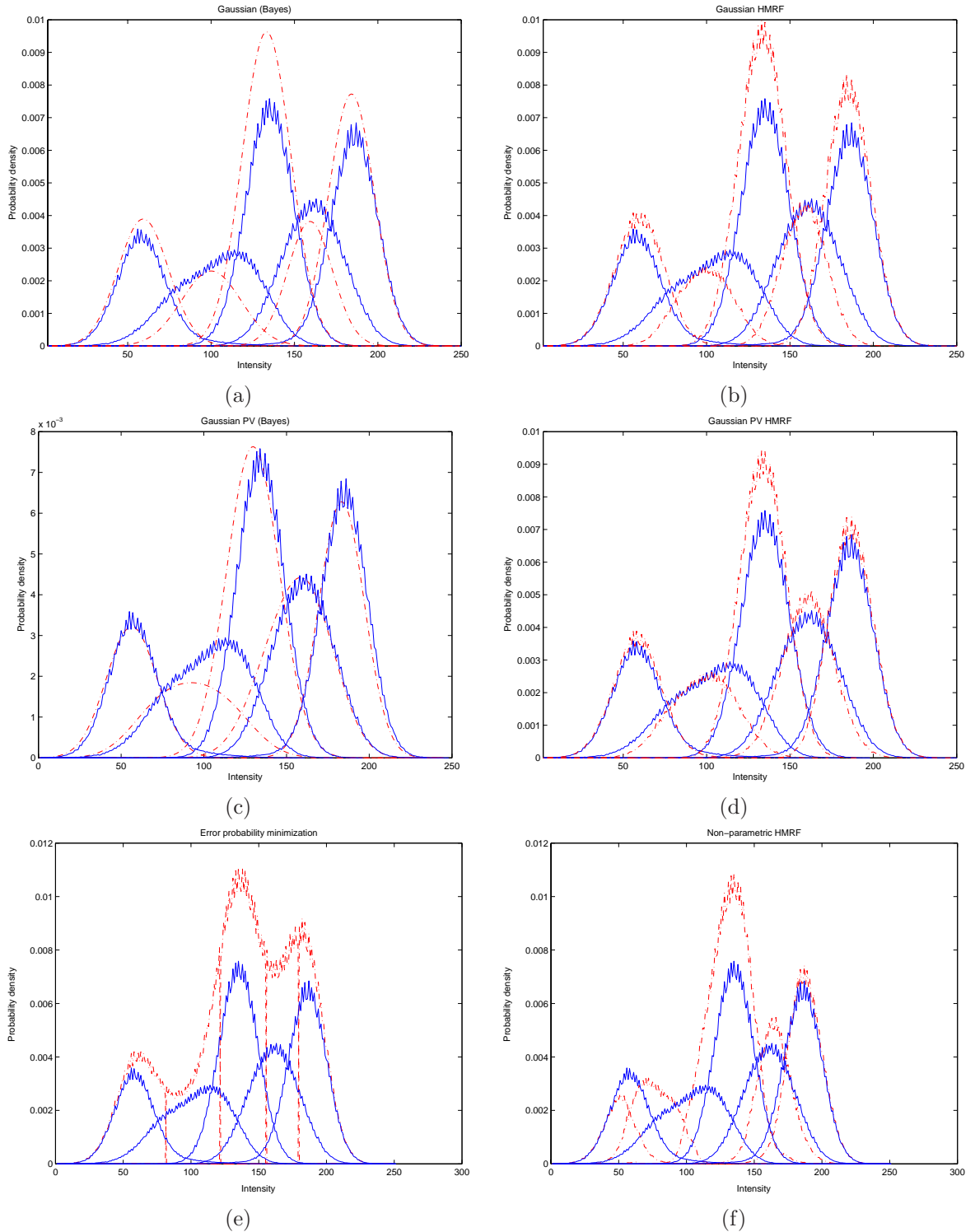


Figure 6.11: Histogram fitting of the Brainweb phantom 7N20RF. Results are in dotted line. (a) Method A: FGMM. (b) Method B: GHMRF. (c) Method C: GPV. (d) Method D: GPV-HMRF. (e) Method E: EP. (f) Method F: NP-HMRF.

		Reference							Reference				
		CSF	CG	GM	GW	WM			CSF	CG	GM	GW	WM
A	CSF	92.3	20.9	0.1	0.0	0.0	B	CSF	89.9	11.5	0.1	0.0	0.0
	CG	6.5	33.6	3.3	0.1	0.0		CG	9.5	47.2	2.3	0.0	0.1
	GM	1.2	44.9	87.8	36.3	2.2		GM	0.6	41.2	88.9	19.3	0.6
	GW	0.0	0.6	7.7	26.9	8.4		GW	0.0	0.1	8.8	59.4	5.6
	WM	0.0	0.0	1.2	36.6	89.4		WM	0.0	0.0	0.0	21.2	93.7

		Reference							Reference				
		CSF	CG	GM	GW	WM			CSF	CG	GM	GW	WM
C	CSF	67.0	9.4	0.1	0.0	0.0	D	CSF	90.5	10.8	0.1	0.0	0.0
	CG	31.7	48.3	7.0	0.6	0.1		CG	9.1	57.2	4.7	0.1	0.2
	GM	1.3	39.0	69.8	26.3	2.6		GM	0.3	31.9	84.4	18.8	0.3
	GW	0.0	3.2	21.8	45.8	26.9		GW	0.0	0.1	10.8	66.3	10.6
	WM	0.0	0.1	1.3	27.3	70.4		WM	0.0	0.0	0.0	14.8	88.9

		Reference							Reference				
		CSF	CG	GM	GW	WM			CSF	CG	GM	GW	WM
E	CSF	91.5	19.8	0.1	0.0	0.0	F	CSF	54.1	2.0	0.1	0.0	0.0
	CG	8.0	55.0	17.3	1.4	0.1		CG	44.5	39.9	0.3	0.0	0.0
	GM	0.5	24.7	74.8	36.9	2.4		GM	1.5	58.1	93.7	30.8	0.9
	GW	0.0	0.5	7.7	45.7	30.6		GW	0.0	0.1	6.0	55.5	13.6
	WM	0.0	0.0	0.1	16.0	66.9		WM	0.0	0.0	0.0	13.7	85.5

Table 6.3: Confusion table of the phantom 7N20RF. Percentages are computed overall voxels for each tissue type.

	PerGood	PerFault	PerHalf+	PerHalf-
FGMM	66.67	1.13	13.91	18.29
GHMRF	76.68	0.28	12.65	10.45
GPV	65.58	1.6	11.3	21.53
GPV-HMRF	77.7	0.20	9.42	12.69
EP	65.61	1.06	22.63	10.7
NP-HMRF	69.51	0.43	9.81	20.26

Table 6.4: Percentage of total classification of the phantom 7N20RF.

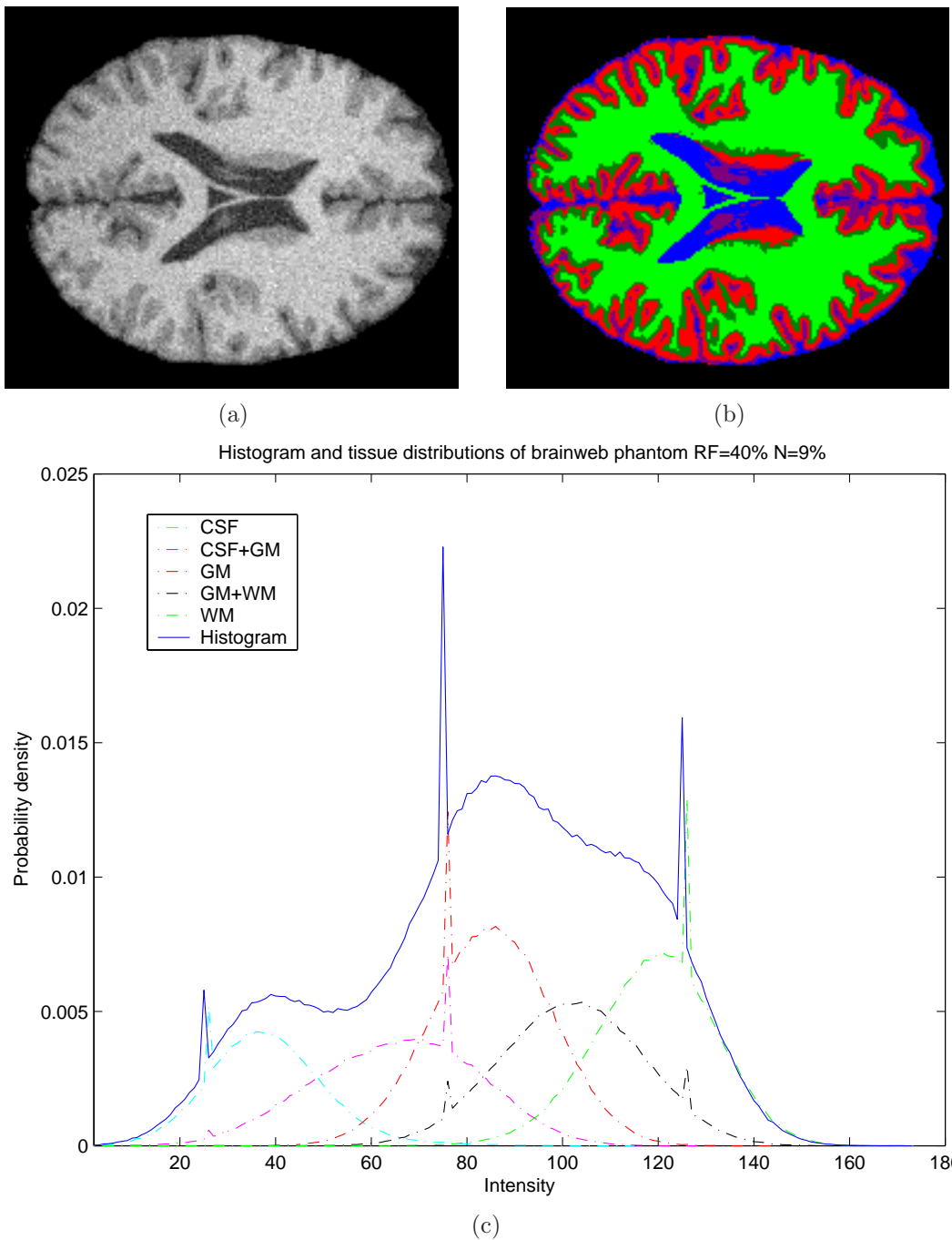


Figure 6.12: (a) Brainweb phantom simulated T1-MRI with 9% noise and 40% RF. (b) Ground truth created from Brainweb classification. 5 class (c) Histogram and tissue distributions. Notice the *picks* in the original image histogram. We think that is just an error in the 40% RF bias field simulation. However, that does not influence anyway the classification results. This effect will be reported to the corresponding authors.

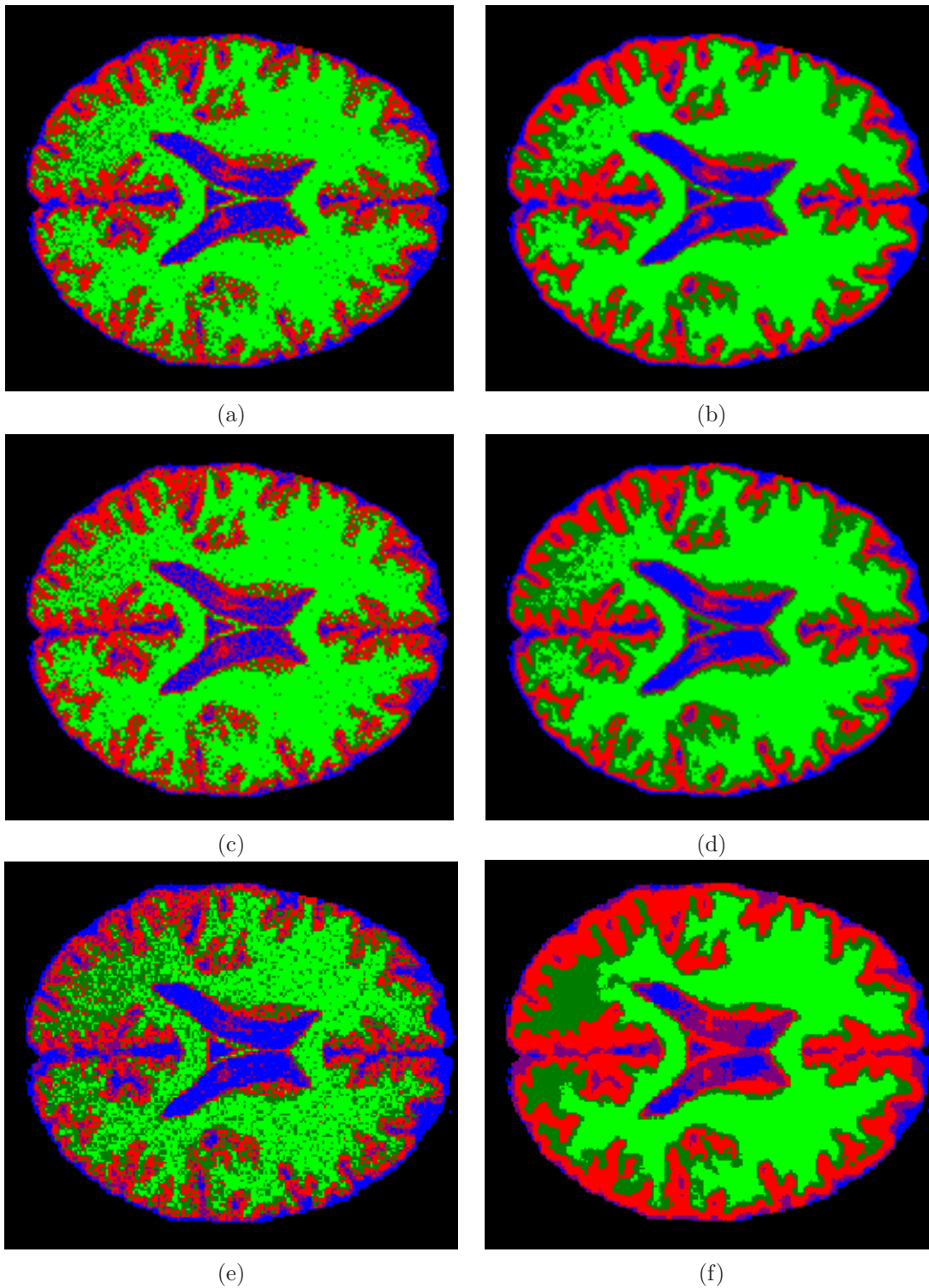


Figure 6.13: Classification of the phantom 9N40RF. (a) Method A: FGMM. (b) Method B: GHM-RF. (c) Method C: GPV. (d) Method D: GPV-HMRF. (e) Method E: EP. (f) Method F: NP-HMRF.

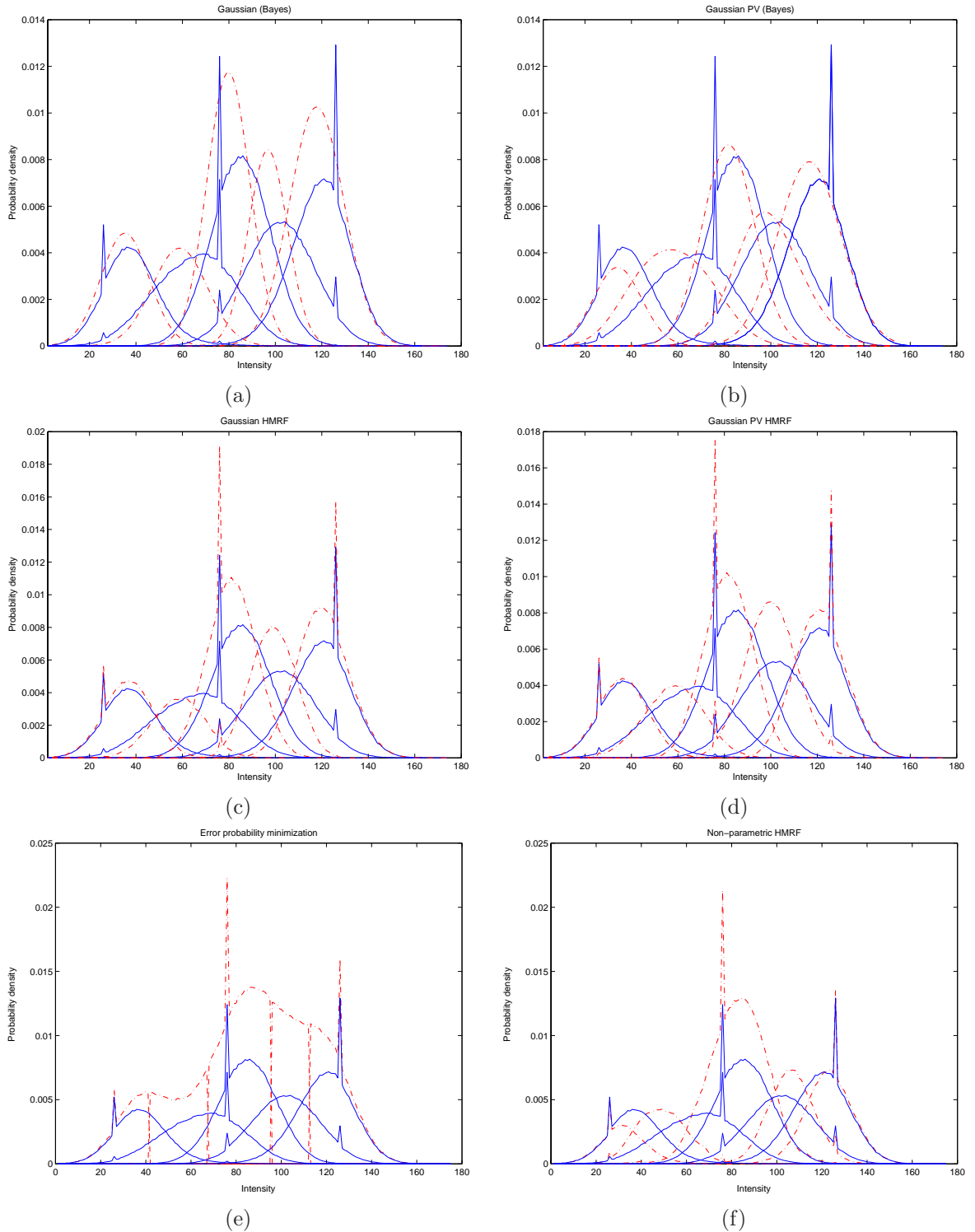


Figure 6.14: Histogram fitting of the phantom 9N40RF. Results are in dotted line. (a) Method A: FGMM. (b) Method B: GHMRF. (c) Method C: GPV. (d) Method D: GPV-HMRF. (e) Method E: EP. (f) Method F: NP-HMRF.

		Reference							Reference				
A		CSF	CG	GM	GW	WM	B		CSF	CG	GM	GW	WM
	CSF	79.5	15.4	0.2	0.0	0.0		CSF	83.8	9.1	0.1	0.0	0.0
	CG	18.1	32.7	5.8	0.6	0.0		CG	15.0	43.6	3.3	0.1	0.0
	GM	2.3	46.4	63.7	24.0	2.0		GM	1.0	44.9	70.0	18.8	0.5
	GW	0.1	5.0	25.2	34.5	11.7		GW	0.1	2.4	26.4	55.4	13.3
	WM	0.0	0.5	5.2	40.9	86.3		WM	0.0	0.0	0.3	25.8	86.2

		Reference							Reference				
C		CSF	CG	GM	GW	WM	D		CSF	CG	GM	GW	WM
	CSF	77.2	14.1	0.2	0.0	0.0		CSF	82.8	8.7	0.1	0.0	0.0
	CG	20.9	38.4	7.9	0.9	0.0		CG	16.3	51.1	6.4	0.2	0.1
	GM	1.8	41.2	58.9	21.7	1.7		GM	0.7	37.6	64.7	16.9	0.3
	GW	0.1	6.3	32.6	60.5	37.4		GW	0.1	2.6	28.6	62.5	16.3
	WM	0.0	0.0	0.5	16.8	60.9		WM	0.0	0.0	0.2	20.4	83.3

		Reference							Reference				
E		CSF	CG	GM	GW	WM	F		CSF	CG	GM	GW	WM
	CSF	92.1	28.1	1.0	0.1	0.0		CSF	54.3	3.0	0.1	0.0	0.0
	CG	7.4	51.2	33.2	7.0	0.3		CG	43.4	37.1	1.6	0.0	0.0
	GM	0.5	18.2	47.6	28.9	3.9		GM	2.2	59.2	87.7	39.2	2.3
	GW	0.0	2.5	17.7	47.2	34.9		GW	0.0	0.6	10.5	46.9	25.6
	WM	0.0	0.0	0.5	16.8	60.9		WM	0.0	0.0	0.1	13.8	72.1

Table 6.5: Confusion table of the phantom with 9N40RF. Percentages are computed overall voxels for each tissue type.

	PerGood	PerFault	PerHalf+	PerHalf-
FGMM	59.35	3.28	11.86	25.51
GHMRF	67.73	0.8	9.37	22.10
GPV	58.31	2.13	17.59	21.98
GPV-HMRF	68.36	0.79	10.41	20.45
EP	56.77	3.34	27.65	12.25
NP-HMRF	62.62	0.97	14.83	21.58

Table 6.6: Percentage of total classification for the phantom 9N40RF .

Percentage of Correct Classification

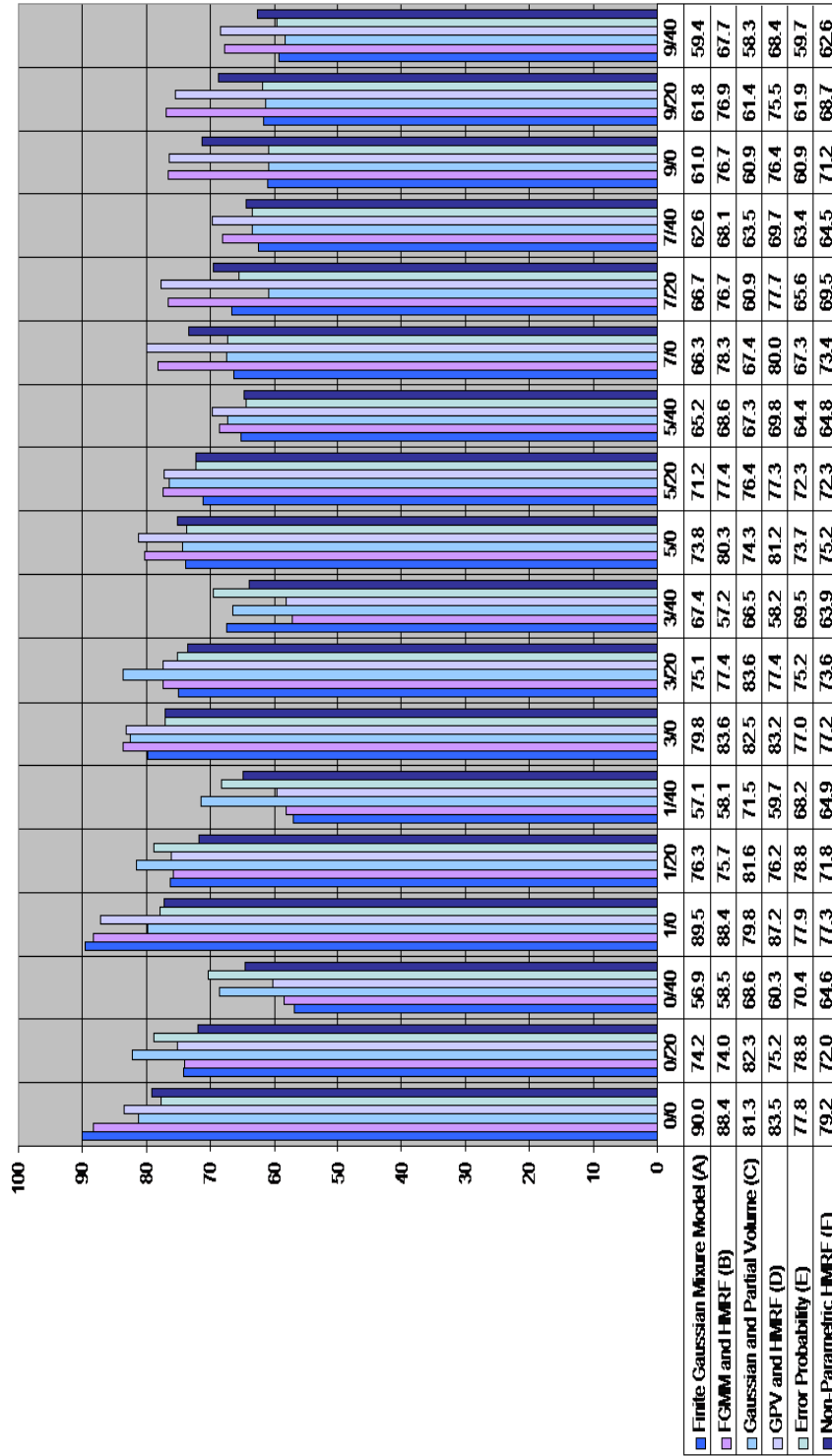


Figure 6.15: Percentage of correct classified voxels.

Percentage of Completely False Classification

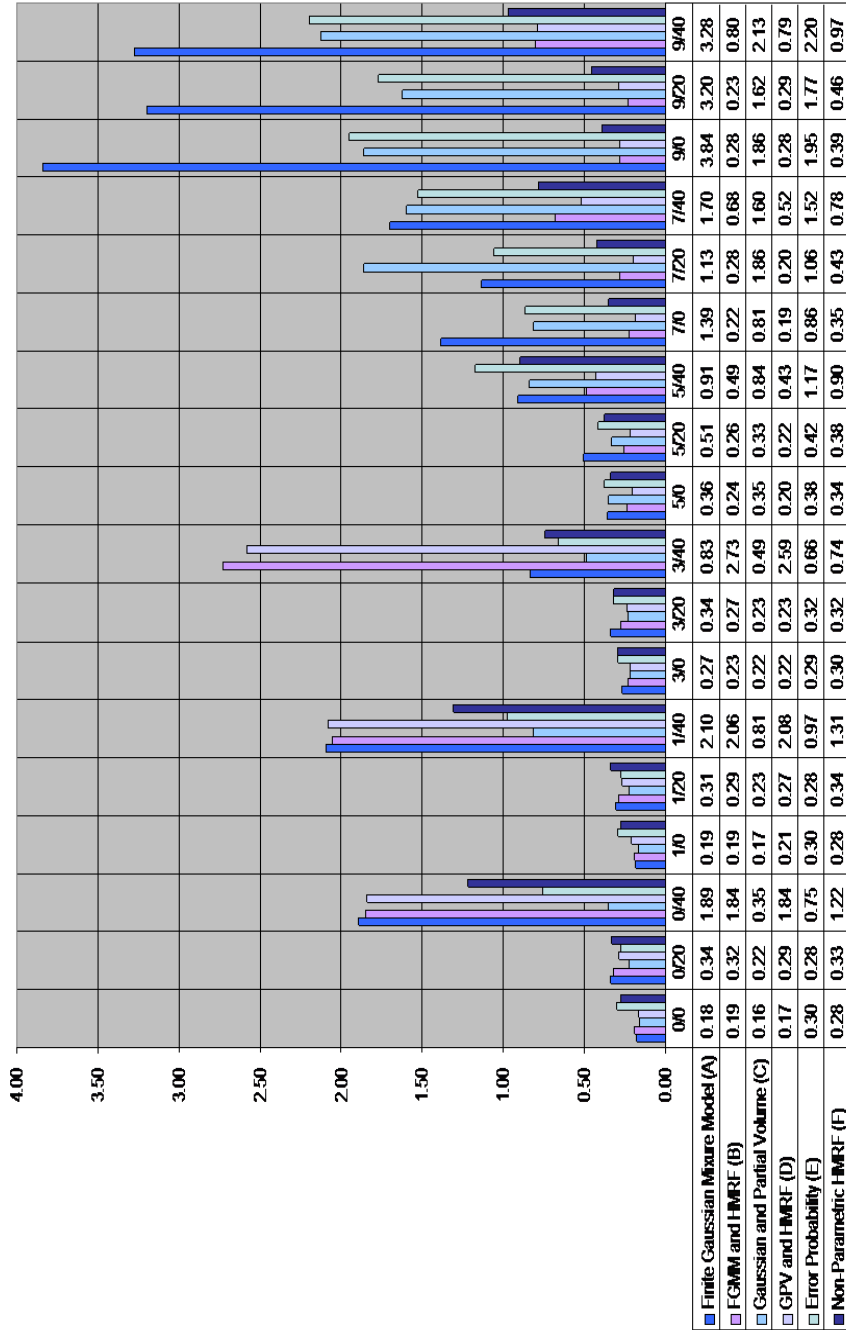


Figure 6.16: Percentage of false classified voxels.

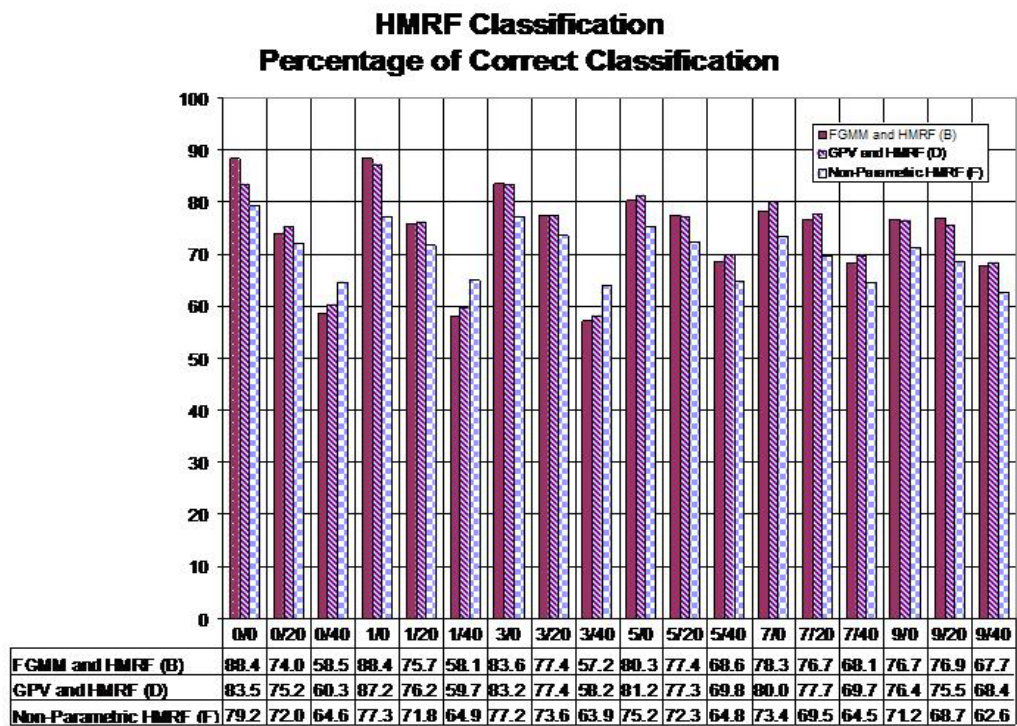
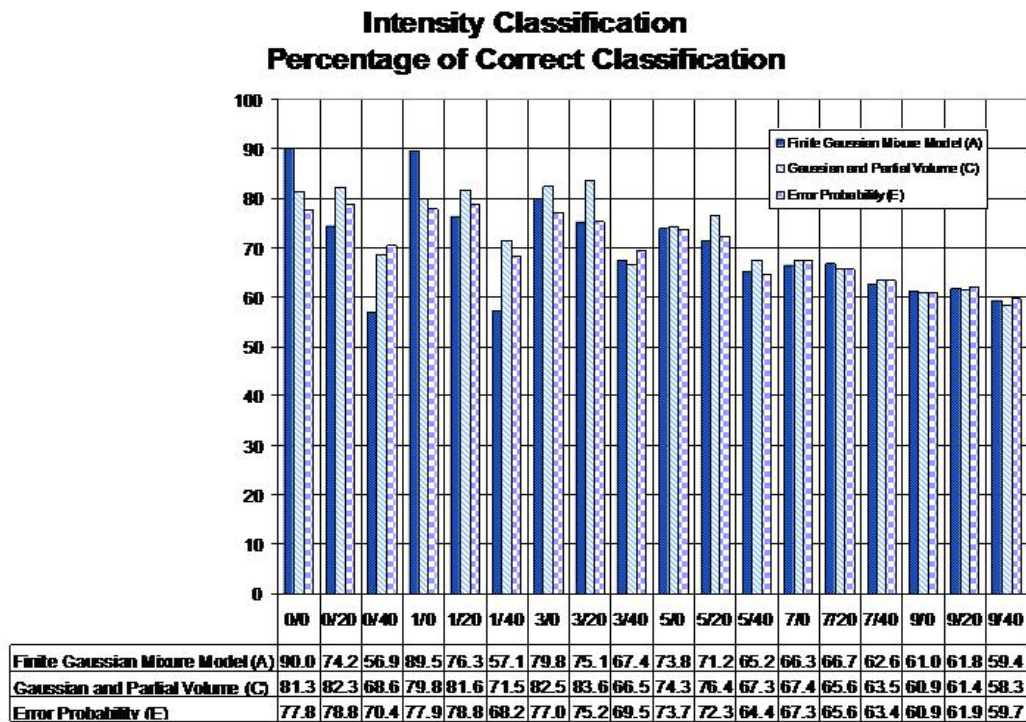
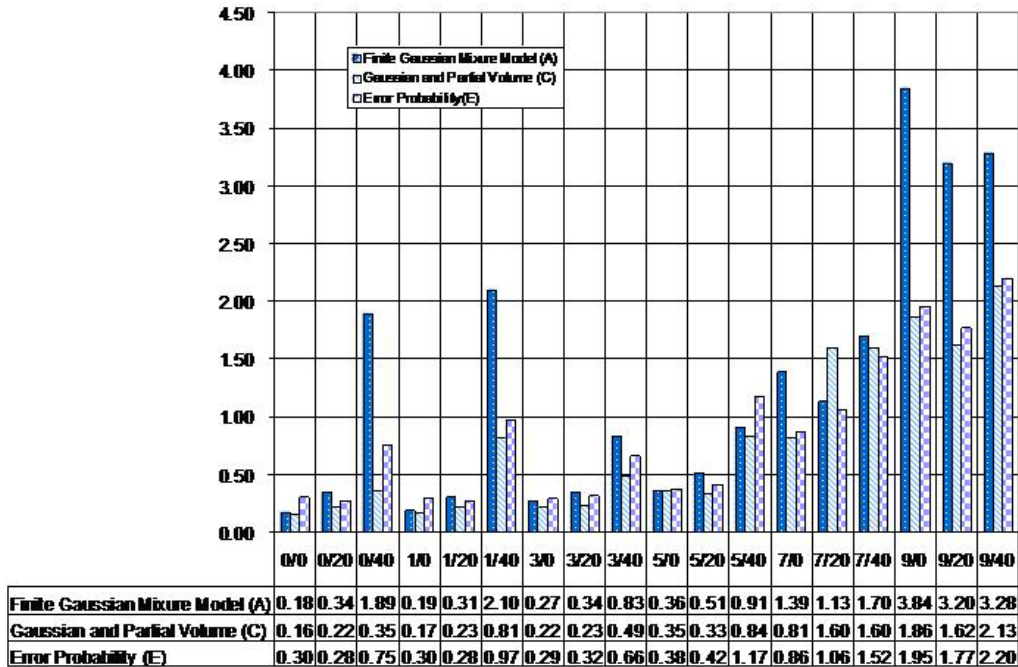


Figure 6.17: Percentages of correct classified voxels.

Intensity-based Classification Percentage of Completely False Classification



HMRP Classification Percentage of Completely False Classification

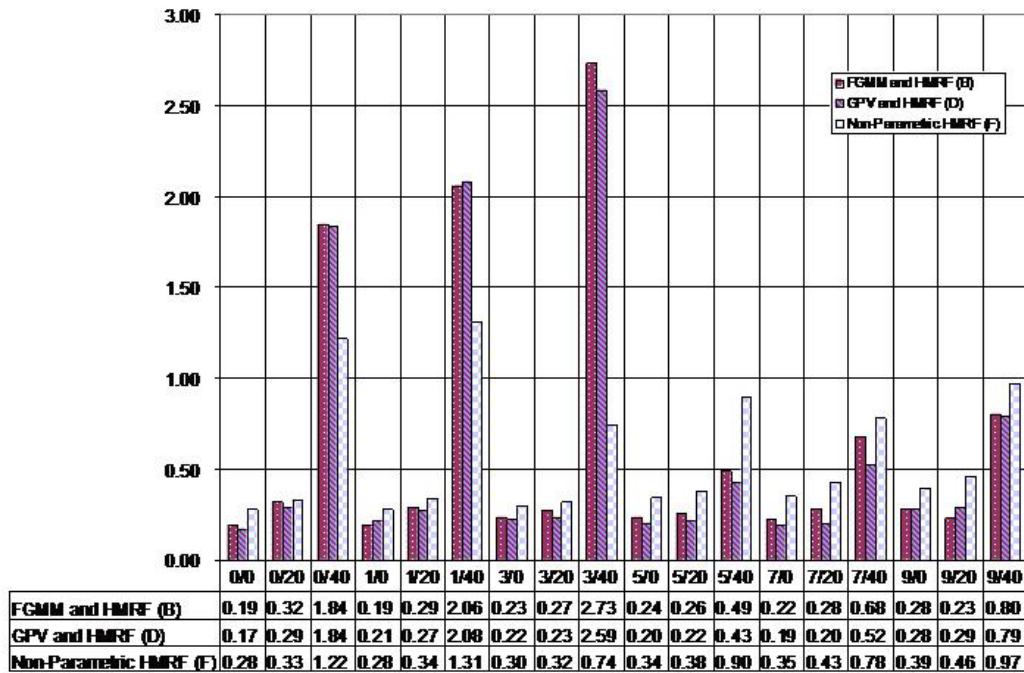


Figure 6.18: Percentages of completely false classified voxels.

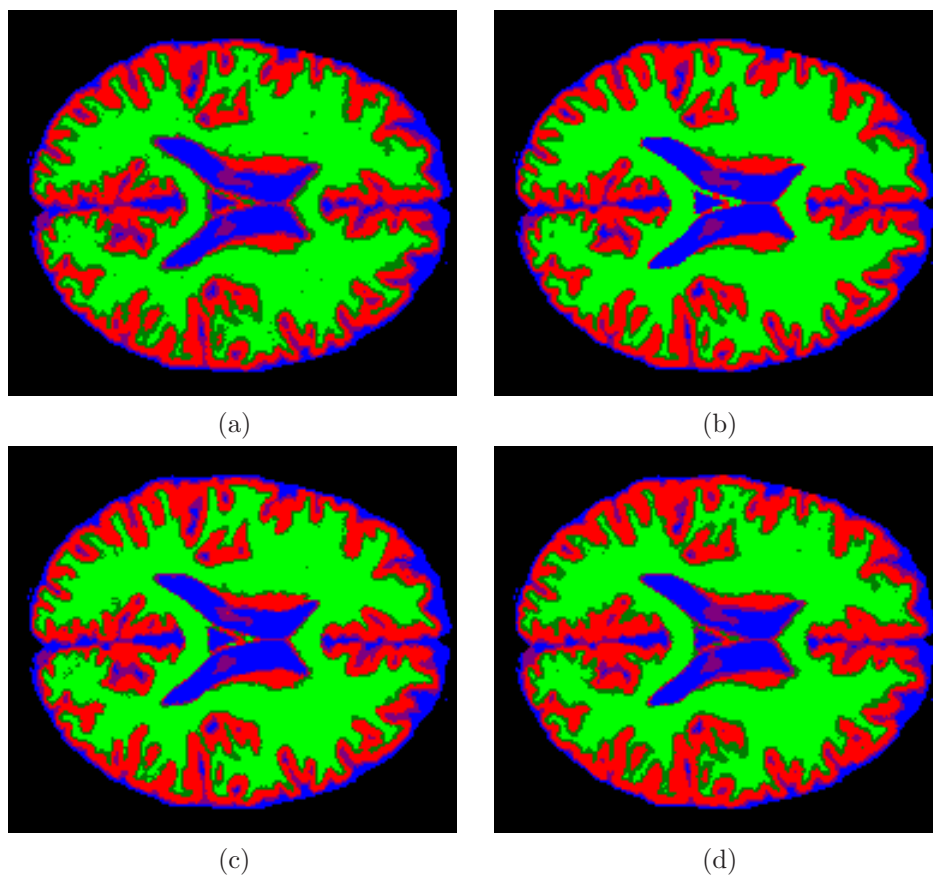


Figure 6.19: Classification image results of 5NORF using atlas prior. (a) Method D: GPV-HMRF. (b) Method D with GT. (c) Method D GTC. (d) Method D with SPM.

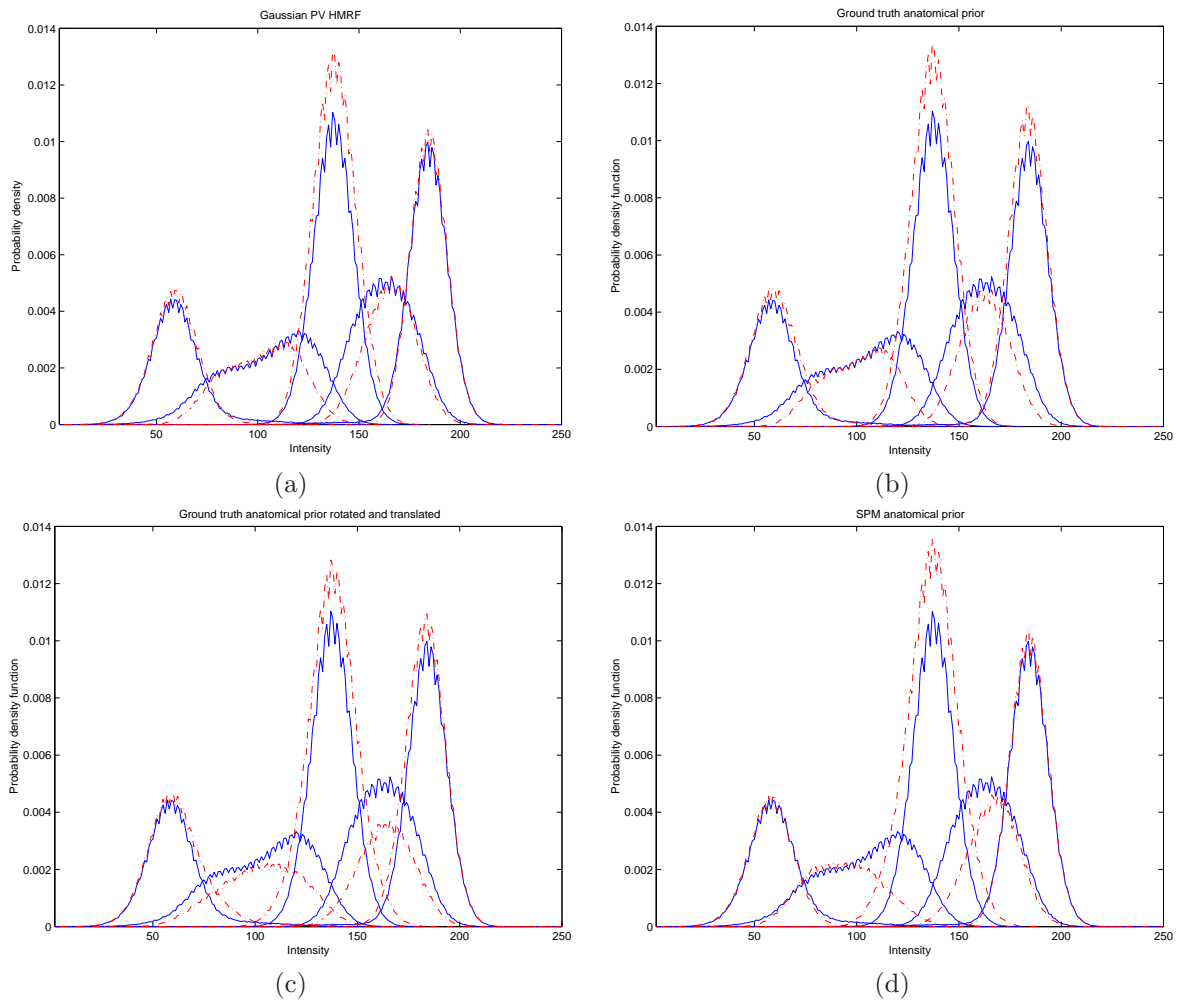


Figure 6.20: Histogram fitting of the phantom with 5N0RF using atlas prior. Results are in dotted line. (a) Method D: GPV-HMRF. (b) Method D with GT. (c) Method D GTC. (d) Method D with SPM.

		Reference							Reference						
D		CSF	CG	GM	GW	WM	GT		CSF	CG	GM	GW	WM		
		CSF	91.2	9.8	0.1	0.0		0.0		CSF	98.9	8.6	0.1	0.0	0.0
		CG	8.7	63.9	5.0	0.0		0.2		CG	0.9	66.5	0	0	0.4
		GM	0.1	26.2	92.0	24.4		0.5		GM	0.2	24.8	99.9	15.8	0
		GW	0.0	0.0	2.9	64.8		8.1		GW	0	0	0	69.8	0
		WM	0.0	0.0	0.0	10.7		91.2		WM	0	0	0	14.4	99.4

		Reference							Reference						
GTC		CSF	CG	GM	GW	WM	SPM		CSF	CG	GM	GW	WM		
		CSF	93.3	15.1	0.5	0		0		CSF	87.2	6.7	0.1	0.0	0.0
		CG	6.6	52.7	5.3	0.1		0.3		CG	12.6	51	1.8	0	0.2
		GM	0.1	32.1	91.1	28.8		0.4		GM	0.2	42.2	95.7	31.6	0.4
		GW	0	0	3	51.4		4.5		GW	0.0	0.0	2.4	57.5	7.4
		WM	0	0	0	19.7		94.9		WM	0.0	0.0	0.0	10.9	91.9

Table 6.7: Confusion table of phantom 5N0RF using atlas prior.

	PerGood	PerFault	PerHalf+	PerHalf-
D	81.18	0.20	9.91	8.71
GT	87.60	0.17	4.76	7.48
GTC	77.32	0.33	10.97	11.37
SPM	78.04	0.19	9.81	11.96

Table 6.8: Percentage of total classification for the phantom 5N0RF with atlas prior.

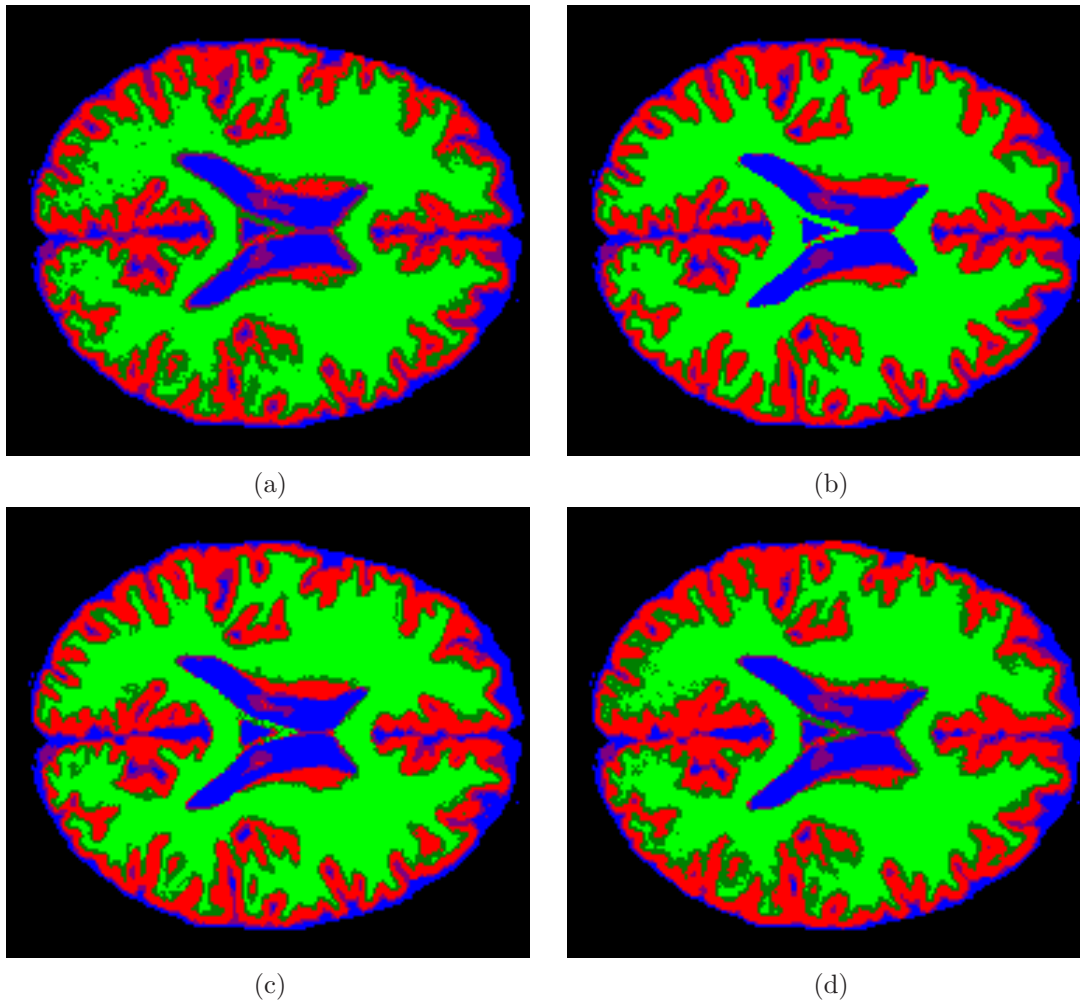


Figure 6.21: Classification image results of 7NRF using atlas prior. (a) Method D: GPV-HMRF. (b) Method D with GT. (c) Method D GTC. (d) Method D with SPM.

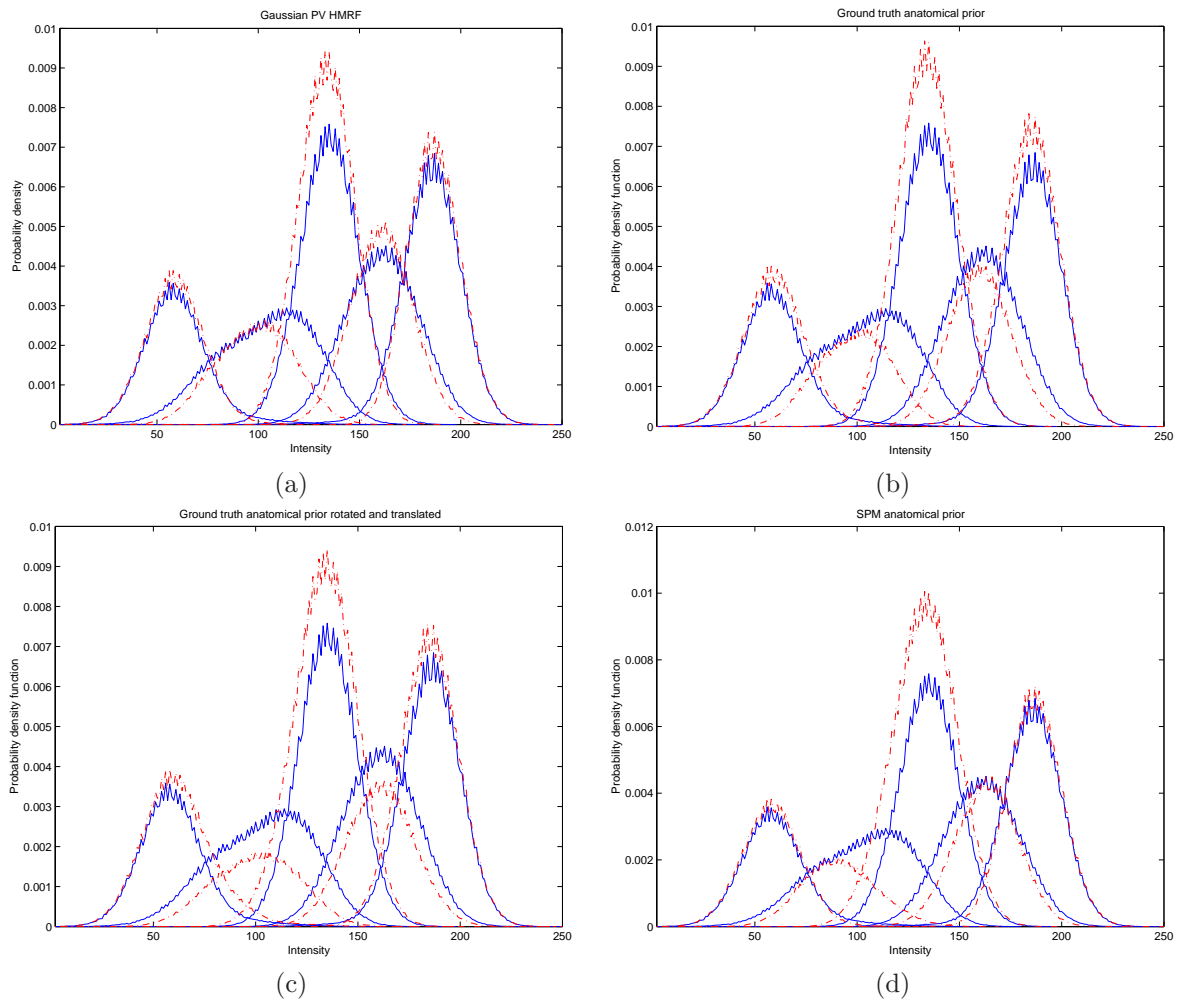


Figure 6.22: Histogram fitting of the phantom 7N20RF using atlas prior. Results are in dotted line. (a) Method D: GPV-HMRF. (b) Method D with GT. (c) Method D GTC. (d) Method D with SPM.

		Reference				
		CSF	CG	GM	GW	WM
D	CSF	90.5	10.8	0.1	0.0	0.0
	CG	9.1	57.2	4.7	0.1	0.2
	GM	0.3	31.9	84.4	18.8	0.3
	GW	0.0	0.1	10.8	66.3	10.6
	WM	0.0	0.0	0.0	14.8	88.9

		Reference				
		CSF	CG	GM	GW	WM
GT	CSF	99.1	10	0.1	0.0	0.0
	CG	0.4	61.3	0	0	0.2
	GM	0.2	28.7	99.9	10	0
	GW	0	0	0	74.1	0
	WM	0.2	0	0	15.9	99.8

		Reference				
		CSF	CG	GM	GW	WM
GTC	CSF	94.4	17.7	0.5	0	0
	CG	5.3	44.5	4	0	0.1
	GM	0.2	37.6	89	22.9	0.2
	GW	0.1	0.1	6.4	57.3	5.5
	WM	0	0	0	19.8	94.1

		Reference				
		CSF	CG	GM	GW	WM
SPM	CSF	89.8	10.1	0.1	0.0	0.0
	CG	9.9	56	4.2	0	0.2
	GM	0.2	33.8	85.6	20.2	0.3
	GW	0.	0.1	10.1	67.5	12.7
	WM	0.0	0.0	0.0	12.2	86.6

Table 6.9: Confusion table of the phantom 7N20RF using atlas prior.

	PerGood	PerFault	PerHalf+	PerHalf-
D	77.7	0.20	9.42	12.69
GT	87.65	0.12	3.81	8.42
GTC	76.44	0.32	10.13	13.10
SPM	77.45	0.19	9.93	12.43

Table 6.10: Percentage of total classification for the phantom 7N20RF with atlas prior.

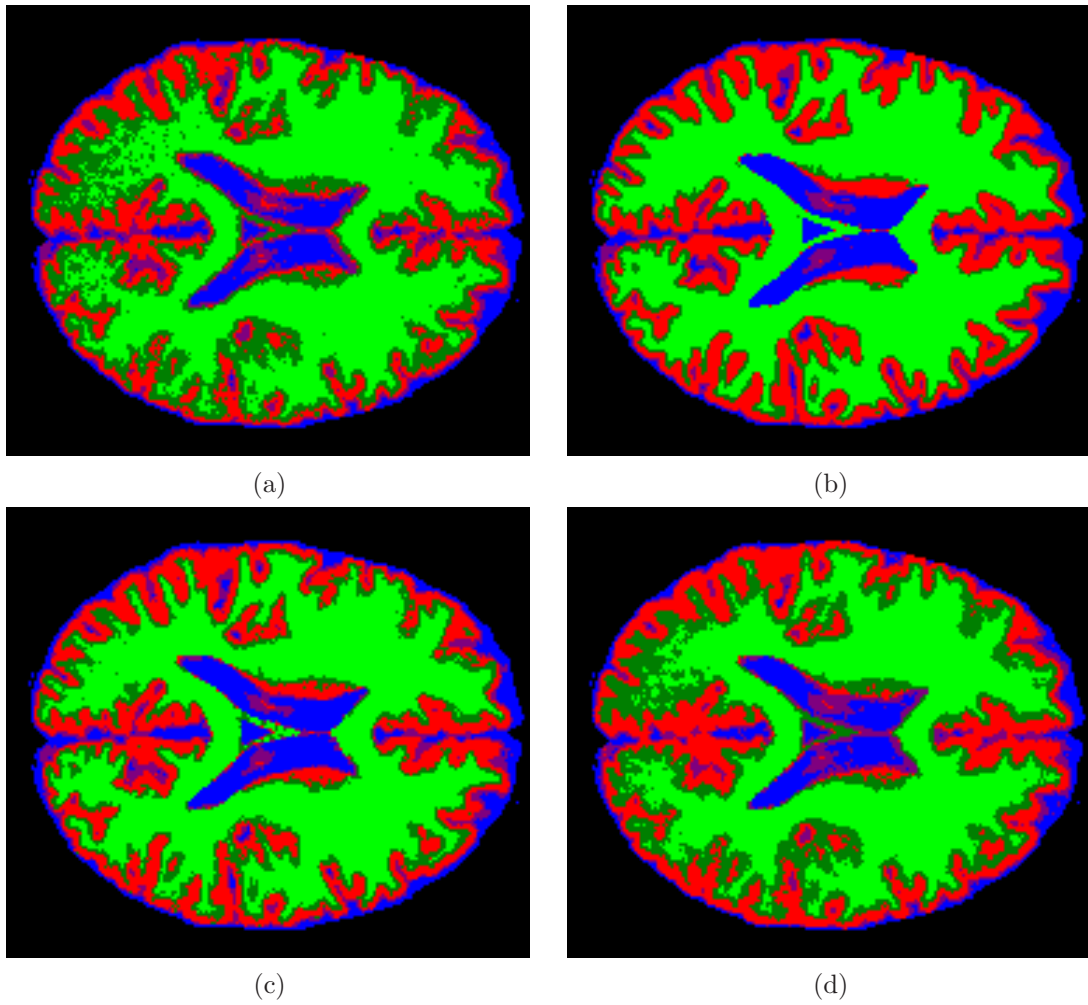


Figure 6.23: Classification image results of 9N40RF using atlas prior. (a) Method D: GPV-HMRF. (b) Method D with GT. (c) Method D GTC. (d) Method D with SPM.

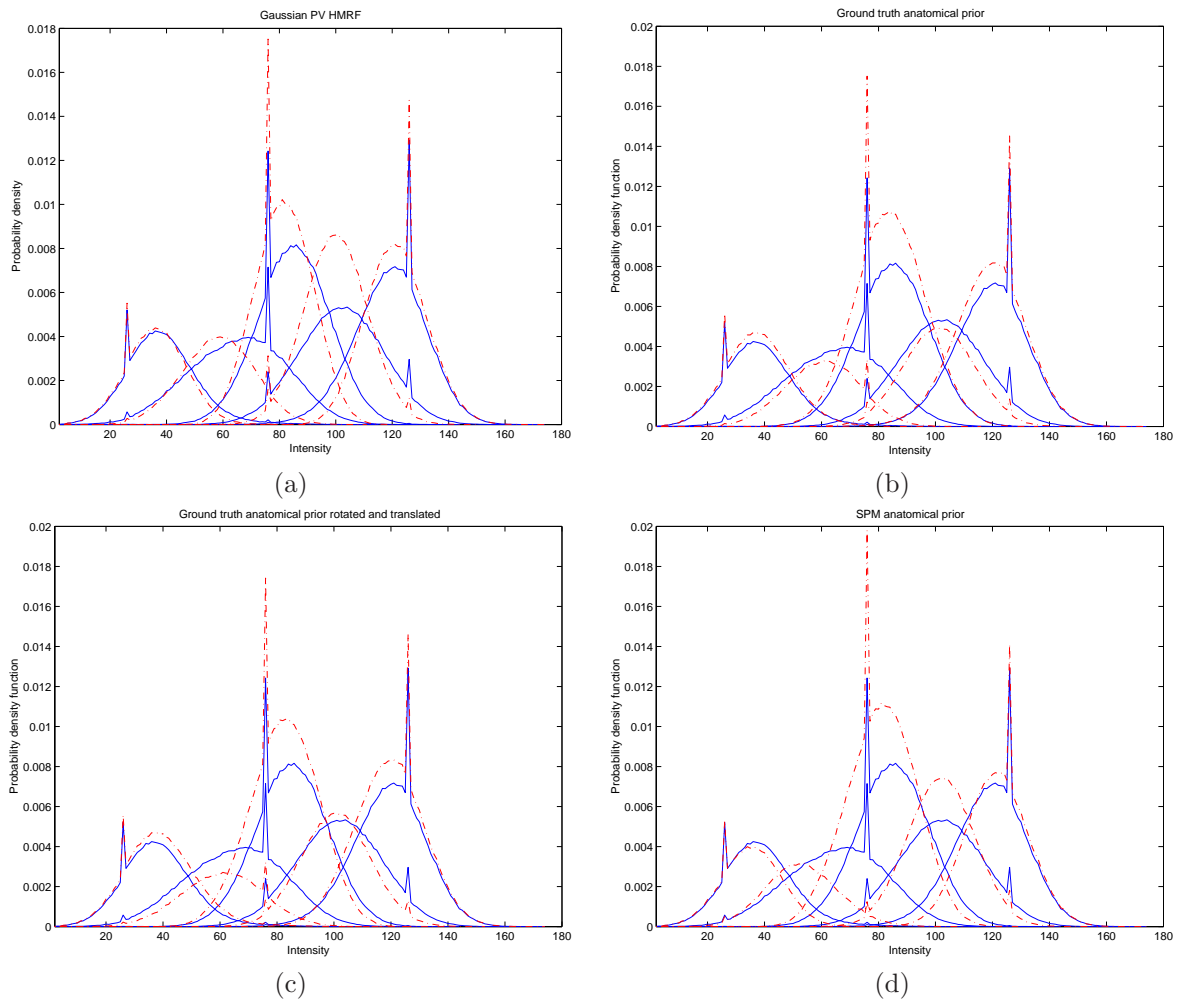


Figure 6.24: Histogram fitting of the phantom with 9N40RF using atlas prior. Results are in dotted line. (a) Method D: GPV-HMRF. (b) Method D with GT. (c) Method D GTC. (d) Method D with SPM.

		Reference							Reference						
D		CSF	CG	GM	GW	WM	GT		CSF	CG	GM	GW	WM		
		CSF	82.8	8.7	0.1	0.0		0.0		CSF	98.8	7.1	0.1	0.0	0.0
		CG	16.3	51.1	6.4	0.2		0.1		CG	0.3	60.9	0	0	0
		GM	0.7	37.6	64.7	16.9		0.3		GM	0.5	32	99.8	9.1	0.1
		GW	0.1	2.6	28.6	62.5		16.3		GW	0	0	0.1	76.6	0
		WM	0.0	0.0	0.2	20.4		83.3		WM	0.4	0.0	0.1	14.3	99.8

		Reference							Reference						
GTC		CSF	CG	GM	GW	WM	SPM		CSF	CG	GM	GW	WM		
		CSF	91.7	15.4	0.6	0		0		CSF	76.5	6.4	0.1	0.0	0.0
		CG	7.6	43.8	4	0.1		0.1		CG	22.7	38	1.2	0.0	0.1
		GM	0.1	39.8	80.3	19.5		0.2		GM	0.6	53.8	78.3	23.2	0.3
		GW	0.1	0.1	6.4	57.3		5.5		GW	0.2	1.9	20.4	60.7	17.6
		WM	0	0	0	19.8		94.1		WM	0.0	0.0	0.1	16	82

Table 6.11: Confusion table of phantom 9N40RF with atlas prior.

	PerGood	PerFault	PerHalf+	PerHalf-
D	68.36	0.79	10.41	20.45
GT	88.01	0.21	3.12	8.66
GTC	73.51	0.56	9.13	16.79
SPM	68.15	0.57	10.20	21.09

Table 6.12: Percentage of total classification for the phantom 9N40RF with atlas prior.

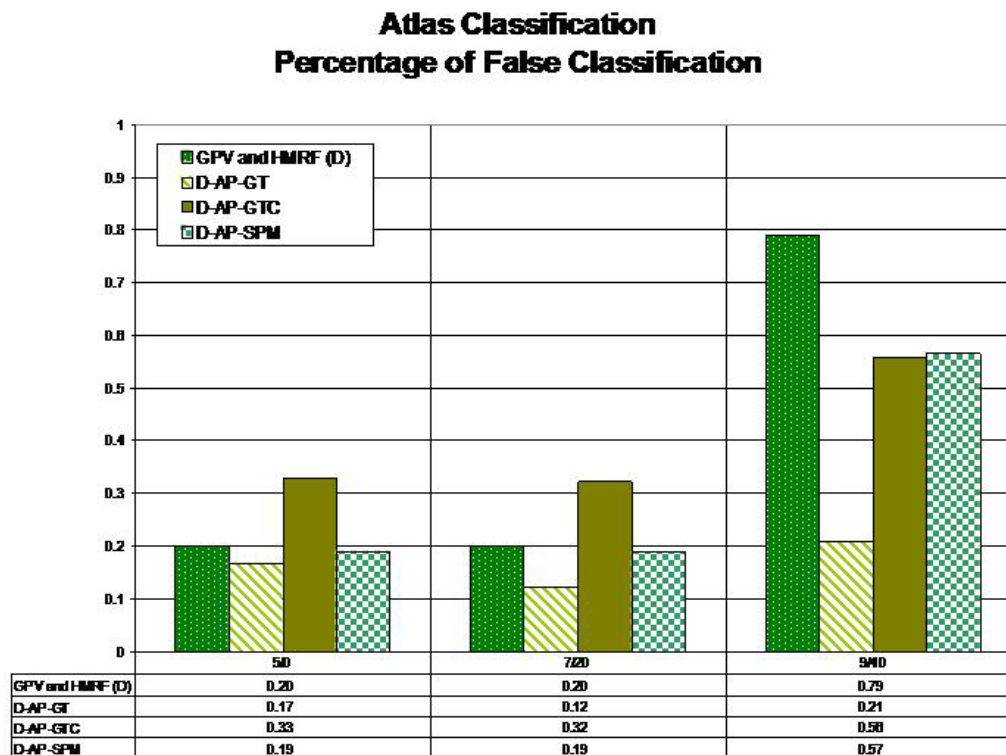
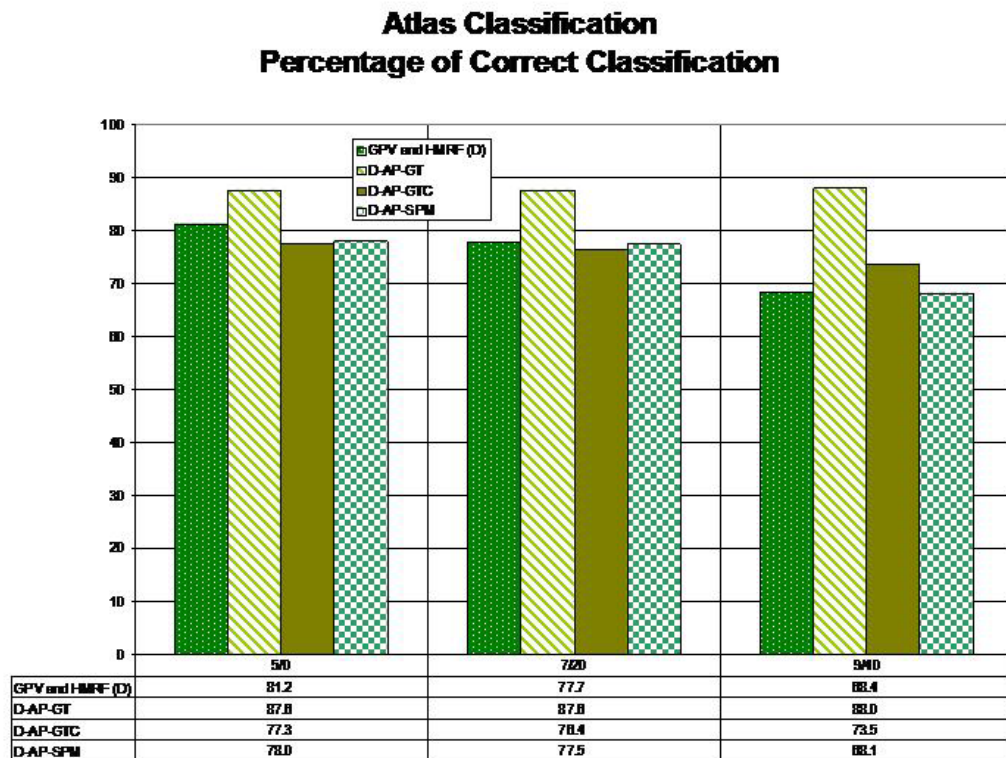


Figure 6.25: Percentages of classification of methods using atlas information.

Part IV

Applications

7

Potential applications

No! Try not. Do or do not. There is no try.

Yoda, "Star Wars: Episode V - The Empire Strikes Back"(1980).

7.1 Introduction

In this chapter, the concept of *evolution study* in medical image analysis is discussed. Then, two different approaches leading with this concept of change detection are presented: the static and the dynamic analysis. Also, two examples that exploit these ideas are shown: the cortical degeneration study is done using brain tissue segmentation, and the study of multiple sclerosis (MS) lesion evolution is performed by non-rigid deformation analysis. In the first case, a new method to detect the cortical degeneration is proposed and preliminary results are shown. In the second case, the study of MS evolution is made using the method proposed by J.-Ph. Thirion in [108].

7.2 In continuous evolution

In the previous chapters the concepts of *template*, *registration* and *classification* have been presented as key issues of medical image analysis. Also, important applications grouping these three disciplines have been proposed. In Chapter 4 and Chapter 5 the *atlas-based segmentation* of deep structures of the brain in either normal or pathological anatomy have been shown. Then, in Chapter 6, the *brain tissue segmentation* techniques including an *a priori template* information have been validated among other classification methods.

All these applications have the objective of performing *static* analysis of one single image. But, in some cases, there exists also the implicit idea of *evolution study**. Intuitively, since the human body is continuously changing, we would like to analyze it from a *dynamic* point of view, that is, to detect these changes and to study them afterwards to know if they are *normal*. The need of such an approach is much more evident in the case of many brain pathologies such as tumors, multiple

*It is assumed from now on that a set of sequence images are available for such a study.

sclerosis or degenerative diseases. In these cases, the key point is not only to detect but also to quantify and even characterize the evolving pathology. The evaluation of lesion variations over time can be very useful for instance in pharmaceutical research and clinical follow up.

There are two main approaches in the study of an evolutive process. The first one consists in performing a *static* analysis of each image forming the data set and, then, in comparing the results. That is denoted in this chapter as **static analysis**. However, another promising solution has recently emerged. It consists of analyzing the non-rigid transformation between the sequence of images instead of the images itself. This approach is denoted here as **dynamic analysis**.

7.2.1 Static analysis: image segmentation

The static analysis denotes here the study of an evolving process by means of the analysis of each image of the sequence. The object of interest, such as a lesion, is first segmented in each image. In some cases this segmentation is still performed manually which involves a time consuming and subjective procedure [40, 41]. But fast and automatic classification and registration techniques are emerging in order to improve the segmentation process [69, 120]. Then, the evolution process is quantified by computing the differences between the resulting segmentations. This of course requires an accurate segmentation of the objects of interest. Finally, the object *changes* are quantified, e.g. by counting voxels. An example of pathology evolution study using a classification technique is presented in Section 7.3.

Unfortunately, the influence of segmentation errors on the final results can be a critical point of the static analysis. Also, these methods are somewhat limited because they cannot represent the evolution but only quantify it.

7.2.2 Dynamic analysis: deformation field study

An emerging approach for evolving process study is the analysis of a non-rigid registration. As has been presented in Chapter 3, the common objective of all the non-rigid registration applications is to capture the morphometrical and morphological variability of the anatomy. Thus, a non-rigid transformation may also have medical significance since the transformation can be used to localize, quantify and represent anatomical variability.

A non-rigid transformation field can be for instance used to create both anatomical and deformation templates. Pioneer work in the creation of an average anatomical brain by means of the deformation field has been done in [48]. Later on, the concept of 3D *statistical deformation model (SDM)* has been presented in [95] which allows the creation not only of an average pattern of the brain anatomy but also a template of anatomical variability. Actually, SDMs are created by the statistical analysis of the deformation field recovered after non-rigid registration*. Finally, patterns of growth in developing brains are proposed by [112]. Then, these *deformation atlas* can be used to detect abnormal deformations (i.e. abnormal anatomy) or to guide a new deformation within the space of the deformation atlas .

The non-rigid deformation field can also be used for the quantification of *changes* between images. For instance, in [57, 80] intra-operative deformation is detected and quantified by means of non-rigid transformation. Non-rigid registration analysis is also used in the particular case of multiple sclerosis (MS) in order to detect and quantify this pathology evolution over time [93, 108]. An example of MS pathology evolution study by means of non-rigid registration is presented in Section 7.4. This

*SMDs are created following the same principle as the *active shape models (ASM)* or the *active appearance models (AAM)* [28, 105].

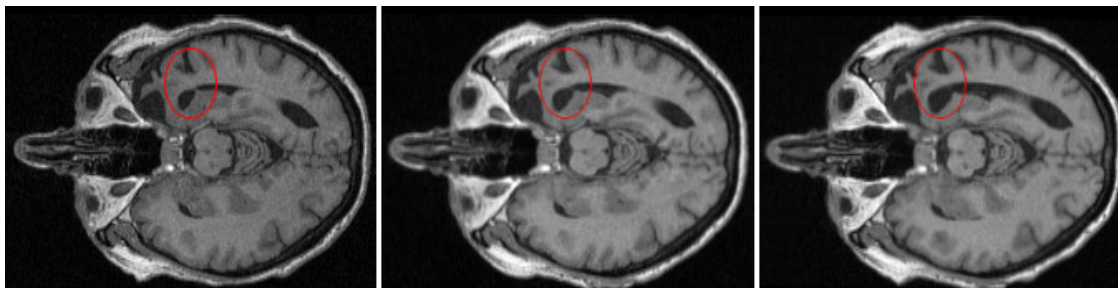


Figure 7.1: Cortical degeneration: sequence of T1-MR brain images original images after affine registration. The images are plotted according their evolution in time. From left to right: image 1, 2, and 3.

is just an illustrative example where the approach proposed by J.-Ph. Thirion in [108] is applied to our MS data set.

7.3 Gray Matter Degeneration

Cerebral degeneration is one of the most important families of neurological diseases containing for instance semantic dementia, Alzheimer’s disease or frontotemporal dementia, and it is also one of the most difficult pathologies to quantify objectively. Studies on patterns of brain atrophy in medical images are done mainly by two different approaches. The first consists of the manual detection and classification of a region of interest (ROI), leading to a time consuming and subjective procedure [40, 41]. The second and most used approach is the *voxel-based morphometry* (VBM) [5] which usually has the following steps:

1. the normalization of all the subjects into the same stereotaxic space,
2. the gray matter extraction and smoothing of the normalized images,
3. and, finally, the statistical analysis between an *a priori* reference data and the subjects.

In what follows, the method proposed in this thesis is explained. It is based on the VBM but as opposed to most existing implementation [39], it considers not only pure but also mixture tissue concentrations and does not use *a priori* statistical group knowledge.

7.3.1 Data set

The case of a 60-year old right-handed patient presenting primary progressive aphasia is presented here. The data set consists of 3 T1-MR images of that patient acquired through a 2-year period (see Figure 7.1). They are chronologically denoted as image 1, 2, and 3. Image size and resolution are $256 \times 256 \times 128$ and $1 \times 1 \times 1.3mm^3$. This case has been already studied by the experts. Thus, the gray mater degeneration area is known *a priori* and it has been outlined by a red contour in Figure 7.1. This makes the data set very well-suited for testing the automatic approach proposed here.

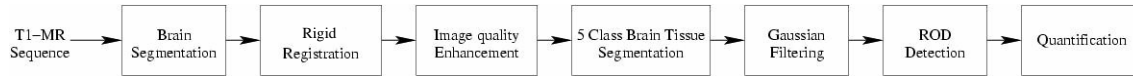


Figure 7.2: Block diagram of the proposed method.

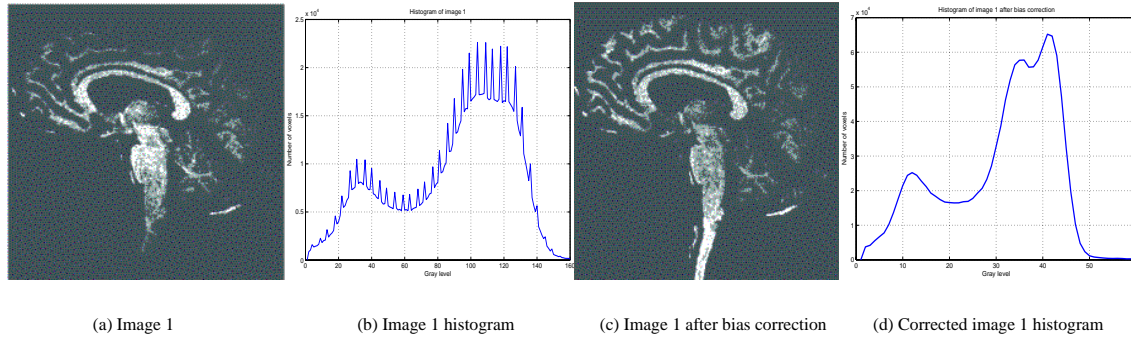


Figure 7.3: Inhomogeneity correction of the image 1.

7.3.2 Proposed method

As it has been said before, the method proposed in this work is based on the VBM theory. It differs though from the most existing implementation [39] in two main aspects. First, 5 tissue class (CSF,CG,GM,GW,WM) are taken into account into the classification step while usually only three main pure tissues are considered.

Instead of successively comparing each of the image sequence to an *a priori* statistical group knowledge, the evolving degeneration is only studied from the sequence images. The complete scheme of the method is presented in Figure 7.2.

Pre-processing

Some pre-processing of the input data is need. Brain segmentation (i.e. removal of scalp) is performed by morphological operations as presented in [100]. Then, the images are globally registered with the method presented in [29]. After that, inhomogeneity correction is done [5] because of a bias field present in the images, mainly in the image 1 (see Figure 7.3).

Brain tissue segmentation

The brain segmentation into the main tissues and their mixtures is performed by GPV-HMRF method as presented in Section 6.6.4. The brain tissue segmentation in the three main tissues only has though been applied also in order to compare it later with the use of 5 brain tissue classes. Results of both 3 and 5 classes segmentation of image 1 are presented in Figure 7.4(b) and (c).

The assessment of the classification is done visually. Classification using 3 classes tends to underestimate white matter tissue. This is clearly improved by 5 classes classification even if the classification could be improved. As it will be seen later, the quality achieved is good enough to detect and quantify the degeneration area.

The interest is not however in the final tissue classification but in the probability tissue maps. Thus, as GM degeneration is studied, CSF, CG and GM posterior probability maps are retained from the classification step (only CSF and GM in the case of 3 class segmentation). All the tissue

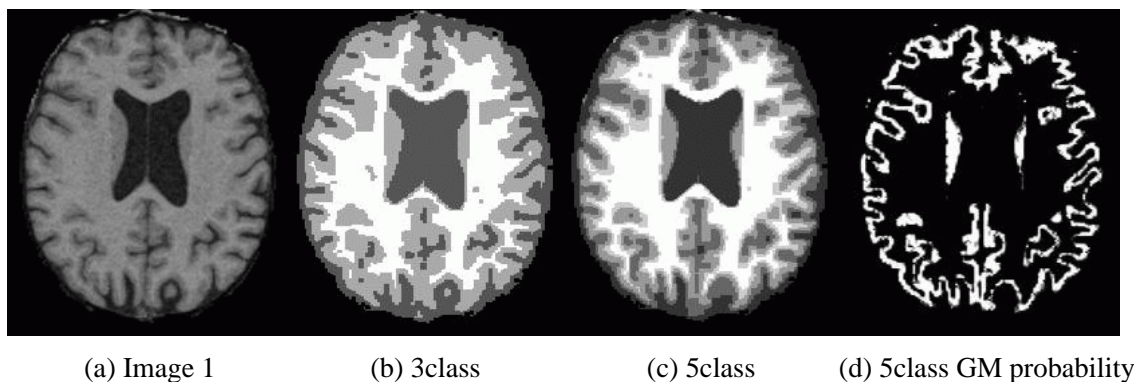


Figure 7.4: Brain tissue segmentation results of image 1. (a) Original image sequence. (b) 3 tissues classification. (c) 5 tissues classification. (d) GM probability map after 5 classes segmentation.

probability maps are re-scaled to a gray level from 0 to 255. Figure 7.4(d) shows the GM posterior probability of the sequence image 1.

Voxel based morphometry

As has been said before, the morphometry theory statistically analyzes the obtained results. A smoothing of the tissue probability maps by a large Gaussian kernel is applied for two main reasons:

1. to transform each voxel into a region of interest. Actually, by applying a Gaussian filter a voxel represents the mean concentration around the voxel of the corresponding tissue.
2. In the case of statistical studies, data distribution tends to be normalized by applying a Gaussian filter as the central limit theorem states.

Only the first point is justified in the method proposed here since no statistical study is actually done. So, each voxel is transformed into a region of interest representing the tissue concentration within this region. Now, the σ parameter defining the Gaussian filter has to be determined. Morphometry theory, as described in [5], suggests a standard deviation of a size similar to the size of the *changes* that are expected to be found. For the particular case of the image sequence under study, the value of $\sigma = 11mm$ has been empirically found. The resulting concentration of CSF, CG and GM maps for the image 1 segmented with 5 tissue classes are shown in Figure 7.5.

Detection and quantification of GM degeneration

The goal is to first localize and, then to quantify the brain regions where the GM has significantly degenerated. Since only a sequence of 3 volume images is available, the statistical analysis proposed in [5] and used for instance in [46] is not possible. Thus, the different tissue concentration maps of the sequence images are compared two-by-two in order to produce what is denoted here as a *degeneration* map. Let us define the GM degeneration map as

$$D_{i,j} = \prod_t |C_i^t - C_j^t|, \quad i \neq j \quad (7.1)$$

where C_i^t is the concentration map of tissue t at time i , for $t \in \{\text{CSF}, \text{CG}, \text{GM}\}$, $i, j \in \{1, 2, 3\}$, and $D_{i,j}$ shows the regions with more probable gray matter loss between images i and j . The

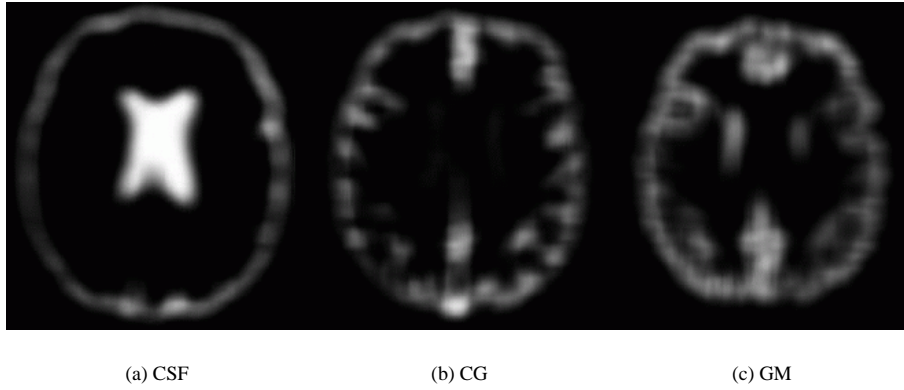


Figure 7.5: Smoothing of CSF, CG partial volume and GM posterior probabilities after 5 tissue classification.

obtained degeneration maps can contain some regions that actually do not correspond to a real GM degeneration. However, the most important regions of degeneration (ROD) can be isolated by simply thresholding $D_{i,j}$. This is shown in Figure 7.7 where the *a priori* known ROD has been perfectly localized. Further analysis and discussion of the resulting GM degeneration maps using either 3 or 5 tissue segmentation is done in Section 7.3.3.

Once the candidates of the GM degeneration region have been detected it would be necessary to quantify the degeneration within these regions in order to discriminate the possible errors from the real degenerative regions. The quantification in a ROD is done by simply computing

$$Q_{i,j} = \sum_{k=1}^{N_{ROD}} D_{i,j}(k), \quad i \neq j, \quad i, j \in \{1, 2, 3\}, \quad (7.2)$$

where N_{ROD} is the number of voxels within the ROD.

7.3.3 Results

As has been presented in the previous section, maps of possible GM degeneration areas can be obtained by comparing the sequence images two-by-two. Figure 7.6 shows the same slice of all the possible GM degeneration maps $D_{1,2}$, $D_{2,3}$, and $D_{1,3}$. The first row shows the original sequence of images after affine registration, the second and third rows present respectively the D maps obtained after 3 and 5 brain tissue segmentation. Note that in the case of 3 class segmentation only C^{CSF} and C^{GM} are considered. All D maps have succeeded in localizing the *a priori* known degeneration area. However, D maps that use only C^{CSF} and C^{GM} are less precise in delineating the *candidate* regions than the maps that add the PV information. It is assumed also that the GM degeneration will be better captured by using the two sequence images most separated in time. Thus, the degeneration map $D_{1,3}$ obtained with C^{CSF} , C^{CG} , and C^{GM} has been chosen for further ROD analysis.

Figure 7.8, Figure 7.9 and Figure 7.10 show the most important RODs detected in $D_{1,3}$. The red circle marks the known *a priori* temporal lobe GM loss and very well-extracted by the proposed algorithm. There are though other brain areas where a possible GM degeneration has been detected. These regions are outlined by a green circle. These new areas should be carefully inspected by the experts to determine if a loss of GM is really produced. Also, other regions appear as possibly having a GM loss while they have not: the remainder of the skull, 3th ventricle or brain to cerebellum

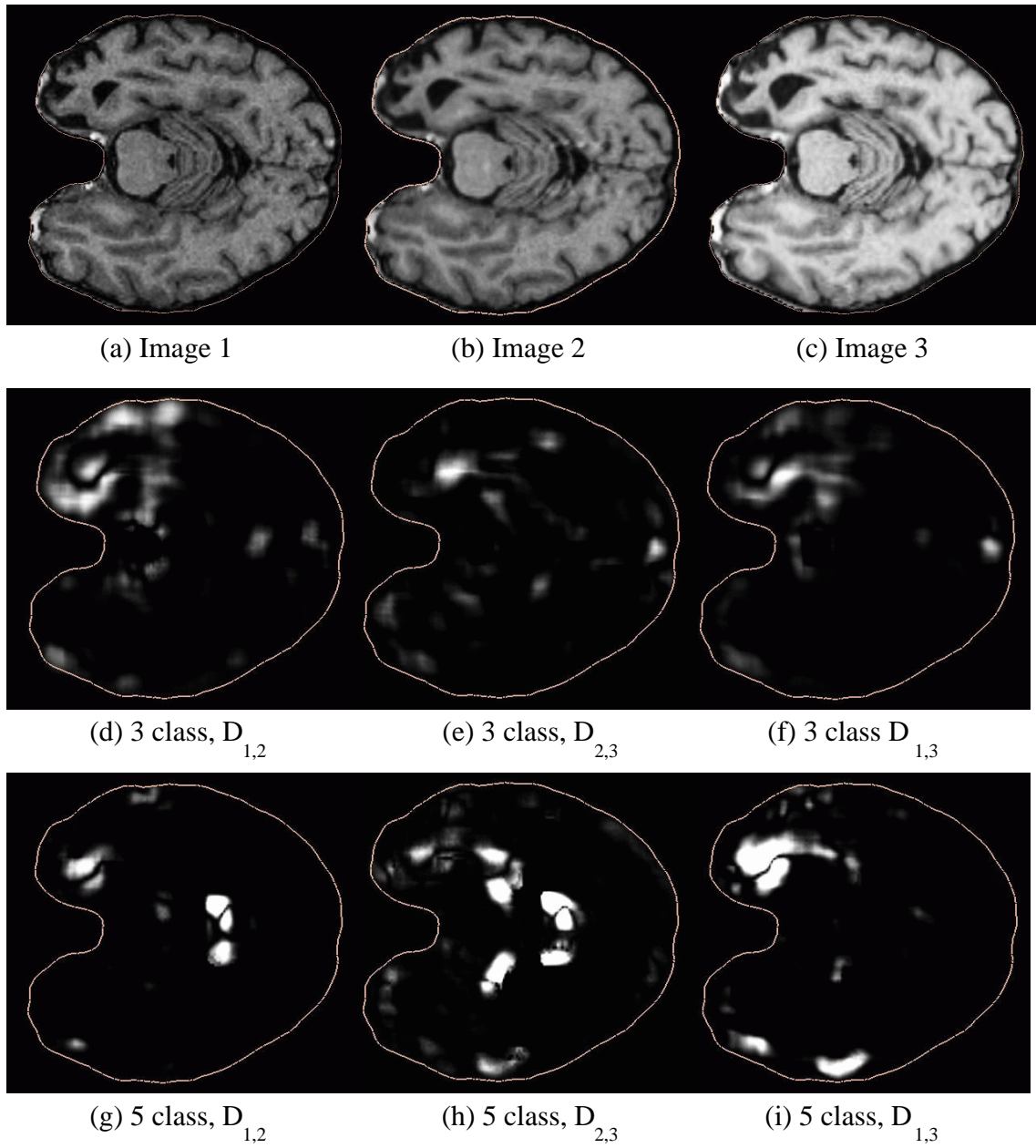


Figure 7.6: GM degeneration maps.

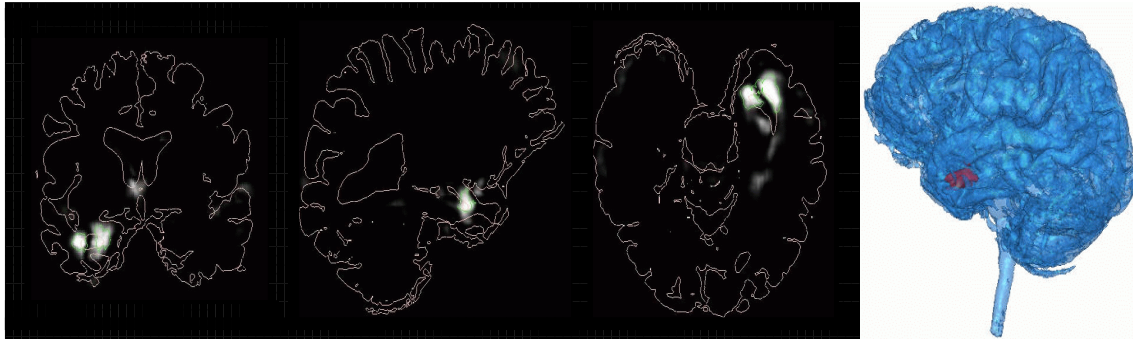


Figure 7.7: Region of degeneration found after threshold of $D_{1,3}$ using CSF, CG and GM probability maps.

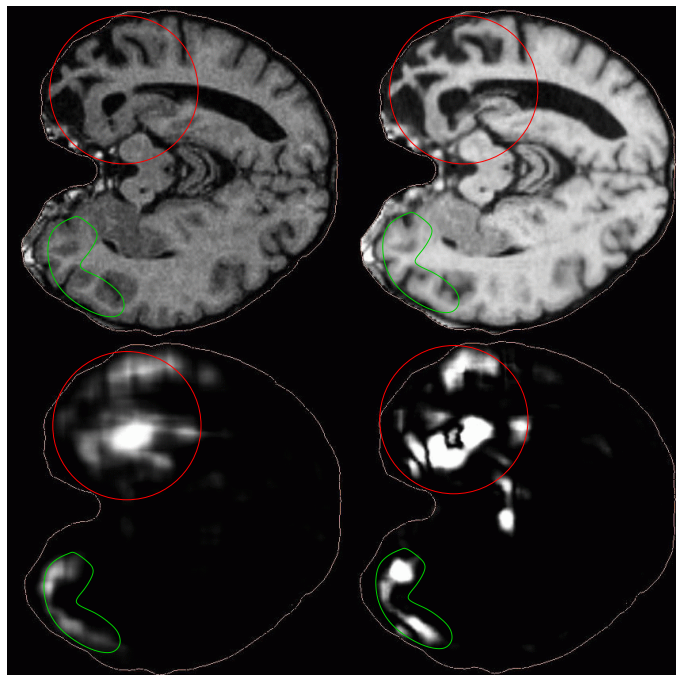


Figure 7.8: Candidate to degeneration region 1. Top: sequence image 1 and 3. Bottom: Results of the proposed method using 3 tissue and 5 tissue types classification. The *a priori* known ROD is in red. The new candidates to ROD are in green.

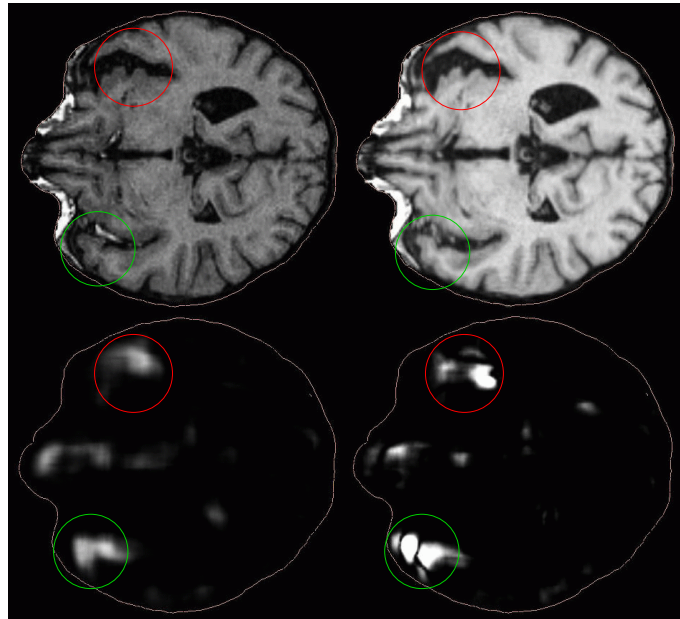


Figure 7.9: Candidate to degeneration region 2. Top: sequence image 1 and 3. Bottom: Results of the proposed method using 3 tissue and 5 tissue types classification. The *a priori* known ROD is in red. The new candidates to ROD are in green.

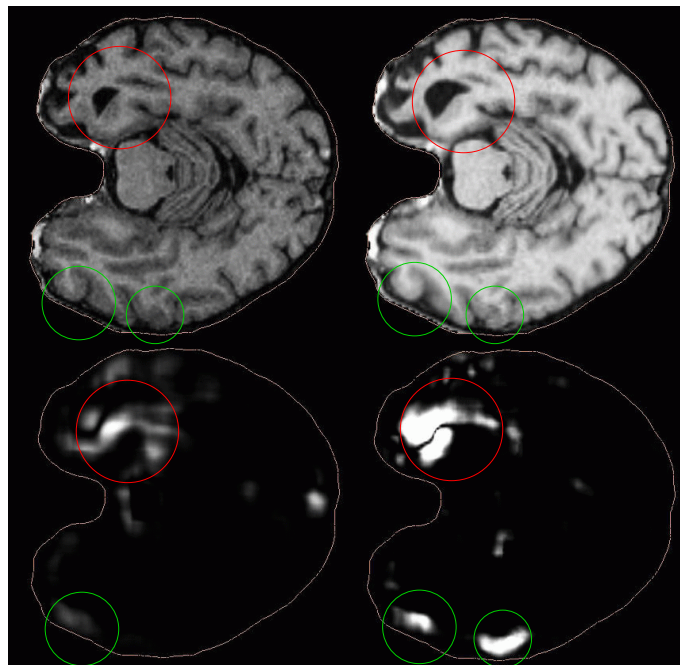


Figure 7.10: Candidate to degeneration region 3. Top: sequence image 1 and 3. Bottom: Results of the proposed method using 3 tissue and 5 tissue types classification. The *a priori* known ROD is in red. The new candidates to ROD are in green.

interface. These regions are however easily eliminated by thresholding since they are much less important than the others.

Finally, the degeneration has been quantified in the most important ROD for all frames: $Q_{1,2} = 16 \times 10^6$, $Q_{2,3} = 28 \times 10^6$, and $Q_{1,3} = 133 \times 10^6$. Thus, it is shown how the degeneration has accelerated over time, which is major diagnostic and therapeutic information for the physicians. This result has been validated both in comparison with the clinical evolution of the patient and by a careful visual inspection of the images. However, these quantitative measures are relative to this patient only. Consequently, to really assess how pathological this degeneration is, it should be compared with gray matter evolution in a *normal* subject.

7.3.4 Discussion

A method to detect and quantify brain atrophy has been presented. The approach we propose has been applied to a real patient presenting gray matter degeneration and it has been able to detect the region where the brain atrophy appears. The quantification measures have efficiently characterized the gray matter atrophy showing an acceleration of the degeneration process over time. However, these quantitative measures are relative to this patient only. Consequently, to really assess how pathological this degeneration is, the comparison with the Q evolution in *normal* subjects should be made.

Note that the size of the region of degeneration depends on the σ of the Gaussian filter. Voxel-based morphometry theory suggests that σ should correspond to the size of the differences we are looking for. However, here, the choice has been done empirically.

It has been shown that the use of CSF, CG, and GM tissue information makes the method more robust when faced with classification errors compared to only using CSF and GM probability maps. However, a deep study on the robustness of the algorithm is still needed. In a future study, the influence of registration, brain segmentation and classification errors as well as noise and image inhomogeneities should be analyzed.

7.4 Multiple Sclerosis

In this section, an example of deformation field analysis in the particular case of MS is shown. This example illustrates only a part of the pioneer works of Thirion et al in [108]. In the method applied here, the main idea is to avoid the difficult problem of precise delineation in two sequence images. Instead, in this approach, a less precise ROI is detected in one single image of the sequence. Then, a volume variation profile along the distance to the center of the lesion is applied.

7.4.1 Data set

The sequence of MS images used here have been previously used in section Section 4.3.5. Two T2-weighted MR brain images of $256 \times 256 \times 64$ voxels with $0.92 \times 0.92 \times 3mm^3$ voxel size form the data set. These images are denoted by the indices 1 (reference image) and 2 (floating image). They are of the same patient and they show evolving multiple sclerosis where image 2 was acquired about one year after image 1. Manual segmentation of the two images is also available. The lesions have been outlined by the expert (around 15) and only few of them are actually active. Figure 7.13 shows some of the lesions present in image 2 where the red contour is the manual segmentation of the lesions at time 1 and the green contour is the manual segmentation at time 2. Among all the segmented lesions, only 7 nodules are considered as evolving lesions since they have either appeared or grown in image 2 with respect to the image 1.

7.4.2 Method and results

The method used here can be summarized in four main steps. First, a rigid registration [19] of the two successive images is done. Second, a local non-rigid registration field is computed using the demons algorithm (Section 3.4). The analysis of a deformation field usually implies the use of some operators on the transformation which are briefly described in the following section. Lesion localization is done thanks to this analysis that leads to a region of interest (ROI) containing the detected evolving lesions. Finally, the volume variation is quantified by computing a lesion variation profile.

Mathematical operators

The operators presented here are separated into two categories. On the one hand, the *vector field operators* or geometric operators such as Jacobian or divergence, that are directly related to the volume variation and can therefore detect an expanding or shrinking processes. On the other hand, the *intensity operators* such as the norm, gradient or laplacian operators, that are closely related to the intensity of the displacement vectors and can therefore be used to detect uniform displacement areas or maximum amplitude areas, that could be associated to evolving lesions. Some examples of these operators are shown in Figure 7.11.

The **Jacobian** operator of the deformation field $\vec{D} = (D_x, D_y, D_z)$ is defined as

$$J(\vec{D}) = \begin{pmatrix} \frac{\delta D_x}{\delta x} + 1 & \frac{\delta D_x}{\delta y} & \frac{\delta D_x}{\delta z} \\ \frac{\delta D_y}{\delta x} & \frac{\delta D_y}{\delta y} + 1 & \frac{\delta D_y}{\delta z} \\ \frac{\delta D_z}{\delta x} & \frac{\delta D_z}{\delta y} & \frac{\delta D_z}{\delta z} + 1 \end{pmatrix}. \quad (7.3)$$

It is useful to recall a physical interpretation of the Jacobian operator in terms of the local variation of volume. The following relationship holds between the Jacobian of the displacement vector field and the local volume variation: when $\det(J(\vec{D})) \geq 1$, there is a local shrinking at point P, and when $\det(J(\vec{D})) \leq 1$ there is a local expansion at point P.

The value of the **divergence** of the deformation field (see Eq. (7.4)) has no simple physical meaning even if the sign of the operator gives information about shrinking (negative values) or expansion (positive values).

$$\text{div} \vec{D} = \left(\frac{\delta D_x}{\delta x} + \frac{\delta D_y}{\delta y} + \frac{\delta D_z}{\delta z} \right). \quad (7.4)$$

As we have no physical interpretation of the value, it is difficult to automatically threshold the resulting image to extract the regions of interest. Therefore, this operator should be used in combination with an intensity operator such as the norm operator.

The **norm** is the more intuitive operator that allows a simple analysis of the displacement vector field. Indeed, it is easy to segment regions with large or small displacement norm. Another possibility is to segment values that correspond to the expected displacement norm for a given situation. For example, in multiple sclerosis pathologies we expect expansion or shrinking processes to be in a 1 to 5 millimeter interval.

Lesion localization

The lesion is localized by combining the information obtained by the operators presented above. Thirion et al proposed in [108] to combine the norm of the transformation with the divergence. This is actually very intuitive since we are interested in extracting the areas presenting large deformations but also, since MS nodules have a rather special shape, places where the divergence is high. But also

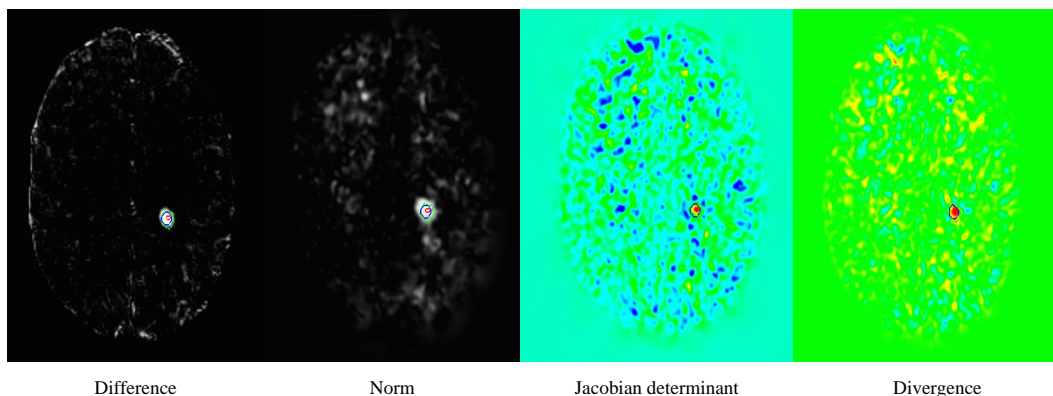


Figure 7.11: Mathematical operators on either original images (intensity difference) and deformation field (norm, Jacobian and divergence).

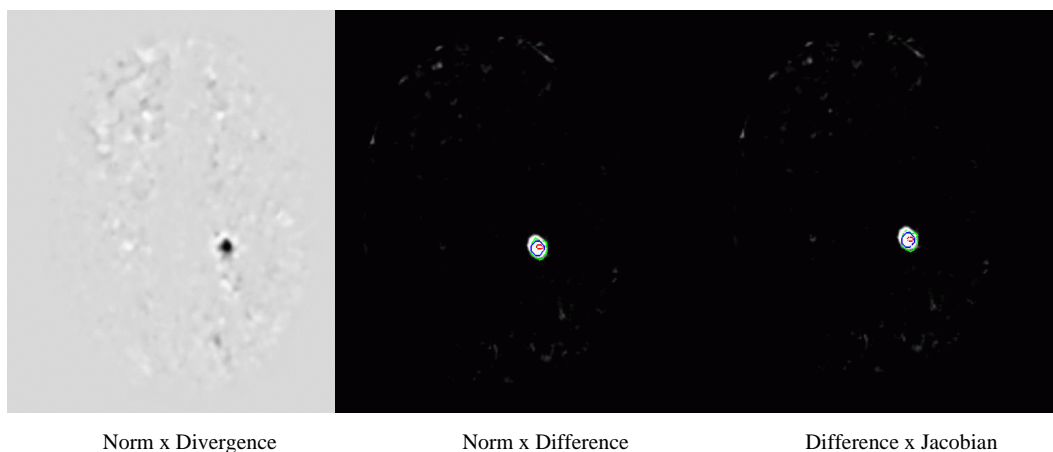


Figure 7.12: Selection of the regions of interest: threshold on the mathematical operators.

other combinations have been tested successfully. For instance, combining image intensity evolution (difference image) with the Jacobian determinant. Results are shown in Figure 7.12.

A threshold is applied to the operator $Difference \times Jacobian$ to extract the most important regions which are the candidates of having an evolving lesion named ROIs. Here, this threshold is empirically chosen (see the blue contour in Figure 7.11, Figure 7.12, Figure 7.14, and Figure 7.16). Five lesions have been correctly defined as active lesions (Figure 7.14), three lesions have not been detected (Figure 7.15), and two regions have been detected as having a lesion but they have not been detected by the experts (Figure 7.16). Actually, they can be discarded as being multiple sclerosis since they are not placed at the white matter.

Lesion quantification

The method proposed in [108] to compute a profile of the lesion volume variation is based on the integration of the vector field for a set of concentric shapes, either spherical or defined by a set of iso-contours. For its simplicity, the method of *concentric spheres* is used here. It is assumed that the center of the lesion can be defined and that only one lesion is present at every ROI. Then, a group

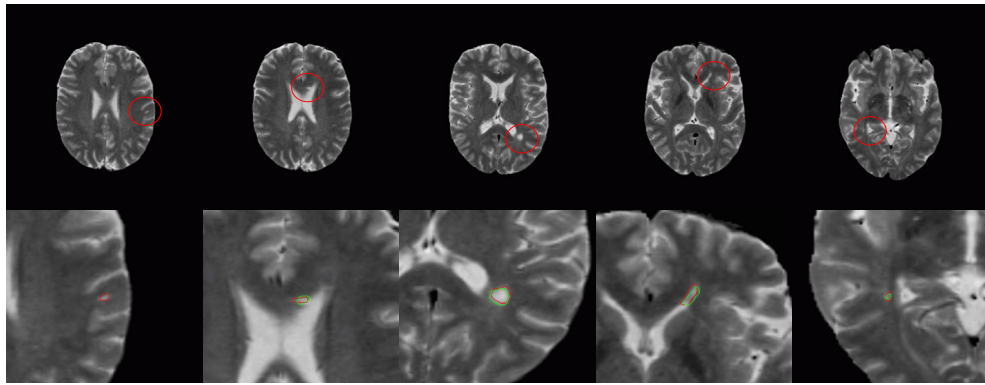


Figure 7.13: Contours are outlined on image 2. Manual segmentation of image 1 in red. Manual segmentation of image 2 in green. Not evolving lesions.

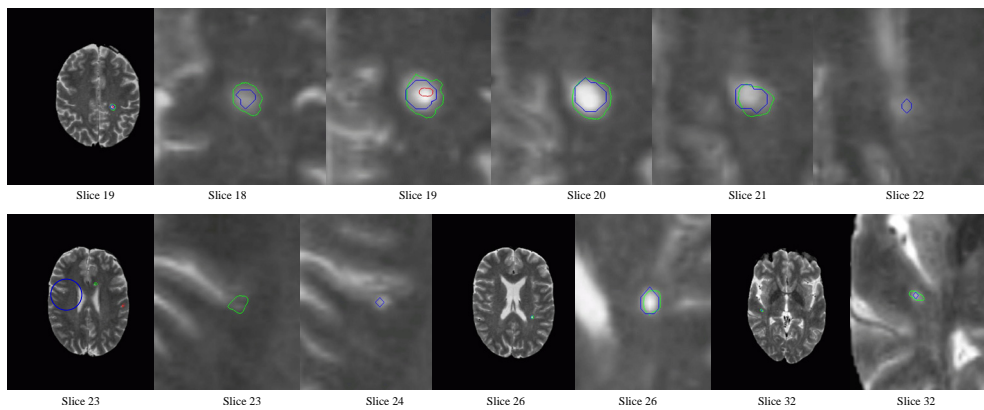


Figure 7.14: Evolving lesions: automatically detected.

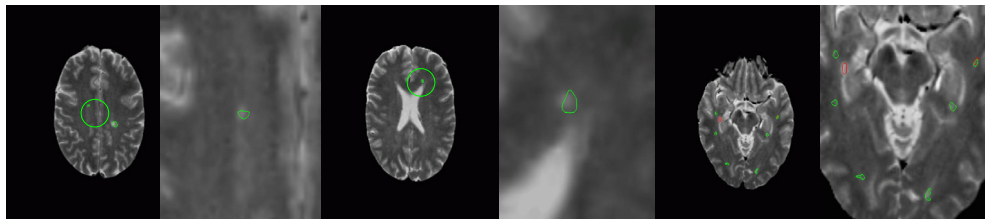


Figure 7.15: Evolving lesions: not detected.

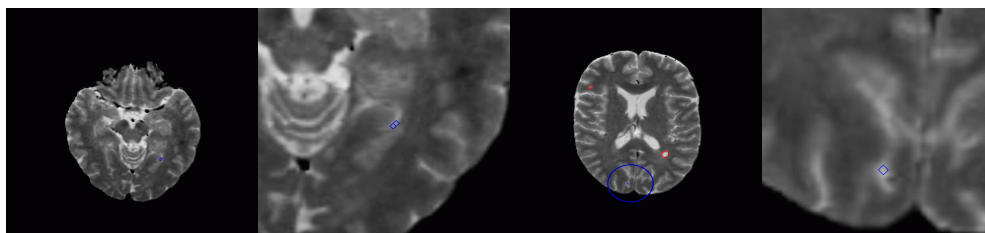


Figure 7.16: Candidates to lesion or false alarms.

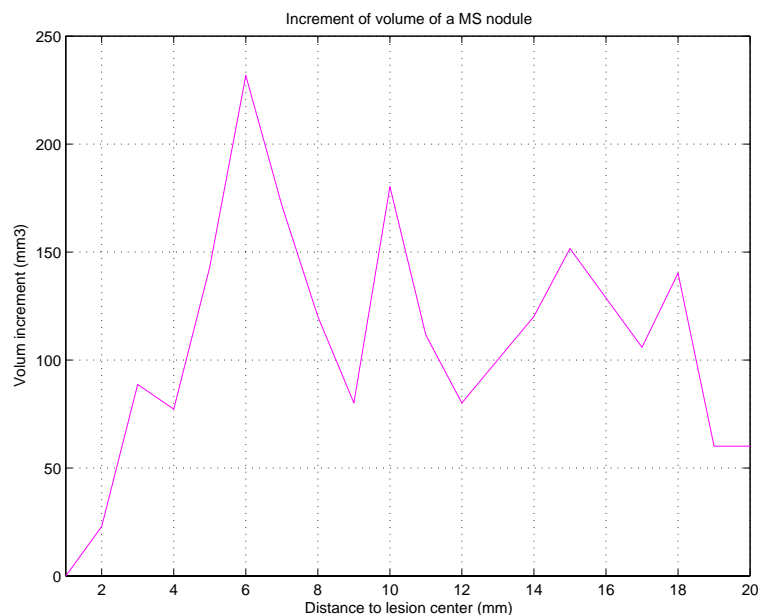


Figure 7.17: Lesion increment volume profile of the lesion present from slice 19 to slice 22 shown in Figure 7.14.

Lesion	Increment of Volume	
	$\Delta V_{spheres}$	ΔV_{seg}
slice 19	225	380
slice 24	25	50
slice 26	125	74
slice 32	25	34

Table 7.1: Increment of the active detected lesions. Values are in mm^3 . $\Delta V_{spheres}$ denote the estimated value from the stochastic computation in concentric spheres. ΔV_{seg} denotes the value computed from the manual segmentation masks.

of concentric spheres large enough to contain the lesion are defined. Here, the radii are arbitrarily set from 1 to 20 mm. Finally, the quantization of the lesion volume increment is made for every radius by stochastic computation (the difference between the total number of voxels of the original grid and of the deformed grid within each radius is computed) which gives a profile of the lesion volume variation. Then, in order to get a single value of volume variation, the maximal value of the profile is computed which approximates the real volume increment.

An example of volume increment profile is shown in Figure 7.17 and the quantification results for the detected active lesions are shown in Table 7.1.

7.4.3 Discussion

The main idea of the approach presented in [108] is to use the analysis on a 3D deformation field to first detect the active lesions and then evaluate their volume variations. Rather than a single value of volume variation, the method provides a volume *profile*. An example of the approach they proposed is presented here. The obtained results are discussed in what follows. First the lesion

localization and then the quantization are reviewed.

The results show that some areas of active lesions have been missed even if some lesions have been successfully detected and other regions have been detected as false alarms. This is mainly due to the noise. But also other regions where large deformations have been detected (for instance to compensate rigid registration errors or intensity-correspondence errors) can mask the information we are interested in. A prior estimation of the norm of the transformation field that is expected in the case of MS nodule deformation could be introduced in the localization procedure to improve the results. Also, the masking of the brain areas where the lesions are supposed to appear, that is the WM, could be applied. However, the *a priori* knowledge of the physician is indispensable to corroborate or eliminate the regions detected automatically after the threshold of the mathematical morphological operators.

Once the ROI are detected the profile of the volume increment is computed for each active lesion. It is demonstrated in [108] that this profile is more robust than the static segmentation at each image sequence in the case of tissue deformation (i.e. when surrounding tissues have been deformed because of the lesion growth) while static segmentation performs slightly better in the case of tissue transformation (i.e. change in tissue intensity). It is however difficult to validate these results in the example presented here since only manual segmentation, subject to errors, is available. It has been found that deformation field analysis estimates a slightly lower lesion volume increment than manual segmentation. Unfortunately further conclusions cannot be obtained from these results. A more accurate segmentation process should be applied and a careful inspection of every lesion should be made by the experts.

Last, but not least, the effect of the σ parameter of the demons algorithm regularization step in the volume increment profile computation is not clear. Note that the *real* deformation field is smoothed at each iteration by a Gaussian filter. Then, the computation of the volume variation profile and the final estimation of the volume increment are dependent on the σ value that is chosen.

7.5 Summary

The concept of *changes* is centered in this chapter. Two different approaches have been presented here denoted by *static* and *dynamic* image analysis. Both static and dynamic approaches are illustrated with an example: the gray matter degeneration study is done using the brain tissue segmentation, and the study of multiple sclerosis evolution is performed by non-rigid deformation analysis.

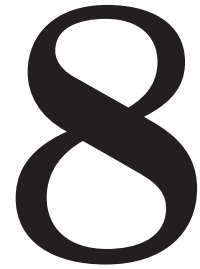
In the static image analysis, the objects of interest are segmented (manual, semi-automatic or fully automatic) in each image of the sequence. Then, they are compared frame by frame. These methods usually need an accurate segmentation at each frame and they are usually limited to the intensity changes in the sequence images, that is, only tissue transformation is usually considered.

Deformation analysis is a dynamic approach that tries to overcome these limitations. It has been seen that methods working with the deformation field analysis are more robust since they are able to capture not only tissue transformation but also the deformation usually induced by the lesion. Also, these approaches have demonstrated their usefulness not only to detect and quantify the lesions but also to encode the anatomic variability of the brain and the patterns of deformation.

Part V

Conclusions

General conclusions



*Where the Lord closes a door,
somewhere He opens a window.*
Maria, "The sound of the music" (1965).

8.1 Introduction

In this chapter we review the most important issues and contributions of this thesis. Following this we discuss possible future directions.

8.2 Review of the discussed topics

Among all the medical image modalities, the potential of Magnetic Resonance (MR) imaging has been shown. Also, the importance of the *a priori* information encoded in the brain atlases has been put in evidence with their wide range of possible applications. The registration techniques are proposed to efficiently combine all these image modalities and a general formulation of the medical image registration problem has been presented.

Atlas-based segmentation is presented in this work as one of the most important ways of using prior anatomical templates. It has been seen how the complex task of segmentation is finally reduced to a non-rigid registration problem between a subject and an atlas. Then, the problem of using atlases in some particular cases is also presented. For instance, there are some cases where some structures, such as a tumor or minor sulcus, are present in the subject but not in the template since the templates are defined to represent the anatomy of the majority of individuals.

The inclusion of a priori atlas information is also presented through a validation study on MR brain tissue classification techniques. Both parametric and non-parametric approaches have been assessed. Intensity-based classification methods are compared to the techniques that add the spatial prior to the intensity information. The effect of considering prior class templates has been finally analyzed in comparison to the spatial local information.

The last issue discussed in this thesis is the idea of *detection of anatomy changes*. Two different approaches have been presented that deal with this concept denoted here as *static* and *dynamic* image analysis. Each of the approaches is illustrated with an application. Dynamic image analysis is presented as a promising research area. It can be a useful approach not only to detect and quantify the lesions but also to encode the anatomic variability of the brain and the patterns of brain deformation.

8.3 Achievements

1. The demons algorithm has been proposed for non-rigid matching. Then, the solutions used in this work to overcome its limitations have been briefly presented. A complete analysis of the demons algorithm input parameters is done. First, different criteria for demon points selection have been presented in order to minimize the effects of the noise to the final transformation. Second, a simply study on the algorithm elasticity has been shown which are the values of σ that are able to compensate anatomical variability. Third, a stopping criterion that performs a good trade-off between the MSE minimization and the computation time has been proposed.
2. A new approach for atlas-based segmentation in the presence of large space-occupying tumors which makes use of a simple model of tumor growth has been proposed. This new method is advantageously compared to the most similar methods found in the literature. It has been shown that the limitations of other methods can be overcome thanks to the use of an *a priori* model, and that a good match is obtained in pathological brains, even when some structures have been drastically altered by the presence of a tumor. Also a new validation method to analyze not only the lesion growth but also the most probable origin of the tumor has been proposed.
3. A validation of brain tissue classification techniques using a whole range of prior information, i.e. intensity, spatial and template information, has been proposed. The robustness and accuracy of some of the most used unsupervised classification methods have been assessed. Then, it is easy to specify the most suitable tissue classification technique depending on the different conditions that could be encountered in T1w-MR brain image.
4. A method to detect and quantify the brain atrophy has been presented. The approach we propose has been applied to a real patient presenting gray matter degeneration and it has been able to detect the region where the brain atrophy appears. The proposed quantification measures have efficiently characterized the gray matter atrophy showing an acceleration of the degeneration process though time.

8.4 Future directions

In what follows, some ideas and new issues are presented as possible lines of future research.

8.4.1 Prior knowledge to guide the registration

Atlas-based segmentation is a good example of how the *a priori* knowledge contained within an atlas can be efficiently profited from to improve the segmentation of the structures of interest in a MR brain image. Another attempt to use this prior information is done in the classification of brain tissues. There, the prior statistical tissue template is used to guide the spatial distribution

model. In these two key applications, prior knowledge can be exploited thanks to the registration step. Then, the idea of including prior information directly in the registration method arises.

It has been seen that the objective of a transformation that registers one image into another one is to optimize some global correspondence (like grey level difference or correlation, statistical or information theoretical measures, etc.), and most of the time the only geometrical constraint on the transformation is its smoothness, ensured by the shape and size of the interpolation or smoothing functions (typically Gaussian) used. But no a priori constraint is imposed to ensure that the transformation is realistic. However, to achieve robust and reliable brain registration we clearly need to constrain the deformation to respect the brain anatomy. Otherwise we can obtain a registration where the grey levels of the two images perfectly correspond, but where the underlying transformation is hieratic. As an extreme example, in such a case a "good" registration algorithm could succeed in registering a brain onto an apple, which is obviously not desirable in terms of reliability.

Intuitively, prior information about the deformability of brain tissue and structures could better guide the registration. In a first step, the natural shape variability of deep brain structures should be analyzed using, for instance, a database of deep brain structures (ventricles, thalamus, putamen, etc.), shapes, relative positions and allowed deformability. Then, the registration might be constrained with respect to this variability: the atlas image will be registered to the patient image by a transformation that will have to maximize the image similarity measure and, at the same time, to keep the transformation field smooth and within the space of the studied deformations, and segmenting shapes that have an admissible shape and relative position, as learned by the previous step.

8.4.2 Atlas-based segmentation of pathological brains

Actually, some of the limitations of the proposed atlas-based segmentation method in the case of pathological brains should be eliminated if prior knowledge of the deformability of some structures is included in the registration itself. Special effort should be made in studying how to better define the possible deformation of a brain under the growth of a tumor, mainly taking into account the deformability characteristics of the different brain structures like the brain matter, the ventricles or the intra-hemispheric dura. In the same way, a deformation analysis of the tumor growth could be included in a more evolved model of lesion growth. Of course, data sets of evolving tumors should be indispensable to do that. Finally, the study of how to model the lesion and brain deformation in case of other lesions like large presence of edema, infiltrated tumors or Cerebral Vascular Accidents could let the proposed atlas-based segmentation method used to these other pathologies.

A validation method has been also proposed in order to assess the proposed model of lesion growth. Unfortunately, only one image was well-suited for the assessment. Thus, both the new atlas-deformation and validation method should be analyzed in different cases. This is a difficult task since data sets containing such a lesions are hardly available.

8.4.3 Prior knowledge to guide the brain tissue segmentation

It has been seen that, in the brain tissue classification problem, the methods that include atlas information have not considerably improved the performance of the approaches that model local spatial priors. On the contrary, classification has shown to be highly sensitive to the registration errors or to the use of a wrong template. It has been seen also that the mixture tissues are particularly affected by the prior class template errors while pure tissue classification have been almost always improved by these methods. This is partially because the initial pure class templates are not precise

enough (the probability tissue templates used in this work are very smooth). However, the use of prior information is not discarded yet. The use of a more precise template that a priori contains all the tissues of interest (including the partial volume tissues) could be used. For instance, the ground truth used in this thesis could be a good prior tissue probability template. First, the registration between the phantom and the subject under study would be done. Then, the ground truth associated the phantom would be deformed with the transformation found in the first step and, after that, it would be largely smoothed to become a prior tissue probability map. The use of the ground truth as an a priori template should of course be assessed firstly by, for instance, studying some cases where the tissue classification was already known.

Some of the issues presented in this thesis will be further studied in our research group. Particularly, the problem of the atlas-based segmentation in the case of pathological brains and the use of prior knowledge to guide the registration process are included as key subjects of investigation of the Swiss Science National Foundation research project from 2003 to 2005.

Part VI

Annex

Notation



A.1 Registration

- f denotes the target image, also called *reference image* or *scene*.
- g is the image that will be transformed, also called *floating image* or *deformable model*.
- $\vec{P} = (x, y, z)$ and \vec{P}_{demon} denote the spatial position of a voxel and a demon point position in the 3D space respectively.
- N is the total number of voxels in an image.
- \vec{D} is the total displacement field associated to a voxel.
- $\vec{T} = \vec{P} + \vec{D}(\vec{P})$ is the transformation in a *Lagrangian* reference frame.
- \vec{d} is the *instantaneous* displacement field associated to a voxel.
- ϵ is the threshold of the intensity gradient norm that determines the demon points.
- \vec{v} is the motion vector.
- \vec{v}_p is the demon pushing force. Note that $\vec{d} = -\vec{v}$.
- $G(\sigma)$ denotes a Gaussian filter characterized by the parameter σ , called also *elasticity parameter*.
- T^* and T' denote the *direct* and *inverse* transformation fields, respectively.
- $R = T^* \circ T'$ is the *residual* vector field.
- α_i denotes the mean squared error (MSE) at an iteration i , m_i is the averaged MSE over the M past iterations, and q is an arbitrarily *quality* factor.
- \vec{S} is the voxel seed of a tumor.

- $\overrightarrow{DM}_{seed}$ is the distance map from the seed voxel to the tumor surface.
- \vec{d}_{lesion} denotes the instantaneous field inside the tumor.
- Nit denotes the number of iterations.

A.2 Classification

- $\mathcal{S} = \{1, 2, \dots, N\}$ is the set of indexes of the image.
- $\mathcal{N}_i, i \in \mathcal{S}$ is the set of sites neighboring the site i .
- $\mathbf{y} = \{y_1, y_2, \dots, y_N\} \in \mathcal{D}^N \subset \mathbb{R}^N$ is a configuration of Y , where $\mathcal{D} \subset \mathbb{R}$ is the state space representing the image intensity.
- $\mathcal{Y} = \{\mathbf{y} | y_i \in \mathcal{D}, i \in \mathcal{S}\}$ is the space of possible configurations.
- $Y = \{Y_i, i \in \mathcal{S}\}$ is the family of random variables.
- State space $\mathcal{L} = \{csf, cg, gm, gw, wm\}$ of all brain tissues.
- State space $\mathcal{L}_p = \{csf, gm, wm\}$ of pure tissues of the brain.
- $X = \{X_i, i \in \mathcal{S}\}$ is the family of random variables representing the underlying class labels indexed by \mathcal{S} .
- $\mathbf{x} = \{x_1, x_2, \dots, x_N\} \in \mathcal{L}^N$ denotes a configuration of X .
- $\mathcal{X} = \{\mathbf{x} | x_i \in \mathcal{L}, i \in \mathcal{S}\}$ is the space of possible configurations.
- $\theta = \{\mu, \sigma\}$ are the parameters, mean and variance, defining a Gaussian distribution that is denoted by $N(\mu, \sigma)$.
- $P(x)$ is the probability of x .
- $P(y|x)$ is the conditional probability.
- $P(y, x)$ is the joint probability.
- \mathbf{k} indexes the iterations in time.
- $U(\mathbf{x}, \beta)$ is the energy function of a Gibbs distribution and β is called *spatial* factor.
- Z is the normalization factor of the Gibbs distribution.
- $P_A(\mathbf{x})$ is the anatomical prior probability map.

MAP for GHMRF

B

The objective is to assign a tissue type label $x \in \mathcal{L}$ to each voxel in the image. A labelling of S is denoted by \mathbf{x} where $x_i, i \in S$ is the corresponding class label of voxel i . The true but unknown labelling configuration is denoted by \mathbf{x}^* , which is a particular realization of a random field X , which is an MRF with a specified distribution $P(\mathbf{x})$. The observable image itself is denoted by \mathbf{y} , which is a realization of a GHMRF as described in section 14. According to the MAP criterion (see Eq. 6.33), we can define the problem as:

$$\hat{\mathbf{x}} = \arg \max_{\mathbf{x} \in \mathcal{X}} \{P(\mathbf{y}|\mathbf{x})P(\mathbf{x})\}. \quad (\text{B.1})$$

The prior probability of the class and the likelihood probability of the observation need to be computed. As presented in Sec. 6.3.2, since \mathbf{x} is considered as a realization of an MRF, its prior probability can be derived from

$$P(\mathbf{x}) = \frac{1}{Z} \text{Exp}[-\beta U(\mathbf{x})]. \quad (\text{B.2})$$

The voxel intensity y_i is assumed to follow a Gaussian distribution with parameters $\theta_x = \{\mu_x, \sigma_x\}$, given the tissue type label x_i :

$$p(y_i|x_i) = g(y_i; \theta_{x_i}) = \frac{1}{\sqrt{2\pi\sigma_{x_i}^2}} \text{Exp} \left[-\frac{(y_i - \mu_{x_i}^2)}{2\sigma_{x_i}^2} \right]. \quad (\text{B.3})$$

Based on the conditional independence assumption of \mathbf{y} (see Eq. 6.17), the joint likelihood probability takes the form of

$$P(\mathbf{y}|\mathbf{x}) = \prod_{i \in S} p(y_i|x_i),$$

so,

$$P(\mathbf{y}|\mathbf{x}) = \prod_{i \in S} \left(\frac{1}{\sqrt{2\pi}} \text{Exp} \left[-\frac{(y_i - \mu_i^2)}{2\sigma_i^2} - \log(\sigma_{x_i}) \right] \right),$$

which can be written as

$$P(\mathbf{y}|\mathbf{x}) = \frac{1}{Z'} \text{Exp}[-U(\mathbf{y}|\mathbf{x})], \quad (\text{B.4})$$

with the *likelihood energy*

$$U(\mathbf{y}|\mathbf{x}) = \sum_{i \in S} U(y_i|x_i) = \sum_{i \in S} \left(\frac{(y_i - \mu_{x_i})^2}{2\sigma_{x_i}^2} + \log(\sigma_{x_i}) \right), \quad (\text{B.5})$$

and the constant normalization term $Z' = (2\pi)^{(\mathcal{N}/2)}$. It appears that

$$\log(P(\mathbf{x}|\mathbf{y})) \propto -U(\mathbf{x}|\mathbf{y}), \quad (\text{B.6})$$

where

$$U(\mathbf{x}|\mathbf{y}) = U(\mathbf{y}|\mathbf{x}) + U(\mathbf{x}) + \text{const} \quad (\text{B.7})$$

is the *posterior energy*. The MAP estimation is equivalent to minimizing the posterior energy function

$$\hat{\mathbf{x}} = \arg \min_{\mathbf{x} \in \mathcal{X}} \{U(\mathbf{y}|\mathbf{x}) + \beta U(\mathbf{x})\}. \quad (\text{B.8})$$

This minimization problem is mathematically simple but computationally infeasible. However, optimal solutions can be computed using iterative minimization techniques such as *iterated conditional modes (ICM)* [123].

Bibliography

- [1] (1991). The visible human project. http://www.nlm.nih.gov/research/visible/visible_human.html.
- [2] Y. Amit (1994). A nonlinear variational problem for image matching. *SIAM Journal on Scientific Computing* **15**(1):207–224.
- [3] P. Anandan (1989). A computational framework and an algorithm for the measurement of visual motion. *International Journal of Computer Vision* **2**:283–310.
- [4] J. Ashburner, K. Friston (1999). Nonlinear spatial normalization using basis functions. *Human Brain Mapping* **7**:254–266.
- [5] J. Ashburner, K. Friston (2000). Voxel-Based Morphometry - The Methods. *NeuroImage* **11**:805–821.
- [6] R. Bajcsy, S. Kovacic (1989). Multiresolution elastic matching. *Computer vision, Graphics and Image Processing* **46**:1–21.
- [7] R. Bajcsy, R. Lieberman, M. Reivich (1983). A computerized system for the elastic matching of deformed radiographic images to idealized atlas images. *Journal of Computer Assisted Tomography* **7**(4):618–625.
- [8] P. Basser, J. Mattiello, D. L. Bihan (1994). Mr diffusion tensor spectrography and imaging. *Biophys. J.* pp. 259–267.
- [9] C. Bernard (1999). *Wavelets and ill posed problems: optic flow and scattered data interpolation*. Ph.D. thesis, Ecole Polytechnique, France.
- [10] J. Besag (1974). Spatial interaction and the statistical analysis of lattice systems. *J. Roy. Stat. Soc.* **36**:192–326.
- [11] J. Besag (1986). On the statistical analysis of dirty pictures. *Journal of the Royal Statistical Society* **48**(3):259–302.
- [12] F. Bloch, W. Hansen, M. Packard (1947). Nuclear induction. *Phys. Rev.* **69**:127.
- [13] F. Bookstein (1989). Principal Warps: Thin-plate splines and the decomposition of deformations. *IEEE Transactions on Pattern Analysis and Machine Intelligence* **11**(6):567–585.
- [14] K. Bowyer, M. Loew, H. Stiehl, M. Viergever (2001). *Methodology of evaluation in medical image computing*. Tech. Rep. 301, Dagstuhl Seminar 01111, International Conference and Research Center for Computer Science.

-
- [15] M. Bro-Nielsen, C. Gramkow (1996). *Fast Fluid registration of medical images*, pp. 267–276. Lecture Notes in Computer Science, Springer Verlag, Berlin.
- [16] K. Brodmann (1909). *Vergleichende lokalizationslehre der Grosshirnrinde in ihren Prinzipien dargestellt auf Grund des Zellenbaues*. Leipzig, Barth, Germany.
- [17] L. G. Brown (1992). A survey of image registration techniques. *ACM Computing Surveys* **24**(4):325–376.
- [18] T. Butz (2003). *From error probability to information theoretic signal and image processing*. Ph.D. thesis, Signal Processing Institut, Swiss Federal Institut of Technology, Switzerland.
- [19] T. Butz, J.-P. Thiran (2002). Feature-space mutual information for multi-modal signal processing, with application to medical image registration. In *EUSIPCO*, Toulouse, France.
- [20] T. Butz et al. (2003). A new brain segmentation framework. In *Medical Image Computing and Computer-Assisted Intervention (MICCAI)*.
- [21] P. Cachier, X. Pennec, N. Ayache (1999). *Fast Non-Rigid Matching by Gradient Descent: Study and Improvements of the "Demons" Algorithm*. Tech. Rep. 3706, INRIA.
- [22] G. Celeux, F. Forbes, N. Peyrard (2002). *EM-based image segmentation using Potts models with external field*. Tech. Rep. 4456, INRIA.
- [23] B. Chalmond (2000). *Elements de modelization pour l'analyse d'images*. Springer-Verlag.
- [24] G. Christensen, R. Rabbitt, M. Miller (1996). Deformable templates using large deformations kinematics. *IEEE Transactions on Image Processing* **5**(10):1435–1447.
- [25] L. P. Clarke et al. (1995). Mri segmentation: Methods and applications. *Magnetic Resonance Imaging* **13**:343–368.
- [26] C. Clifford, K. Langley, D. Fleet (1995). Centre-frequency adaptative IIR temporal filters for phase information. *Image Processing and its Applications* **4**(6):173–177.
- [27] D. Collins et al. (1998). Design and construction of a realistic digital brain phantom. *IEEE Transactions on Medical Imaging* **17**(3):463–468. [Http://www.bic.mni.mcgill.ca/brainweb/](http://www.bic.mni.mcgill.ca/brainweb/).
- [28] T. F. Cootes, C. J. Taylor (2001). *Statistical Models of Appearance for Computer Vision*. Tech. rep., Wolfson Image Analysis Unit, University of Manchester.
- [29] O. Cuisenaire et al. (1996). Automatic Registration of 3D MR images with a Computerized Brain Atlas. In *SPIE Medical Imaging*, vol. 1719, pp. 438–449.
- [30] C. Davatzikos (1996). Spatial normalization of three-dimensional brain images using deformable models. *Journal of Computer Assisted Tomography* **20**(4):656–665.
- [31] B. Dawant et al. (1999). Automatic 3-D segmentation of internal structures of the head in MR images using a combination of similarity and free-form transformations : Part I, methodology and validation on normal subjects. *IEEE Transactions on Medical Imaging* **18**(10):902–916.
- [32] B. M. Dawant, S. L. Hartmann, S. Gadamsetty (1999). Brain Atlas Deformation in the Presence of Large Space-occupying Tumors. In *Medical Image Computing and Computer-Assisted Intervention*, pp. 589–596.

-
- [33] J. Dengler, M. Schmidt (1988). The dynamic pyramid - a model for motion analysis with controlled continuity. *International Journal of Pattern Recognition and Artificial Intelligence* **2**(2):275–286.
- [34] P.-F. D’Haese et al. (2003). Automatic segmentation of brain structures for radiation therapy planning. In *SPIE Medical Image Processing*.
- [35] R. O. Duda, P. E. Hart (1973). *Pattern Classification and Scene Analysis*. John Wiley and Sons.
- [36] M. Esiri, J. Morris (eds.) (2002). *The Neuropathology of Dementia*. Cambridge University Press.
- [37] A. Evans et al. (1994). Three-dimensional correlative imaging: applications in human brain mapping. *Functional Imaging: Technical Foundations* pp. 145–162.
- [38] M. Ferrant (2001). *Physics-based Deformable Modeling of Volumes and Surfaces for Medical Image Registration, Segmentation and Visualization*. Ph.D. thesis, Laboratoire de Télécommunications et Télédétection, Université Catholique de Lovain, Belgium.
- [39] K. Friston, J. Ashburner, J. H. C. D. Frith, J.-B. Poline, R. Frackowiak (1995). Spatial registration and normalization of images. *Human Brain Mapping* **2**:165–189.
- [40] C. J. Galten et al. (2001). Differing patterns of temporal atrophy in alzheimer’s disease and semantic dementia. *Neurology* **57**(2):216–225.
- [41] C. J. Galton et al. (2001). Temporal lobe rating scale: Application to alzheimer’s disease and frontotemporal dementia. *Journal of Neurology, Neurosurgery, and Psychiatry* **70**:165–173.
- [42] J. Gee et al. (1995). *Bayesian approach to the brain image matching problem*. Tech. Rep. 95-08, Inst. for Res. in Cogn. Sci.
- [43] S. Geman, D. Geman (1984). Stochastic relaxation, gibbs distributions, and the bayesian restoration of images. *IEEE Trans. Pattern Anal. Mach. Intell.* **PAMI-6**:721–741.
- [44] P. Golland (2001). *Spatial Encoding In MRI And How To Make It Faster*. Tech. rep., MIT Artificial Intelligence Laboratory. [Http://www.ai.mit.edu/people/polina/Papers/mri.pdf](http://www.ai.mit.edu/people/polina/Papers/mri.pdf).
- [45] C. Goodall (1991). Procrustes methods in the statistical analysis of shape. *Journal of Royal Statistical Society* **53**(2):285–339.
- [46] M. Gorno-Tempini et al. (2002). Patterns of cerebral atrophy in primari progressive aphasia. *American Journal of Psychiatry* **10**:89–97.
- [47] T. Greitz, C. Bohm, S. Holte, L. Eriksson (1991). A computerized brain atlas: construction, anatomical content and some applications. *Journal of Computer Assisted Tomography* **15**(1):26–38.
- [48] A. Guimond, J. Meunier, J.-P. Thirion (1999). *Average Brain Models: A Convergence Study*. Tech. Rep. 3731, INRIA.
- [49] A. Guimond, A. Roche, N. Ayache, J. Meunier (1999). *Multimodal Brain Warping Using the Demons Algorithm and Adaptive Intensity Corrections*. Tech. Rep. 3796, INRIA.

- [50] C. Guttman et al. (2000). White matter abnormalities in mobility-impaired older persons. *Neurology* **54**(6):1277–83.
- [51] P. Haese et al. (2003). Automatic segmentation of brain structures for radiation therapy planning. *Medical Imaging Conference SPIE* .
- [52] P. Hagmann et al. (2003). Dti mapping of human brain connectivity: Statistical fibre tracking and virtual dissection. *NeuroImage* .
- [53] J. Hajnal, D. Hill, D. Hawkes (eds.) (2001). *Medical Image Registration*. CRC Press.
- [54] J. Haller et al. (1997). 3d hippocampal morphometry by high dimensional transformation of a neuroanatomical atlas. *Radiology* **202**(2):504–510.
- [55] J. W. Haller (1999). *Brain Warping*, chap. Brain Templates, pp. 297–310. In [115].
- [56] B. A. Hargreaves (2001). *Spin-manipulation methods for efficient magnetic resonance imaging*. Ph.D. thesis, Department of Electrical Engineering, Stanford University, United States.
- [57] T. Hartkens et al. (2003). Measurement and analysis of brain deformation during neurosurgery. *IEEE Transactions on Medical Imaging* **33**(1):82–92.
- [58] P. Hellier (2000). *Recalage non rigide en imagerie cerebrale: methodes et validation*. Ph.D. thesis, École doctorale, Irista, Rennes, France.
- [59] J. R. Hesselink (1996). Basic principles of mr imaging. <http://spinwarp.ucsd.edu/NeuroWeb/>.
- [60] K. Hohne et al. (1992). A volume based anatomical atlas. *IEEE Computer Graphics and Applications* **12**(4):72–78.
- [61] B. Horn, B. Schunck (1981). Determining optical flow. *Artificial Intelligence* **17**:185–204.
- [62] B. Horwitz, K. Friston, J. Taylor (2000). Neural modeling and functional brain imaging: an overview. *Neural Networks* **13**(Special Issue):829–846.
- [63] J. West et al. (1997). Comparison and evaluation of retrospective intermodality brain image registration techniques. *Journal of Computer Assisted Tomography* **21**(4):554–566.
- [64] L. Jonasson et al. (2003). White matter mapping in dt-mri using geometric flows. *Eurocast: 9th International Workshop in Computer Aided Systems Theory* pp. 80–82.
- [65] M. Kaus et al. (1999). Segmentation of Meningiomas and Low Grade Gliomas in MRI. In *Medical Image Computing and Computer-Assisted Intervention*, pp. 1–10. [Http://spl.bwh.harvard.edu:8000/warfield/tumorbase/tumorbase.html](http://spl.bwh.harvard.edu:8000/warfield/tumorbase/tumorbase.html).
- [66] B. Kim, J. Boes, K. Frey, C. Meyer (1997). Mutual information for automated unwarping of rat brain autoradiographs. *Neuroimage* **5**(1):31–40.
- [67] S. Kyriacou, C. Davatzikos (1999). Nonlinear elastic registration of brain images with tumor pathology using a biomechanical model. *IEEE Trans. Med. Imaging* **18**(7):580–592.
- [68] P. Lauterbur (1973). Image formation by induced local interactions: Examples employing nuclear magnetic resonance. *Nature* **242**:190–191.

- [69] K. V. Leemput (2001). *Quantitative Analysis of Signal Abnormalities in MRI imaging for Multiple Sclerosis and Creutzfeldt-Jacob Disease*. Ph.D. thesis, Faculteit Toegepaste Wetenschappen, Faculteit Geneeskunde, Katholieke Universiteit Leuven, Belgium.
- [70] K. V. Leemput, F. Maes, D. Vandermeulen, P. Suetens (1999). Automated model-based bias field correction of mr images of the brain. *IEEE Transactions on Medical Imaging* **18**:885–896.
- [71] K. V. Leemput, F. Maes, D. Vandermeulen, P. Suetens (2003). A unifying framework for partial volume segmentation of brain mr images. *IEEE Transactions on Medical Imaging* **22**:105–119.
- [72] H. Lemke et al. (eds.) (2002). *White paper: Validation of Medical Image Processing in Image-guided Therapy*. Computer Assisted Radiology and Surgery (CARS), Paris, France.
- [73] H. Lester, S. Arridge (1999). A survey of hierarchical non-linear medical image registration. *Pattern Recognition* **32**(1):129–149.
- [74] M. Bach Cuadra and O. Cuisenaire and R. Meuli and J.-Ph. Thiran (2001). Automatic segmentation of internal structures of the brain in MRI using a tandem of affine and non-rigid registration of an anatomical atlas. In *International Conference in Image Processing (ICIP)*.
- [75] M. Bach Cuadra, B. Platel, E. Solanas, T. Butz, J.-Ph. Thiran (2002). Validation of Tissue Modelization and Classification Techniques in T1-Weighted MR Brain Images. In *In Medical Image Computing and Computer-Assisted Intervention (MICCAI)*, pp. 290–297.
- [76] M. Bach Cuadra, C. Pollo, A. Bardera, O. Cuisenaire, J.-G. Villemure, J.-Ph. Thiran (2003). Atlas-Based Segmentation of Pathological Brain MR Images. In *International Conference in Image Processing (ICIP)*.
- [77] M. Bach Cuadra, J. Gomez, P. Hagmann, C. Pollo, J.-G. Villemure, B. M. Dawant, J.-Ph. Thiran (2002). Atlas-Based Segmentation of Pathological Brains Using a Model of Tumor Growth. In *In Medical Image Computing and Computer-Assisted Intervention (MICCAI)*, pp. 380–387.
- [78] B. Mackiewich (1995). *Intracranial Boundary Detection and Radio Frequency Correction in Magnetic Resonance Images*. Ph.D. thesis, School of Computing Science, University of British Columbia, Canada.
- [79] J. A. Maintz, M. A. Viergever (1998). A survey of medical image registration. *Medical Image Analysis* **2**(1):1–36.
- [80] C. R. Maurer et al. (1998). Investigation of intraoperative brain deformation using a 1.5t interventional mr system: preliminary results. *IEEE Transactions on Medical Imaging* **17**(5):817–825.
- [81] J. C. Mazziotta, A. W. Toga, R. S. J. Frackowiak (2000). *Brain Mapping: The Disorders*. Academic Press.
- [82] M. Miller, G. Christensen, Y. Amit, U. Grenander (1993). Mathematical textbook of deformable neuroanatomies. *Proc. Nat. Acad. Sci.* pp. 11944–11948.
- [83] M. Nielsen, L. Florack, R. Deriche (1994). *Regularization and Scale Space*. Tech. Rep. 2352, INRIA.

-
- [84] A. Noe, J. C. Gee (2001). Partial volume segmentation of cerebral mri scans with mixture model clustering. In *Information Processing in Medical Imaging: 17th International Conference (IPMI)*.
- [85] A. Noe, S. Kovacic, J. C. Gee (2001). Segmentation of cerebral mri scans using a partial volume model, shading correction, and an anatomical prior. In *SPIE Medical Image Processing*.
- [86] W. Nowinski et al. (1997). Multiple brain atlas database and atlas-based neuroimaging system. *Computer Aided Surgery* **2**(1):42–46.
- [87] P. Hellier et al. (2001). Retrospective evaluation of inter-subject brain registration. *Medical Image Computing and Computer-Assisted Intervention* pp. 258–265.
- [88] P. Hellier et al. (2003). Retrospective evaluation of inter-subject brain registration. *IEEE Transactions on Medical Imaging* **22**(9):1120–1130.
- [89] N. Peyrard (2001). *Approximations de type champ moyen des modèles de champ de Markov pour la segmentation de données spatiales*. Ph.D. thesis, Université J. Fourier, Grenoble.
- [90] W. H. Press, B. P. Flannery, S. A. Teukolsky, W. T. Vetterling (2002). Numerical recipes in c.
- [91] E. Purcell, H. Torrey, R. V. Pound (1946). Resonance absorption by nuclear magnetic moments in solid. *Phys. Rev.* **69**:37–38.
- [92] R. Kikinis et al. (1996). A digital brain atlas for surgical planning, model driven segmentation and teaching. *IEEE Transactions on Visualization and Computer Graphics* **2**(3). [Http://splweb.bwh.harvard.edu:8000](http://splweb.bwh.harvard.edu:8000).
- [93] D. Rey, G. Subsol, H. Delingette, N. Ayache (2002). Automatic detection and segmentation of evolving processes in 3d medical images: Application to multiple sclerosis. *Medical Image Analysis* **6**(2):163–179.
- [94] S. Ruan, C. Jaggi, J. Xue, J. Bloyet (2000). Brain tissue classification of magnetic resonance images using partial volume modeling. *IEEE Transactions on Medical Imaging* **19**(12):172–186.
- [95] D. Rueckert, A. Frangi, J. Schnabel (2001). Automatic construction of 3d statistical deformation models using non-rigid registration. In *Medical Image Computing and Computer-Assisted Intervention (MICCAI)* **2208**:77–84.
- [96] D. Rueckert et al. (1999). Non-rigid registration using free-form deformations: Application to breast MR images. *IEEE Transactions on Medical Imaging* **18**(8):712–721.
- [97] P. Santago, H. D. Gage (1993). Quantification of mr brain images by mixture density and partial volume modeling. *IEEE Trans. Medical Imaging* **12**:566–574.
- [98] G. Schaltenbrand, W. Wahren (1977). *Guide of the Atlas for Stereotaxy of the Human Brain*. Thieme Stuttgart, New York.
- [99] J. A. Schnabel et al. (2001). Validation of non-rigid registration using finite element methods. In Lecture Notes in Computer Science, Springer Verlag, Berlin (ed.), *Information Processing in Medical Imaging (IPMI)*, pp. 345–358.

-
- [100] P. Schroeter (1996). *Unsupervised two-dimensional and three-dimensional image segmentation*. Ph.D. thesis, Laboratoire de Traitement des signaux, École Polytechnique Fédérale de Lausanne.
- [101] P. Schroeter, et al. (1998). Robust parameter estimation of intensity distributions for brain magnetic resonance images. *IEEE Transactions on Medical Imaging* **17**(2):172–186.
- [102] R. Seitz et al. (1990). Accuracy and precision of the computerized brain atlas programme for localization and quantification in positron emission tomography. *Journal of Cerebral Blood Flow and Metabolism* **10**(4):443–457.
- [103] D. W. Shattuck et al. (2001). Magnetic resonance image tissue classification using a partial volume model. *NeuroImage* **13**:856–876.
- [104] S.K. Warfield et al. (2001). A binary entropy measure to assess nonrigid Registration algorithms. *MICCAI* pp. 266–274.
- [105] G. Szekely, A. Kelemen, A. Brechbuhler, G. Gerig (1996). Segmentation of 2d and 3d objects from mri volume data using constrained elastic deformations of flexible fourier surface models. *Medical Image Analysis* **1**(1).
- [106] J. Talairach, P. Tournoux (1988). *Coplanar stereotaxis atlas of the human brain*. Stuttgart: Mark Rayport, Trans. Thieme.
- [107] J. Talairach et al. (1957). *Atlas d’anatomie stereotaxique des noyaux gris centraux*. Paris: Masson.
- [108] J. Thirion, G. Calmon (1999). Deformation analysis to detect and quantify active lesions in three-dimensional medical image sequences. *IEEE Transactions on Medical Imaging* **18**(5):429–441.
- [109] J.-P. Thirion (1995). *Fast Non-Rigid Matching of 3D Medical Images*. Tech. Rep. 2547, INRIA.
- [110] J.-P. Thirion (1998). Image matching as a diffusion process: an analogy with Maxwell’s demons. *Medical Image Analysis* **2**(3):243–260.
- [111] P. Thompson, A. W. Toga, M. S. Mega (2000). *Brain Mapping: The Disorders*, chap. Disease-Specific Brain Atlases. In [81].
- [112] P. Thompson et al. (2000). Growth patterns in the developing brain detected by using continuum mechanical tensor maps. *Nature* **404**:190–193.
- [113] L. Thurjfell, C. Bohm, T. Greitz, L. Eriksson (1993). Transformations and algorithms in a computerized brain atlas. *IEEE Transactions on Nuclear Sciences* **40**:1187–1191.
- [114] A. Tikhonov, V. Arsenin (1977). *Solutions of Ill-Posed Problems*. Winston and Salem, Washington, DC.
- [115] A. W. Toga (1999). *Brain Warping*. Academic Press.
- [116] A. W. Toga, M. S. Mega, P. Thompson (2002). *The Neuropathology of Dementia*, chap. Neuroimaging Alzheimer’s Disease. In [36].
- [117] M. Unser, A. Aldroubi, M. Eden (1993). B-spline signal processing: Part I - Theory. *IEEE Transactions on Signal Processing* **41**(2):821–832.

-
- [118] P. A. van den Elsen, E.-J. D. Pol, M. A. Viergever (1993). Medical image matching - a review with classification. *IEEE Engineering in Medicine and Biology* (12):26–39.
- [119] S. K. Warfield, M. Kaus, F. A. Jolesz, R. Kikinis (2000). Adaptive, Template Moderated, Spatially Varying Statistical Classification. *Medical Image Analysis* 4(1):43–55.
- [120] W. Wells, R. Kikinis, W. Grimson, F. Jolesz (1996). Adaptive segmentation of mri data. *IEEE Transactions on Medical Imaging* 15:429–442.
- [121] R. Woods et al. (1999). Creation and use of a talairach-compatible atlas for accurate, automated, nonlinear intersubject registration, and analysis of functional imaging data. *Human Brain Mapping* 8(2-3):73–79.
- [122] T. Yoo, M. Ackerman, M. Vannier (2000). Toward a common validation methodology for segmentation and registration algorithms. *Proc. of Medical Image Computing and Computer-Assisted Intervention 2000, Lecture Notes in Computer Science* 1935:422–431.
- [123] Y. Zhang, et al. (2001). Segmentation of brain mr images through a hidden markov random field model and the expectation-maximization algorithm. *IEEE Trans. Medical Imaging* 20:45–57.

Curriculum Vitæ

Name: Meritxell Bach Cuadra
Citizenship: Spanish
Birthdate: June 9, 1975
Birthplace: Barcelona, Spain
Marital status: Single



Contact information

Address: Chemin des Clochetons 16
1004 Lausanne, Switzerland
Phone: +41 21 693 56 52
Fax: +41 21 693 76 00
Email: Meritxell.Bach@epfl.ch

Work experience

- **December 1999 – present:** research assistant, Swiss Federal Institute of Technology (EPFL), Lausanne, Switzerland
 - Development of registration and segmentation algorithms within medical image analysis framework.
 - Teaching: supervision of master thesis and responsible of exercises and laboratory of the Image Processing and Pattern Recognition courses.
- **2002:** Organization of IEEE International Conference on Multimedia and Expo (ICME).
 - Member of the technical support group and responsible of material distribution.
 - Collaboration in the registration desk.
- **1998-1999:** Technical engineer at Communication Laboratory in Universitat Politècnica de Catalunya (UPC).
 - Responsible of the material maintenance of the laboratory.
 - Evaluation and supervision of precision devices.

Education

- **December 1999 – 2003:** *Ph. D student* in biomedical image processing. Swiss Federal Institute of Technology (EPFL), Lausanne, Switzerland.
- **March 1999 – September 1999:** *Master Thesis* as Erasmus student in Investigation of excitation models and de-embedding techniques for wire antennas and line-fed microstrip patch antennas at Electromagnetism and Acoustic Laboratory (LEMA), EPFL.
- **January 1993 – February 1999:** *Electrical Engineer*. Orientation: Telecommunications. Escola Superior d'Enginyeria de Telecomunicacions de Barcelona (ETSETB), Universitat Politècnica de Catalunya (UPC).

Post-graduate Education

- 5th IEEE EMBS International Summer School on Biomedical Imaging, Berder Island, France, 2002.
- Symposia in Interactive Medical Image Visualization and Analysis, MICCAI 2001, Utrecht.

Skills

Languages

Catalan:	mother tongue
Spanish:	mother tongue
English:	fluent oral and written
French:	fluent oral and written

Computing

Operating systems:	Linux, Unix, Windows
Programming languages:	C, C++, MPI
Other:	HTML, LaTeX, Matlab, CVS

Extra-curricular Activities

- Water polo: 2nd Swiss league player with Lausanne Waterpolo Club (since October 2001).
- Swimming: competition level (from 1985 until 1991).
- Cinema: classic movies.

Publications

- M. Bach Cuadra, C. Pollo, A. Bardera, O. Cuisenaire, J.-G. Villemure, and J.-P. Thiran. 'Atlas-Based Segmentation of Pathological Brains MR Images'. *International Conference on Image Processing, ICIP 2003*. Barcelona, Spain.

-
- T. Butz, M. Bach Cuadra, and J.-Ph. Thiran. 'From Error Probability to Information Theoretic Classification'. *Submitted to IEEE Transactions on Pattern Analysis and Machine Intelligence*.
 - M. Bach Cuadra, C. Pollo, A. Bardera, O. Cuisenaire, J.-G. Villemure, and J.-Ph. Thiran. 'Atlas-based Segmentation of Pathological MR Brain Images using a Model of Lesion Growth'. *Submitted to IEEE Transactions on Medical Imaging*.
 - Meritxell Bach Cuadra, Bram Platel, Eduardo Solanas, Torsten Butz, and Jean-Philippe Thiran. 'Validation of Tissue Modelization and Classification Techniques in T1-Weighted MR Brain Images'. *Medical Image Computing and Computed Assisted Intervention, MICCAI 2002*, pp. 290-297; Tokyo; Japan; 2002.
 - Meritxell Bach Cuadra, Jesus Gomez, Patric Haggmann, Claudio Pollo, J.-G. Villemure, B. M. Dawant, and Jean-Philippe Thiran. 'Atlas-Based Segmentation of Pathological Brains Using a Model of Tumor Growth'. *Medical Image Computing and Computed Assisted Intervention, MICCAI 2002*. pp. 380-387; Tokyo; Japan; 2002.
 - Meritxell Bach Cuadra, Olivier Cuisenaire, Reto Meuli and Jean-Philippe Thiran. 'Automatic Segmentation of Internal Structures of the Brain in MR Images using a Tandem of Affine and Non-Rigid Registration of an Anatomical Brain Atlas'. *International Conference on Image Processing, ICIP 2001*, Thessalonica, October 2001.
 - Eric Suter, Meritxell Bach Cuadra, and JuanR.Mosig. 'A Comparative Study of the Input Parameter De-embedding Techniques for Integral Equation Methods'. *European Congress on Computational Methods in Applied Sciences and Engineering, ECCOMAS 2000*, Barcelona, September 2000.